



RESEARCH & DEVELOPMENT

Mechanically-Fastened FRP to Retrofit Existing Prestressed Concrete Bridge Beams

**Sheng-Hsuan Lin, PhD
Rudolf Seracino, PhD
Brad McCoy, PhD, PE
Zakariya Bourara, EIT
Gregory Lucier, PhD**

**Department of Civil, Construction, and Environmental
Engineering
North Carolina State University**

NCDOT Project 2018-16

FHWA/NC/2018-16

June 2022

**Mechanically-Fastened FRP to Retrofit Existing
Prestressed Concrete Bridge Beams**

Principal Investigator Dr. Rudolf Seracino

Key Researcher Dr. Gregory Lucier

Research Assistants Dr. Sheng-Hsuan Lin

Dr. Brad McCoy

Mr. Zakariya Bourara

Department of Civil, Construction, and Environmental Engineering
North Carolina State University
Raleigh, NC

Prepared for:
North Carolina Department of Transportation
Research and Development Unit

June, 2022

Technical Report Documentation Page

1. Report No. FHWA/NC/2018-16	2. Government Accession No.	3. Recipient's Catalog No.	
4. Title and Subtitle Mechanically-Fastened FRP to Retrofit Existing Prestressed Concrete Bridge Beams		5. Report Date June, 2022	
		6. Performing Organization Code	
7. Author(s) Sheng-Hsuan Lin, Rudolf Seracino, Brad McCoy, Zakariya Bourara, Gregory Lucier		8. Performing Organization Report No.	
9. Performing Organization Name and Address North Carolina State University Department of Civil, Construction, and Environmental Engineering Raleigh, NC 27695-7908		10. Work Unit No. (TRAIS)	
		11. Contract or Grant No.	
12. Sponsoring Agency Name and Address North Carolina Department of Transportation Research and Development Unit 1020 Birch Ridge Drive Raleigh, North Carolina 27610		13. Type of Report and Period Covered Final Report August, 2017 – June 2022	
		14. Sponsoring Agency Code NCDOT Project 2018-16	
Supplementary Notes:			
16. Abstract Prestressed concrete (PC) C-channel and cored slab bridges have been in-service in North Carolina for more than 40 years. Increasing numbers of these bridges have deteriorated due to corrosion of the prestressing strands, overload traffic, and natural aging, to the extent that they require load-posting or closure before superstructure replacement can be scheduled. The research program presented herein developed a rapid and easy-to-install repair using a prestressed mechanically-fastened fiber-reinforced polymer (MF-FRP) system. It has been shown through full-scale experimental testing that the system improves the response of repaired deteriorated bridge beams such that inventory and operating load limits can be increased by restoring the lost prestress from the corroded steel strands. Critical components of the MF-FRP repair system were developed through a series of small-scale tests to optimize the efficiency and installation of the system. The long-term behavior of the MF-FRP system, including sustained load and fatigue effects, were also studied to help quantify the expected service life of the repair. A layered-sectional analysis approach (LSA) was developed and shown to give a good prediction of the full flexural behavior of repaired C-channel beams and cored slabs. In addition to flexural deterioration, deterioration at the end region of C-channel beams, which was recently observed on-site, was also considered in the design of the MF-FRP system. A shear strengthening plate was designed to integrate with the original flexural MF-FRP repair system at the end regions. Full-scale C-channel beams were tested to study the member shear behavior using the flexural/shear MF-FRP repair system. Finally, a field application using the designed MF-FRP system was conducted on an in-service deteriorated C-channel bridge, along with instrumentation to enable long-term monitoring. The repair system remains in good and stable condition after being in-service for more than one year.			
17. Key Words Prestressed concrete bridge beams; deterioration; FRP; mechanically-fastened; repair; retrofit		18. Distribution Statement	
19. Security Class if. (of this report) Unclassified	20. Security Class if. (of this page) Unclassified	21. No. of Pages 346	22. Price

Form DOT F 1700.7 (8-72)

Reproduction of completed page authorized

DISCLAIMER

The contents of this report reflect the views of the authors and not necessarily the views of the University. The authors are responsible for the facts and the accuracy of the data presented herein. The contents do not necessarily reflect the official views or policies of either the North Carolina Department of Transportation or the Federal Highway Administration at the time of publication. This report does not constitute a standard, specification, or regulation.

ACKNOWLEDGMENTS

The research team would like to thank the North Carolina Department of Transportation Steering and Implementation Committee who oversaw this project. The Steering and Implementation Committee included the following members:

Brian Hanks (Chair)
Gichuru Muchane
Trey Carroll
Daniel Muller
Tim Sherril
Chris Peoples
Brian Hunter
Cabell Garbee
Michael Pettijohn
Wendy McAbee (FHWA)
Neil Mastin
Mustan Kadibhai

Additional thanks go to Mr. William Briley of the NCDOT Division 5 Bridge Maintenance Division in Wake County, NC, for providing the C-channel beams used for the full-scale testing. Thanks also to Mr. Adam Britt and Mr. Matt Spell and his team of the NCDOT Division 3 Bridge Maintenance Division in Sampson County, NC, for providing the opportunity to repair a deteriorated C-channel bridge using the proposed repair system.

Lastly, the research team would like to thank technicians Mr. Jerry Atkinson and Mr. Johnathan McEntire at NC State's Constructed Facilities Laboratory (CFL) for their help with the laboratory testing.

EXECUTIVE SUMMARY

Prestressed concrete C-channel and cored slab bridges have been in-service in North Carolina for more than 40 years. Increasing numbers of these bridges have deteriorated due to corrosion of the prestressing strands, overload traffic, and natural aging, to the extent that they require load-posting or closure before superstructure replacement can be scheduled. The research program presented herein developed a rapid and easy-to-install repair using a prestressed mechanically-fastened fiber-reinforced polymer (MF-FRP) system.

The MF-FRP is designed to restore the lost prestress force due to corroded strands so that inventory and operating load rating limits may be increased until such time that the bridge superstructure may be scheduled for replacement. A research program was undertaken to optimize the structural efficiency of critical components of the MF-FRP repair system, considering ease of installation, inspection and monitoring. Critical elements of the system were subjected to long-term sustained loading and cyclic fatigue loading to help quantify the expected service life of the repair. Both flexural and shear deterioration was considered and the performance was demonstrated through full-scale testing of C-channel and cored slab beams taken from previously in-service bridges. A layered-sectional analysis procedure was developed to predict the full flexural behavior of repaired C-channel beams and cored slabs. Simplified analysis procedures were also developed suitable for load rating assessment.

Specific details of the MF-FRP repair system are summarized in the following. A comprehensive series of small-scale tests was undertaken to maximize the useable capacity of the MF-FRP system. The tensile capacity of the system using the commercially available SAFSTRIP Strengthening Strip manufactured by Strongwell is 46.4 kips using the designed 22-bolt pattern with 0.5 in. diameter bolts. Using a turnbuckle system the MF-FRP system may be prestressed to

a level of 22 kips, similar to the jacking force of the steel prestressing strand used in typical C-channel and cored slab beams. Specimens with sustained load of 22 kips showed that the MF-FRP connection experienced creep due to bolt bearing within the first 14 days after installation. The ultimate tensile capacity was unaffected after 30 months of sustained loading. Premature fatigue failure can be avoided by using a 60 ft.-lb. torque to tighten the 0.5 in. diameter bolts, with 454,000 cycles of load (ranging between 22 kips and 29 kips) before failure. It is likely the fatigue life is longer than this limit as the actual cyclic load range on the MF-FRP system in the field is less. The flexural MF-FRP repair system was successfully tested on six C-channel beams and five cored slabs taken from previously in-service bridges. Overall, the flexural performance was enhanced and the flexural capacity increased compared to that of deteriorated beams. A layered-sectional analysis (LSA) procedure was developed and shown to give good predictions of the full flexural behavior of repaired C-channel beams and cored slabs. The ultimate capacity of the repaired C-channel beams and cored slabs predicted by the LSA was within 5% of the experimental results. The shear behavior of deteriorated C-channel beams was quantified through full-scale experimental testing and a shear strengthening plate that is integrated with the flexural MF-FRP repair system was developed to improve the behavior of shear deteriorated C-channel beams. It was observed experimentally that even severe levels of shear deterioration did not affect the flexural behavior. A field repair application using the designed MF-FRP system was successfully installed by an NCDOT crew on an in-service deteriorated C-channel bridge. The bridge was reopened following installation of the repair. Long-term monitoring is being conducted on the repaired C-channel bridge. The system remains in good condition after being in-service for more than 1 year.

TABLE OF CONTENTS

DISCLAIMER	iv
ACKNOWLEDGMENTS	v
EXECUTIVE SUMMARY	vi
TABLE OF CONTENTS	viii
LIST OF TABLES	xiv
LIST OF FIGURES	xvi
CHAPTER 1 – INTRODUCTION.....	1
1.1 – Background	1
1.2 – Research Objective.....	5
1.3 – Research Phases and Intermediate Research Objectives.....	8
1.4 – Layout of Report	11
CHAPTER 2 – LITERATURE REVIEW.....	14
2.1 – Fiber-Reinforced Polymer Strengthening Systems	14
2.1.1 – Externally-Bonded Fiber Reinforced Polymer.....	14
2.1.2 – Mechanically-Fastened Fiber-Reinforced Polymer.....	16
2.1.3 – Prestressed Fiber Reinforced Polymer	21
2.2 – Long-Term Behavior of MF-FRP	23
2.2.1 – Cyclic Loading	23
2.2.2 – Sustained Loading	26
2.3 – Prestressed Concrete Members with Unbonded Tendons.....	26
2.3.1 – Internal Unbonded Tendons	27
2.3.2 – External Unbonded Tendons	27
2.4 – Shear Strengthening of Concrete Beam Members	30
2.4.1 – Shear Strengthening using Fiber Reinforced Polymer (FRP)	31
2.4.2 – Shear Strengthening using Steel Plates	32
2.5 – Summary of the Literature Review	34
CHAPTER 3 – ANCHOR BOLT PATTERNS FOR MACHANICALLY FASTENED FRP PLATES	36
3.1 – Methodology	36

3.1.1 – Test Treatment Groups	36
3.1.2 – Number of Replicates for Each Test	38
3.1.3 – Instrumentation.....	42
3.1.4 – Tension Test Treatments and Specimen Preparation	43
3.1.5 – Universal Testing Machine Tension Test Setup.....	46
3.2 – Results and Discussion.....	48
3.2.1 – No-Hole Treatment Condition.....	50
3.2.2 – Open-Hole Treatment Condition.....	51
3.2.1.1 – Single-Hole Condition	51
3.2.1.2 – Aligned and Staggered Hole Conditions.....	53
3.2.3 – Bolt-Bearing Treatment Condition.....	54
3.2.3.1 – Single-Bolt Bearing	54
3.2.3.2 – Multi-Bolt Bearing.....	59
3.2.3.3 – Multi-Bolt Bearing with different bolt diameter.....	66
3.3 – Observations	72
CHAPTER 4 – LONG-TERM BEHAVIOR OF ANCHOR BOLT DESIGN	75
4.1 – Sustained Loading	75
4.1.1 – Strongwall Configuration	76
4.1.2 – Loading Requirements.....	77
4.1.3 – Construction and Assembly.....	80
4.1.4 – Hydraulic Circuit	83
4.1.5 – Measuring Creep	84
4.1.6 – Test Matrix	84
4.1.7 – Results	85
4.1.7.1 – Displacement over Time	85
4.1.7.2 – Residual Capacity	91
4.1.8 – Observations	96
4.2 – Cyclic Loading	96
4.2.1 – Cycling Range	98
4.2.2 – Experimental Program and Results	102
4.2.3 – Case Study	112

4.2.4 – Observations	114
4.3 – Assessment of Long-Term Performance by Bridge Inspection	114
CHAPTER 5 – FULL-SCALE FLEXURAL EXPERIMENTS	117
5.1 – MF-FRP Retrofit Design	117
5.1.1 – MF-FRP 1.0	117
5.1.2 – MF-FRP 2.0	120
5.1.3 – Concrete Splitting	123
5.1.4 – Post-Tensioning	124
5.2 – Experimental Program – C-Channel Beams	127
5.2.1 – Test Setup, Instrumentation, and Procedure	129
5.2.2 – Experimental Results	130
5.3 – Experimental Program – Cored Slabs	136
5.3.1 – Test Setup and Test Matrix	137
5.3.2 – Retrofit Application Procedure	139
5.3.3 – Experimental Results	141
5.4 – Observations	150
5.4.1 – C-channel Beams	150
5.4.2 – Cored Slabs	151
CHAPTER 6 – ANALYTICAL FLEXURAL MODELING OF RETROFITTED C- CHANNEL BEAMS AND CORED SLABS	153
6.1 – Modeling of Repaired C-Channel Beams	153
6.1.1 – Constitutive Models	161
6.1.1.1 – Concrete	161
6.1.1.2 – Prestressing Strand	168
6.1.1.3 – Reinforcement Steel	171
6.1.1.4 – MF-FRP	172
6.1.2 – Modeling Challenges	173
6.1.2.1 – Prestressing Strand Profile	173
6.1.2.2 – Total Prestress Losses	174
6.1.2.2.1 – Measuring Total Prestress Losses using Strand Cutting Method	176

6.1.2.2.2 – Measuring Total Prestress Losses using the Cracking Moment Method.....	178
6.1.2.2.3 – Calculated Prestress Losses using Design Guide.....	181
6.1.2.3 – Development Length.....	184
6.1.2.4 – Modeling Damage Condition.....	186
6.1.3 – Results and Comparison of Repaired C-channel Beams	187
6.2 – Modeling of Repaired Cored Slabs	191
6.2.1 – Modeling Procedure	191
6.2.2 – Modeling Challenges	194
6.2.2.1 – Prediction of Failure Point	195
6.2.2.2 – Contact at Midspan	196
6.2.2.3 – Prediction of Camber	196
6.2.3 – Comparison to Experimental Results	197
6.2.3.1 – Undamaged-Unstrengthened.....	197
6.2.3.2 – Damaged-Unstrengthened 1.....	198
6.2.3.3 – Damaged-Unstrengthened 2.....	198
6.2.3.4 – Damaged-Strengthened 1.....	199
6.2.3.5 – Damaged-Strengthened 2.....	200
6.2.4 – Ultimate Strength Analysis.....	201
6.3 – Observations	204
6.3.1 – Repaired C-Channel Beams	204
6.3.2 – Repaired Cored Slabs	205
CHAPTER 7 – DESIGN AND VALDATON OF A SHEAR STRENGTHENING SYSTEM FOR C-CHANNEL BEAMS	207
7.1 – Design of the Shear Strengthening System	208
7.2 – Experimental Program.....	210
7.2.1 – C-channel Beams.....	210
7.2.2 – Failure Envelope of the PC C-channel Beam.....	211
7.2.2.1 – Moment Envelope.....	211
7.2.2.2 – Shear Envelope	212
7.2.2.3 – Failure Envelope	213

7.2.3 – Test Setup and Instrumentation	215
7.2.4 – Test Matrix	218
7.2.4.1 – Specimen ID Nomenclature	218
7.2.4.2 – Test Description	219
7.2.5 – Specimen Preparation	223
7.2.5.1 – Control Specimens	223
7.2.5.2 – Retrofitted Specimens	224
7.2 – Experimental Results.....	229
7.2.1 – C-U-S2.....	231
7.2.2 – C-U-S1.....	233
7.2.3 – C-IDS-S1	235
7.2.4 – C-DS-S1	238
7.2.5 – S-DS-S1-F	239
7.2.6 – S-DS-S1-FS	242
7.2.7 – S-DFS-F-FS	244
7.3 – Predicted Shear Capacity of Unstrengthened Specimens.....	250
7.4 – Observations	254
CHAPTER 8 – RETROFIT OF AN IN-SERVICE DETERIORATED PC	
C-CHANNEL BRIDGE.....	256
8.1 – Condition Assessment of Bridge 810003	257
8.2 – Retrofit Design	259
8.3 – Retrofit Procedure	261
8.4 – Long-term Monitoring.....	266
8.5 – Results and Discussions	269
8.5.1 – Beam Camber	269
8.5.2 – FRP Elongation	269
8.5.3 – FRP Strain – Long-term behavior and Temperature Effect	271
8.5.4 – Prestressed MF-FRP Retrofit System.....	276
8.5.5 – Cost Benefits	277
8.6 – Observations and Repair Application Recommendations.....	278
8.6.1 – Observations	278

8.6.2 – Repair Application Recommendations	279
CHAPTER 9 – CONCLUSIONS AND RECOMMENDATIONS	281
9.1 – Conclusions	281
9.1.1 – Anchor Bolt Pattern for MF-FRP Plate	281
9.1.2 – Long-term Behavior	281
9.1.3 – Full-scale Flexural Experiments	283
9.1.3.1 – Repaired C-channel Beams	283
9.1.3.2 – Repair Cored Slabs	283
9.1.4 – Analytical Modeling	284
9.1.4.1 – C-channel Beams	284
9.1.4.2 – Cored Slabs	285
9.1.5 – Full-scale Testing and Modeling of Shear Deteriorated C-channel Beams	285
9.1.6 – Field Application	287
9.2 – Design Recommendations, and Field Inspection	288
9.2.1 – Design Recommendations	288
9.2.2 – Field Inspection	289
9.3 – Recommendations for Future Work	290
REFERENCES	291
APPENDICES	298
Appendix A: Detailed Installation Procedure of the MF-FRP Repair System	299

LIST OF TABLES

Table 2.1: Advantages and disadvantages of FRP systems.	16
Table 2.2: MF-FRP literature summary (adopted from Martinelli et al., 2014).	18
Table 3.1: Test matrix.	38
Table 3.2: Data provided by the manufacturer.	41
Table 3.3: Calculated data and sample size for 90% CL.	42
Table 3.4: Summary test results.	49
Table 3.5: Mean specimen measurements.	50
Table 3.6: Multi-factor ANOVA results.	54
Table 3.7: Single Factor ANOVA Results (DBL16, DBL18, DBL20, DBL22).	60
Table 3.8: Single-factor ANOVA results (DBL18, DBL20, DBL22).	60
Table 3.9: Supplementary test matrix.	64
Table 3.10: Average Maximum Displacement By Treatment Group.	69
Table 4.1: Sustained loading experiment test matrix.	85
Table 4.2: Summary of sustained load data.	88
Table 4.3: Results of residual capacity of sustained loading specimens.	95
Table 4.4: Cyclic loading experiment test matrix.	102
Table 5.1: Test matrix of C-channel beam flexural test.	128
Table 5.2: C-channel test results summary.	131
Table 5.3: Test matrix of cored slab flexural test.	139
Table 5.4: Cored slab test results summary.	146
Table 6.1: Schmidt-Hammer measured results.	164
Table 6.2: Concrete core data.	166

Table 6.3: Strain measurement data and remaining stress.	178
Table 6.4: Measured total prestress losses.	178
Table 6.5: Calculated prestress losses.	183
Table 6.6: Comparison of experimental and analytical results of ultimate capacity.	190
Table 7.1: Specimen identification for full-scale testing.	218
Table 7.2: Test matrix.	221
Table 7.3: C-channel test results summary.	230
Table 7.4: Predicted shear capacity using ACI 318 (2019).	252
Table 7.5: ACI 318 (2019) predicted shear capacity using modified parameters.	253
Table 8.1: Measured beam camber.	269
Table A.1: Required material for a single C-channel beam stem repair.	300
Table A.2: Required tools for the installation.	311
Table A.3: Detailed installation procedure.	317

LIST OF FIGURES

Figure 1.1: Examples of deteriorated concrete C-channel and cored slab bridge beams.	2
Figure 1.2: Moment-deflection response of undamaged and damaged prestressed concrete bridge beams with AASHTO limits.	3
Figure 1.3: Types of strengthening with composite laminate materials.	4
Figure 1.4: Prestressed MF-FRP retrofit concept sketch.	6
Figure 2.1: Types of fasteners in the current literature (adopted from Martinelli et al., 2014). ...	18
Figure 2.2: Fastener bearing examples.	20
Figure 2.3: Prestressed EB-FRP device (adapted from Piatek et al., 2020).	22
Figure 2.4: Typical MF-FRP strengthening (continuously bonded along length).	24
Figure 2.5: Experimental vs. analytical results (adapted from Harajli et al., 1999).	29
Figure 2.6: Design charts for strengthening with external tendons (adapted from Tan et al., 2007).	30
Figure 2.7: Detail of the end anchorage of an FRP U-wrap (adapted from Khalifa and Nanni, 2000).	32
Figure 2.8: Shear strengthening schemes (adapted from Adhikary and Mutsuyoshi, 2005).	33
Figure 2.9: Experimental result at failure (adapted from Adhikary and Mutsuyoshi, 2005).	34
Figure 3.1: FRP plate sample examined in this study.	36
Figure 3.2: Example DIC strain field and specimen speckle pattern.	43
Figure 3.3: Test treatment configurations and specimen identification.	45
Figure 3.4: UTM setup (no-hole and open-holes) and failed specimen.	46
Figure 3.5: Bolted connection test schematic.	48
Figure 3.6: Shear strain map of disturbed regions and shear failure.	52

Figure 3.7: Load-displacement curves for single-bolt tests with 1.5 in. edge distance.	55
Figure 3.8: Single-bolt bearing failure modes with DIC inset showing shear strain.	57
Figure 3.9: Box plots of multibolt peak load distributions.	61
Figure 3.10: Mean multibolt load-displacement curves (DBL series).....	62
Figure 3.11: FRP failure modes.	63
Figure 3.12: Variation of mean peak load and FRP failure modes.....	64
Figure 3.13: S-B-X-0.375 load-displacement curves.	67
Figure 3.14: Failure modes for 0.5 in., 0.375 in., and 0.75 in. diameter treatment groups.	68
Figure 3.15: 0.5 in. and 0.375 in. bolt diameter peak load distribution.....	69
Figure 3.16: Load-displacement behavior for DBL22-B and DBL22-B-0.375 treatment groups.	70
Figure 3.17: Load-displacement behavior for DBL14-B-4-0.75 treatment group.....	71
Figure 4.1: Configuration of strongwall web.....	77
Figure 4.2: Cross-section of steel racks.	78
Figure 4.3: Bending moment diagram of loaded steel racks.	79
Figure 4.4: Full test setup of sustained loading experiment.	80
Figure 4.5: Drilling steel components.....	81
Figure 4.6: Welding angles to square HSS tubes.....	81
Figure 4.7: Sustained load test setup (a) before and (b) after attaching specimens.....	82
Figure 4.8: Calibration of pressure gauges in universal testing machine.	84
Figure 4.9: Displacement over time (0.5 in. bolts).	86
Figure 4.10: Displacement over time (0.375 in. bolts).	87
Figure 4.11: Early ages displacements (0.5 in. bolts).	87
Figure 4.12: Early ages displacements (0.375 in. bolts).	88

Figure 4.13: State of extracted specimens after 6 months of sustained loading.	91
Figure 4.14: State of extracted specimens after 30 months of sustained loading.	92
Figure 4.15: Residual capacity after 6 and 30 months of sustained loading.....	94
Figure 4.16: Residual capacity test after 6 and 30 months of sustained loading.	95
Figure 4.17: Individual stress profiles considered.	99
Figure 4.18: Candidate bridge cross-section information and geometry.	100
Figure 4.19: Fatigue cracking near 600000 cycles.	103
Figure 4.20: Fatigue failure by longitudinal shear crack spreading at 820000 cycles.....	104
Figure 4.21: Fatigue failure envelope for 0.375 in. bolts at 30 in.-lbs. of torque.	105
Figure 4.22: Estimate of fatigue failure envelope for 0.375 in. bolts at 30 ft.-lbs. of torque.	106
Figure 4.23: Hysteretic load-displacement plots for 0.375 in. bolts.	106
Figure 4.24: Hysteretic secant stiffness per cycle for 0.375 in. bolts.	107
Figure 4.25: Displacement per number of cycles for 0.375 in. bolts.....	108
Figure 4.26: Fatigue failure envelope for 0.5 in. bolts at 60 ft.-lbs. of torque.....	109
Figure 4.27: Hysteretic load-displacement plot for 0.5 in. bolts at 60 ft.-lbs. of torque.....	110
Figure 4.28: Hysteretic secant stiffness per cycle for 0.5 in. bolts at 60 ft.-lbs. of torque.	110
Figure 4.29: Displacement per number of cycles for 0.5 in. bolts at 60 ft.-lbs. of torque.	111
Figure 4.30: Witness mark before prestressing the MF-FRP system.	115
Figure 4.31: MF-FRP repair system labeling after prestressing.	115
Figure 4.32: MF-FRP repair system labeling 14 days after prestressing.....	116
Figure 4.33: MF-FRP repair system labeling condition during the bi-annual bridge inspection.	116
Figure 5.1: MF-FRP 1.0 design details.	118

Figure 5.2: MF-FRP 1.0 connection photos.....	120
Figure 5.3: MF-FRP 2.0 design details.....	121
Figure 5.4: MF-FRP 2.0 connection photos.....	121
Figure 5.5: ΔL_{TOT} measurement marks for MF-FRP 2.0 at $P_{FRP} = 18.5$ kips.	126
Figure 5.6: C-channel cross-section details. (data from NCDOT, 1966).	128
Figure 5.7: Damaged C-channel beam.....	128
Figure 5.8: Test setup of C-channel beam flexural test.	130
Figure 5.9: Full-scale C-channel beam load-deflection results.	132
Figure 5.10: FRP failure mode for MF-FRP 1.0.....	134
Figure 5.11: Specimens delivered to the lab.	136
Figure 5.12: Specimens cross-section.....	137
Figure 5.13: Full-scale test setup and instrumentation.	138
Figure 5.14: Full-scale test setup.	138
Figure 5.15: Exposed and cut prestressing strands.	140
Figure 5.16: MF-FRP retrofit applied on PC cored slab.....	142
Figure 5.17: Concrete crushing failure.	143
Figure 5.18: FRP LS (bottom) and R (top) failures (Specimen D-S1).	143
Figure 5.19: Condition of wedge anchors after full-scale test.	144
Figure 5.20: Full-scale experimental results.....	146
Figure 5.21: Full-scale results for 2 lost strands.	147
Figure 5.22: Full-scale results for 4 lost strands.	148
Figure 6.1: LSA approach.....	155

Figure 6.2: First moment of area theorem to calculate member deflection (three-point bending).	156
Figure 6.3: Idealized relationship to consider second-order effect.	157
Figure 6.4: Concept of beam deflection limit.	161
Figure 6.5: Schmidt-Hammer conversion curves (adapted from Schmidt-Hammer user's manual).	163
Figure 6.6: Application of Schmidt-Hammer.	163
Figure 6.7: Coring a tested C-channel beam.	165
Figure 6.8: Cutting cores using a wet tile saw.	165
Figure 6.9: Concrete core compression test.	166
Figure 6.10: Stress-strain relationship for concrete.	167
Figure 6.11: C-channel beam cross-section (adapted from NCDOT, 1966).	168
Figure 6.12: Prestressing strand tension test and failure mode.	170
Figure 6.13: Experimental results of one tension test.	170
Figure 6.14: Stress-strain relationship of prestressing strand from experiments and Mattock (1979).	171
Figure 6.15: Idealized elastic-perfectly plastic stress-strain relationship for reinforcing bar.	172
Figure 6.16: Moment-curvature response of cross-section at different locations.	174
Figure 6.17: Moment-curvature response of mid-span cross-section at different total prestress losses.	175
Figure 6.18: Moment-deflection response of a member at different total prestress losses.	175
Figure 6.19: Procedure of obtaining the total prestress losses.	177
Figure 6.20: Strain map obtained from DIC at third load stage after cracking.	180

Figure 6.21: Strain response from strain gauge and DIC.....	180
Figure 6.22: Stress-development length response.	185
Figure 6.23: Variation of flexural capacity.....	186
Figure 6.24: Moment-deflection response with different damage conditions.	187
Figure 6.25: Comparison of moment-deflection results.	189
Figure 6.26: MF-FRP strain-to-member deflection relationship of the experimental and analytical results.....	190
Figure 6.27: Visualization of LSA procedure.....	193
Figure 6.28: Example comparison of experimental result and prediction.	196
Figure 6.29: Comparison of analytical prediction to experimental result (U-U).....	197
Figure 6.30: Comparison of analytical prediction to experimental result (D-U1).....	198
Figure 6.31: Comparison of analytical prediction to experimental result (D-U2).....	199
Figure 6.32: Comparison of analytical prediction to experimental result (D-S1).	200
Figure 6.33: Comparison of analytical prediction to experimental result (D-U2).....	201
Figure 6.34: Equivalent stress block model.....	202
Figure 7.1: Shear deterioration at beam end-region observed on Bridge 810003.	207
Figure 7.2: Shear strengthening plate.	209
Figure 7.3: Flexural/shear repair system.....	210
Figure 7.4: C-channel beams used in this test program.	210
Figure 7.5: Moment envelope of undamaged and damaged C-channel beams.	212
Figure 7.6: Shear envelope along the C-channel beams.	213
Figure 7.7: Failure envelope along the length of C-channel beams.	214
Figure 7.8: North Carolina non-interstate legal vehicles (adapted from Weiger, 2017).	216

Figure 7.9: Test setups for different loading conditions.	217
Figure 7.10: Strain gauges installed on the FRP plate.	218
Figure 7.11: Shear damage conditions.	220
Figure 7.12: Shear damage comparison.	220
Figure 7.13: Flexural deterioration at midspan.	221
Figure 7.14: C-U-S2 (Test 1 on Beam 1).	221
Figure 7.15: C-DS-S1 (Test 2 on Beam 1).	222
Figure 7.16: C-U-S1 (Test 3 on Beam 2).	222
Figure 7.17: C-IDS-S1 (Test 4 on Beam 2).	222
Figure 7.18: S-DS-S1-F (Test 5 on Beam 3).	222
Figure 7.19: S-DS-S1-FS (Test 6 on Beam 3).	223
Figure 7.20: S-DFS-F-FS (Test 7 on Beam 4).	223
Figure 7.21: Different shear damage levels.	224
Figure 7.22: Drilling holes for the MF-FRP system.	226
Figure 7.23: Shear deterioration patched with fast setting cement.	226
Figure 7.24: Concrete splitting during prestressing of the MF-FRP system in beam No. 3.	228
Figure 7.25: Stem condition after drilling fixed anchor plate bolt holes.	228
Figure 7.26: MF-FRP repair system applied on beam No. 3.	229
Figure 7.27: MF-FRP repair system applied on beam No. 4.	229
Figure 7.28: Full-scale experimental results (1- point load shear tests).	231
Figure 7.29: Load combination for calculating HS-15 applied shear force (adapted from AASHTO, 2018).	231
Figure 7.30: Experimental result of C-U-S2.	232

Figure 7.31: First flexural-shear crack occurred at the 45 kips load stage (C-U-S2).	233
Figure 7.32: Failure mode of C-U-S2.	233
Figure 7.33: Formation of first shear crack at 58 kips (C-U-S1).....	234
Figure 7.34: Failure mode of C-U-S1 at 58.4 kips.	234
Figure 7.35: Crack angle of C-U-S1 at failure.....	235
Figure 7.36: Shear crack at 45 kips (C-IDS-S1).	236
Figure 7.37: Failure mode of C-IDS-S1 at 57.4 kips.....	236
Figure 7.38: Corrosion on the prestressing strand after chipping away the concrete.	237
Figure 7.39: Pull-out of strand after testing (C-IDS-S1).	237
Figure 7.40: Measuring stirrup spacing and orientation (C-IDS-S1).	238
Figure 7.41: Formation of first shear crack at 33.2 kips (C-DS-S1).....	239
Figure 7.42: Failure mode of C-DS-S1 on both stems.....	239
Figure 7.43: Shear crack formed at 28 kips (S-DS-S1-F).....	241
Figure 7.44: Additional shear cracks initiated at 35 kips load stage (S-DS-S1-F).....	241
Figure 7.45: Failure mode of S-DS-S1-F at 37.3 kips.	241
Figure 7.46: Formation of first inclined shear cracks at 35 kips (S-DS-S1-FS).....	243
Figure 7.47: Additional shear cracks at the 40 kips load stage (S-DS-S1-FS).....	243
Figure 7.48: Failure mode of S-DS-S1-FS at 45 kips.....	244
Figure 7.49: Flexural failure by concrete crushing (S-DS-S1-FS).	244
Figure 7.50: Full-scale C-channel beam moment-deflection results.	246
Figure 7.51: Flexural failure by concrete crushing at 27.1 kips (S-DFS-F-FS).	247
Figure 7.52: Minor longitudinal splitting on FRP plates.	247
Figure 7.53: Minor local concrete splitting on concrete stem.	248

Figure 7.54: Location of strain gauges installed on the FRP plate.	249
Figure 7.55: FRP strain variation at different locations along length of plate.....	249
Figure 7.56: FRP strain distribution across plate at mid region.	250
Figure 7.57: Concrete web width used for calculating concrete shear strength.	253
Figure 8.1: Condition of retrofit on Bridge 340080 in Franklin County, NC, after 18 months in-service.	256
Figure 8.2: Overview of Bridge 810003.	257
Figure 8.3: Concrete spalling and exposed prestressing strands near mid-span.....	258
Figure 8.4: Loss of concrete section and exposed prestressing strand and stirrup at end regions.	259
Figure 8.5: Retrofit plan for Bridge 810003.	259
Figure 8.6: Elevation view of the retrofit system.	260
Figure 8.7: Cross-section view of the retrofit system.	260
Figure 8.8: Key steps in retrofit installation.	264
Figure 8.9: Overview of installed retrofit.	265
Figure 8.10: Beam camber measurement system.	266
Figure 8.11: Witness mark measurement.....	267
Figure 8.12: Measured FRP elongation after installation.	270
Figure 8.13: Long-term monitoring of FRP strain.....	272
Figure 8.14: Measured temperature location.	273
Figure 8.15: Variation of FRP strain and temperature.....	274
Figure 8.16: Measured temperature gradient over the section height.....	275
Figure 8.17: Longitudinal cracks on MF-FRP plate.	276

Figure 8.18: Repair system after 1 year after installation.	277
Figure A.1: MF-FRP repair system installed on typical C-channel beam.	301
Figure A.2: MF-FRP repair system on typical cored slab.	301
Figure A.3: Fixed anchor plate design detail.	302
Figure A.4: FRP connector plate 1 design detail.	302
Figure A.5: FRP connector plate 2 design detail.	303
Figure A.6: FRP connector plate 2 – weld detail.	303
Figure A.7: Turnbuckle plate design detail.	304
Figure A.8: Turnbuckle plate - weld detail.	304
Figure A.9: Fixed anchor plate machinist as-built drawing.	305
Figure A.10: Shoulder bolt (pin) machinist as-built detail.	306
Figure A.11: Fixed anchor plate-pin as-built assembly detail.	307
Figure A.12: FRP connector plate 1 machinist as-built drawing.	308
Figure A.13: FRP connector plate 2 machinist as-built drawing.	309
Figure A.14: Turnbuckle (TB) plate machinist as-built drawing.	310
Figure A.15: Witness mark before prestressing the MF-FRP system.	314
Figure A.16: MF-FRP repair system labeling after prestressing.	315
Figure A.17: MF-FRP repair system labeling 14 days after prestressing.	315
Figure A.18: MF-FRP repair system labeling condition during the bi-annual bridge inspection.	316
Figure A.19: Repair elements.	318
Figure A.20: Locating steel using a pachometer.	319
Figure A.21: Precutting FRP plates with a wet tile saw.	319

Figure A.22: Drilling holes in the FRP plates.....	319
Figure A.23: Wooden template on stem.	319
Figure A.24: Drilling anchor plate holes	319
Figure A.25: Installing bolts of the fixed anchor.....	319
Figure A.26: Tightening of FRP bolts to 60 ft.-lbs. torque.....	320
Figure A.27: Elongation witness mark.	320
Figure A.28: Prestressing the MF-FRP plates.	320

CHAPTER 1 – INTRODUCTION

1.1 – Background

Prestressed concrete (PC) C-channel and core slab beams are among the standard shapes and forms of bridge structures commonly used by North Carolina Department of Transportation (NCDOT) and across the United States since the 1960s. Since being in-service for more than 40 years, these bridge structures are deteriorating due to corrosion of the prestressing strands, overloaded traffic, and natural aging, which has raised concerns for DOTs. Figure 1.1 shows examples of PC deteriorated C-channel and cored slab bridge beams. Corrosion of prestressing strand is one of the common factors that causes bridge deterioration and reduces bridge capacity due to the prestress losses. The reduced capacity can violate the load limits defined by the American Association for State Highway and Transportation Officials (AASHTO) and result in replacement, load-posting, or closure. Replacement is the most effective way to solve the problem; however, it requires time and budget to start the work. Therefore, load-posting or closure have become a common solution for such deteriorated bridges. Load-posting (or closure), though commonly adopted, is undesirable as it may cause long and costly detours, as well as a plethora of socio-economic disruptions. An immediate retrofit action for DOTs that is able to restore prestress loss for PC bridges to comply with AASHTO load limits needs to be considered to prevent the deterioration from getting worse, obviating load-posting or reopening bridges or delaying plans for replacement, which can minimize the inconvenience to the community.



(a) C-channel Beam – Bridge No. 340080



(b) Cored Slab – Bridge No. 150035

Figure 1.1: Examples of deteriorated concrete C-channel and cored slab bridge beams.

AASHTO rates bridges under the load limits based on two criteria: inventory and operating rating. The purpose of the retrofit is to restore these criteria. The inventory rating is defined such that no incremental damage initiates in an indefinite amount of time under routine traffic. In this research, a zero tensile stress limit in concrete is applied to avoid cracking on the extreme concrete fibers to propagate. This zero stress limit is based on the studied structures located in the coastal area and provide a conservative prediction. Inventory ratings are typically based on elastic stress limit states. The operating rating allows small incremental damage to occur under infrequent but heavier-than-routine traffic. It is considered by the maximum permissible live load moment that the bridge may be subjected to and is related to the beam length and types of vehicles.

The limits can be better understood through a load-deflection graph. Figure 1.2 shows a typical load-displacement response of an undamaged and damaged PC beam, with the AASHTO load limits defined above. The inventory limit intersects the curve within the linear-elastic portion, meaning the beam does not suffer permanent damage at this load. At a higher load, tension stresses will be generated on the extreme flexural face of the beam, and cracking will occur. The operating limit of the undamaged beam intersects the curve at the softening stage (loss of stiffness), just past the elastic limit, meaning that the beam will incur some minor permanent damage at this level of

loading. On the other hand, with the deterioration, the operating limit of the damaged beam occurs at a higher deflection level, which leads to more permanent damage accumulated over time. In most cases, the operating rating controls bridge capacity and load restrictions; however, to adequately remove posted load restrictions from deteriorated prestressed concrete bridge superstructures, both operating and inventory rating criteria must be addressed.

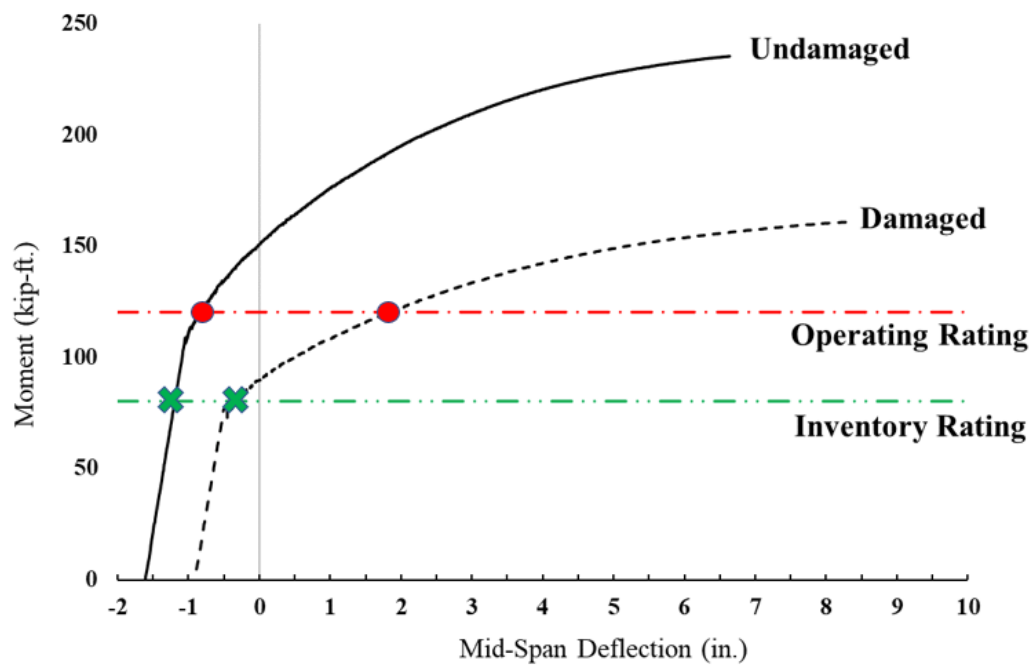
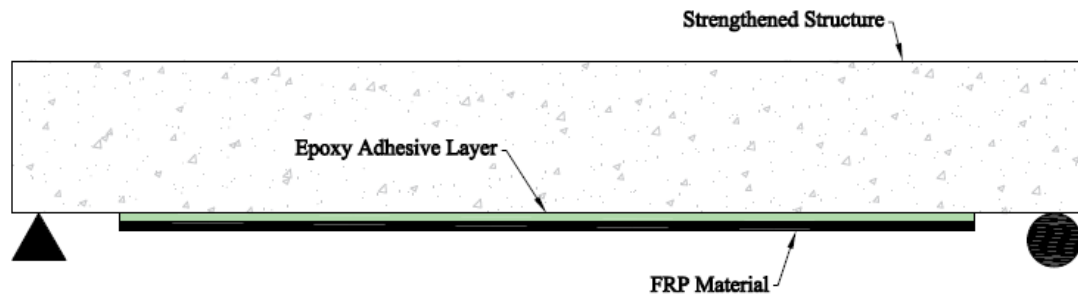
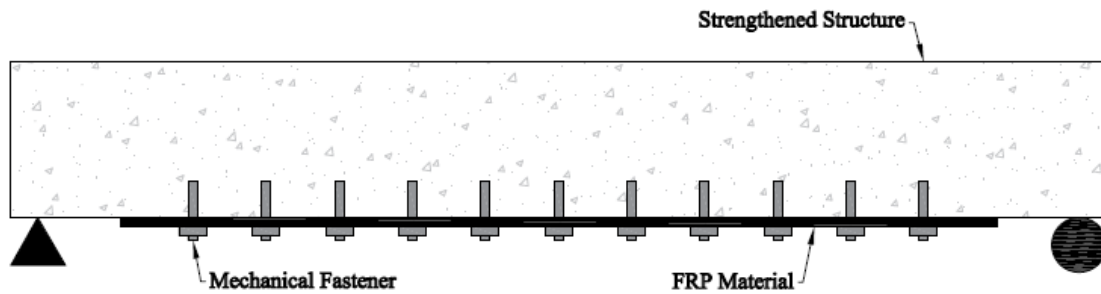


Figure 1.2: Moment-deflection response of undamaged and damaged prestressed concrete bridge beams with AASHTO limits.

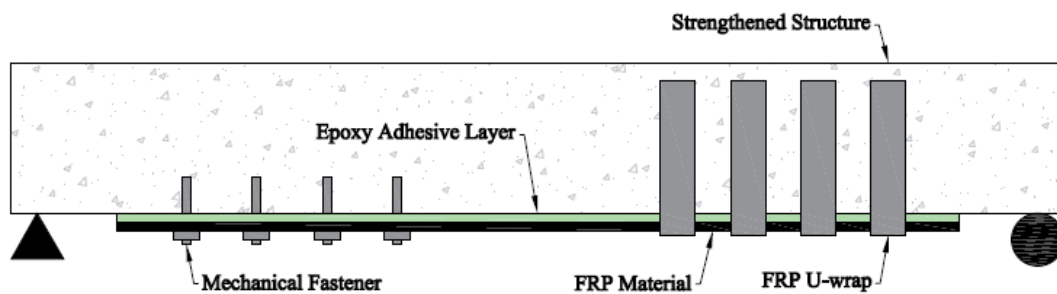
Typical strengthening systems include those that attach steel plate or composite laminate materials to the tension face of the structures and provide additional capacity; however, they are insufficient to achieve the bridge's original inventory and operating rating limits according to AASHTO. Figure 1.3 presents typical strengthening applications in the positive bending region using composite laminate material, including external adhesive bonding (EB) (Figure 1.3a), mechanically fastened (MF) (Figure 1.3b), or a combination of both (hybrid) Figure 1.3c).



(a) Externally Bonded FRP (EB-FRP)



(b) Mechanically Fastened FRP (MF-FRP)



(c) Hybrid (with Mechanically Fastened or FRP U-wrap)

Figure 1.3: Types of strengthening with composite laminate materials.

Externally bonded FRP and hybrid systems are effective methods of strengthening the deteriorated bridge structures; however, they present challenges which do not exist with mechanically fastened systems. The strengthening applications require additional installation time due to surface preparation and epoxy cure time, leading to longer bridge closure time and increases direct and indirect costs from delaying and extending travel time because of detours. In addition, the bond quality of the epoxy adhesive between the FRP and the concrete substrate is hard to control, which is critical to the load-carrying capacity, and monitor for future bridge inspections.

Therefore, the retrofit system developed in this research emphasizes the use of mechanical fastening only to present an application that can provide repaid installation, is traffic ready upon installation, and can be easily inspected during the installation and in-service throughout the life of the system. Most importantly, the system must be able to restore the prestress losses due to deterioration and achieve the original design inventory and operating rating limit addressed in (AASHTO, 2018).

1.2 – Research Objective

The number of deteriorated C-channel bridges built prior to the 1970s that have met their expected service life is a big concern for state DOTs. The North Carolina Bridge Management System (NCDOT BMS, 2018) shows that around 85% of the 269 C-channel bridges in North Carolina are load posted. Load posted or closed bridges due to deterioration result in an average detour length of more than 7 mi. for both single vehicles (SV) and truck tractor semi-trailers (TTST). The vehicle operating cost (VOC) for industries affected by the detour increases due to the larger travel distance and time. Cavalline et al. (2015) showed that the VOC is \$2.59 per mi. for vehicles greater than 26 tons, and \$1.86 per mi. for vehicles less than 26 tons. It can be said that on average, the VOC increases by \$14-20 each way. In addition, detours affect the response time of emergency services and public transportation. For emergency services, time is the critical factor directly impacting people or infrastructure. Based on the average detour length of the C-channel bridges being considered, the average response time of emergency services increases by around 9 and 12 minutes for pumper trucks and aerial ladder trucks, respectively. For the reasons mentioned above, a rapid retrofit system needs to be considered to extend the service life and minimize the inconvenience of detours and closure to the local community until replacement can be scheduled. However, the flexural MF-FRP repair system previously developed requires

additional experimental and analytical research and field applications to better understand the behavior and demonstrate its efficiency.

Temporary repair and restoration of prestress losses are necessary to maintain structures' original inventory and operating rating to keep deteriorated bridges functional while replacement is scheduled. The primary objective of this research is to develop a methodology and experimental program that is fundamental to extend the service life of existing infrastructure through rapid restoration of prestress losses in deteriorated prestressed concrete bridge superstructures. The retrofit solution is a mechanically-fastened fiber-reinforced polymer (MF-FRP), which can be applied to deteriorated prestressed concrete bridge superstructures and prestress to a level that prestress losses due to deterioration are restored. Restoration of the prestress losses must result in concrete tensile stresses that are within allowable AASHTO limits permitting the retrofitted bridge to remain open, without posted load restrictions, until member replacement, or complete bridge reconstruction can occur. A concept sketch of the retrofit solution applied to a C-channel beam is presented in Figure 1.4.

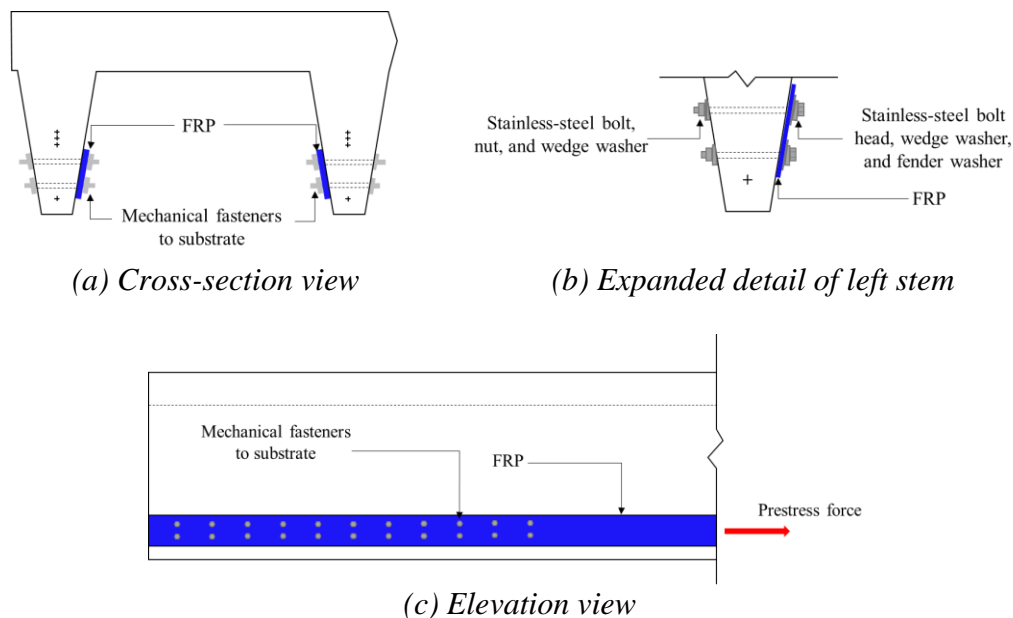


Figure 1.4: Prestressed MF-FRP retrofit concept sketch.

The key summary tasks of this research project include 1) understanding of AASHTO inventory and operating rating requirements for prestressed concrete bridges, 2) development of an MF-FRP anchor system capable of developing the necessary prestress levels in the applied FRP plate to restore inventory and operating rating loads, 3) development of a field expedient prestressing mechanism which can be incorporated into the MF-FRP retrofit design, 4) complete design of an MF-FRP retrofit solution which can be installed with common tools and labor skill, 5) investigation of the long-term behavior of the MF-FRP connection, 6) full-scale testing of both C-channel beams and cored slabs for proof-of-concept of the developed prestressed MF-FRP repair system and installation time minimization, 7) design a shear strengthening system that can be accommodated to the current flexural repair system for both shear and flexure deteriorated beams, 8) develop an analysis methodology to provide accurate predictions of both C-channel beams and cored slabs using the proposed retrofit application, and 9) retrofit in-service deteriorated prestressed concrete C-channel bridge using proposed retrofit system to reopen and lift the load posting.

While the MF-FRP retrofit solution and installation processes and procedures are of particular interest to the NCDOT, the methodology, experimental program, retrofit solution, and installation methods are of interest to departments of transportation across the country and in other nations where deteriorated prestressed concrete bridge superstructures are in need of restoration or replacement. The retrofit techniques developed during this project could also be of interest to a broader set of applications, including those within the Department of Defense (DOD) in theaters of operations where rapid restoration or strengthening of bridges may be necessary for the success of military operations. The MF-FRP retrofit solution developed in this research can be applied to

both prestressed C-channel beams and cored slabs. The methodology and experimental program are more suitable to the beams with mild to moderate prestress loss due to deterioration.

1.3 – Research Phases and Intermediate Research Objectives

The primary research objective is addressed through the following phases:

- 1) Small-scale material testing - The intermediate research objective of this phase is to gain a fundamental understanding of the FRP material behavior within the context of the primary research objective. The following tests are presented with a sufficient number of replicates for each test treatment to provide statistical significance to the results. All tests are conducted using Digital Image Correlation measurement techniques to provide continuous strain mapping of the test specimens.
 - a. No holes: The ultimate capacity, strain behavior, and failure mode of the FRP plate with no holes can be obtained through uniaxial tension testing.
 - b. Open holes: Uniaxial tension testing of FRP plate with open holes to inform the material tensile capacity, strain behavior, and failure mode with holes without bearing. Different hole patterns, aligned and staggered, will be considered and tested to determine the effect of each pattern on material behavior.
 - c. Single-bolt bearing: The localized bearing capacity and strain behavior of the FRP plate in a single bolt bearing can be obtained through uniaxial tension testing. The results can inform the number of bolts considered in subsequent multi-bolt bearing tests.
 - d. Multi-bolt bearing: The desired fastener patterns and numbers of bolts can be obtained by conducting uniaxial tension testing of the FRP plate in multi-bolt bearing. The results can be used to understand the material behavior and

examine the FRP strain development through the fastener pattern as load increases.

- 2) Design of prestressing mechanism and MF-FRP connection – The intermediate research objective of this phase is to provide a field-ready prestressing mechanism and MF-FRP connection that is capable of developing the necessary prestress force with common tools and no specialty labor skills. The development of the MF-FRP retrofit solution includes the design of the prestressing mechanism and connection of the FRP plate to the prestressing mechanism and the connection of the MF-FRP retrofit to the concrete substrate. Design of the prestressing mechanism and connection consider steel yielding due to tension and bearing, bolt shear, and concrete splitting and crushing due to bearing of the mechanical fasteners. The MF-FRP retrofit is designed with A572 Grade 50 steel and A325 Grade 8 bolts for the purposes of concept development in the lab; however, it is recommended that the MF-FRP retrofit connections and prestressing mechanism be constructed of A306 or A316 stainless steel or A572 steel with an additional coating to resist corrosion in the field.
- 3) The long-term behavior of the MF-FRP connection - The intermediate research objective of this phase is to understand the long-term behavior of the MF-FRP connection under sustained (creep) and cyclic (fatigue) loading. With the expectation that the MF-FRP repair will remain in-service for durations of at least three to five years, sustained load and fatigue effects must be considered.
- 4) Full-scale flexural experiment - The intermediate research objective of this phase is a proof-of-concept of the designed retrofit solution and optimization to enable rapid installation of the solution. This phase, divided into two sections with different

specimen section types, C-channel beams and cored slabs, provides a validation of methodology and experimental program developed in this research. The experiments include testing the MF-FRP retrofit concept on undamaged and damaged full-scale C-channel beams as well as undamaged and different damaged level full-scale cored slabs. Testing includes installation (anchorage and prestressing) and post-installation loading of the member. The time required to install the MF-FRP retrofit is also recorded and design adjustments recommended to reduce installation time and increase the efficiency of the MF-FRP retrofit solution. Deflection controlled loading is applied statically through beam failure. Data collection during testing for both sections includes applied load, vertical deflection, FRP strain, concrete cracking pattern, and failure mode. Digital Image Correlation is also used to record FRP strain development at the end-anchorage region of the MF-FRP retrofit for repaired C-channel beams.

- 5) Full-scale shear experiment: The intermediate research objective of this phase is to understand the behavior of shear deteriorated C-channel beam. The shear deterioration observed in some bridges occurred at the end region of the C-channel beam, including the loss of concrete section and exposed prestressing strands. The shear repair system accommodates the current MF-FRP flexural repair and is designed to provide additional shear capacity. Both shear and flexural testing will be conducted in this phase. Deflection controlled loading is applied statically through beam failure for both types of testing. Data collection during testing for C-channel beams includes applied load, vertical deflection, FRP strain, concrete cracking pattern, and failure mode. Digital Image Correlation is also used to record concrete strain development at the shear critical region of the C-channel beams.

- 6) Analytical modeling of retrofitted C-channel beams and cored slabs: The intermediate research objective of this phase is to develop a methodology to provide accurate predictions of both retrofitted C-channel beams and cored slabs using layered section analysis (LSA). The analytical results can predict the flexural capacity and full moment-displacement response and validate the experimental results. The completed moment-displacement response of retrofitted specimens can then be compared to the AASHTO load rating limits.
- 7) Field application: The intermediate research objective of this phase is to conduct field applications on in-service deteriorated bridges. The proposed MF-FRP retrofit system was applied on two bridges located in Wake and Sampson County, North Carolina. The retrofit system applied on the bridge in Wake County serves as a field demonstration; however, the system applied on the Sampson County bridge serves as a formal bridge repair to reopen a closed bridge. Field application and long-term monitoring can provide evidence of the retrofit system behavior and benefits applied on an in-service deteriorated bridge. Long-term monitoring was only conducted on the repair system installed on the Sampson County bridge.

1.4 – Layout of Report

The research presented in the report starts with the introduction and background of the research purpose and is then organized into chapters by key topic. The layout of the report is presented in the following chapters:

- Chapter 2 contains a review of existing research and available literature. This is used to address the knowledge gaps of the current studies.

- Chapter 3 investigates the capacity of several mechanical fastener patterns using 0.5 in. diameter bolts. Statistical rigor is applied to provide results that are statistically significant at the 90% confidence limit or higher. Additional studies using different fastener diameters are also presented.
- Chapter 4 studies the long-term behavior of the MF-FRP retrofit connection. It is organized into two sections: the effects of sustained loading (creep) and the effects of cyclic loading (fatigue). The experimental program, results, and observations are included in each section.
- Chapter 5 contains the full-scale experimental program of flexural testing and is divided into two sections: C-channel beams and cored slabs. The experimental results and discussions are presented in each section.
- Chapter 6 presents the analytical modeling of C-channel beams and cored slabs retrofitted with the prestressed MF-FRP system. The predicted results are then compared with the experimental results in Chapter 5 using the repair design presented in this research.
- Chapter 7 presents the full-scale experimental program to investigate the shear behavior and capacity of beams with deteriorated end regions. The C-channel beams used in the full-scale experiments here are obtained from the same C-channel bridge tested in Chapter 5. The additional experiments help obtain missing data from the full-scale flexural tests presented in Chapter 5 and improve the analytical predictions.
- Chapter 8 shows the field retrofit of an in-service deteriorated C-channel bridge in North Carolina. The concept of the retrofit design, strengthening procedure, and available results of the long-term monitoring are included in this chapter. In addition, a cost-benefit assessment of the retrofit system is also discussed.

- Chapter 9 summarizes the conclusions, design and inspection recommendations, and recommendations for future research.

Supplementary materials related to the research are presented in an Appendix, including the required materials, equipment, detailed procedure to install the repair and the excel spreadsheet for the analytical prediction and load rating calculation.

CHAPTER 2 – LITERATURE REVIEW

This chapter presents a summary of the literature review conducted for this research and the knowledge gaps and conclusions relevant to the research are identified. This chapter starts with a review of FRP strengthening systems, long-term behavior of MF-FRP, prestressed concrete members with unbonded tendons, and shear strengthening of concrete beams. More detailed literature review related to this research can be found in McCoy (2019), Bourara (2019), and Lin (2021).

2.1 – Fiber-Reinforced Polymer Strengthening Systems

Compared to structural steel, FRP provides advantages in durability (Rahman et al., 1998) and material weight, which reduces overall cost of the system. The weight of the FRP plate presented in this research is significantly less than an A572 Grade 50 (50 ksi yield strength) structural steel plate of appropriate geometry to achieve the desired strengthening effects. A structural steel plate would need to have a cross sectional area of 1.2 in² to achieve the desired strengthening effects. The length of the plate examined in this study is approximately 275 in., resulting in a 90 lb., 23-ft.-long steel plate, compared to just 8 lb. for the same length of the FRP plate. Further, the FRP plate examined in this research can be rolled and carried by a single worker, making the FRP much easier to transport to the job site and install. Therefore, because of the durability, weight, and installation advantages over a comparable steel plate, FRP is desired for the primary strengthening element of the retrofit developed in this research.

2.1.1 – Externally-Bonded Fiber Reinforced Polymer

Externally-bonded FRP (EB-FRP) strengthening systems are among the common methods for strengthening concrete structures, to include bridge superstructures. The primary advantage to EB-FRP systems is the efficiency of the system (Oehlers and Seracino, 2004). The adhesive bond between the FRP material and concrete substrate allows full-interaction to develop, and therefore,

efficiently transfers force to the bonded FRP to increase strength and stiffness. Additionally, FRP sheets can take many geometric forms, allowing for installation on a wide-range of cross-sections, which is one of the advantages of using a wet-layup EB-FRP system.

There are, however, a number of disadvantages to EB-FRP systems, as outlined by Oehlers and Seracino (2004): 1) the quality of the bond along the length of the applied FRP is often difficult to verify in the field which causes quality assurance problems at time of installation, and subsequent inspections throughout the life of the installed system; 2) debonding occurs through intermediate crack (IC) debonding, critical diagonal crack (CDC) debonding, and plate end (PE) debonding; 3) brittle failure mechanisms for EB-FRP systems occur from mechanical debonding or environmental factors which cause chemical deterioration of the adhesive; 4) performance of the system depends largely upon the strength of the concrete cover in the strengthened element, which is typically the most degraded concrete in deteriorated concrete structures; and 5) installation requires time consuming and labor intensive preparation of the concrete surface, application of the adhesive, and adhesive curing, all of which delay use of the strengthened structure. A summary of advantages and disadvantages, with a focus on bridge strengthening applications, is presented in Table 2.1.

For the purposes of this research, the disadvantages of the EB-FRP systems prohibit the feasible consideration of the system as a rapid retrofit solution for deteriorated prestressed concrete superstructures.

Table 2.1: Advantages and disadvantages of FRP systems.

	FRP Application Method	
	Externally-bonded	Mechanically-Fastened
Advantages	<ul style="list-style-type: none"> -full-interaction offers efficient system -In-situ wet-layup FRP installation can take many geometric forms 	<ul style="list-style-type: none"> -ductile failure -environmental impacts reduced with treated fasteners -installation in hours -installed with simple tools -no concrete surface preparation required immediate loading after installation
Disadvantages	<ul style="list-style-type: none"> -surface preparation required -increased labor skill required -epoxy cure time -deterioration of epoxy in exposed environments -bond quality difficult to inspect -premature debonding in flexural elements (IC, CDC, PE) -brittle failure -requires sound concrete for complete 	<ul style="list-style-type: none"> -partial interaction due to bolt slip -potential for concrete damage due to fastener installation -requires sound concrete for fastener bearing in anchor zones

2.1.2 – Mechanically-Fastened Fiber-Reinforced Polymer

Strengthening of reinforced concrete bridge decks and girders to increase the Federal Highway Administration (FHWA) load rating using MF-FRP was the subject of previous research projects (Bank et al., 2002; Lamanna et al., 2004a; Lamanna et al., 2004b; Borowicz et al., 2004; and Lamanna et al., 2001), which focus on various types of fasteners, and the interactions between the concrete and fasteners. Additional experimental projects for the Wisconsin DOT and Missouri DOT which examine the increased load rating and construction procedures required to strengthen reinforced concrete bridge decks using MF-FRP plates are presented by Bank (2004).

Compared to externally-bonded systems, MF-FRP offers several advantages: 1) failure modes are generally ductile in nature due to bolt bearing in the FRP material or concrete substrate which propagates progressively prior to complete failure of the system (Oehlers, 2001); 2) the mechanical fasteners can be treated to withstand environmental effects in marine environments and in situations where elevated temperatures are of concern (Oehlers, 2001); 3) installation of

MF-FRP systems are quick – often completed within a matter of hours; 4) installation requires no special tools or labor skills, no concrete surface preparation; and 5) MF-FRP systems can be loaded immediately after installation (Sena-Cruz et al., 2012) (Table 2.1).

However, MF-FRP strengthening systems also present disadvantages compared to EB-FRP systems. Due to bolt-slip at each fastener, MF-FRP systems only develop partial interaction at the concrete-FRP interface which reduces the efficiency of the system (Oehlers, 2001). Additionally, depending upon the type of fastener, moderate to significant damage of the concrete substrate may occur during installation, weakening the interaction between the FRP material and concrete substrate (Oehlers, 2001) (Table 2.1).

Ebead and Saeed (2014) examined the behavior of reinforced concrete beams strengthened with externally bonded FRP, MF-FRP, and hybrid solutions that use both external bonding and mechanical fasteners. The research presented concludes that mechanically fastening the FRP to the strengthened member increases shear transfer across the interface between the FRP and reinforced concrete beam when compared to externally bonded solutions – a desirable effect for the prestressed MF-FRP application examined during this project. Further, Elsayed et al. (2009) examined two types of mechanical fasteners and compared the performance to external bonding alone for FRP strengthening of concrete elements using SAFSTRIP®. The results of the study conclude a sufficient number and proper spacing of fasteners enables a higher load in MF-FRP plates compared to externally bonded FRP plates – 19.4 kips and 11.3 kips, respectively – with the failure modes resulting in FRP rupture in the mechanically fastened system with a sufficient number of fasteners, and debonding of the FRP from the strengthened element in the EB system.

Table 2.2 provides a summary of the available MF-FRP research with the size and type of fasteners used. While Table 2.2 does not include all available literature on MF-FRP studies, the

studies listed represent the majority of available studies specific to MF-FRP systems using powder-actuated fasteners (PAF), wedge anchors, or screw anchors (Figure 2.1) and are all conducted using the commercially available SAFSTRIP® FRP plate material.

Table 2.2: MF-FRP literature summary (adopted from Martinelli et al., 2014).

Source	Fastener				Test Type
	Type	d_f (in.) ¹	l_f (in.) ¹	# lines ²	
Borowicz (2002)	PAF	0.175	1.85	2-a	4P Bending
Ebead (2011)	Screw	0.187	1.5	1-a / 2-a	
Ekenel et al. (2006)	Wedge	0.375	1.6	1-s	
	PAF	0.157	1.26	2-a	
El-Maaddawy (2014)	Screw	0.315	2.17	1-s	
	Wedge	0.315	2.17	1-s	
			1.26	1-a / 2-a	
El-Maaddawy et al. (2013)	PAF	0.157	2.05	1-a / 2-a	
			3.93	1-s / 2-a	
Galati et al. (2007)	Wedge	0.472	0.866	2-a	
Lamanna (2002)	PAF	0.146	1.06	1-a	
		0.146	1.26	1-a	
		0.137	1.06	2-a	
Lamanna et al. (2001)	PAF	0.146	1.26	1-a	
Bank et al. (2002)	PAF	0.177	1.26	2-a	
Lamanna et al. (2004)	PAF	0.177	1.85	2-a	
Lee et al. (2009)	PAF	0.137	0.984	2-a	
		0.137	1.26	2-a	
Bank and Arora (2007)	PAF / Wedge	0.158 / 0.50	1.75 / 2.75	1-a	
Martin and Lamanna (2008)	Screw	0.50	2.0	1-a / 1-s	
Napolin et al. (2010)	Screw	0.375	1.75	1-s	
Dempsey and Scott (2006)	Screw	0.177	2.0	2-a	
Realfonzo et al. (2013)	Screw	0.236	1.77	1-a	Tension
Elsayed, Ebead, and Neale (2009)	PAF	0.147	1.85	2-s	
	Screw	0.187	1.45	1-a / 2-a	

Notes:¹value converted from SI units; ²“a” denotes “aligned” lines; “s” denotes “staggered” lines; lines are in the longitudinal direction; ³MF-FRP applied to timber elements.

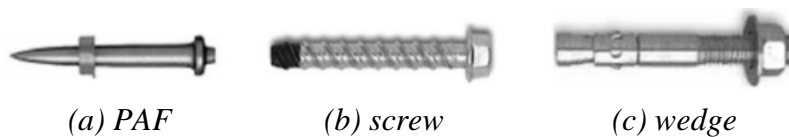
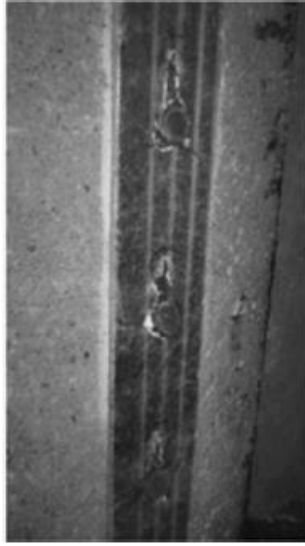


Figure 2.1: Types of fasteners in the current literature (adopted from Martinelli et al., 2014).

Results for each study were reported in various ways – percent increase from a control test, total applied load to a strengthened beam in four-point bending, and maximum applied load for pure tension tests – therefore, it is difficult to draw direct comparison across the studies presented

in Table 2.2. However, many of the studies show similar results. Those examining powder-actuated fasteners as a means for attaching the FRP to the strengthened member concluded fastener pull-out is the primary failure mode in all cases (Borowicz, 2002; Lamanna et al., 2001; Elsayed et al. 2009). This pull-out failure is likely due to a combination of concrete damage during application of the PAF, smooth shank, and relatively short fastener length (l_f) compared to many of the wedge and screw anchors examined.

Studies that examine fastener arrays with relatively thin wedge and screw anchor systems, a fastener diameter (d_f) less than 0.50 in., failed in bearing – a typical example is shown in Figure 2.2a – due to the small diameter of the anchors (Realfonzo et al., 2013; Ebead, 2011; Martinelli et al., 2014; Elsayed et al., 2009). Martin and Lamanna (2008) used 0.50 in. diameter screw fasteners to attach a single FRP plate to a reinforced concrete beam and reported a 38.5% increase in strength with minimal bearing in the FRP at each fastener location (Figure 2.2b). A combined failure of bearing (ductile failure) and FRP rupture (brittle failure) is desired to create a ductile strengthening system as noted by Lee, Lopez and Bakis (2009). These findings indicate that an efficient anchorage which fully develops the capacity of the FRP plate with slight bearing at each fastener can be obtained with fastener diameters of 0.50 in. or greater.



(a) 0.15 in. PAF

(Elsayed, Ebead, and Neale, 2009)



(b) 0.50 in. screw

(Martin and Lamanna, 2008)

Figure 2.2: Fastener bearing examples.

The fastener patterns presented throughout the research are predominantly single or double aligned fastener rows. While five of the studies presented in Table 2.2 examine staggered fastener patterns, only Realfonzo et al. (2012) presents a staggered pattern with sufficient transverse spacing for consideration in this study. The remaining four staggered fastener patterns presented in the literature are of systems in which the fastener pattern extends along the length of the FRP plate, with the holes offset from the centerline only slightly (referred to in much of the literature as a single-row staggered pattern). Realfonzo et al. (2012) presents a two-row staggered pattern of four (4) total fasteners which fail in bearing in a similar manner to the two-row and single-row fastener patterns presented throughout the literature. Because the predominance of available research examines either single or two-row aligned fastener patterns, or patterns with only slight staggering, there is a knowledge gap with respect to the behavior of MF-FRP using staggered fastener patterns. This apparent gap in the current research indicates that a study to determine the

effect and statistical significance of a two-row staggered fastener pattern on the ultimate anchorage capacity of MF-FRP systems could be useful in the development of the proposed retrofit system.

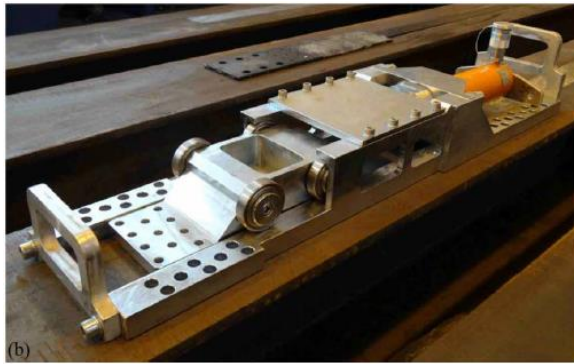
2.1.3 – Prestressed Fiber Reinforced Polymer

Previous studies which examine the application of prestressed FRP sheets to strengthen reinforced concrete elements also exist. Triantafillou and Deskovic (1991) examined the short-term behavior of prestressed FRP fabric sheets adhesively bonded to reinforced concrete beams to determine the optimum combination of materials and geometry to achieve the desired performance. Diab et al. (2009) conducted experimental work to determine the long-term effectiveness of a prestressed FRP sheet anchorage system which relies on adhesive bonding only, and a hybrid system (similar to that of Ebead and Saeed, 2014) which uses both adhesive bonding and mechanical fastening to strengthen reinforced concrete beams. The level of prestressing in the Diab et al. (2009) study varied from 20% of ultimate stress (σ_u) and 2.01 kips for the externally bonded system to 40% of σ_u and 11.6 kips for the hybrid system. The study concluded that for prestress levels less than 30% σ_u , debonding between the bonded FRP and concrete did not occur within 500 days, and the use of a hybrid anchor system enhanced the composite action of the FRP-concrete interface.

Yang et al. (2009) investigated flexural beam strengthening by cambering the beam element using hydraulic jacks. The CFRP strip was bonded to the compressed surface while the beam was cambered and then tensioned after releasing jacking force. Stocklin and Meier (2003) studied a method to provide gradual anchoring at the end of the prestressed EB-FRP element using a unique device to transfer the FRP stress to the substrate and avoid the premature peeling-off failure using a stepwise approach. A gradually anchored FRP concept increases the development length of the prestressing force so that the interface shear stress of the FRP system remains within the concrete shear stress limit. The cracking and ultimate load were increased by 325 and 235%,

respectively, for the specimen with prestressed and gradually anchored CFRP strips, compared to the control specimen.

Piatek et al. (2020) developed a prestressed EB-FRP system using a novel anchor and tension system to provide easy installation. With the prefabricated device used in the study, the prestressing process and FRP anchorage can be done together without moving the device. The full installation time of one CFRP strip can be done in 2 hours. The flexural capacity of the strengthened beam increased more than 50% compared to the control specimen. It was also presented that the strengthening system can reduce the beam deflection and crack widths. Figure 2.3 illustrates the tensioning device and prestressing operation from Piatek et al. (2020). The literature shows that prestressed EB-FRP can provide active prestressing and increase the flexural capacity. However, the repair system still needs to be bonded to the concrete surface and requires additional surface preparation to provide an appropriate concrete substrate and accommodate the tensioning device.



(a) Tension device



(b) Prestressing operation

Figure 2.3: Prestressed EB-FRP device (adapted from Piatek et al., 2020).

While prestressed MF-FRP systems are not present in the available literature, there is limited literature available describing a hybrid prestressed system which incorporates mechanical fasteners at the anchored ends and adhesive bonding along the entire length of, or along a partial

length (gradient zone) of an attached unidirectional FRP laminate (Michels et al., 2014). The hybrid systems examined by Michels et al. (2014) are commercially available solutions and represent the current state of strengthening available for prestressed members using external, prestressed FRP laminates.

Studies suggest that hybrid systems provide the greatest stress transfer across the interfacial zone between FRP and concrete (Ebead and Saeed, 2014; Michels et al., 2014); however, installation time constraints, impacts on traffic, maintenance and inspection procedures, and the associated costs with each, support a proposed bridge retrofit solution which excludes any external bonding. Therefore, this research focuses on the on the development of a mechanical fastener system which can achieve the maximum capacity of the applied FRP plate, with holes, and without external bonding and the associated costs.

2.2 – Long-Term Behavior of MF-FRP

The MF-FRP connection in the retrofit used in this research utilizes a unique design. Indeed, the arrangement of bolts, and their type, size, and quantity are all different from what was previously explored in other research. As such, an experimental study of the long-term effects of creep and fatigue specific to this 22-bolt connection needs to be investigated. However, it is worthwhile to review the current body of knowledge on the long-term behavior of MF-FRP.

2.2.1 – Cyclic Loading

The first fatigue experiment for an MF-FRP strengthened member was conducted on two concrete beams using power-actuated fasteners (PAFs) (Bank et al., 2002). The FRP was fastened continuously throughout the length of the beams (similar to the schematic in Figure 2.4), which were loaded cyclically in four-point bending between 20% and 80% of the unstrengthened beam capacity at a frequency of 2 Hz. The goal of the tests was to reach 2,000,000 cycles. The first beam failed at 1,780,000 cycles as a result of the supporting rollers translating, leading the beam to crash

against the load frame. It was noted that all fasteners were intact and firmly embedded in the concrete, and that the composite strip had no visible signs of wear or degradation. Special bracing was constructed for the second beam to prevent support translation. However, it failed at 759,000 cycles at a large flexural crack, where, upon inspection, the main reinforcing bars had fractured. The fasteners were reported to have remained intact, and the strip showed no visible signs of damage.

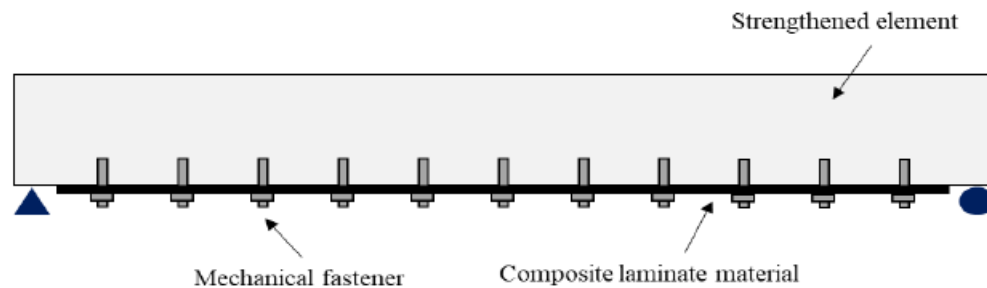


Figure 2.4: Typical MF-FRP strengthening (continuously bonded along length).

To prevent end-delamination failures, a study investigated the use of expansion anchors with MF-FRP plates (Bank, 2004). Part of this study was a fatigue test on one full-size T-beam strengthened with FRP plates fastened continuously throughout its length (Figure 2.4). It was loaded cyclically up to 50% of the yield moment in three-point bending for 2,000,000 cycles. It was reported that the beam survived the experiment with neither observed degradation of the MF-FRP nor loss of stiffness of the beam.

In a study comparing near-surface mounted, conventional adhesive, and mechanically-fastened flexural retrofit applications, six reinforced concrete beams were tested in cyclic loading (Quattlebaum et al., 2005). Two of these used hybrid FRP plates continuously anchored to the soffit through PAFs. This study noted that the hybrid FRP retrofit outperformed the others in terms of fatigue life for the high stress range, failing by fracture of the first reinforcing steel bar after 1,235,087 cycles. The test was continued up to cycle 1,237,118, when the PAFs sheared off the

specimen. This shearing off was raised as a concern by the authors for long-term fatigue applications, but the retrofit was deemed perfectly acceptable for short-term monotonic applications.

Another study compared the flexural fatigue behaviors of reinforced concrete (RC) beams strengthened with two FRP systems: CFRP fabrics and FRP precured laminates (Ekenel et al., 2006). One beam out of seven used 0.375 in. concrete wedge anchors to mechanically fasten the precured FRP laminate continuously over its length. Results indicate this beam survived 2,000,000 cycles but lost 22% of its initial stiffness by the end.

The fatigue of MF-FRP strengthened concrete members was further investigated by Tan and Saha (2007). They performed tests on six 2 m beams with rectangular cross-sections, cycling between a lower limit of 35% and an upper limit of 55-85% of the static flexural strength of the strengthened beams. The researchers found that the stiffness of the strengthened beams degraded rapidly, and believed it to be due to degradation in anchorage bond between the fasteners and the concrete as a result of cracking caused by installation of the fasteners as well as cyclic loading.

In summary, the literature indicates that MF-FRP exhibits good short-term fatigue behavior, which is sufficient considering it is reserved for temporary applications. Though the strengthening is not as effective as externally-bonded applications due to significant anchor slip, it is a viable alternative, especially for applications requiring rapid implementation. Potential weaknesses lie in the more significant loss of stiffness over time, as well as noticeable crushing damage caused by bearing of the fasteners against the plates (Quattlebaum et al., 2005). The experiments to-date deal mostly with small-diameter PAFs and expansion anchors attached directly and continuously to concrete.

2.2.2 – Sustained Loading

The long-term behavior of MF-FRP from sustained loads is, to the author's knowledge, an unexplored topic in previous literature. This makes sense, since in a traditional strengthening application, the dead load is already taken by the structure when the MF-FRP is applied. As a result, the sustained loading effects have not been a cause for concern. The prestressed nature of the MF-FRP in the retrofit used for this research makes creep a concern, and it must be investigated for the design bolt connection using different diameter bolts at the design level of prestressing.

2.3 – Prestressed Concrete Members with Unbonded Tendons

In typical prestressed concrete structures, prestressing strands are usually bonded within the concrete. The change in strain in the strands is equal to the concrete strain according to strain compatibility, and the plane section remaining plane assumption can be applied to the section. However, unbonded prestressed strands are also used in prestressed concrete structures due to its lower unit cost and simplicity in construction compared to bonded strands for structures requiring a lot of prestress force by reducing the net concrete cross-sectional area by introducing voids along the member span (Du and Tao, 1985). Unbonded strands represent prestressing strands that are not bonded to the surrounding concrete. The concept of strain compatibility and plane sections remaining plane for concrete members are not appropriate to this type of structural system. Without bonding to the surrounding concrete, the change in strain in the strands between the anchorages will be equal to the change in length of the surrounding concrete at the same level and introduces difficulties in the analysis of the cross-sectional flexural capacity (Collins and Mitchell, 1997). Unbonded tendons can be differentiated as internal or external unbonded tendons located inside or outside the concrete section, respectively. External prestressing is preferred for strengthening applications due to its reduced installation effort, ease of long-term monitoring, and possibility of future retensioning or replacement (Naaman and Breen, 1990).

2.3.1 – Internal Unbonded Tendons

For specimens with internal unbonded tendons, the effective depth of the tendon remains the same when the member deforms under the externally applied load. Naaman and Alkhairi (1991 a,b) proposed a design model to calculate the stress in prestressing reinforcement of internal unbonded tendon at the nominal flexural strength of the section, f_{ps} , by considering cross-sectional property detailing and a bond reduction coefficient based on the tendon profile and loading patterns. It indicated that the stress in unbonded tendons depends on the member deformation and can be considered as constant along the length. The proposed bond reduction coefficient was divided into elastic uncracked, elastic cracked, and ultimate state to use in the analysis. The predicted results compared with the experimental results showed a better correlation than other models by accounting for the loading condition and the span-to-depth (L/d_{ps}) of the member.

Lee and Kim (2011) studied the existing approaches and then proposed an improved provision to calculate the ultimate strength of prestressed members with internal unbonded tendons using the simplified maximum curvature distribution and applied a moment distribution coefficient related to the loading pattern. The research found that the loading pattern affected the distribution of cracks more compared to the use of bonded prestressing steel. New coefficients related to the maximum moment zone and loading pattern were introduced to determine the ultimate stress of the unbonded tendons. The proposed new coefficients can provide an improved prediction compared to the existing approaches and predicted the flexural strength of members with normal or high-strength concrete well.

2.3.2 – External Unbonded Tendons

Existing structures are usually strengthened using external unbonded strands. Unlike internal unbonded strands where the effective depth remains constant as the member deforms, the global position of the external tendon remains constant while the member deflects as the

connection to the concrete member is through the anchorages or both the anchorages and deviator(s). This behavior is known as a second-order effect where the effective depth of the unbonded tendon reduces with increasing applied load that causes the member to deflect. The second-order effect can be neglected under the small member deflection, as the change in eccentricity is small and the behavior is similar to the internal unbonded tendons. However, as the beam continues to deflect, the second-order effect becomes significant and needs to be considered.

Tan and Ng (1997) investigated the second-order effect on externally prestressed beams under different load and tendon configurations and presented a method to predict member behavior. The results showed that the second-order effect for a straight external tendon led to a lower load-carrying capacity compared to a tendon profile with the presence of the deviators. Specimens with harped external unbonded tendons experienced a wider spread of cracks, larger deflection at failure, and higher increased tendon stress compared with the straight tendon profile. Based on the bond reduction coefficients from Naaman and Alkhairi (1991 a, b), the analytical results provided a good prediction of the ultimate strength with an average difference of 5% compared to experimental results.

Harajli et al. (1999) conducted a nonlinear analysis to predict the load-deflection response of repaired specimens. The analysis results were then used to validate the experimental results of Khairallah and Harajli (1997) and Tan and Ng (1997). The research was focused on the parameters that influence the second-order effect, including external prestressing force, deviator configuration, external tendons profile, and applied load pattern. An iterative procedure was applied to satisfy the member deformation compatibility and force equilibrium at each response level in the analysis. Multiple iterations were conducted in the analysis by assuming the stress in the external prestressing tendon and concrete strain in the compression fiber at the critical section. The

analytical moment-deflection diagram presented a good prediction compared to experimental results from the literature. Figure 2.5 shows the nonlinear analysis prediction compared to the experimental results. Tendons without deviators experienced a lower nominal flexural strength. A similar load-deflection response was observed for the specimens with one or two deviators. Three-point bending has less second-order effect than four-point bending or uniform applied load due to the lower post-elastic deformation.

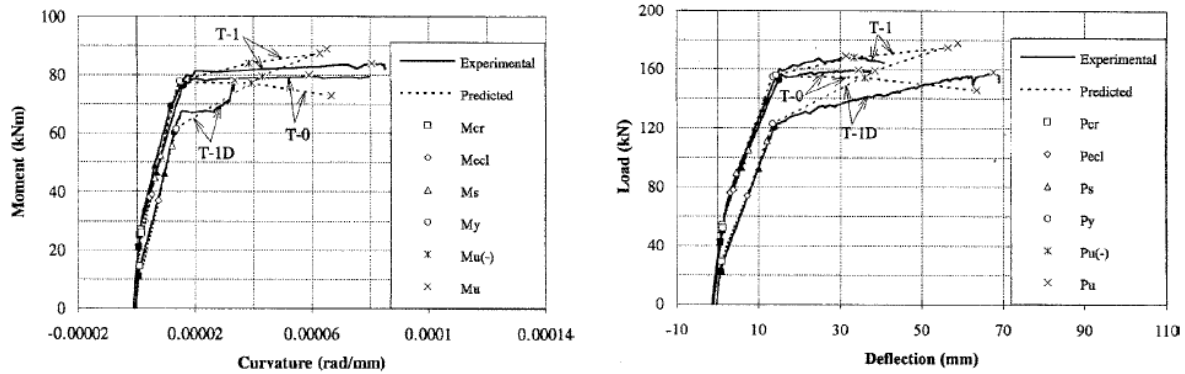


Figure 2.5: Experimental vs. analytical results (adapted from Harajli et al., 1999).

Tan and Tjandra (2007) presented a topic related to strengthening continuous reinforced concrete beams using external prestressing. Unlike most experiments, which tested simple supports and single span, this research emphasized the flexural behavior of continuous beams. Different variables were studied in this research, such as the effect of tendon type (steel and CFRP), strengthened region (positive and/or negative moment region), tendon configuration (straight, draped, and parabolic), and the loading pattern (symmetrical and unsymmetrical). Although the elastic modulus of the CFRP tendons used in the study was lower than the steel tendons, it presented a similar response after strengthening. Beams strengthened in both positive and negative moment regions experienced 13% more load-carrying capacity compared to the control specimen than the beam strengthened in the positive region only. In all tendon configurations, tendons with parabolic profile and overlapping at the interior support, which strengthened both positive and

negative moment regions, experienced the best improvement in both ductility and ultimate load-carrying capacity compared to other profiles. Shear distress at the unstrengthened interior region of the beam with anchored parabolic tendons led to a less ductile failure. Specimens with symmetrical applied loading exhibited a higher ultimate load-carrying capacity compared to the beams subjected to the unsymmetrical loading, which underwent an uneven deflection. The design procedure for strengthening a continuous beam using external tendons can be done using charts, as in Figure 2.6, related to the global prestressing index, concrete strength, and tendon effective depth.

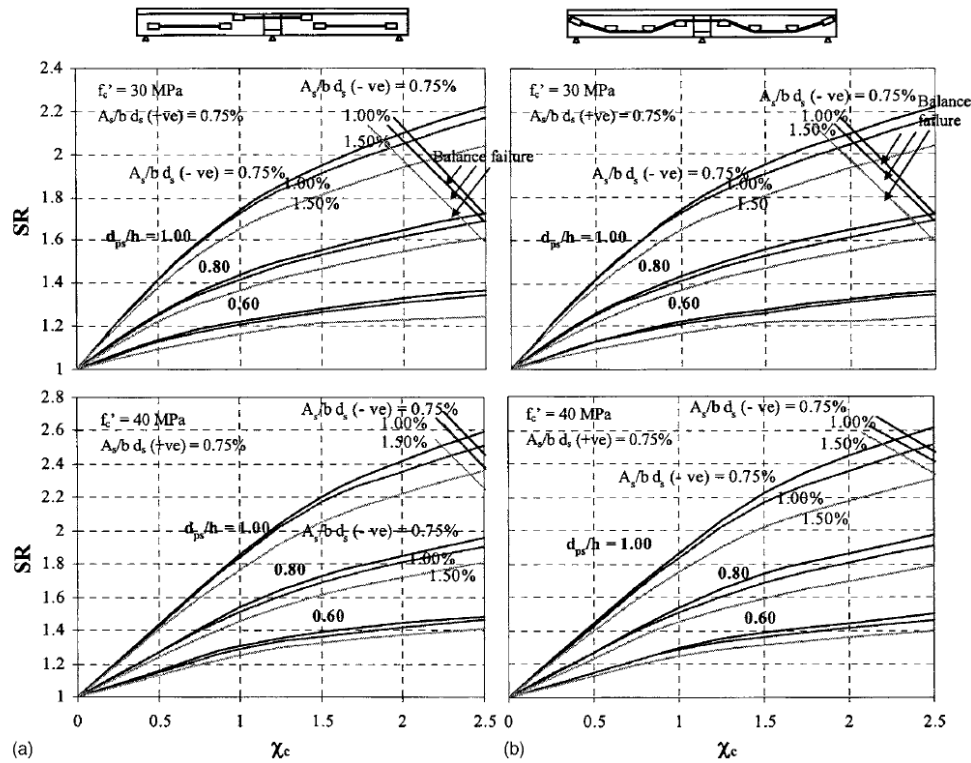


Figure 2.6: Design charts for strengthening with external tendons (adapted from Tan et al., 2007).

2.4 – Shear Strengthening of Concrete Beam Members

Flexural and shear failures are the primary failure modes observed in typical concrete beams. Unlike a ductile flexural failure mode, which is more desirable, shear failure tends to be

brittle and causes catastrophic damage. Therefore, quantifying the shear capacity is critical in structural design, maintenance, and retrofit. To repair shear deterioration, steel and FRP plates are considered the common repair application since the 1960s by either adhesive bonding or bolting.

2.4.1 – Shear Strengthening using Fiber Reinforced Polymer (FRP)

Shear strengthening of reinforced concrete beams using an externally bonded system has been widely studied since the 1990s. Due to the flexibility of an FRP sheet compared to a steel plate, which is usually applied on the side of the specimen, U-jacketing and wrapping of the FRP sheet at the desired orientation and configuration has served as an alternative method for the retrofit. Khalifa and Nanni (2000) studied the shear strengthening application with different parameters, including the amount and distribution of CFRP, bond surface, FRP fiber direction, and end anchorage. Figure 2.7 shows the detail of the end anchorage of the U-wrap. The experimental results indicated that specimens strengthened with continuous U-wraps with end anchorage experienced the highest increased in shear capacity with 145% and 42% compared to the control specimen and U-wrap without end anchorage, respectively. The retrofit with end anchorage was sufficient to change the failure mode from debonding of the U-wrap to member flexural failure. The results presented that the same strengthened shear capacity was achieved by continuous U-wraps and CFRP strips in the form of U-wraps (40% of CFRP used as continuous U-wraps). However, the field application was not recommended due to the damage of individual strips, which reduces the total strengthened shear capacity.

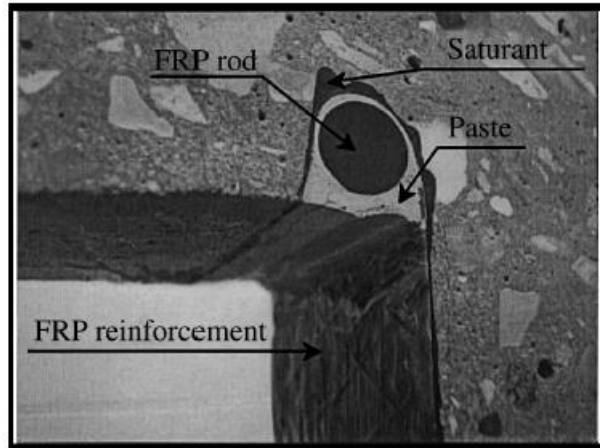


Figure 2.7: Detail of the end anchorage of an FRP U-wrap (adapted from Khalifa and Nanni, 2000).

In the observation from the studies on the shear strengthening of RC beams using the EB-FRP system, FRP rupture and debonding are the primary failure modes. Of the current design models, FRP debonding is considered the controlling failure mode of the system. Chen and Teng (2003) developed a simple, accurate, and reasonable model for the shear strengthened RC beams controlled by FRP debonding failure. The current ACI 440.2R (2017) design model from Khalifa et al. (1998) considers the angle and spacing of the FRP strips, section properties, and bond reduction coefficient, resulting in an effective strain. Chen and Teng (2003) proposed a model that can apply to FRP strips and continuous sheets. A strip spacing limit was applied to ensure that at least one FRP U-wrap intercepts the assumed diagonal crack. The governing failure mode was used to determine the effective FRP stress. The proposed model showed a good prediction compared to the experimental data.

2.4.2 – Shear Strengthening using Steel Plates

Adhikary and Mutsuyoshi (2006) and Adhikary et al. (2000) performed research to investigate adhesively-bonded continuous steel plates on reinforced concrete beams to increase the member shear capacity. The improvement of the shear capacity was related to the plate depth and the thickness of the plate. The maximum shear contribution can be achieved by covering the

section depth with steel plates. Although the use of thicker plates can increase shear capacity, it was found not as efficient as increasing the depth of the plates. Adhikary and Mutsuyoshi (2005) presented different techniques to enhance the shear capacity, including steel brackets, bonded steel plates, anchored steel plates, and anchored steel strips and stirrups. The specimen with externally anchored stirrups experienced the highest improved shear capacity compared to the other strengthening methods. Figure 2.8 presents the strengthening schemes used to improve beam shear behavior.

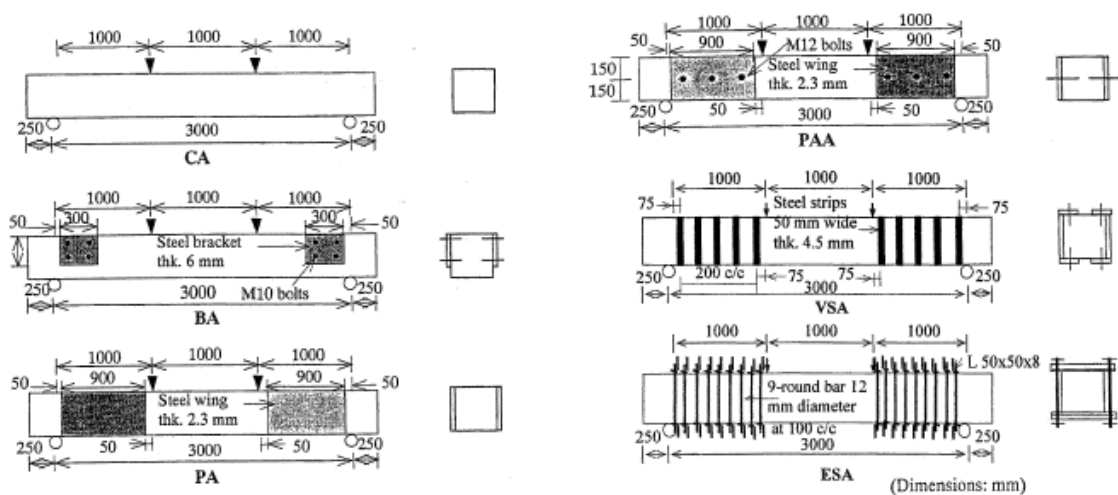
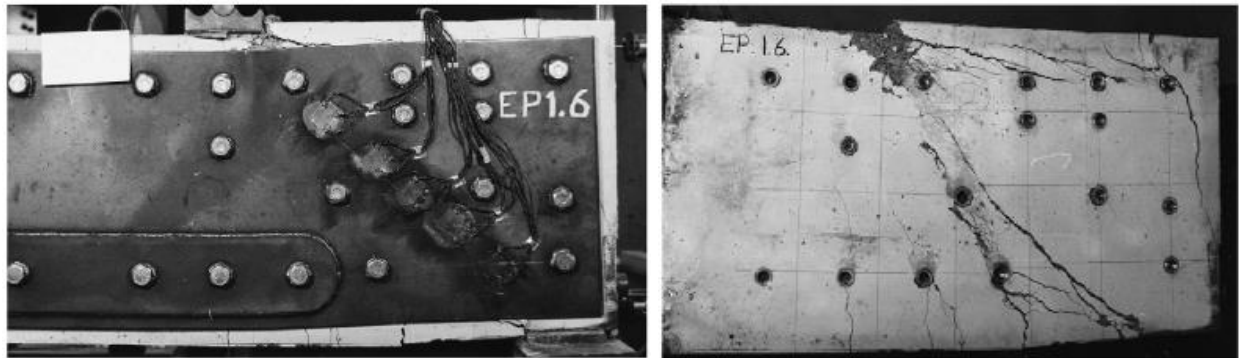


Figure 2.8: Shear strengthening schemes (adapted from Adhikary and Mutsuyoshi, 2005).

Barnes et al. (2000) studied shear strengthening using external steel plates attached to the concrete surface under two methods: adhesive bonding and bolting. The advantages and disadvantages of using adhesive bonding or bolting were described in the literature. For the bolting application, 70 ft.-lbs. torque was applied to the bolt to achieve a positive connection and then welded to prevent slip due to the clearance of the bolt hole. Surface preparation of the plate and concrete was conducted before applying the adhesive bonding. The literature showed that a significant improvement of serviceability and ultimate capacity could be achieved if sufficient plate anchorage is provided. A proper bolt arrangement needs to be considered to provide enough

plate anchorage to reach ultimate capacity. Figure 2.9 shows one of the experimental results using the bolted plate strengthening method.



(a) Before the removal of the steel plates

(b) After the removal of the steel plates

Figure 2.9: Experimental result at failure (adapted from Adhikary and Mutsuyoshi, 2005).

2.5 – Summary of the Literature Review

A brief review of the literature presented in this chapter indicates the following needs to be accomplished to address current research gaps:

1. The bearing behavior of the FRP plate with 0.50 in. diameter fasteners is not well documented within the literature; however, Martin and Lamanna (2008) indicated that a 0.50 in. diameter fastener is likely necessary to fully develop the capacity of the FRP plate with holes prior to complete bearing failure between the fastener and FRP plate. Small-scale material testing to determine the bearing capacity of the FRP plate used in this project is necessary. Single-bolt bearing and multi-bolt bearing tests are likely needed to understanding the development of the full anchorage system capable of developing the necessary prestressing forces for the retrofit solution.
2. The fatigue study for this research needs to specifically address the behavior of the design bolt connection using different diameter bolts.

3. A realistic cycling range must be defined, with a lower-bound at the design prestressing level, and an upper-bound representative of stress increases caused by traffic.
4. For the purposes of design and quality control, the design bolt connection's fatigue life, visual damage over time, stiffness degradation, and failure envelope under cyclic loading are all of interest.
5. A sustained loading experiment needs to be designed for the design bolt connection to investigate creep effects at the design prestressing level.
6. Develop an analysis procedure that includes the second-order effect of external unbonded tendons. The reinforcing strain (FRP in the current research) will not be compatible with the concrete strain as it is treated as an external unbonded strand.
7. A shear strengthening system compatible with the flexural prestressed MF-FRP retrofit system needs to be designed for prestressed concrete C-channel beams that experience both flexure and shear deterioration.

CHAPTER 3 – ANCHOR BOLT PATTERNS FOR MACHANICALLY FASTENED FRP PLATES

This chapter presents the study of anchor pattern and fastener diameter necessary to develop the maximum capacity possible of a commercially available hybrid glass and carbon FRP plate material manufactured with longitudinal, pultruded carbon fiber tows encased in a random glass fiber mat (Figure 3.1) – hereafter referred to as FRP – typically used in MF-FRP application. The small-scale material tests presented in this chapter were conducted in three phases: 1) uniaxial tension without holes, 2) uniaxial tension with open holes, and 3) uniaxial tension with single- and multi-bolt connections. Results are presented and discussed to show the designed fastener patterns and capacity to optimize mechanically fastened anchor system for the retrofit solution. Besides, the use of different mechanical fastener diameters in varying numbers was also studied to provide engineers a suite of solutions for varying situations.

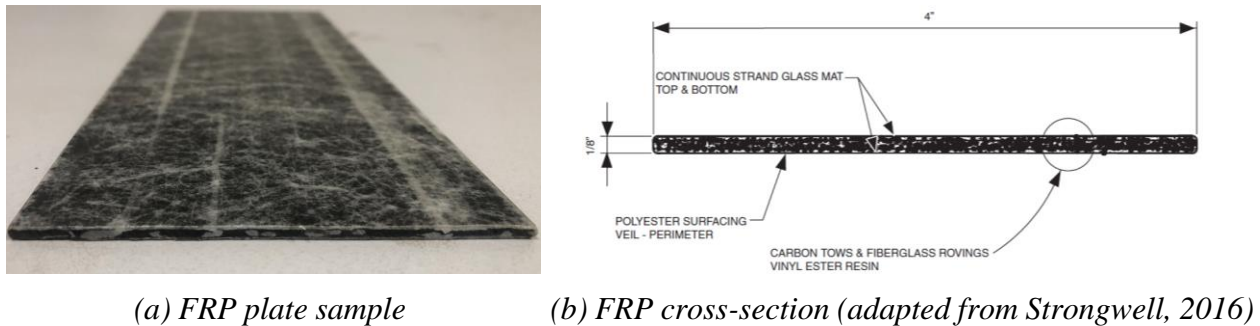


Figure 3.1: FRP plate sample examined in this study.

3.1 – Methodology

3.1.1 – Test Treatment Groups

To identify the optimal anchor bolt pattern, an experimental program was designed to explore the effects of different anchoring parameters: longitudinal spacing, transverse spacing, number of bolts, and bolt pattern (aligned versus staggered). Therefore, a test matrix (Table 3.1) with a total of 14 tension test treatments was developed with three distinct categories: no hole,

openhole, and bolted. All treatment groups were tested in uniaxial tension. The no-hole group consisted of 28 in. long FRP plates without holes. The open-hole group consisted of five specimens, all 28 in. long, with varying number of holes, transverse spacings, and hole patterns. The bolted group considered single-bolt connections, as well as 16-, 18-, 20-, and 22-bolt connections. ASTM D5766/D5766M-11 (ASTM 2014a) specifies a width-to-diameter (w/D) ratio of 6 for open-hole tests. However, given the fixed width of the FRP material tested and the desired 0.5 in. bolt diameter, the w/D ratio for open-hole tests in this paper was adjusted to 7 and 3.5 for singlehole and multihole test treatments, respectively, corresponding to the nominal specimen width (4 in.) and actual hole diameter (9/16 in.).

Table 3.1: Test matrix.

Specimen ID	No. of Replicates	Treatment Description	ASTM
T	8	No holes	D3039
S-OH	6	Single open hole centered in gauge length	D5766 ^a
DBL4-OH-1.5	6	4 open holes; 2-by-2; 1.5 in. transverse spacing; 4 in. longitudinal spacing	D5766 ^a
DBL4-OH-2.0	6	4 open holes; 2-by-2; 2 in. transverse spacing; 4 in. longitudinal spacing	D5766 ^a
STG4-OH-1.5	6	4 open holes; staggered with 2 in. offset; 1.5 in. transverse spacing; 4 in. longitudinal spacing	D5766 ^a
STG4-OH-2.0	6	4 open holes; staggered with 2 in. offset; 2 in. transverse spacing; 4 in. longitudinal spacing	D5766 ^a
S-B-X-1.5	6	Single bolt bearing with 1.5 in. edge distance excluding threads	D5961
S-B-N-1.5	6	Single bolt bearing with 1.5 in. edge distance including threads	D5961
S-B-X-4.0	6	Single bolt bearing with 4 in. edge distance excluding threads	NA
S-B-N-4.0	6	Single bolt bearing with 4 in. edge distance including threads	NA
DBL16-B-1.5	6	16 bolts; 0.5 in. diameter; 2-by-2; 1.5 in. transverse spacing; 4 in. longitudinal spacing	NA
DBL18-B-1.5	6	18 bolts; 0.5 in. diameter; 2-by-2; 1.5 in. transverse spacing; 4 in. longitudinal spacing	NA
DBL20-B-1.5	6	20 bolts; 0.5 in. diameter; 2-by-2; 1.5 in. transverse spacing; 4 in. longitudinal spacing	NA
DBL22-B-1.5	6	22 bolts; 0.5 in. diameter; 2-by-2; 1.5 in. transverse spacing; 4 in. longitudinal spacing	NA
S-B-X-0.375-1.5	6	1 bolt; 0.375 in. dia.; 4 in. edge distance excluding threads	NA
DBL18-B-0.375-1.5	6	18 bolts; 0.375 in. diameter; 2-by-2; 1.5 in. transverse spacing; 4 in. longitudinal spacing	NA
DBL20-B-0.375-1.5	6	20 bolts; 0.375 in. diameter; 2-by-2; 1.5 in. transverse spacing; 4 in. longitudinal spacing	NA
DBL22-B-0.375-1.5	6	22 bolts; 0.375 in. diameter; 2-by-2; 1.5 in. transverse spacing; 4 in. longitudinal spacing	NA
DBL14-B-4-0.75-1.5	6	14 bolts; 0.75 in. diameter; 2-by-2; 1.5 in. transverse spacing; 4 in. longitudinal spacing	NA
DBL14-B-6-0.75-1.5	6	14 bolts; 0.75 in. diameter; 2-by-2; 1.5 in. transverse spacing; 6 in. longitudinal spacing	NA

^aASTM D5766 specifies a single hole with a $w:D$ ratio = 6; test was adapted to accommodate desired hole diameters for single- and multibolt treatment conditions.

3.1.2 – Number of Replicates for Each Test

To achieve statistical significance, the number of replicates necessary for each group needed to be calculated. It was desired that conclusions be statistically significant at least to the 90% confidence level (CL) with a 5% limit of error (e). The CL for a desired test result can be calculated in terms of the coefficient of variation (COV) on the tension strength of the material

and a sufficient number of sample replicates using either a Student's t-distribution (fewer than 30 replicates), or a standard normal distribution (greater than 30 replicates). For the purposes of this research, a Student's t-distribution was used to determine the sample size (n) required for each test to achieve the desired 90% CL. The development of the sample size calculation is shown in Eqs. (1)-(3) for n number of independent and identically distributed (*iid*) samples (X) that follow a standard normal distribution (N) with mean, μ , and variance, σ^2

$$X_1, \dots, X_n \sim iid N(\mu, \sigma^2) \quad (3.1a)$$

and

$$\hat{\mu} = \bar{x} \quad (3.1b)$$

and

$$\hat{\sigma}^2 = \frac{1}{n-1} \sum_{i=1}^n (x_i - \bar{x})^2 \quad (3.1c)$$

and

$$\hat{\sigma} = \sqrt{\hat{\sigma}^2} = s \quad (3.1d)$$

where $\hat{\cdot}$ indicates an estimate of the parameter (e.g., $\hat{\mu}$ is the estimator for the population mean, which is the sample mean, \bar{x}). The 90% CL of μ is defined as

$$\hat{\mu} \pm t_{(0.95, df=n-1)} \frac{\hat{\sigma}}{\sqrt{n}} \quad (3.2a)$$

and

$$e = t_{(0.95, df=n-1)} \frac{\hat{\sigma}}{\sqrt{n}} \quad (3.2b)$$

where t = critical value that corresponds to the 95th percentile on the Student's t-distribution with $n-1$ degrees of freedom (df); and e = limit of error defined as half of the confidence interval. If n is sufficiently large, the critical value, $t_{(0.95, df=n-1)}$, is approximately 1.7, therefore Eq. (3.2b) can be rewritten in terms of s as

$$e = 1.7 \frac{s}{\sqrt{n}} \quad (3.2c)$$

where s = sample standard deviation.

The goal is to determine the minimum number of replicates required to achieve the 90% CL and a limit of error of 5%. Therefore, Eq. (3.2c) is rewritten in the following form to solve for n in terms of a limit of error that is normalized with respect to the sample mean, \bar{x} , such that e is expressed as a percentage:

$$n = \left(1.7 \frac{\frac{s}{\bar{x}}}{\frac{e}{\bar{x}}} \right)^2 \quad (3.2d)$$

and, the normalized standard deviation with respect to the sample mean is known as the COV

$$COV = \frac{s}{\bar{x}} \quad (3.2e)$$

Substituting COV in Eq. (3.2d) gives the following final form of the statistical equation that is routinely used to determine the minimum number of replicates required for a 90% CL:

$$n = \left(1.7 \frac{COV}{e} \right)^2 \quad (3.3)$$

where COV = coefficient of variation (%) of a material property; and e = limit of error (%) desired, typically taken as 0.5 (1 – CL).

The number of replicates required to achieve a CL that is different from 90% can be calculated using the t critical value which corresponds to the desired CL and degrees of freedom.

For example, a 95% CL with 40 degrees of freedom would be calculated using a critical value of approximately 2.0, and a 99% CL would be calculated using a critical value of 2.7.

Material test data from the manufacturer were used to determine the COV (Equation 3.2e) of the material for pure tension, open-hole tension, and bolt bearing. The material test data available for the FRP used in this paper included the mean value for each set of material tests and the design value, which is published as three standard deviations below the mean in accordance with ACI 440.2R (2017). Therefore, the standard deviation for each test was determined as

$$s_{test} = \frac{mean\ value - design\ value}{3} \quad (3.4)$$

where s_{test} = material standard deviation for the given test; *mean value* = mean test value for a given condition (e.g., mean tensile strength based on a sample size of 20 replicates); and *design value* = published material design value for a given condition (e.g., design tensile strength).

Equation 3.3 was used to determine the number of replicates needed for each test condition. The material test data provided by the manufacturer is provided in Table 3.2 and the resulting number of replicates required to achieve the 90% CL, with various limits of error, is provided in Table 3.3. Each material test result provided by the manufacturer is based on a sample size of 20, which is sufficiently large to use a Student's t-distribution to determine the number of replicates needed for each condition tested.

The minimum number of replicates for the pure tension tests (no-hole condition) in this paper is eight and the minimum number of replicates for tension tests using open-hole, unclamped singlebolt bearing, and unclamped multibolt bearing conditions is four for each condition, all of which correspond to the 90% CL with a 5% limit of error (Table 3.3). In some tests a greater number of replicates (Table 3.1) was used and therefore the actual CL for each test will be discussed later.

Table 3.2: Data provided by the manufacturer.

Property	No. of Replicates	Mean Value (ksi)	Design Value (ksi)	ASTM
Tensile Strength	20	123.6	92.9	D638
Open Hole Strength	20	94.6	78.8	D5766
Unclamped Bearing Strength	20	31.0	26.0	D5961

Source: Adapted from Strongwell (2016)

Table 3.3: Calculated data and sample size for 90% CL.

Property	s^a (ksi)	COV^b (%)	No. of Replicates for 90% Confidence Level ^c				
			e	2.5%	5.0%	7.5%	10.0%
Tensile Strength	102.5	8.29	n	32	8	4	2
Open Hole Strength	5.3	5.57	n	15	4	2	1
Unclamped Bearing Strength	1.6	5.30	n	13	4	2	1

^a Calculated using Eq. (3.4)^b Calculated using relationship between Eqs. (3.2d) and (3.3).^c Calculated using Eq. (3.3)

3.1.3 – Instrumentation

DIC techniques are used in this research to develop a continuous strain map over the entire specimen during testing. A detailed description and discussion of DIC is provided by Xie and Kang (2015). The accuracy of DIC compared to conventional strain gauge measurements is a common topic in the literature with the general understanding that when the system is properly calibrated, the accuracy of strain measurement using DIC is equal to foil strain gauge measurements (Hoult et al. 2013; Bomarito et al. 2017). The benefits of DIC include the ability to visualize strain (longitudinal, transverse, and shear) over the entire surface of a specimen (Figure 3.2(b and c)) rather than only at the location of an applied strain gauge, and the ability to measure strain well beyond the point at which typical strain gauges debond from the surface of the test specimen.

DIC uses a series of photos taken of the material surface during testing to measure the relative distance between speckles which are applied to the material before testing. The speckle pattern in this research was applied to each test specimen using an ink roller with a nonuniform pattern and 0.33-mm dot size (Figure 3.2(a)) which was calibrated to the camera resolution and field of view used during the test. This calibration ensures the accuracy of the commercial DIC system used in this paper to within 10 microstrain and is consistent with the calibration requirements discussed by Hoult et al. (2013) and Bomarito et al. (2017). The contrast between

the specimen and the speckle pattern was achieved by painting the material surface with white spray paint before applying the black ink speckle pattern.

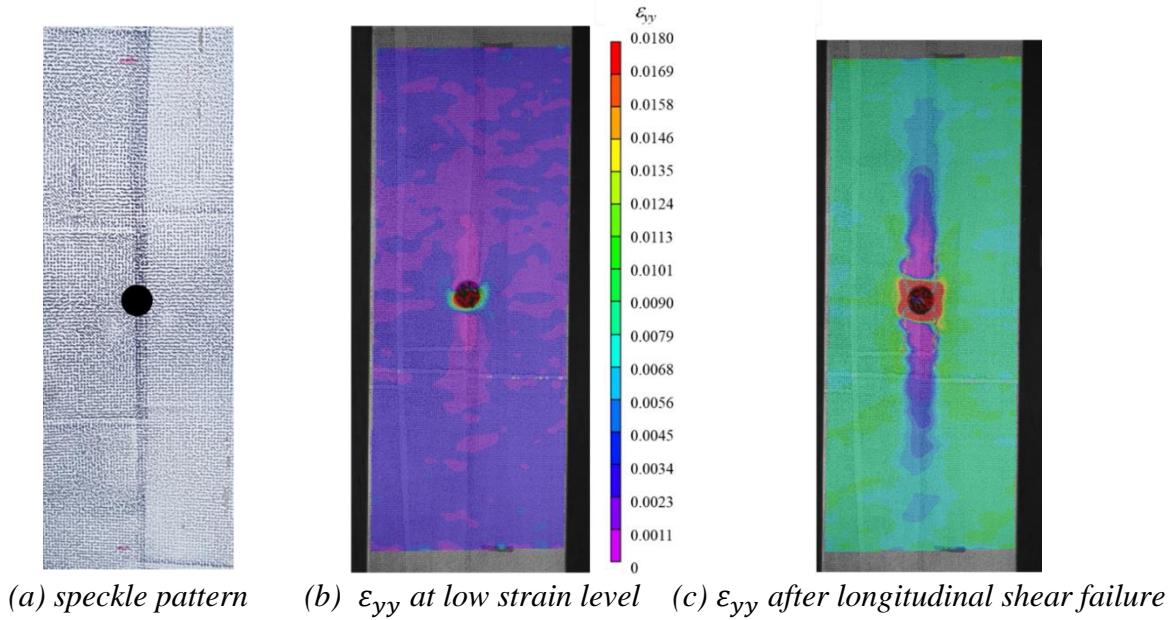


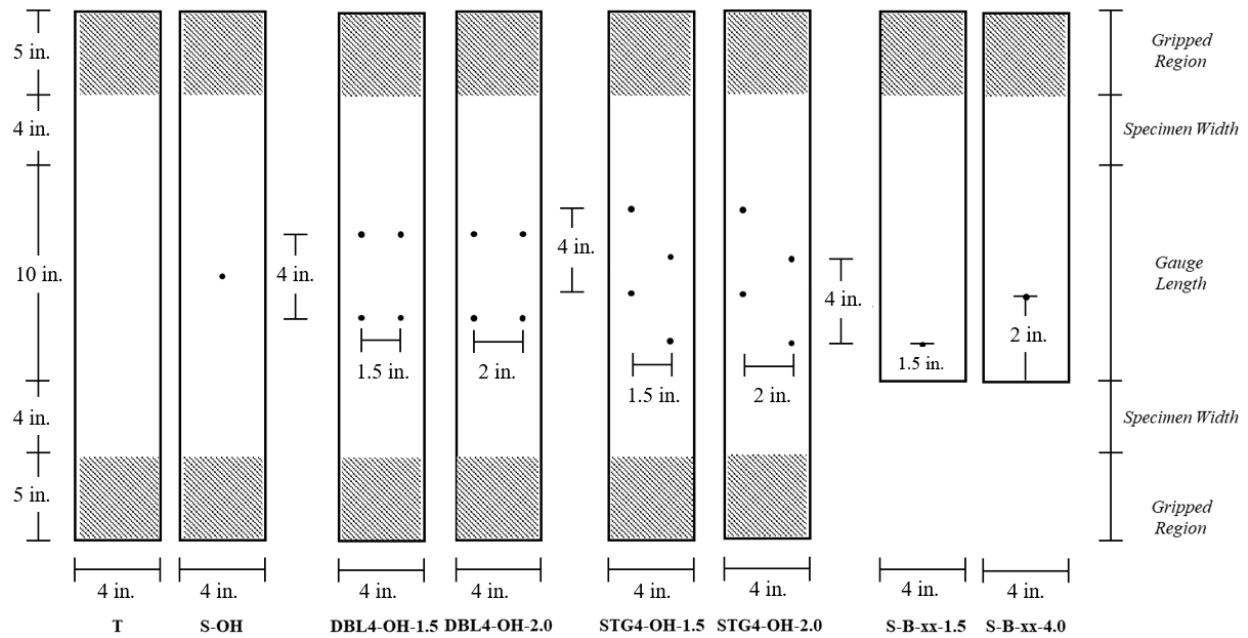
Figure 3.2: Example DIC strain field and specimen speckle pattern.

3.1.4 – Tension Test Treatments and Specimen Preparation

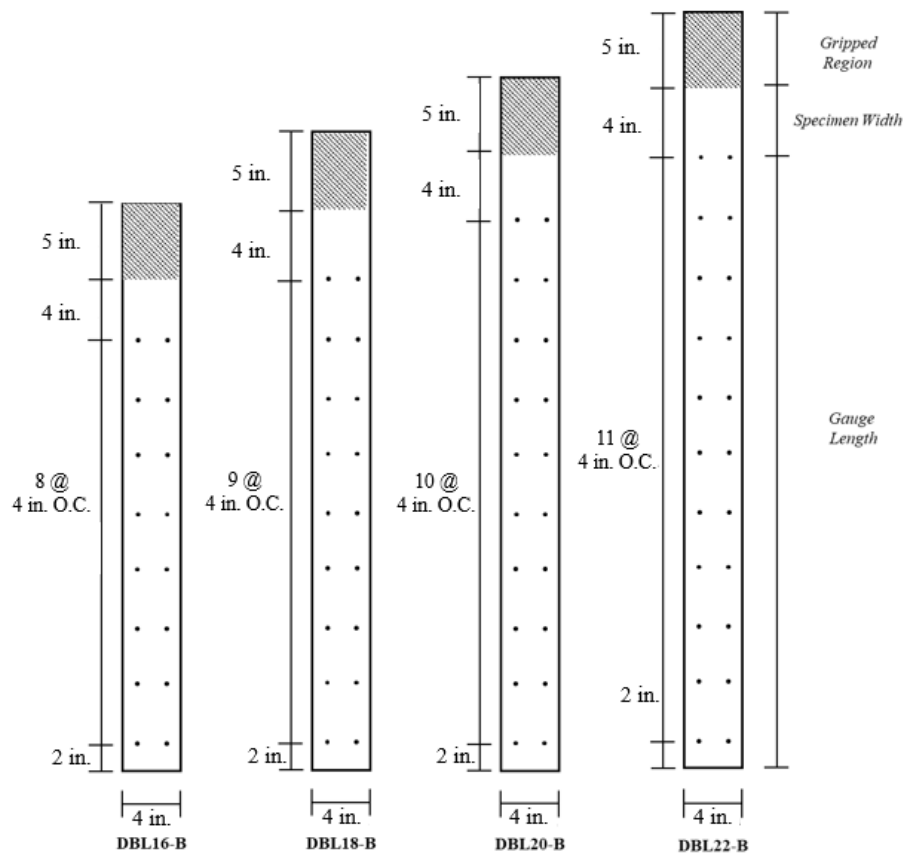
A universal testing machine (UTM) with an 200 kips \pm 0.25% capacity load cell was used to conduct a series of tension tests using nine different hole patterns: no holes, single hole, four holes aligned in two columns, four holes staggered, single-bolt bearing, and multibolt bearing. All holes had a 9/16 in. nominal diameter to accommodate a 0.5 in. diameter fastener. Statistical analysis of the results presented subsequently in this paper refers to each test variation as a treatment to be consistent with terminology used in statistical modeling. For each 4-hole treatment, two transverse spacing distances were examined, and for the single-bolt bearing pattern, two edge distances, bearing on threads, and excluding threads were examined. The variations of each pattern created a total of 14 treatment groups. Figure 3.3(a) shows the no-hole, openholes, and single-bolt bearing test treatment configurations, and Figure 3.3(b) shows the multibolt treatment configurations. The corresponding specimen identification referenced in the test matrix (Table 3.1)

is also shown for each treatment in Figure 3.3(a and b). The results of the statistical analysis for the open-hole treatment groups (discussed in detail subsequently in this report) indicate that there is no statistically significant difference between the staggered and aligned hole patterns, and between the 1.5 and 2 in. transverse spacing hole patterns. Therefore, the 1.5 in. aligned hole patterns were the only patterns used for the multibolt treatment conditions shown in Figure 3.3(b). Each tension test treatment contains at least the minimum number of replicates to achieve the 90% CL as discussed previously. The ASTM standards which apply to each test are also provided in Table 3.2.

Each specimen was cut from one of three rolls of FRP material using a standard wet tile saw. An equal number of specimens from each roll was taken for each treatment group to ensure variation between rolls was reflected in each sample set. Prior to painting and applying the DIC speckle pattern, 9/16 in. diameter holes were drilled in the samples using a tungsten carbide hole saw in accordance with the dimensions in Figure 3.3, and the actual thickness, width, and hole diameter for each specimen were measured and recorded.



(a) No hole, open holes, and single-bolt bearing



(b) Multi-bolt bearing

Figure 3.3: Test treatment configurations and specimen identification.

3.1.5 – Universal Testing Machine Tension Test Setup

Tensile forces developed in the UTM were transferred to the test specimen through 5 × 5 in. knurled, steel wedge grips. Care was taken to ensure each specimen was plumb with the axis of the UTM to minimize eccentric load effects. Pilot tests were also conducted to determine if the wedge grips of the UTM required alignment, or if tabs needed to be bonded to the FRP material to properly grip each specimen such that rupture in the FRP occurred before slipping at the grips. It was determined that the wedge grips alone were sufficient to develop rupture in the FRP without slipping between the steel grips and the FRP plate, and no local rupture occurred at the grips. An example test setup with the FRP specimen gripped in the UTM is shown in Figure 3.4(a). The UTM setup shown in Figure 3.4(a) was used for the no-hole and open-hole treatment conditions. Figure 3.4(b) shows an example of a failed specimen in the no-hole treatment condition.



(a) UTM setup (no-hole)



(b) failed specimen (no-hole)

Figure 3.4: UTM setup (no-hole and open-holes) and failed specimen.

Tension tests without holes (specimens T-1–T-8) were conducted in accordance with ASTM D3039/3039M (ASTM, 2014c). Tests with open holes were conducted in general accordance with ASTM D5766/D5766M-11 (ASTM, 2014a); however, the $w:D$ ratio was adjusted to accommodate a 0.5 in. diameter bolt and multiple hole configurations. Each test specimen had a nominal thickness of 0.125 in. and a nominal width of 4 in. Actual thickness and width were recorded for each specimen prior to testing. Total specimen length (Figure 3.3(a)) was determined using a 10 in. gauge length, plus 8 in. (two times plate width), plus 10 in. (5 in. for each grip), as specified in ASTM D3039/ D3039M (ASTM, 2014c). Each specimen was loaded at a constant displacement rate of 0.05 in./min., and load-displacement data were recorded at a frequency of 1 Hz, in addition to the DIC strain data for each test. Tests were conducted until rupture, and each failure mode was recorded in accordance with ASTM D3039/D3039M (ASTM, 2014c) failure codes.

Single-bolt bearing tests were conducted in general accordance with ASTM D5961/D5961M (ASTM, 2017) using two edge distances, 1.5 in. (three times bolt diameter to be in strict accordance with ASTM D5961/D5961M) and 4 in. edge distance (corresponding to the longitudinal spacing in the open-hole and multibolt treatment conditions). Additionally, tests were conducted to examine the effects of bearing on threads (threads included) and on the bolt shank (threads excluded), as provided in Table 3.1.

A steel plate with an offset in the grip region was designed for the test to ensure the centerline of the FRP test specimen coincided with the centerline of the UTM axial load (Figure 3.5). The plate was also sized to accommodate multiple bolt patterns. Bolts were tightened to 30 lbs.-in., corresponding to a field specification of finger tight plus 1/4 turn, for all tests so as not to create a slip-critical connection between the FRP and steel plate. The test was designed as an

idealization of the bolted connection, the goal of which was to achieve the maximum capacity of the FRP plate with holes. The steel plate is used in place of the concrete substrate to which the MF-FRP will typically be attached; therefore, concrete failure modes, which can be analyzed using traditional design techniques, are not considered in this test.

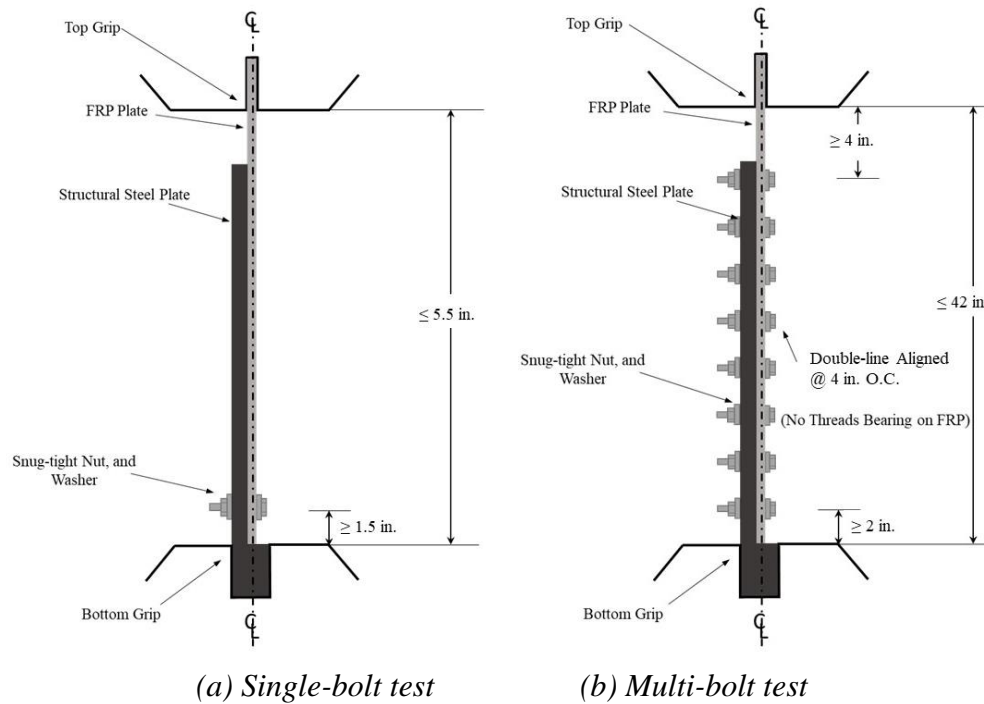


Figure 3.5: Bolted connection test schematic.

3.2 – Results and Discussion

The results for all tests are summarized in Table 3.4. Mean peak load was determined directly from available load data and mean peak stress was calculated using the peak load and either (1) net cross-sectional area of the test specimen for no-hole and open-hole treatment groups, or (2) bolt-bearing area, calculated in accordance with ASTM D5961/D5961M (ASTM 2017) for single-bolt and multibolt treatment groups. Individual measurements for specimen width, thickness, and hole diameter were taken for each test specimen using a digital caliper (0.001 in. precision). The mean values, standard deviations, and coefficients of variation for these

measurements are provided in Table 3.5. The mean measurement values were used for calculating stress levels for all multibolt treatment groups.

Sample peak stress standard deviations were recorded for each sample set and used to determine the peak stress coefficient of variation within each sample set (Table 3.4). Equation (5) was used to calculate the confidence limit for sample sets and the population (defined as the manufacturer-provided data)

$$t_{(0.95,df=n-1)} = \frac{e\sqrt{n}}{COV} \quad (3.5)$$

The lowest CL based on population (manufacturer) data was 90% for the no-hole (T) treatment condition; however, all other treatment condition tests resulted in higher CL because of the lower COV with respect to the number of specimens tested for each treatment group. All multibolt treatment conditions obtained results at the 92% CL.

Table 3.4: Summary test results.

Specimen ID	No. of Replicates	Mean Peak Load (kips)	Mean Peak Stress ^a (ksi)	Sample Peak Stress Standard Deviation (ksi)	Sample Peak Stress COV (%)	CL based on Sample COV (%)	Population Peak Stress (ksi)	Population Peak Stress COV (%)	CL based on Population COV (%)
T	8	76.4	146.5	5.9	3.99	99	123.6	8.28	90
S-OH	6	66.5	150.8	6.1	4.06	96	94.6 ^a	5.56	97
DBL4-OH-1.5	6	51.5	136.9	4.4	3.18	97	NA	5.56 ^b	97
DBL4-OH-2.0	6	52.4	131.8	6.5	4.89	95	NA	5.56 ^b	97
STG4-OH-1.5	5	52.6	138.9	2.3	1.63	99	NA	5.56 ^b	93
STG4-OH-2.0	5	51.3	135.9	1.8	1.35	99	NA	5.56 ^b	93
S-B-X-1.5	6	2.9	45.7	2.2	4.75	95	31.0 ^a	5.37	92
S-B-N-1.5	6	3.1	47.0	2.7	5.72	91	NA	5.37 ^c	92
S-B-X-4.0	6	3.4	50.6	2.9	5.77	90	NA	5.37 ^c	92
S-B-N-4.0	6	3.6	55.8	3.9	6.94	86	NA	5.37 ^c	92
DBL16-B-1.5	6	42.5	39.9	1.2	2.91	99	NA	5.37 ^c	92
DBL18-B-1.5	6	45.4	38.0	0.7	1.95	99	NA	5.37 ^c	92
DBL20-B-1.5	6	45.2	33.9	1.2	3.60	99	NA	5.37 ^c	92
DBL22-B-1.5	6	46.4	32.1	0.5	1.48	99	NA	5.37 ^c	92
S-B-X-0.375	6	3.0	61.1	4.0	6.53	89	31.0 ^a	5.37 ^c	92
DBL18-B-0.375	6	43.0	48.5	2.6	5.34	93	NA	NA	NA
DBL20-B-0.375	6	45.0	45.7	1.2	2.71	99	NA	NA	NA
DBL22-B-0.375	6	48.5	44.7	1.6	3.62	98	NA	NA	NA
DBL14-B-4-0.75	6	30.9	75.9	3.8	5.02	94	NA	NA	NA
DBL14-B-6-0.75	6	36.3	89.0	3.2	3.57	98	NA	NA	NA

^aASTM D5766 stress calculation uses gross cross-sectional area, sample peak stress is calculated using net cross-sectional area.

^bMultiple hole population COV values are assumed to follow single-hole testing values.

^cAll single- and multibolt population COV values are assumed to follow S-B-X-1.5 value for population.

Table 3.5: Mean specimen measurements.

Specimen Dimension	No. of Measurements	Mean Value (in)	Sample <i>s</i> (in.)	Sample COV (%)
Width	205	3.98	0.00379	0.0951
Thickness	207	0.131	0.00207	1.57
Hole Diameter	138	0.555	0.01063	1.92

3.2.1 – No-Hole Treatment Condition

A total of eight individual replicates were tested in the no-hole condition (Table 3.1). The material COV for pure tension is 8.28% (considered the population COV for this paper) in accordance with the manufacturer’s available data provided in Table 3.2. Therefore, using Equation 3.3, a 90% CL with a 5% limit of error is achieved with a sample size of eight. The mean peak load for the eight tests was 76.4 kips, and the mean peak stress for the sample set was 146.5 ksi with a sample COV of 3.99% based on recorded peak loads. The manufacturer data provides a mean peak stress of 123.6 ksi (Table 3.2) which is 18.9% lower than the peak stress from the sample set. This difference is more than double the population COV value, indicating a significant discrepancy between the sample set tested in this report and the manufacturer’s data. It is difficult to determine the source of this difference with certainty, but it is likely due to differences in testing procedures and specimen preparation. The manufacturer’s tests were conducted using ASTM D638 (ASTM 2014b), a specification for testing plastic polymers, whereas the standard applied to the tension tests conducted in this report is ASTM D3039/D3039M (ASTM 2014c), a specification for testing polymer matrix composite materials such as the FRP used in this paper. The main difference between ASTM D638 (ASTM 2014b) and ASTM D3039/D3039M (ASTM 2014c) is the use of specimens with reduced cross sections in ASTM D638 (ASTM 2014b). This reduced cross-section testing is believed to be the probable source of the mean peak stress and COV differences. A reduced cross section for the nonhomogeneous FRP plate tested in this paper would produce variable results highly dependent upon the longitudinal carbon fibers remaining after the

cross section was cut down in each specimen. The 3.99% COV yields an actual CL = 99% with $n = 8$ (Table 3.4), assuming the COV is representative of the true population COV. However, without further testing with a greater number of replicates to determine the true population COV for the FRP material in tension, the assumed population COV of 8.28% is sufficient to report a mean peak load at the 90% CL. The observed mode of failure for all tests was explosive rupture located near the middle of the gage length (XGM in accordance with ASTM D3039/D3039M (ASTM 2014c)). The representative failure mode is shown in Figure 3.4(b).

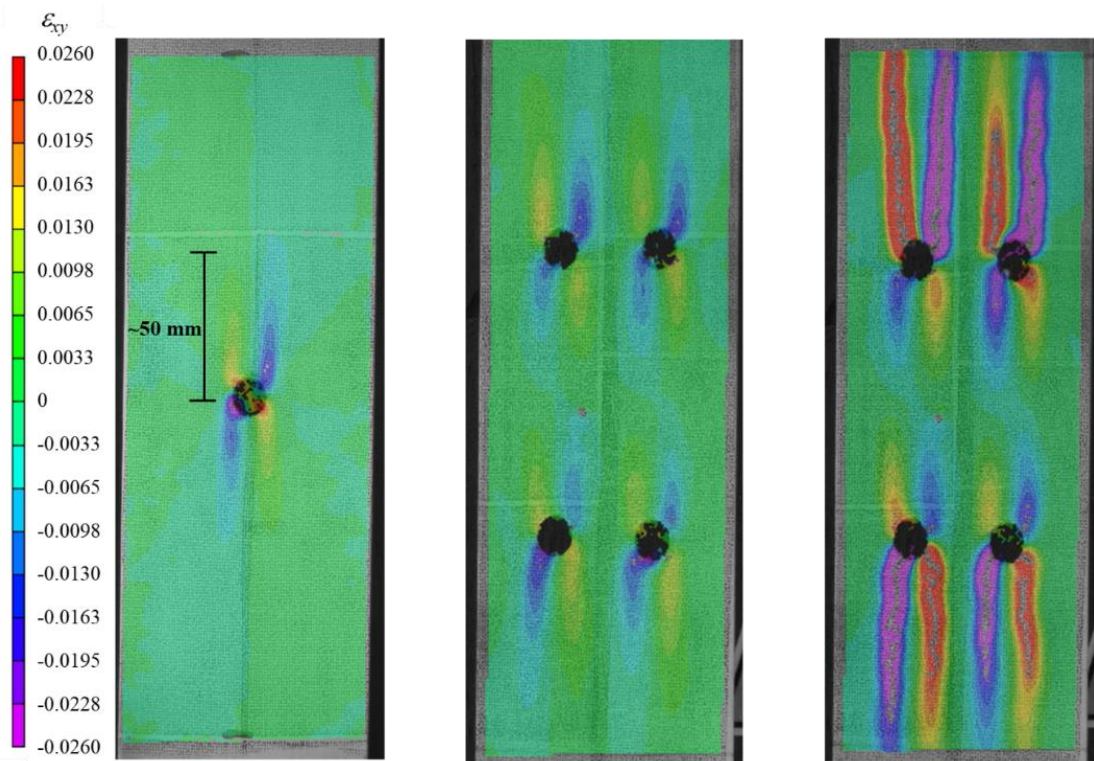
3.2.2 – Open-Hole Treatment Condition

3.2.1.1 – Single-Hole Condition

Six total specimens were tested in the single, open-hole condition providing a 97% CL with 5% limit of error (Table 3.4) based on the COV determined from the manufacturer's testing (Table 3.3). The test procedure for this paper was adapted from ASTM D5766/D5766M-11 (ASTM 2014a) which, as previously described, specifies a $w:D$ ratio equal to 6. The desired $w:D$ ratio in this report is 7.1 to incorporate the hole diameter of 9/16 in. necessary for a 0.5 in. diameter fastener. Further, the stress calculation using ASTM D5766/D5766M-11 (ASTM 2014a) uses the gross cross-sectional area of the test specimen whereas the stress calculation in this study uses the net cross-sectional area. The mean peak load for the single-hole test condition was 66.5 kips and the mean peak stress using the net cross-sectional area was 150.8 ksi. The mean peak stress reported by the manufacturer using the gross cross-sectional area and $w:D$ ratio = 6 is 94.6 ksi. The calculated mean peak stress using the manufacturer test data and the net cross-sectional area based on a $w:D$ ratio = 6 is 114 ksi. The net cross-sectional area mean peak stress for the sample set in this study (150.8 ksi) and net cross-sectional area mean peak stress using the manufacturer test data (114 ksi) differs by 32.4% of the manufacturer mean peak stress using the net cross-sectional area. This difference is likely due to the nonhomogeneity of the material and to the exact amount of

longitudinal carbon fiber included in the net cross section for each test specimen; carbon fiber lost from the cross section due to drilling holes would result in a lower peak stress as compared to the gross section results.

The DIC shear strain results show the development of a disturbed region approximately 2 in. above and below the hole just before a longitudinal shear failure in the glass fibers begins (Figure 3.6(a)). Therefore, the longitudinal spacing between holes for multiple hole test conditions was selected to be 4 in. (Figure 3.3) to minimize interaction between disturbed regions developing at adjacent holes. Longitudinal shear failure of the glass fibers results in shear splitting which propagates and joins from the holes until ultimate failure occurs with complete shear failure of glass fibers along the length of the test specimen.



(a) *S-OH pre-splitting* (b) *DBL4-OH pre-splitting* (c) *DBL4-OH at failure*
Figure 3.6: Shear strain map of disturbed regions and shear failure.

3.2.1.2 – Aligned and Staggered Hole Conditions

Two transverse spacing distances were tested for each of the aligned (DBL4) and staggered (STG4) hole spacing conditions: 1.5 and 2 in. (shown in Figure 3.3(a)). The mean peak stress for each of the four treatments is 137, 132, 139, and 136 ksi for DBL4-OH-1.5, DBL4-OH-2.0, STG4-OH-1.5, and STG4-OH-2.0, respectively (Table 3.4). Six replicates were tested for each of the four treatments; however, one of the STG4 replicates slipped in the UTM wedge grips during testing, creating an extreme outlier result. Therefore, for the STG4 treatment group, only five tests were considered in the analysis of the results to eliminate the effects of the slip that occurred during one test.

A multifactor analysis of variance (ANOVA) test was conducted to determine if there is a statistically significant difference between the DBL4, STG4, 1.5 and 2 in. treatments. The following null (H_0) and alternate (H_a) hypotheses were tested:

$$H_{0A}: \alpha_1 = \alpha_2 = 0 \text{ and } H_{0B}: \beta_1 = \beta_2 = 0 \quad (3.6a)$$

and

$$H_{aA}: \text{at least one } \alpha_i \neq 0 \text{ and } H_{aB}: \text{at least one } \beta_i \neq 0 \quad (3.6b)$$

where α_i = effect of the hole pattern treatment (DBL4 or STG4) on the mean peak load; and β_i = effect of the transverse spacing treatment on the mean peak load.

The results of the multifactor ANOVA are provided in Table 3.6. When tested at the 90% CL ($\alpha = 0.1$), the P-value for α_i is 0.443 and the P-value for β_i is 0.855 (both are greater than α); therefore, there is a failure to reject both null hypotheses. This failure to reject both null hypotheses indicates no statistically significant difference exists on the mean peak load for each test (at the 90% CL) due to the effects of both the hole pattern (DBL4 or STG4) and the transverse spacing (1.5 or 2 in.).

Table 3.6: Multi-factor ANOVA results.

<i>Source of Variation</i>	<i>SS</i>	<i>df</i>	<i>MS</i>	<i>F</i>	<i>P-value</i>	<i>F critical</i>
Hole Pattern	22.532	10	2.253	1.097	0.443	2.978
Transverse Spacing	0.072	1	0.072	0.035	0.855	4.965
Error	20.534	10	2.053	--	--	--
Total	43.137	21	--	--	--	--

The results of the ANOVA are consistent with the manner in which the FRP test specimens carry load in the pure tension tests. The tensile forces are carried in the longitudinal carbon fibers of the FRP plate, and the staggered nature of the STG4 treatment does not change the manner in which the longitudinal fibers carry load that is applied in the same direction as the carbon fibers. For the same reason, the transverse spacing between the holes does not affect the capacity of FRP plate in axial tension. The lack of statistical significance between the DBL4 and STG4 treatments provides critical information regarding the behavior of the FRP material tested in this study, which is not examined in the available literature. This finding enables the remainder of this study to focus on a single transverse spacing and single-hole pattern; therefore, only 1.5 in. transverse spacing and aligned (DBL) hole pattern are examined in all multibolt treatment conditions.

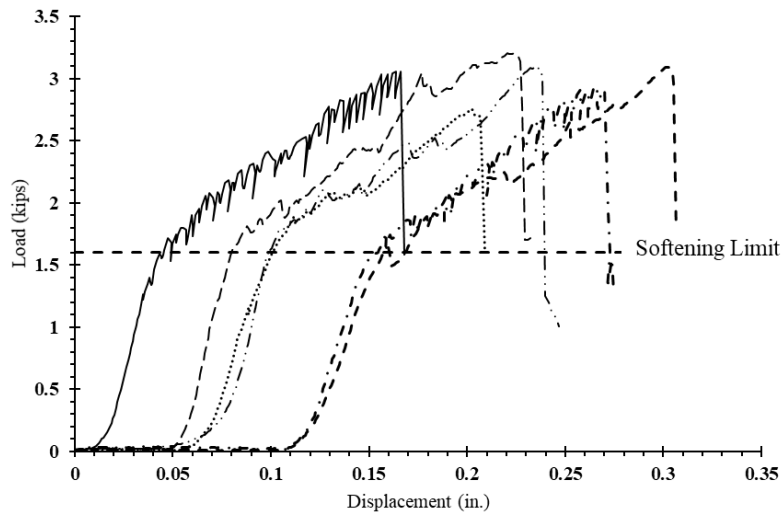
Figure 3.6 shows the DIC shear strain results for both the S-OH (Figure 3.6(a)) and the DBL4-OH-1.5 (Figure 3.6(b and c)) test treatments. Figure 3.6(a and b) illustrate the disturbed regions above and below the holes just prior to initial longitudinal shear splitting (approximately 38.2 kips). Figure 3.6(c) illustrates the shear strain at failure (approximately 51.7 kips). The 4 in. longitudinal spacing between holes is shown to be sufficient to minimize the interaction of shear strain between each hole.

3.2.3 – Bolt-Bearing Treatment Condition

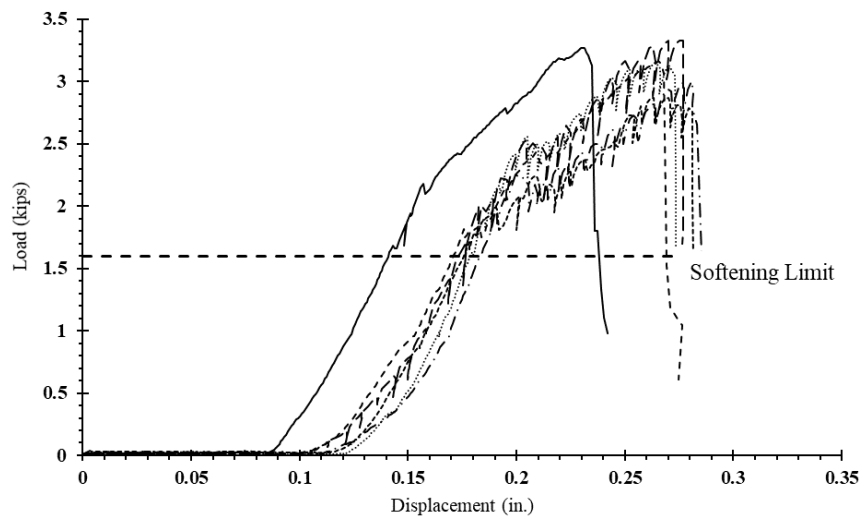
3.2.3.1 – Single-Bolt Bearing

Six tests were conducted for each of the single-bolt bearing test treatment conditions (Table 3.1). The difference between the mean peak load for each of the 1.5 in. edge distance treatment

groups (N and X) is 3.3% of the total force (Table 3.4). However, there is greater variability in the treatment group excluding threads, which is quantified in the higher standard deviation and lower statistical significance as compared to the treatment group including threads (Table 3.4). Figure 3.7 shows the load-displacement curves for the 1.5 in. edge distance treatment group with bearing excluding threads (Figure 3.7(a)) and with bearing including threads (Figure 3.7b)). Single-factor ANOVA testing confirmed that there is no statistically significant difference between the N and X treatment conditions at the 90% CL.



(a) Bearing excluding threads (*S-B-X series*)



(b) Bearing including threads (*S-B-N series*)

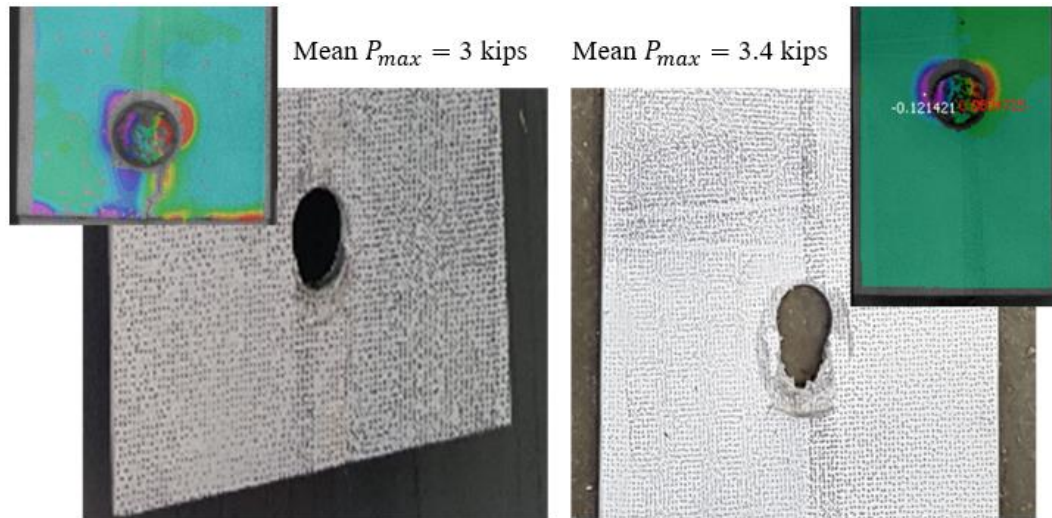
Figure 3.7: Load-displacement curves for single-bolt tests with 1.5 in. edge distance.

There are differences, however, between the two treatment groups shown in Figure 3.7. The treatment bearing on threads has a less defined softening region after 1.6 kips of applied load as compared to the group bearing with threads excluded. There is also greater variability between the tests for the treatment bearing on threads. This difference is likely due to rotation of the bolt relative to the FRP, which was observed when bearing included threads, but not in the condition which excluded threads. This difference is not captured with the ANOVA test because the ANOVA is comparing the mean of the peak values for the two treatment groups. All tests were stopped after longitudinal shear failure, which is marked by a severe decrease in load at the end of each load-displacement curve shown in Figure 3.7.

Every test experienced some level of slip before the applied load started to increase, as shown in the initial displacement under minimal load in Figure 3.7(a and b). The maximum theoretical slip possible for the single-bolt test is equal to the twice the difference between the hole diameter and bolt diameter. This produces a possible slip range between 0 in. and 0.12 in., due to the 0.56 in. holes in the FRP and steel plates relative to the 0.5 in. diameter bolts.

The 4 in. edge distance treatment group resulted in a mean peak load of 3.4 kips, which is 13.5% higher mean peak load than the 1.5 in. edge distance mean peak load of 3 kips (Table 3.4 and Figure 3.8). However, the behavior during loading for the two treatments was similar with initial softening due to bearing of the bolts against the FRP occurring at approximately 1.6 kips (Figure 3.7). The lesser peak loads and stresses in the 1.5 in. edge distance treatment group is due to longitudinal shear failure (shown in the Figure 3.8(a) DIC inset) that occurred in the 1.5 in. edge distance group, but not in the 4 in. edge distance treatment group. This shear failure was the primary source of failure in the 1.5 in. group, whereas failure in the 4 in. edge distance group was a pure bearing failure (Figure 3.8(b)), resulting in greater displacement at peak load values. Both

DIC insets in Figure 3.8 are captured at peak load, which occurred just prior to shear failure in the 1.5 in. edge distance group and bearing failure in the 4 in. edge distance group.



(a) *S-B-X-1.5 bearing and shear failure* (b) *S-B-X-4.0 bearing failure*

Figure 3.8: Single-bolt bearing failure modes with DIC inset showing shear strain.

As provided in Table 3.4, the sample COV for both single-bolt treatment groups is higher than the other treatment groups examined in this study ranging from 4.75% to 6.94%. This is likely due to the effect of the UTM load cell accuracy when failure load are small relative the error range. However, the increased coefficients of variation for the two single-bolt sample sets are sufficient to present the mean results at the 90% CL, with the exception of the S-B-N treatment group which satisfies an 86% CL. The consistency of the single-bolt results and the ANOVA results for the two treatment groups are sufficient for the purposes of this investigation; therefore, further investigation of the single-bolt COV range, or the accuracy of the UTM load cell at lower loads is not considered as part of this report.

The results of the four single-bolt bearing treatment groups confirm that a 4 in. longitudinal spacing between bolts is sufficient to avoid interaction between the disturbed regions that develop at each bolt, as shown in Figure 3.6. Further, the single-bolt bearing results allow for an initial

calculation to be made for the total number of 0.5 in. diameter bolts needed to stay below the softening limit of 1.6 kips/bolt (Figure 3.7), and below the maximum capacity of 3.4 kips/bolt (Table 3.4). Assuming all bolts are equally engaged at the softening limit, Equation 3.7 can be used to calculate the number of bolts needed to stay below the softening limit

$$T_p = n_b F_{b,s} \quad (3.7)$$

where n_b = number of bolts; T_p = tension force in plate (kips); and $F_{b,s}$ = force limit before initial softening (kips/bolt). A maximum value of $F_{b,s} = 1.6$ kips per bolt was selected to ensure the FRP plate remains in the initial, presoftening region of the load-displacement curve. The prestress force range (after initial losses) for a typical 7/16 in. diameter steel prestressing strand is between 18 and 22 kips according to NCDOT structural plans for typical C-channel and hollow-core sections. Using a maximum live load according to NCDOT vehicle loading configurations (NCDOT, 2018), 7.2 kips is a conservative estimate for the force increase in the FRP plate applied to a typical candidate hollow-core cross section. The 7.2 kips estimate assumes full-interaction between the concrete and FRP, which other studies have shown to overestimate the FRP strain by as much as 39% (Lee et al. 2009) for nonprestressed MF-FRP using powder actuated fasteners. However, for initial calculations in this investigation, this conservative estimate is sufficient. Using the 7.2 kips force increase and the 22 kips prestress force, the estimated maximum value for T_p at service load conditions is 29 kips (target prestress force plus projected live load for the retrofit solution). Using Equation 3.7, $n_b = 18.5$; therefore, the projected minimum number of bolts needed to remain in the presoftening region at service load is 20 (after rounding up to the nearest even number of bolts). Additionally, Equation 3.8 can be used to calculate the number of bolts needed to stay below the maximum capacity

$$T_o = n_b F_{b,u} \quad (3.8)$$

where T_o = open-hole capacity (kips); and $F_{b,u}$ = maximum capacity per bolt (kips/bolt). Using $F_{b,u} = 3.4$ kips per bolt, the minimum number of bolts needed to stay below $T_o = 52$ kips (mean capacity for all open-hole treatment groups in Table 3.4) is $n_b = 15.4$; therefore, a minimum of 16 bolts are projected to achieve the open-hole capacity of the plate assuming all 16 bolts are engaged equally throughout the loading of the connection.

3.2.3.2 – Multi-Bolt Bearing

Based on the single-bolt bearing results, and initial calculations using Equations. 3.7 and 3.8, multibolt tests were conducted using 16-, 18-, 20-, and 22-bolt, 2-lines, aligned with 1.5 in. transverse spacing (DBL16-B-1.5– DBL22-B-1.5) configurations shown in Figure 3.3(b). These four treatment groups were selected to provide multiple connection configurations at or near the 20- and 16-bolt results from Equations. 3.7 and 3.8, respectively. Six tests for each treatment were conducted in accordance with Table 3.1. The mean peak loads were 42.5, 45.4, 45.2, and 46.4 kips for the DBL16, DBL18, DBL20 and DBL22 treatments, respectively (Table 3.4). The calculated mean bolt-bearing stresses for each treatment are 39.9, 38.0, 33.9, and 32.1 ksi, respectively (Table 3.4). A single-factor ANOVA test (Table 3.7) determined at least one of the four treatment conditions (DBL16, DBL18, DBL20, DBL22) is statistically different at the 90% CL ($P\text{-value} = 6.89 \times 10^{-5} \ll \alpha = 0.1$) when using peak load as a measure. Therefore, a second ANOVA test (Table 3.8) was conducted to confirm that there is no statistically significant difference between the DBL18, DBL20, and DBL22 treatments at the 90% CL ($P\text{-value} = 0.168 > \alpha = 0.1$). Although this is the case, a reduced confidence limit of 80% ($\alpha = 0.2$) would result in a statistically significant difference for at least one of the treatment groups. However, 90% is the desired CL, and therefore, further ANOVA testing is not necessary for the purposes of understanding the ultimate capacities of the four treatment groups.

Table 3.7: Single Factor ANOVA Results (DBL16, DBL18, DBL20, DBL22).

<i>Source of Variation</i>	<i>SS</i>	<i>df</i>	<i>MS</i>	<i>F</i>	<i>P-value</i>	<i>F critical</i>
Between Groups (DBL16, DBL18, DBL20, DBL22)	50.098	3	16.69	12.777	6.89x10 ⁻⁵	2.380
Within Groups	26.14	20	1.307			
Total	76238	23				

Note: Note: *SS* = sum of squares; *df* = degrees of freedom (previously defined); *MS* = mean square value; *F* = f-test statistic value; and *F critical* = critical f-test statistic value.

Table 3.8: Single-factor ANOVA results (DBL18, DBL20, DBL22).

<i>Source of Variation</i>	<i>SS</i>	<i>df</i>	<i>MS</i>	<i>F</i>	<i>P-value</i>	<i>F critical</i>
Between Groups (DBL18, DBL20, DBL22)	4.973	2	2.487	2.013	0.168	2.695
Within Groups	18.532	15	1.235			
Total	23.505	17				

Box plots (Figure 3.9) of the peak loads for the four treatments indicate a single statistical outlier for the DBL20 treatment (41.2 kips); however, the single outlier is within three standard deviations of the lower quartile, commonly referred to as a mild outlier (Devore, 2015). The presence of this mild outlier does not adversely affect the ANOVA results; therefore, no data were discarded in the analysis. Figure 3.9 also serves as a visual representation of the statistically significant difference with the DBL16 treatment peak load when compared to the DBL18, DBL20, and DBL22 treatment peak loads. The higher peak load and reduced variability of the DBL22 treatment group is the reason the ANOVA test results in Table 3.8 indicate a reduced CL would produce a statistically significant difference.

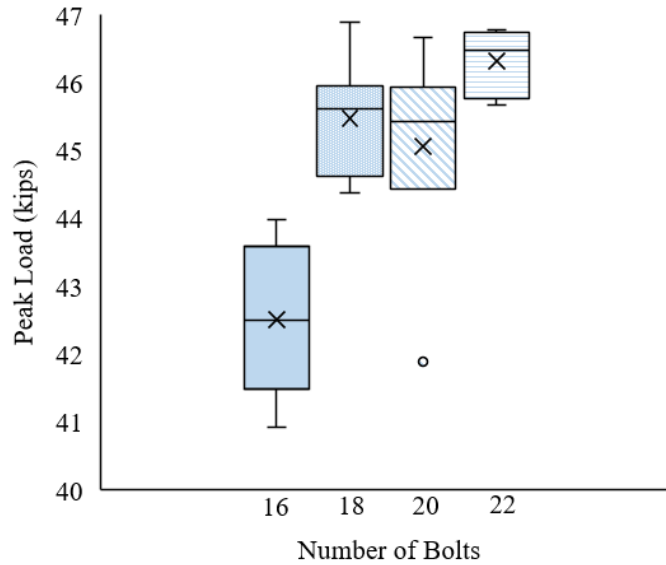


Figure 3.9: Box plots of multibolt peak load distributions.

The load-displacement curves for the four treatment conditions in Figure 3.10 were produced by performing a multiparametric regression analysis of the set of curves for each treatment condition using RStudio, a commercially available statistical software package. The load-displacement curves therefore represent the mean curve for each treatment group. Figure 3.10 shows that the load-displacement behavior for each of the four connections is similar. This indicates that although there is a statistically significant peak load difference between the DBL16 treatment, and the DBL18, DBL20 and DBL22 treatments, the behavior during loading up to ultimate failure for all four treatments is similar. The distinct softening region that is visible in single-bolt bearing (Figure 3.7) is not present in the multibolt behavior due to the effect of multiple bolts experiencing bearing throughout the test. The bolts do not experience initial bearing simultaneously, but rather progressively, such that bearing in the first several rows experience greater bearing than the last row of bolts in the connection. Each of the mean load-displacement curves is calculated using six test specimens, as previously discussed, and therefore, the curves are

statistically significant at the 90% CL or greater. The upper bound curve shown in Figure 3.10 is the upper limit corresponding to the 90% CL for the population of treatments.

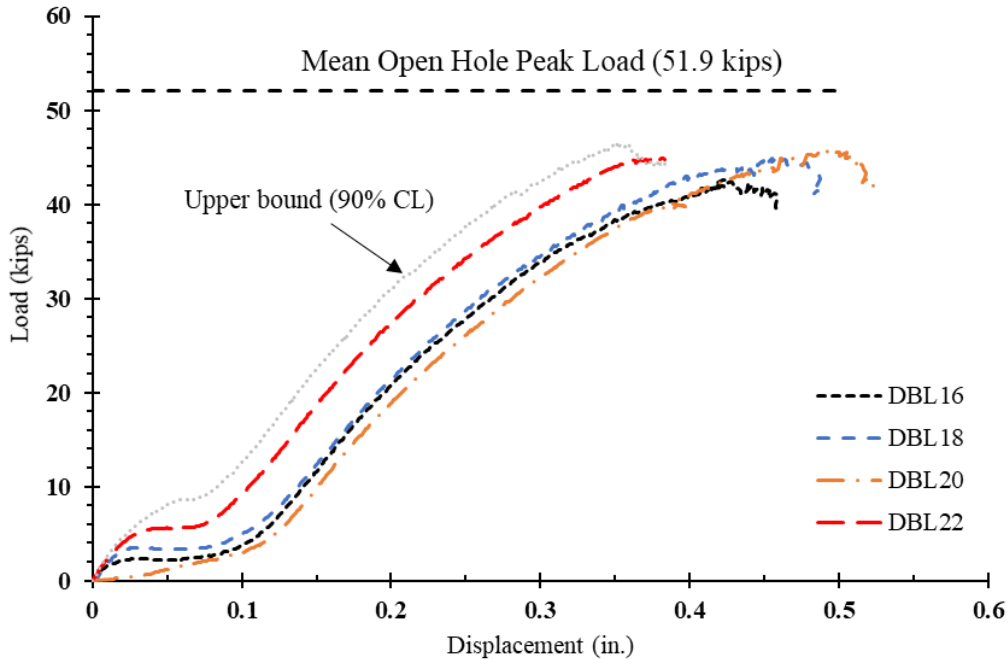


Figure 3.10: Mean multibolt load-displacement curves (DBL series).

The mean open-hole peak load (51.9 kips) in Figure 3.10 is the mean peak load for the open-hole treatment conditions, mean value for peak load of all DBL4 and STG4 results in Table 3.4. As previously discussed, this is the theoretical maximum load for the FRP material tested with holes, which was the peak load goal for the multibolt testing; however, under the current treatment conditions, the mean peak load for the DBL22 treatment is approximately 89% of the theoretical maximum. This difference in the theoretical maximum is due to shear lag effects which cause longitudinal shear failure to propagate in a progressive manner from the first row of bolts (top two holes for each specimen in Figure 3.11(c)), rather than uniform shear failure along the length of the specimen.

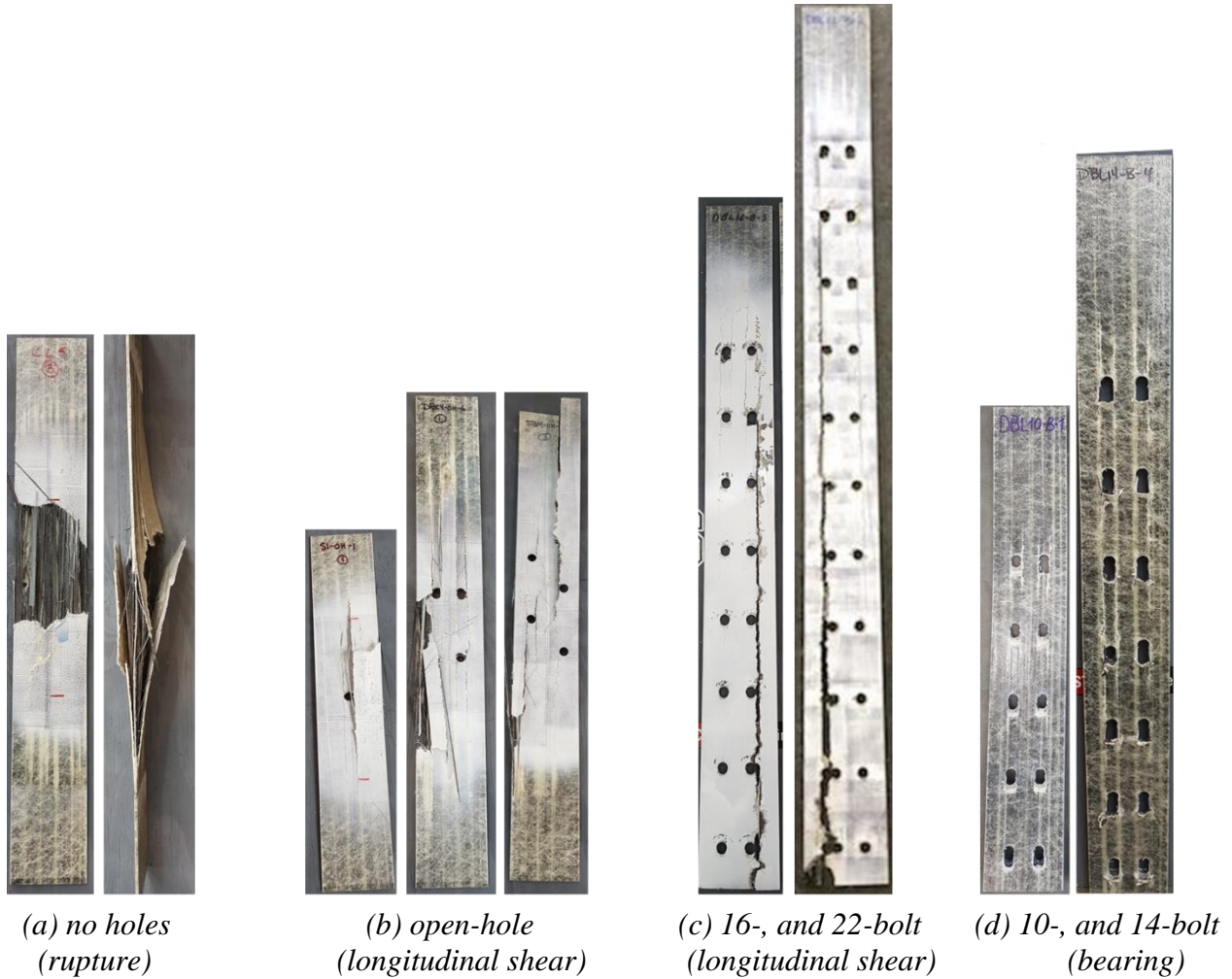


Figure 3.11: FRP failure modes.

The longitudinal shear failure shown in Figure 3.11(b and c) is representative of the failure mode for every treatment group except the T and S-B-X-4.0 treatments which experienced rupture (Figure 3.11(a)) and bearing failure (Figure 3.8), respectively, and the multibolt treatment groups with fewer than 16 bolts which experienced bearing failure (Figure 3.11(d)). All open-hole (Figure 3.11(b)) and all multibolt (Figure 3.11(c)) treatments experienced longitudinal shear failure at the measured peak loads. Therefore, the mean peak load for each of these treatment groups in Figure 3.12 shows the variation in capacity and failure mode as a function of the bearing surface area, defined as

$$A_b = n_b d_b t_p \quad (3.9)$$

where A_b = total bearing surface area; n_b = number of bolts; d_b = diameter of the bolt; and t_p = thickness of the plate. The trendline shown in Figure 3.12 is established using the S-B-X-1.5 and the 16-, 18-, 20-, and 22-bolt treatment groups. Additional testing was then conducted using the supplementary test matrix in Table 3.9 to determine the validity of the trendline to predict mean peak loads for bolt patterns with less than 16 bolts. The mean peak loads for the 10-, 12-, and 14-bolt treatment groups are within 3.0% of the trendline, indicating the curve in Figure 3.12 is sufficient for predicting the capacity of a connection using 0.5 in. diameter bolts and 4 in. longitudinal spacing over the range of bolts from 1 to 22 at the 90% CL.

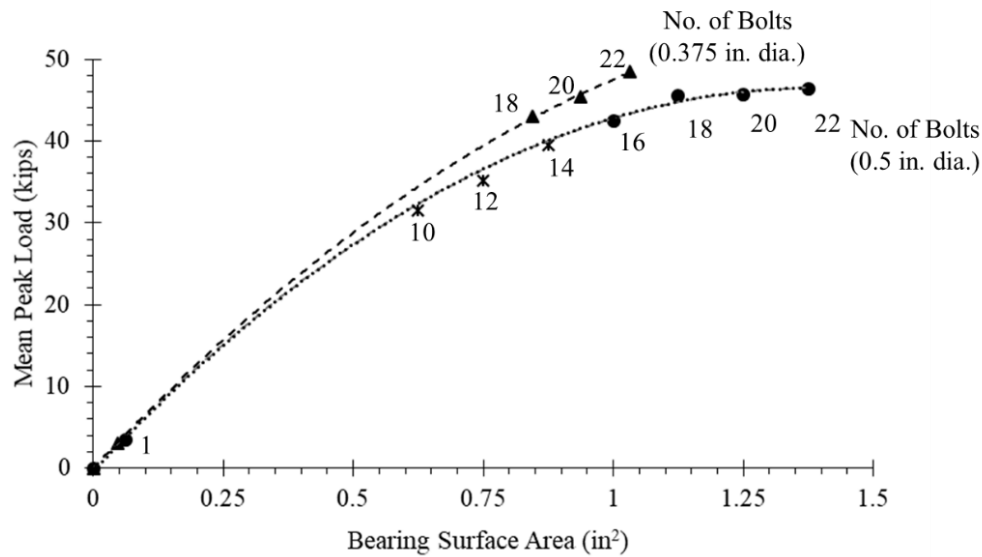


Figure 3.12: Variation of mean peak load and FRP failure modes.

Table 3.9: Supplementary test matrix.

Specimen ID	No. of Replicates	Treatment Description	ASTM
DBL10-B-1.5	1	10 bolts; 0.5 in. diameter; 2-by-2; 1.5 in. transverse spacing; 4 in. longitudinal spacing	NA
DBL12-B-1.5	1	12 bolts; 0.5 in. diameter; 2-by-2; 1.5 in. transverse spacing; 4 in. longitudinal spacing	NA
DBL14-B-1.5	1	14 bolts; 0.5 in. diameter; 2-by-2; 1.5 in. transverse spacing; 4 in. longitudinal spacing	NA

The 10-, 12-, and 14-bolt treatment groups produced a bearing failure (Figure 3.11(d)) rather than the longitudinal shear failure mode experienced in the 16-, 18-, 20-, and 22-bolt treatment groups. The threshold for this change in failure mode is shown with the vertical dashed line in Figure 3.12. Understanding the impacts of this critical finding is necessary to optimize the capacity of the bolt pattern such that a maximum capacity can be achieved, the theoretical maximum of which is the capacity of the plate with holes gripped and loaded in uniaxial tension (51.9 kips in Figure 3.12).

The results presented in this report indicate that a 22-bolt connection with 0.5 in. diameter bolts in a double-line aligned pattern (DBL22-B in Figure 3.4) is sufficient to develop 89% of the open-hole capacity of the FRP plate (Figure 3.10) and remain below the softening limit at service loads of 29.2 kips (prestress + live load).

Although connections with greater than 14-bolts produce a shear failure mode that is more brittle than the bearing failure experienced in connections with 14 or fewer bolts, the progressive nature of the shear failure provides early warning of impending failure, and the number of bolts ensure the connection remains in the presoftening region at service load levels when applied to a typical hollow-core bridge superstructure. Therefore, one prestressed, 22-bolt connection MF-FRP plate approximately restores the prestress effect of the steel section loss equivalent to one 7/16 in. diameter strand stressed to 22 kips after initial losses. In situations where a more ductile bearing failure is desired, and a lower capacity is acceptable, bolted connections with 14 or fewer bolts would be acceptable in accordance with the failure behavior and connection capacity shown in Figure 3.12.

3.2.3.3 – Multi-Bolt Bearing with different bolt diameter

Building upon the results presented in the previous sections, additional fastener diameters in varying numbers are also studied to examine 0.375 in. and 0.75 in. diameter bolts which is shown in Table 3.1. All treatment groups examined aligned hole patterns only as the use of staggered holes does not change the capacity of the FRP in uniaxial tension.

Summary results for all treatment groups with different bolt diameter are also presented in Table 3.4. Mean peak load was determined from measured load data for each test specimen and mean peak stress is a calculated value using bolt bearing area, calculated in accordance with ASTM D5961 (2017). Measurements for specimen width and thickness were taken as the average width and thickness of the 84 test specimens from the previous tests. Three measurements of different hole diameters were taken using a digital caliper (0.001 in. precision) for each specimen. Stress levels in Table 3.4 are calculated using the mean hole diameter, 0.442 in. and 0.884 in. for 0.375 in. and 0.75 in. diameter bolts respectively.

Equation 3.5 was used to calculate the critical t-value for each treatment group, from which the confidence limit for sample sets and the population (manufacturer provided data) was determined, using a Student-t distribution with 5 degrees of freedom (n-1). All treatment groups except for S-B-X-0.375 resulted in a higher sample CL than the population CL because of the lower CV with respect to the number of specimens tested. The higher CV for the S-B-X-0.375 treatment group is visualized in the variability of the load-displacement curves shown in Figure 3.13. Although the S-B-X-0.375 treatment group has increased variability compared to the other treatment groups, the S-B-X-0.375 treatment group still obtained an 89% CL, which is considered acceptable for the purposes of this research.

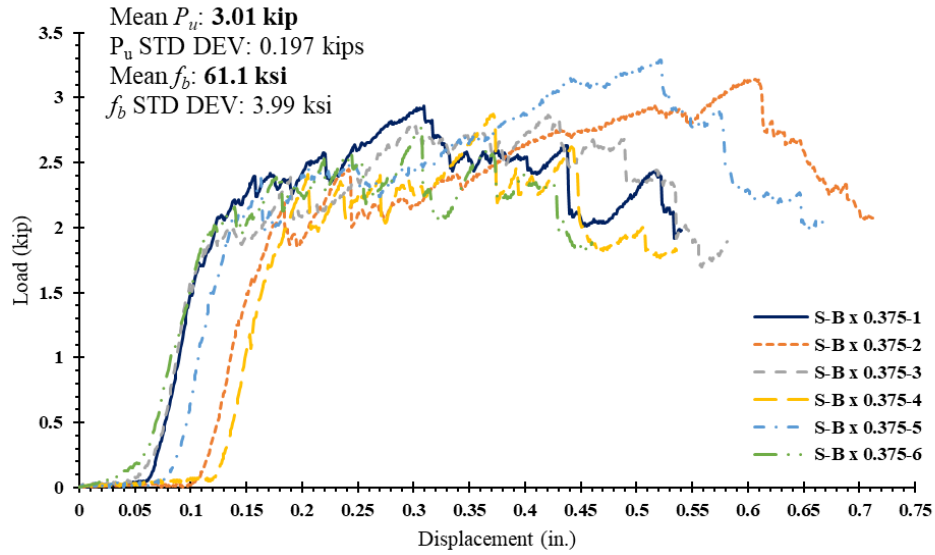


Figure 3.13: S-B-X-0.375 load-displacement curves.

The mean peak loads for the 0.375 in. bolt diameter treatment groups are similar to the 0.5 in. diameter treatment groups, however, the 0.375 in. diameter bolt connections resulted in higher peak stress levels compared to 0.5 in. diameter treatment groups due to the reduced bearing surface area of the 0.375 in. diameter fasteners, which resulted in significant bearing in the FRP prior to longitudinal shear failure. Figure 3.14 shows the bearing failure for the DBL20-B-0.375 treatment group compared to that in the DBL20-B treatment group, and DBL14-B-4-0.75 treatment group (discussed later in this section). In most specimens, the bearing was followed by longitudinal shear failure similar to that which was observed in the 0.5 in. diameter bolt treatments.

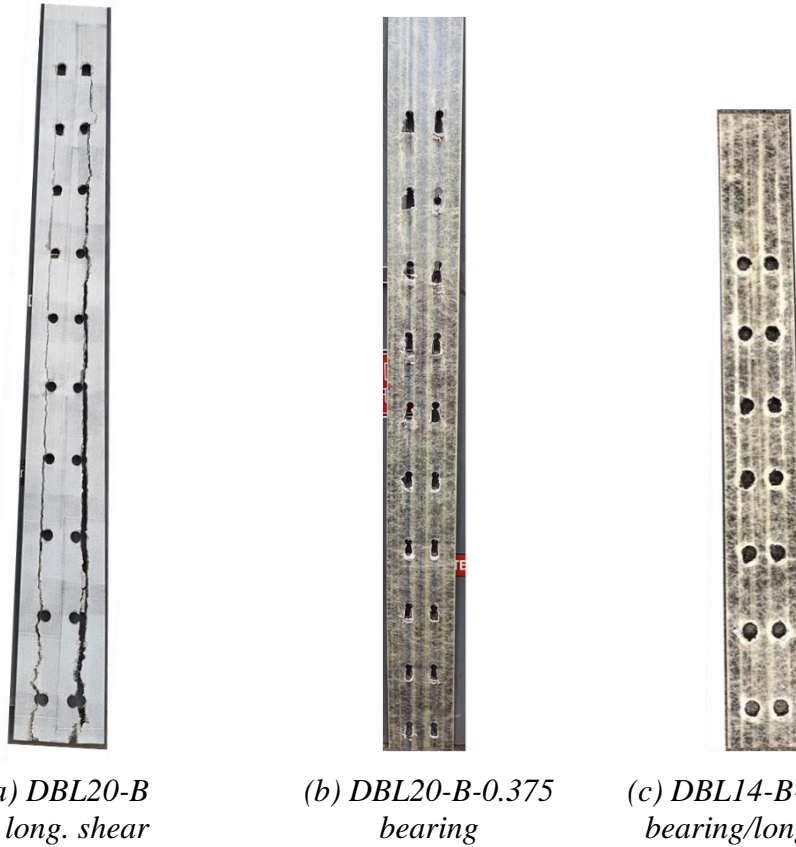
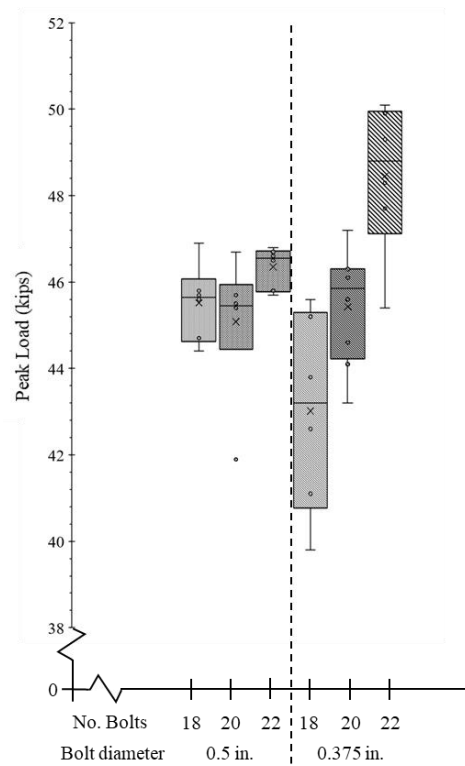


Figure 3.14: Failure modes for 0.5 in., 0.375 in., and 0.75 in. diameter treatment groups.

This bearing failure prior to longitudinal shear failure resulted in greater displacement in all 0.375 in. diameter treatment groups as well (Table 3.10). Figure 3.15 is representative of this increased displacement for all treatment groups (additional load-displacement curves can be found in McCoy (2019)). Also seen in the representative load-displacement curves (Figure 3.15) is the greater displacement variability in the 0.375 in. bolt diameter treatment groups. Specifically, the mean total displacement for the DBL22-B treatment condition is 0.43 in. with a CV of 6.38%, whereas the mean total displacement for the DBL22-B-0.375 is 0.75 in. with a CV of 21.1% (Table 3.10). All 0.375 in. bolt diameter treatment groups experienced significantly higher displacement coefficients of variation compared to the 0.5 in. bolt diameter treatment groups (Table 3.10). This increased variability is also seen in the wider distribution of data compared to the 0.5 in. diameter bolts shown in Figure 3.15.

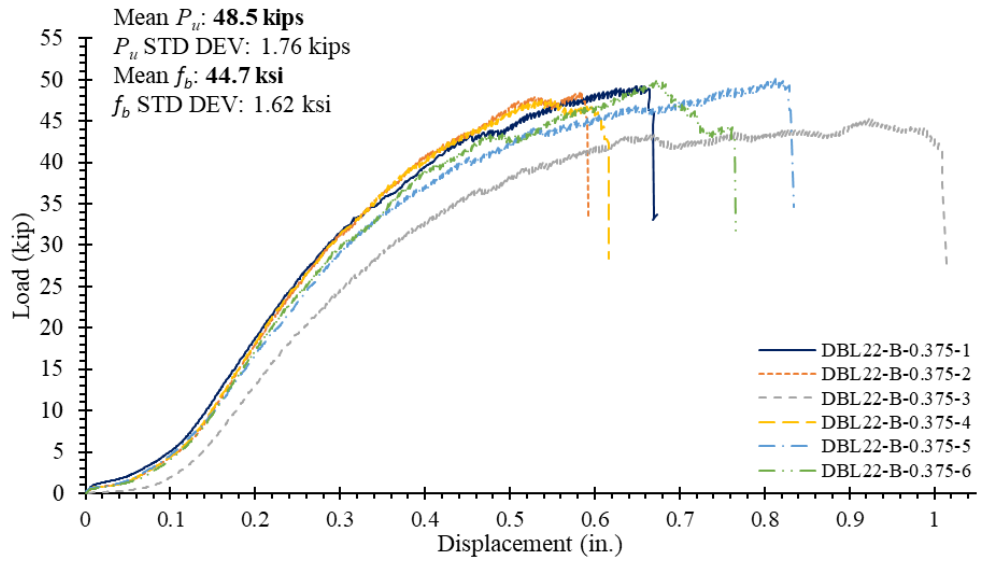
Table 3.10: Average Maximum Displacement By Treatment Group.

Treatment Group	Mean Maximum Displacement (in.)	Displacement Standard Deviation (in.)	Displacement CV (%)
DBL22-B	0.427	0.0272	6.37%
DBL20-B	0.489	0.0325	6.65%
DBL18-B	0.486	0.0324	6.67%
DBL22-B-0.375	0.749	0.158	21.1%
DBL20-B-0.375	0.667	0.172	25.8%
DBL18-B-0.375	0.746	0.146	19.6%

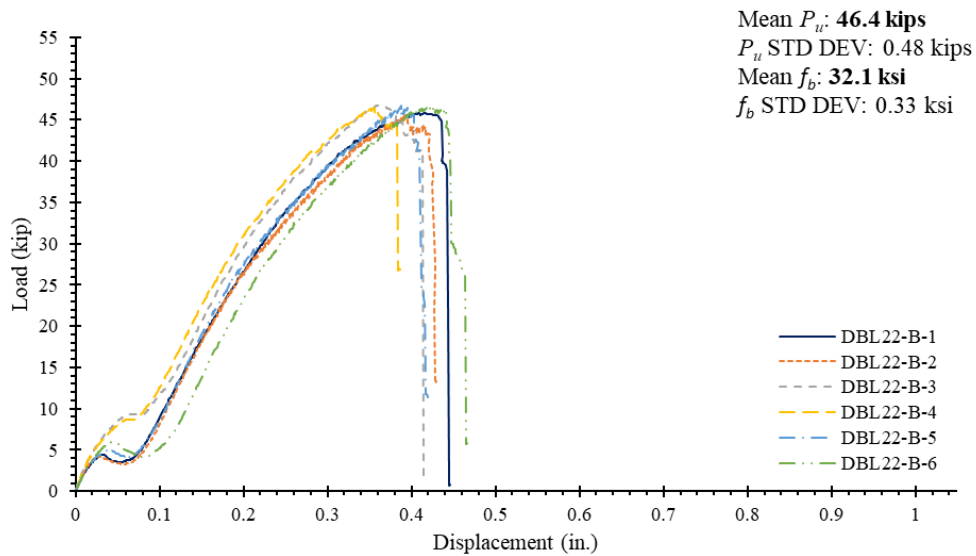
**Figure 3.15:** 0.5 in. and 0.375 in. bolt diameter peak load distribution.

Although the greater displacement of the 0.375 in. diameter treatment groups provides a perceived increase in ductility (prolonged displacement at peak loads) in the system, and early visual warning of failure through bearing at each bolt, the high CV of 21.1%, 25.8%, and 19.6% for DBL22-B- 0.375, DBL20-B-0.375, and DBL18-B-0.375 respectively, indicates that the increased displacement is unreliable, and in some test specimens there was no prolonged

displacement prior to failure, but rather immediate failure at peak load (Figure 3.16(a)) similar to that of the 0.5 in. bolt diameter treatments (Figure 3.16(b)).



(a) DBL22-B-0.375



(b) DBL22-B

Figure 3.16: Load-displacement behavior for DBL22-B and DBL22-B-0.375 treatment groups.

Figure 3.17 shows the load-displacement behavior for the DBL14-B-4-0.75 specimens. Although the 0.75 in. bolt diameter resulted in less variability than the 0.375 in. treatment (visualized in Figure 3.15(a)), the reduction in mean peak load is a concern for the MF-FRP retrofit

solution because the loads in the FRP at operating levels requires greater capacity in the MF-FRP system.

A similar treatment group with greater longitudinal spacing between holes was also examined to determine the effect of increasing the length of the longitudinal shear failure plane. Increasing the longitudinal spacing by 50% (from 4 in. to 6 in.) increased the peak load on the connection by 17.5% (from 30.9 kips to 36.3 kips); therefore, the increased longitudinal shear failure plane does result in a sufficiently higher load capacity of the system. However, the load capacity of both 0.75 in. bolt diameter treatment groups is significantly less than the load capacity of the 0.5 in. and 0.375 in. bolt diameter treatment groups with similar bearing surface areas. Therefore, further investigation of 0.75 in. bolt diameter (or larger) fasteners is not recommended as larger diameters experience reduced FRP performance and decrease the efficiency of the MF-FRP retrofit.

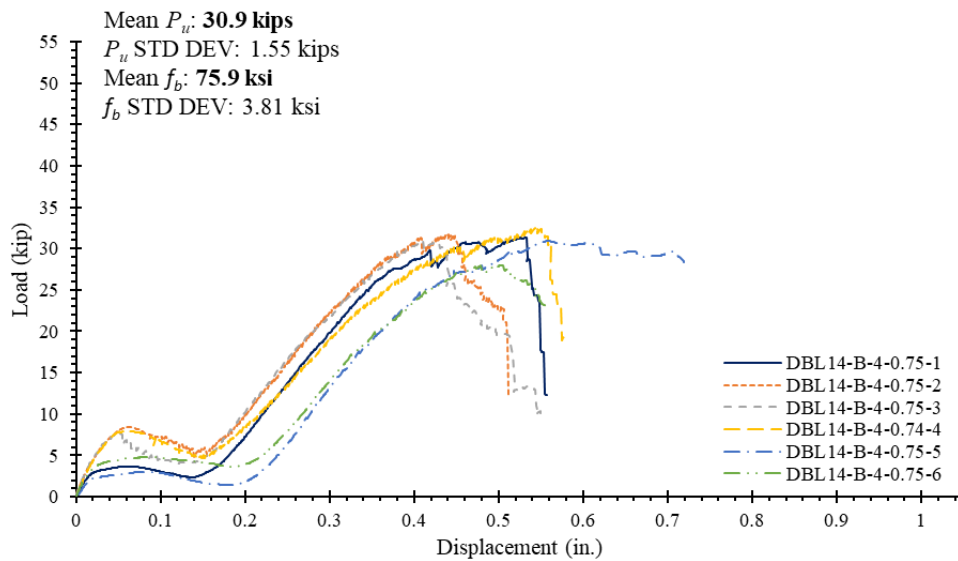


Figure 3.17: Load-displacement behavior for DBL14-B-4-0.75 treatment group.

3.3 – Observations

The following observations are drawn from the study presented in this chapter.

- The current work demonstrated that the coefficient of variance for a specific material property published by a supplier can be combined with a small number of laboratory tests to obtain statistically significant results for a sample of material. This outcome has important consequences for quality control and validation of as-received FRP material.
- There is not a statistically significant impact (at the 90% CL) on the peak load capacity between the staggered and aligned treatment conditions and between the 1.5 and 2 in. transverse spacing treatment conditions for the tested FRP material under uniaxial tension load conditions. This finding allows the experimental work in subsequent studies to be conducted considering a single configuration of the treatment conditions, i.e., aligned with 1.5 in. transverse spacing distance.
- Single-bolt bearing test results indicate that bearing failure (crushing) begins at approximately 1.6 kips per bolt regardless of singlebolt treatment conditions, allowing for initial calculations to determine the number of bolts necessary to prevent bearing at service load conditions.
- There is not a statistically significant impact (at the 90% CL) on the peak load capacity between the 18-, 20-, and 22-bolt treatment conditions.
- The peak load capacity of the 16-bolt treatment condition is statistically different from the 18-, 20-, and 22-bolt treatments. The mean value for the 16-bolt treatment is 8% lower than the mean value for the 18-, 20-, and 22-bolt treatments at the 90% CL.
- The mean peak load for the 18-, 20-, and 22-bolt treatments is approximately 89% of the peak load capacity of the FRP with holes. The 22-bolt treatment is sufficiently optimized

considering peak bearing stress (less than 18- and 20-bolt treatments), peak load (equal to 18- and 20-bolt treatments), and total anchor length (4 in. longer than the 20-bolt treatment) given a 0.5 in. diameter fastener and the FRP plate examined.

- The 0.375 in. bolt diameter treatment groups have load capacities similar to that of the 0.5 in. treatment groups with same 22-bolt pattern.
- The DBL-B-0.375 treatment group have increased displacement behavior compared to the DBL-B treatment groups; however, with increased variability. This increased displacement of the bearing failure at peak loads occurs prior to longitudinal shear failure and gives a desirable early warning of failure; however, the high variability of the behavior introduces unpredictability of the fastener patterns with 0.375 in. diameter bolts. Therefore, it is recommended that the 0.5 in. bolt diameter fasteners be used in the development of the MF-FRP retrofit.
- Although the bearing surface area was similar that of the DBL22-B treatment groups, the DBL14-B-0.75 treatment groups experienced significant reduction in load capacity due to the larger diameter hole reducing the cross-sectional area of the carbon tows and transverse glass fibers. However, the DBL14-B-6 treatment group, with a longitudinal shear plane increase of 50% over the DBL14-B-4 treatment group, experienced a 17.5% increase in load capacity. While increased capacity for the 0.75 in. bolt diameter anchor pattern is desired, increasing the longitudinal shear plane requires increased anchor length for the MF-FRP system, which is not desirable for short span (30 – 40 ft.) bridge beams. Therefore, further investigation of anchor bolt patterns with increased anchor zone lengths is not included in this research.

- Longitudinal shear failure controls the ultimate capacity of the openhole and multibolt treatment conditions with greater than 14 bolts resulting in a progressive, brittle failure.
- Bearing failure controls the ultimate capacity of singlebolt (with $e > 3D$) and multibolt treatment conditions with 14 or fewer bolts resulting in a more ductile failure compared to treatments with greater than 14 bolts.

CHAPTER 4 – LONG-TERM BEHAVIOR OF ANCHOR BOLT DESIGN

This chapter presents the long-term study developed to address the research needs set in the previous chapters. It is divided into two sections. The first presents the sustained loading experimental program, for which a new test setup had to be designed and manufactured. The second section presents the cyclic loading program, and covers the test setup, the definition of the cycling range, and the parameters that shaped the test matrix. Results are presented and discussed at the end of each section to quantify losses from each of sustained loading and fatigue.

4.1 – Sustained Loading

A sustained loading experiment aims to expose the creep behavior of a specimen, or in other words, the time-dependent characteristics of a specimen under constant stress. For the 22-bolt MF-FRP connection used in this research, the effect of a constant stress is a “creep” displacement induced by bolts bearing on the MF-FRP, which relieves some force from the plates. The biggest challenge in designing a creep test setup is to maintain a continuous and constant stress on specimens for durations of months or even years. Typically, researchers are concerned with creep effects on long-term material properties, and so, for convenience, opt for a small-scale setup that uses material “coupons” as specimens. This is not appropriate for the retrofit used in this research, as it relies on a 40 in. long MF-FRP connection; the behavior of MF-FRP is highly sensitive to the number and type of bolts used, and so a shortened connection with fewer or no bolts would not be a fitting substitute for the full 22-bolt connection.

In choosing the best location to support the demands of this experiment, the strongwall was deemed the most efficient option, as it reduces the amount of construction needed to build an adequate reaction frame to accommodate the loading apparatus. The beams targeted by this research’s retrofit are prestressed using 7-wire steel strands, initially jacked to 21.7 kips. As each

MF-FRP plate used in the retrofit aims to replace one fully lost prestressing strand, its target prestressing force is 22 kips. So, naturally, the load sustained by each specimen was set at 22 kips, and with multiple specimens per setup, this amounts to significant load demands. A hydraulic circuit was needed in order to generate and sustain the stress on the specimens, while steel racks needed to be designed and anchored to the strongwall to support the specimens and hydraulic circuit. It follows then that the design of this experiment was controlled by two things: the configuration of the strongwall, and the loading requirements.

4.1.1 – Strongwall Configuration

The strongwall web at NC State's Constructed Facilities Laboratory is a 25 ft. long, 10.5 ft. wide reaction wall, a sketch of which is shown in Figure 4.1. Equipment or specimens can be supported through 2 in. diameter holes spaced at 3 ft. longitudinally and 6 ft. transversely, for a total of 16 holes arranged in two columns and eight rows. This configuration dictated the dimensions of the supporting structure. Custom-built steel racks could run parallel to the width of the strongwall, and specimens could be loaded between them vertically. The number of specimens to fit in this setup would therefore be controlled by the 6 ft. transverse spacing and by the capacity of the steel racks. The space needed for each specimen was determined by the width of the hydraulic cylinders selected to deliver the 22 kips of sustained force, 5 in., and by an additional 5 in. to allow space for assembly and hydraulic circuit components. This amounts to a spacing of 10 in. between specimens, and so, a total of seven specimens may be accommodated by this setup. However, this imposes a load of 154 kips which would have likely required bulky and burdensome steel racks, if standard steel shapes were to be chosen. As the construction of this setup was to be performed in the lab by two people, the cross-section needed to be designed as efficiently as possible to maximize the number of specimens per setup while using elements that can be handled by two people at a time.

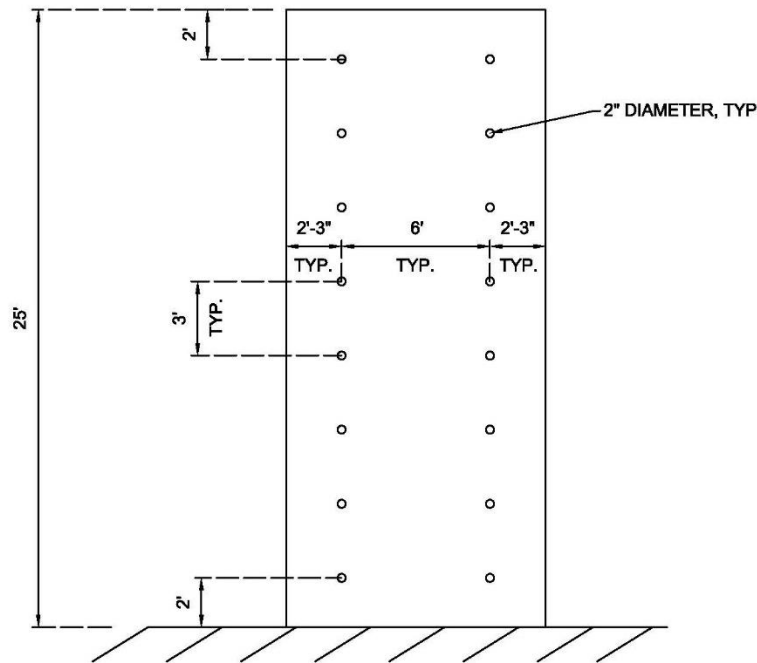


Figure 4.1: Configuration of strongwall web.

4.1.2 – Loading Requirements

Figure 4.2 shows the cross-section designed for the supporting steel racks. Each component needed to be light enough to be handled by two people in the fabrication process. A $4 \times 4 \times 1/2$ in. square HSS steel tube was selected as the main element to connect to the strongwall because it offers a great strength-to-weight ratio, a symmetric shape that minimizes eccentricities, and a shape that offers convenient welding options to customize the final cross-section of the steel racks. One disadvantage of square tubes lies in their “closed” geometry, which makes them accessible only at each end of their length. In the case of this setup, the specimens needed to be attached to the steel racks across a 6 ft. length. To solve this problem, a $4 \times 4 \times 1/2$ in. steel angle was chosen to be welded on one side of the square HSS tube, therefore providing a convenient surface to attach specimens or loading components to. This also had the added benefit of providing increased flexural capacity and can be replicated on the other side of the square HSS tube for even greater bending resistance.

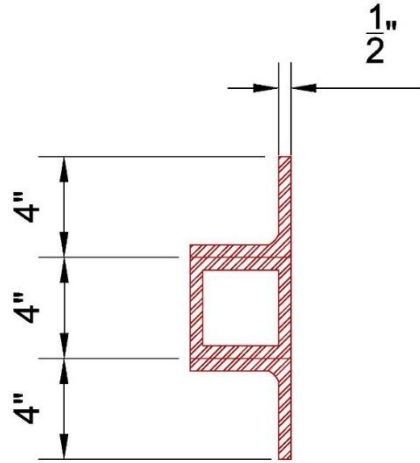


Figure 4.2: Cross-section of steel racks.

The final cross-section of the steel racks is composed of a $4 \times 4 \times 1/2$ in. square HSS tube as the centerpiece, with one $4 \times 4 \times 1/2$ in. steel angle welded on each side. This gives a moment of inertia of $I = 101.7 \text{ in}^4$ and a neutral axis depth of $y_c = 6$ in. Using grade 50 steel with a yield stress $f_y = 50$ ksi gives a yield moment $M_y = 847.5$ kip-in, per Equation 4.1.

$$M_y = \frac{f_y I}{y_c} \quad (4.1)$$

At four specimens per setup arranged in the layout shown in Figure 4.3, the ultimate moment demand imposed by the 22 kips at each loading point amounts to a total of 660 kip-in. This is approximately 78% of M_y , which gives a reasonable margin of safety while maximizing the number of specimens that can be accommodated. Therefore, both the design of the steel racks and the arrangement of specimens is satisfactory.

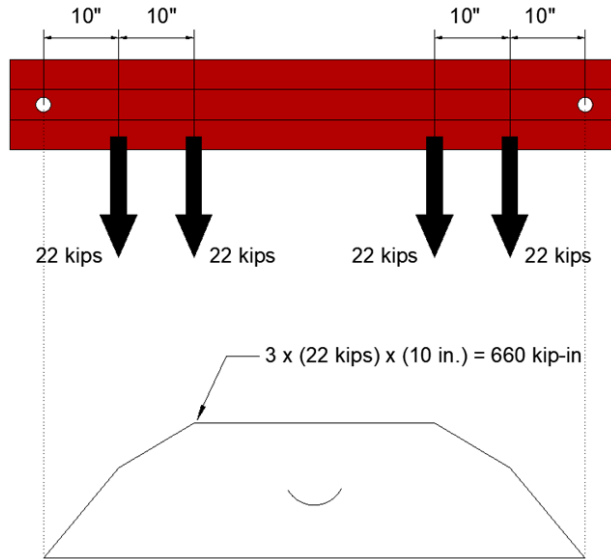


Figure 4.3: Bending moment diagram of loaded steel racks.

The design of the full setup, illustrated in Figure 4.4, uses two of the designed steel racks spaced at 12 ft. on center. Considering the 40 in. length of each MF-FRP connection, this design can accommodate two connections per loading point, which means each setup can accommodate a total of eight specimens. Hydraulic cylinders are attached to the bottom rack, while steel jumper plates are attached to the top rack. At the top, a 1 in. diameter pin connects the jumper plates to an intermediate steel plate with 22 holes, through which one end of an 11 ft. long MF-FRP plate is connected using fasteners. Similarly, at the bottom, a 1 in. diameter pin connects the hydraulic cylinders to an intermediate steel plate with 22 holes, through which the other end of the MF-FRP plate is connected with fasteners. With this arrangement, it was determined that two setups were needed: one using 0.5 in. diameter bolts, and another using 0.375 in. diameter bolts. Two series of bolt diameters conducted in the sustained loading test were based on the design bolt pattern and diameter considered in Chapter 3 to provide long-term data for the two diameters considered.

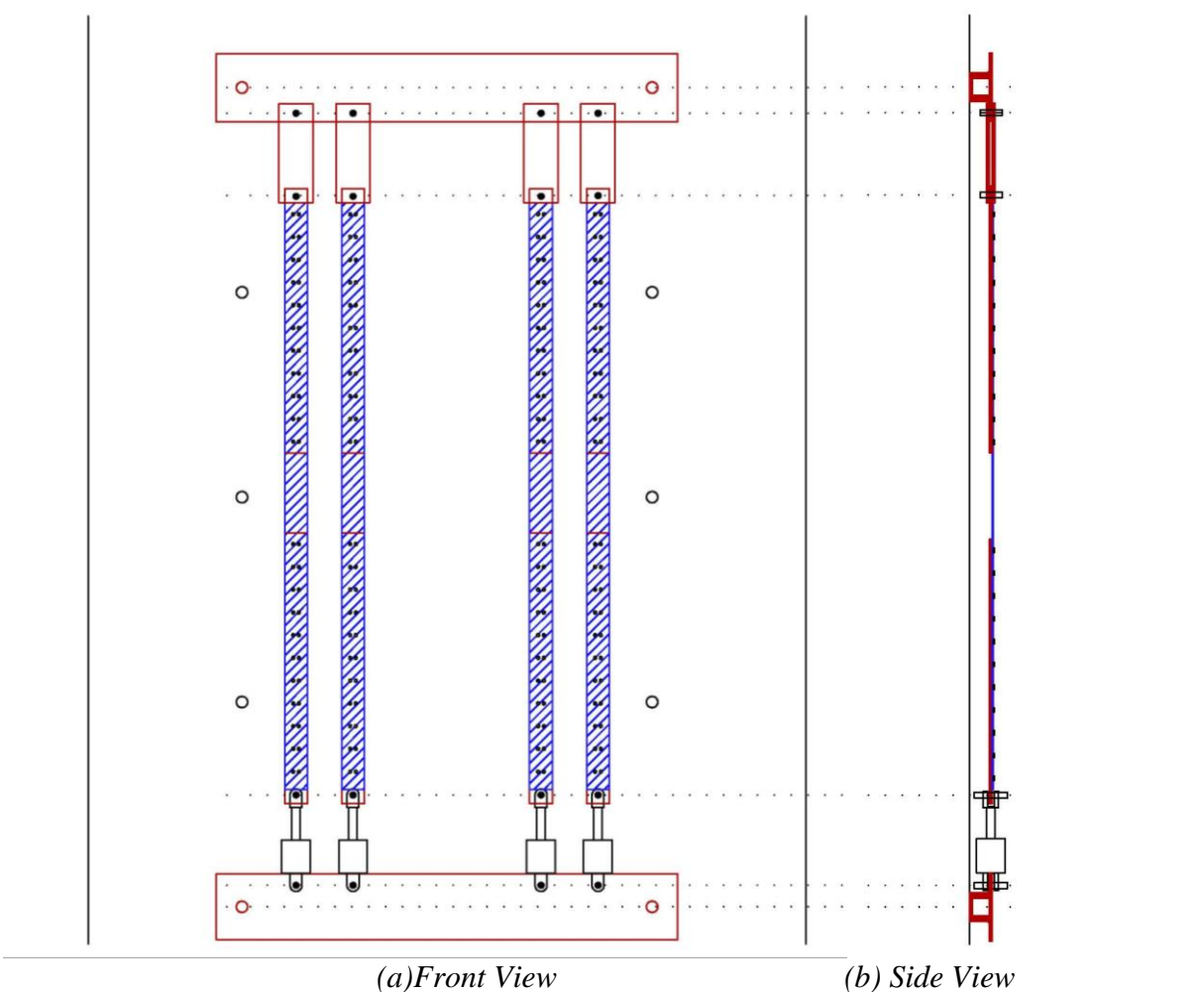


Figure 4.4: Full test setup of sustained loading experiment.

4.1.3 – Construction and Assembly

The construction of the steel racks took place entirely in the lab. Several 20 ft. long $4 \times 4 \times 1/2$ in. steel angles and square tubes were purchased and cut into 7 ft. long pieces. This came to a total of four-square tubes pieces and eight steel angle pieces. Holes of diameter 1.625 in. were drilled into the ends of the tubes, spaced at 6 ft. on center, while 1.125 in. holes were drilled into the angles at the loading points (Figure 4.5). To form the design of the steel racks, each square tube was joined with its pair of angles by a 0.5 in. thick weld applied throughout the 7 ft. length linking these elements, carefully filling the space in between the tubes and angles due to rounded edges (Figure 4.6).



Figure 4.5: Drilling steel components.

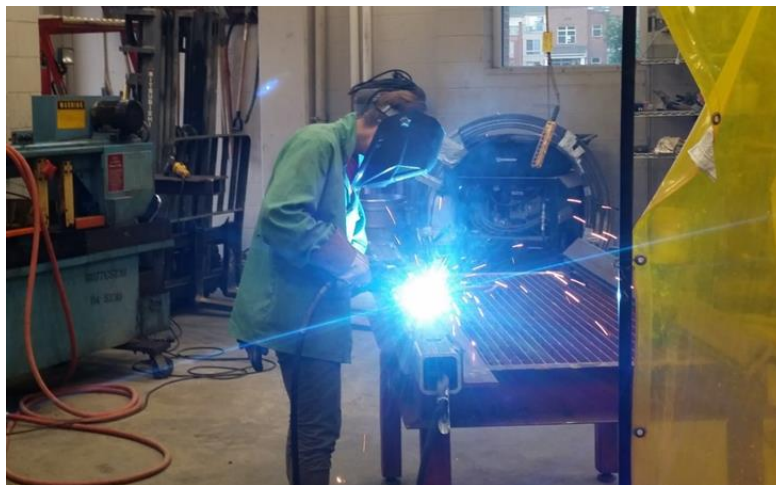


Figure 4.6: Welding angles to square HSS tubes.

Four racks in total were constructed and then painted. These were then attached to the strongwall web with 1.5 in. diameter threaded rods (Figure 4.7a). Two racks were attached on each side of the strongwall, giving two setups in total. The required tensile strength of the threaded rods was approximately 113 ksi, and so the rods selected were Grade B7, with a tensile strength of 120 ksi. Since the sustained load was to be applied along one of the free angle legs, the rods were at risk of bending stresses due to the eccentricity of applied loads. To mitigate this bending, stiffeners were made out of the remaining steel square HSS pieces to fit in between the loaded angle leg and

the strongwall; the smallest amount of bending of the rods would engage the stiffeners against the strongwall, providing a reactive force to halt the process as soon as it starts.



(a) Steel racks attached to strongwall web.



(b) Final assembled sustained load test setup.

Figure 4.7: Sustained load test setup (a) before and (b) after attaching specimens.

The jumper plates and hydraulic cylinders were attached to the top and bottom racks, respectively, through 1 in. diameter pins. The intermediate steel plates were then attached to each of the jumper plates and the hydraulic cylinders. Finally, the MF-FRP plates were attached with 0.5 in. diameter bolts on one side of the strongwall, and 0.375 in. diameter bolts on the other. Washers were used on both sides of the MF-FRP connections, and the bolts were tightened to a torque of 30 in.-lbs. to match the condition of the material testing that determined the design bolt pattern. Figure 4.7(b) shows the final setup, including the hydraulic circuit which is discussed in the following section.

4.1.4 – Hydraulic Circuit

Each setup used two hydraulic circuits, such that each circuit supplied two 11 ft. long MF-FRP plates, or four 5.5 ft. long specimens. The circuit is comprised of three main components: two hydraulic cylinders, a pump, and an accumulator. With the hydraulic cylinders' pistons extended, the pump draws fluid out in order to retract the pistons and generate force in the specimens. The pump can be disconnected after a one-way valve between the pump and the two cylinders is closed. The valve is connected to the hoses leading to the cylinders and the accumulator with a tee-fitting. The accumulator (placed inside the wooden “chairs” to each side of the setup in Figure 4.7(b)) ensures the load is sustained throughout the duration of the experiment; as the specimens elongate (creep), excess fluid is released to the incompressible fluid-side of the accumulator, which, through a piston, compresses the gas on the other side, thereby maintaining the pressure in the circuit. Pressure gauges are used to monitor the loading, with the use of Equation 4.2:

$$R = (A_p - A_r) \times P \quad (4.2)$$

where R is the retraction force, A_p is the piston area, which for the cylinders used in this setup is 12.6 in^2 , and A_r is the rod area, 1.23 in^2 for this setup. Therefore, the required pressure to generate a retraction force of 22 kips is 1,940 psi. This is a useful calculation to check that the force to be delivered is within the limits of the hydraulic cylinder (2,500 psi in this case), but it is recommended that a calibration of the pressure gauges be carried out to determine the actual pressure reading that equates to the retracting force required. Figure 4.8 shows the procedure conducted for this experiment. The cylinders were loaded in a universal testing machine, where the force feedback was related to the pressure gauge reading. The actual reading corresponding to 22 kips varied between 2,100 and 2,200 psi for the pressure gauges used in the two setups.

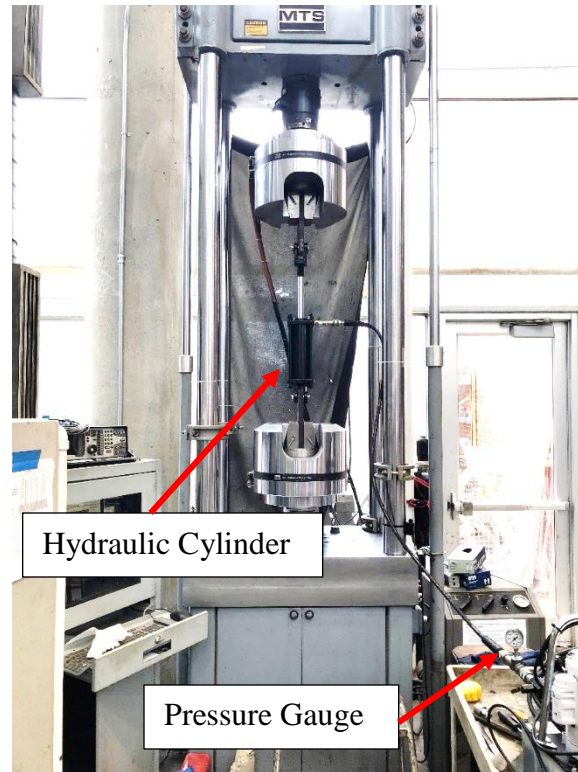


Figure 4.8: Calibration of pressure gauges in universal testing machine.

4.1.5 – Measuring Creep

Elongation of the specimens was measured on a regular basis using steel measuring tapes permanently hanging from the top jumper plate pin. These can be seen in Figure 4.7(b) and have a precision of 0.0625 in. (1/16 in.). This may seem problematic for a typical small-scale creep test but considering the 11 ft. length of the MF-FRP plates of this experiment, 0.0625 in. (1/16 in.) equates to a precision of 0.047%, which was deemed satisfactory. Measurements were taken at two points for each 11 ft. long plate: the middle and end of the plate. This enabled separation of measurements for the top and bottom specimens that constitute each 11 ft. long plate.

4.1.6 – Test Matrix

Specimens were identified by the format “Ci-j”, where, looking at the sketch in Figure 4.4 (a), i is the number of the MF-FRP plate counting left-to-right, and j is 1 for top specimens (on the jumper plate side) and 2 for bottom specimens (on the hydraulic cylinder side). The final test

matrix for each setup is represented in Table 4.1, where it can be seen that two durations were specified: 6, and 30 months. The sustained loading tests were started on November 1st, 2018. Displacement-over-time and residual capacity results for all specimens are presented.

Table 4.1: Sustained loading experiment test matrix.

Specimen ID	Duration
C1-1	30 months
C1-2	
C2-1	
C2-2	
C3-1	6 months
C3-2	
C4-1	
C4-2	

4.1.7 – Results

As two setups were constructed and monitored, one using 0.5 in. and the other using 0.375 in. diameter bolts, two sets of results are presented. Within each set, results for two different tests are given: the sustained loading test which gives displacement over time, and the static tests which give residual capacity for specimens extracted after 6 and 30 months. The latter is used as a comparison to the static tests conducted in Chapter 3 to assess the effects of creep on ultimate capacity. The results are presented in two sections based on the test conducted in order to facilitate comparison in behavior between 0.5 in. and 0.375 in. bolts.

4.1.7.1 – Displacement over Time

Figure 4.9 and Figure 4.10 show the measurements of elongation over time, for all specimens in the 0.5 in. and 0.375 in. setups, respectively. Comparison of the two bolt diameters can be made based on the following points:

Early ages: Figure 4.11 and Figure 4.12 highlight the early ages for 0.5 in. bolts and 0.375 in. bolts, respectively, where most of the displacements occur. For 0.5 in. bolts, the significant levels of elongation occurred within the first five days, while for 0.375 in. bolts, they occurred within the first ten days.

Post-early ages: after the early age phase, no more elongation occurred for 0.5 in. bolts, while some small elongations were observed for 0.375 in. bolts, specifically for specimens C3-1, C3-2, and C4-2.

Creep: treating the displacements at day one (day of loading) as the benchmark allowing for (instantaneous elastic deformations), creep is equated to the change in displacement over time. The total level of creep experienced by each specimen is therefore the difference between the maximum displacements reached over the entire testing time (30 months) and the instantaneous elastic deformations and is shown in Table 4.2. For 0.5 in. bolts, all specimens experienced 0.0625 in. of creep over 30 months of sustained loading, except for specimen C4-2, which experienced 0.125 in. of creep. More variation can be seen in the creep levels of the 0.375 in. bolt specimens, with a range covering 0.0625 in. to 0.375 in. after neglecting specimen C3-1, which is taken as an outlier reaching 1 in. of displacement due to bolt bearing on the FRP plate. The arithmetic mean to calculate the average level of creep gives 0.07 in. for 0.5 in. bolts, and 0.152 in. for 0.375 in. bolts. The standard deviation is 0.021 in. for 0.5 in. bolts, and 0.099 in. for 0.375 in. bolts.

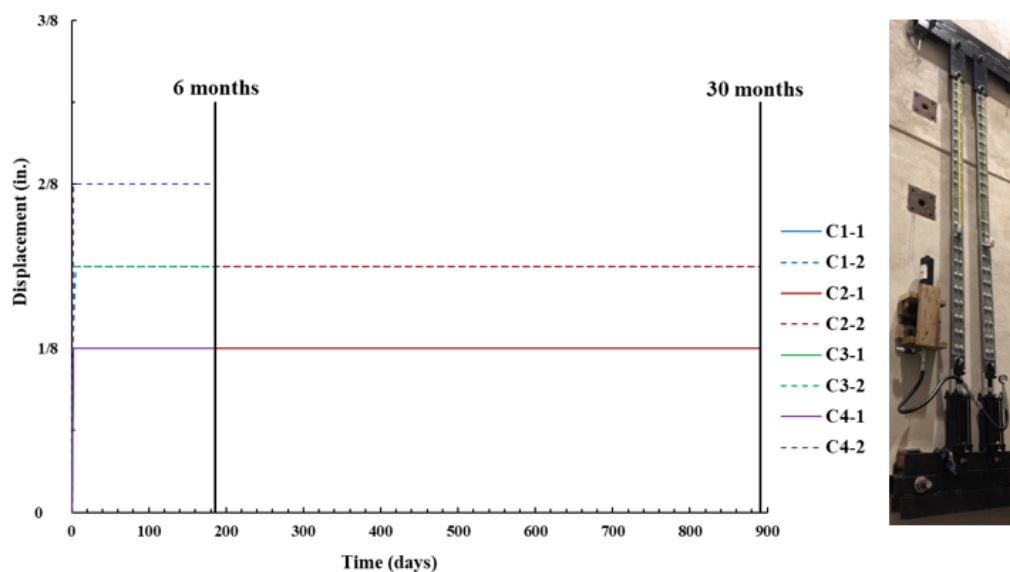


Figure 4.9: Displacement over time (0.5 in. bolts).

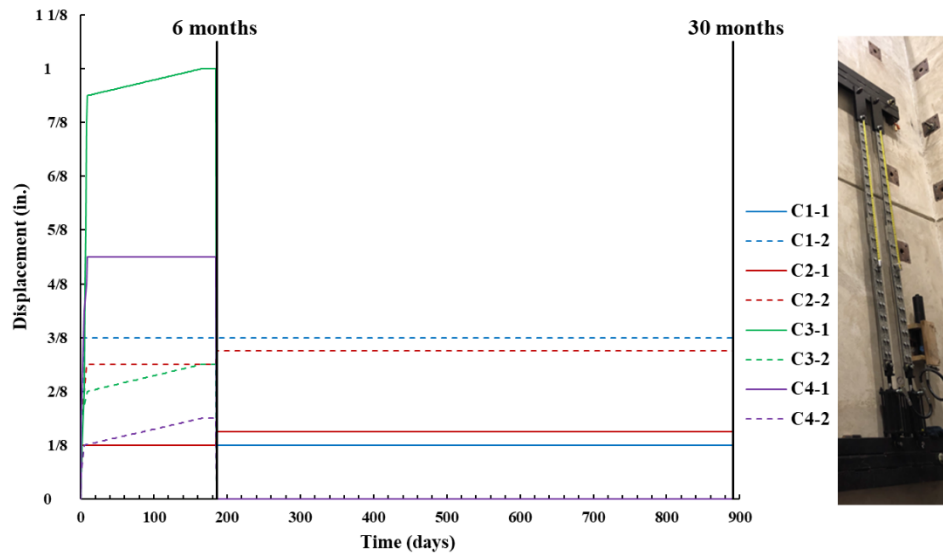


Figure 4.10: Displacement over time (0.375 in. bolts).

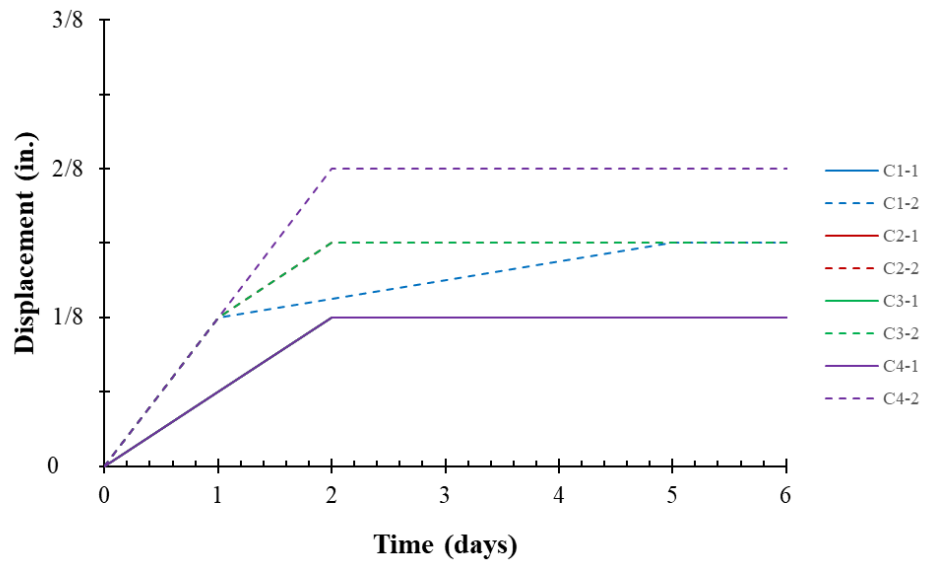


Figure 4.11: Early ages displacements (0.5 in. bolts).

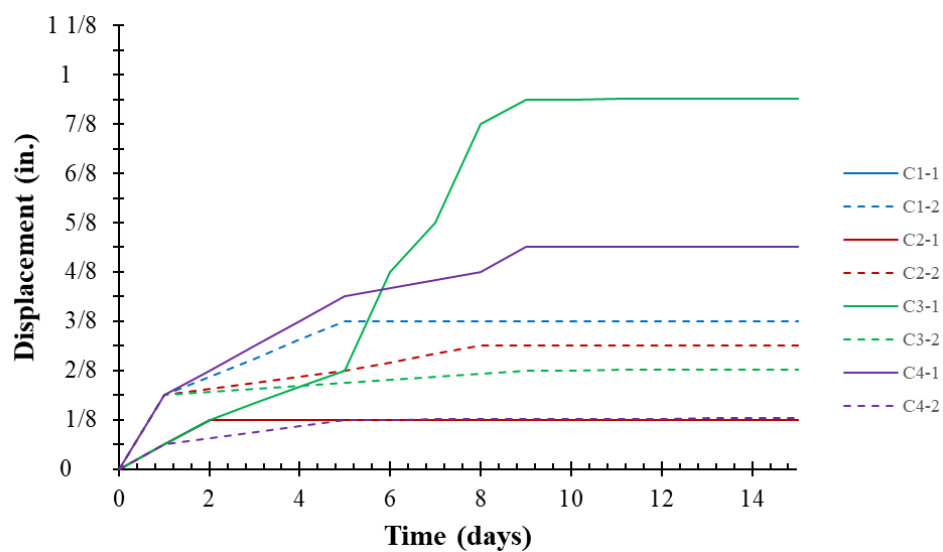


Figure 4.12: Early ages displacements (0.375 in. bolts).

Table 4.2: Summary of sustained load data.

Bolt Diameter (in)	Specimen ID	Initial Displacement (in.)	Max. Displacement (in.)	Max. Creep (in.)	Mean Max. Creep (in.)	Standard Deviation (in.)
0.5	C1-1	0.0625	0.125	0.0625	0.070	0.021
	C1-2	0.125	0.1875	0.0625		
	C2-1	0.0625	0.125	0.0625		
	C2-2	0.125	0.1875	0.0625		
	C3-1*	0.0625	0.125	0.0625		
	C3-2*	0.125	0.1875	0.0625		
	C4-1*	0.0625	0.125	0.0625		
	C4-2*	0.125	0.25	0.125		
0.375	C1-1	0.0625	0.125	0.0625	0.152	0.099
	C1-2	0.1875	0.375	0.1875		
	C2-1	0.0625	0.125	0.0625		
	C2-2	0.1875	0.3125	0.125		
	C3-1* ⁺	0.0625	1	0.9375		
	C3-2*	0.1875	0.3125	0.125		
	C4-1*	0.1875	0.5625	0.375		
	C4-2*	0.0625	0.1875	0.125		

Notes:

*Specimens removed at six months of sustained loading to test the residual capacity

⁺Specimen considered an outlier and neglected from analysis

It can be concluded from the displacement-over-time results that the 0.5 in. diameter bolt specimens exhibit minor creep with a consistent behavior, while the 0.375 in. bolt specimens experience higher levels of creep with larger variance. The different levels of creep variance of 0.5 and 0.375 in. diameter bolt specimens can be observed in Figure 4.13 and Figure 4.14.

Based on the experimental result, a design recommendation is to measure bearing within two weeks of retrofit installation. If the total displacement exceeds 0.5 in., then the FRP plate should be replaced. Two weeks is specified based on the duration of the early ages phase for 0.375 in. bolts (10 days), where most of the displacement occurred, and 0.5 in. is a conservative limit based on the highest displacement during the same phase (neglecting the outlier), 0.563 in.

Half of the specimens were removed from the sustained loading after 6 months in April 2019 to test the residual capacity, while the other half remained under load for 30 months until April 2021 when their residual capacity was tested. During the sustained load period, no indication of damage accumulation was observed. Table 4.2, Figure 4.9 and Figure 4.10 show that the creep experienced by the 0.5 in. diameter bolt specimens under sustained loading remains the same after the first 5 days of loading, while the 0.375 in. diameter bolt specimens experienced minor variation after the first 10 days of loading, respectively.

The effect of the creep levels observed must be determined in order to judge their severity. Creep takes place mostly in the form of displacements induced by bolts bearing on the MF-FRP under a constant stress, which relieves some force from the plates. The force initially sustained corresponds to an initial displacement at the day of loading, after which it drops by an amount proportional to the level of bearing exhibited. A measurement of creep can therefore be used to calculate the prestress losses in the FRP.

For 0.5 in. bolts, the mean maximum creep for 30 months of sustained load is 0.07 in. The total length of the FRP plates used in the full-scale experimental program was approximately 311 in., and so the corresponding strain is 0.00045, calculated as the ratio of the creep over the total length. Using Hooke's Law for a linear-elastic material, and the FRP tensile modulus of 9020 ksi and cross-sectional area of 0.5 in.², the lost force is found to be approximately 2 kips, which is 9% of the 22 kips post-tensioning force. For 0.375 in. bolts, the mean creep is 0.125 in. for specimens with sustained loading for 30 months, which yields a strain of 0.0008. The prestress loss is 3.6 kips, approximately 16% of the initial post-tensioning force. These losses can be compared to that of typical prestressing strand relaxation using Equation 4.3 (Nawy, 2010):

$$\Delta f_{pR} = f'_{pi} \frac{\log t}{10} \left(\frac{f'_{pi}}{f_{py}} - 0.55 \right) \quad (4.3)$$

where, for stress-relieved high-strength (HS) strands, f'_{pi} is the six-hour transfer stress (185 ksi), taken as 98% of the initial jacking stress ($f_{pi} = 189$ ksi), f_{py} is the yield stress (230 ksi), and t is the time in hours. The change in stress due to relaxation, Δf_{pR} , for 30 months of sustained loading (21600 hours) is 20.4 ksi, which translates to a change of force of 2.35 kips considering a strand area of 0.115 in.². This is higher than the losses for the 0.5 in. bolt specimens, but lower than those for the 0.375 in. bolt specimens. According to the losses exhibited by the MF-FRP used in this research, compared to the steel prestressing used, losses of the 0.5 in. bolt specimen should not be a concern. However, and in contrast to prestressing steel, the option to restore those losses is available with this retrofit, by twisting the turnbuckle to stretch the plates by a length equivalent to the creep measured. Furthermore, the losses due to sustained loading can be predicted using the simple calculation presented above following Hooke's Law from the experimental results and considered in long-term design.

4.1.7.2 – Residual Capacity

Specimens C3-1, C3-2, C4-1, and C4-2 were extracted after 6 months of sustained loading, and the remaining specimens C1-1, C1-2, C2-1, and C2-2 were extracted after 30 months of sustained loading. Figure 4.13 and Figure 4.14 show the state of these specimens after extraction. Visually, the 0.5 in. specimens showed very little damage, with short longitudinal shear cracks at each hole. In addition to short shear cracks, the 0.375 in. specimens showed more variable and, in some cases, significant bearing compared to the 0.5 in. specimens.



(a) 0.5 in. bolts



(b) 0.375 in. bolts

Figure 4.13: State of extracted specimens after 6 months of sustained loading.

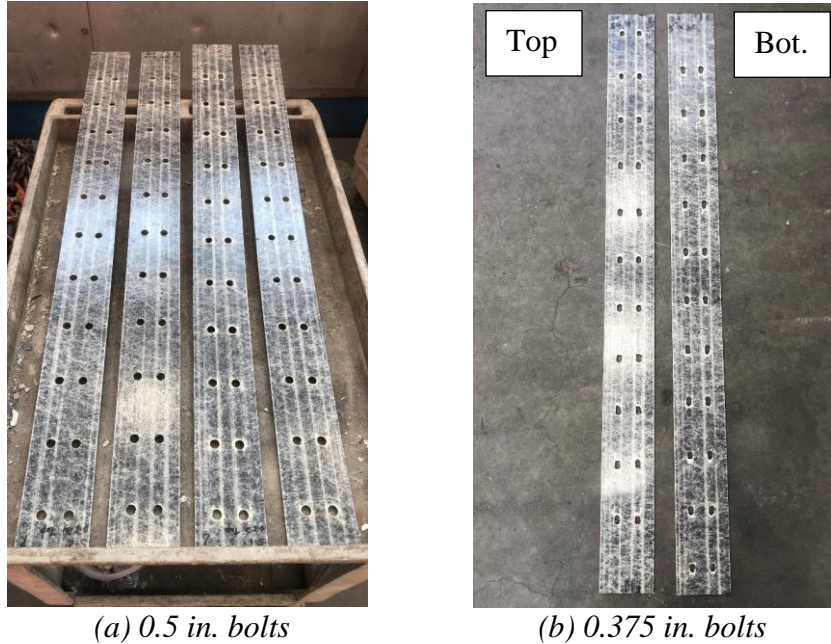


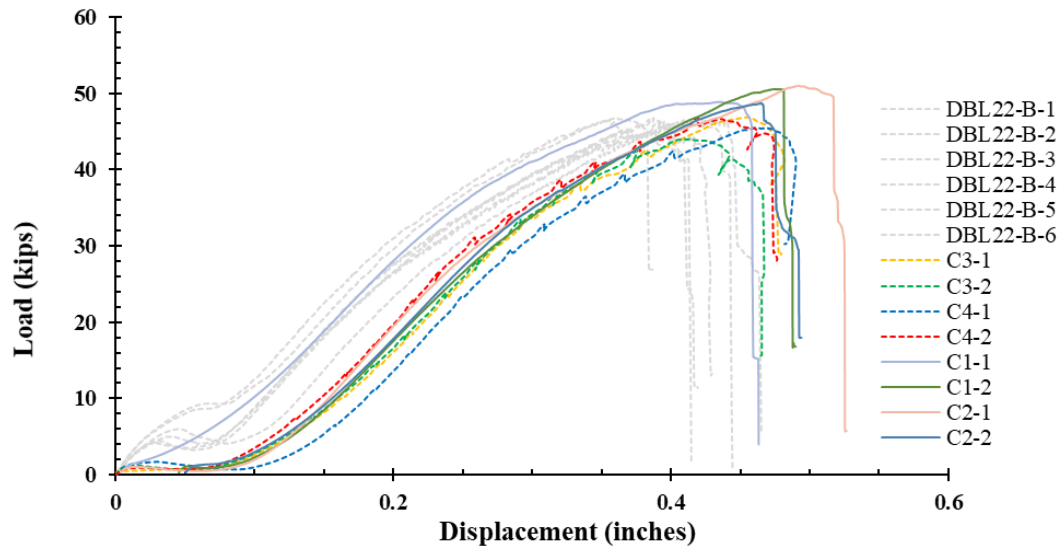
Figure 4.14: State of extracted specimens after 30 months of sustained loading.

In order to determine the residual capacity after sustained loading, all specimens were tested in uniaxial tension in the same setup as the static tests presented in Chapter 3. An intermediate steel plate was gripped at the bottom of a UTM and connected to each specimen through 22 bolts tightened to 30 in-lbs. of torque. The specimen was gripped at the top, and loaded at a rate of 0.05 in./min. The load-displacement graphs obtained are illustrated in Figure 4.15, and pictures of the setup and a failed specimen can be seen in Figure 4.16. For each graph, the uniaxial static tension tests presented in Chapter 3 for each bolt diameter are included as grey curves, representing a useful benchmark for a comparison that will inform the creep effects on capacity. Specimens for each bolt diameter with 6 months of sustained loading are presented with dash curves, showing the comparison for specimens under different sustained loading time frame.

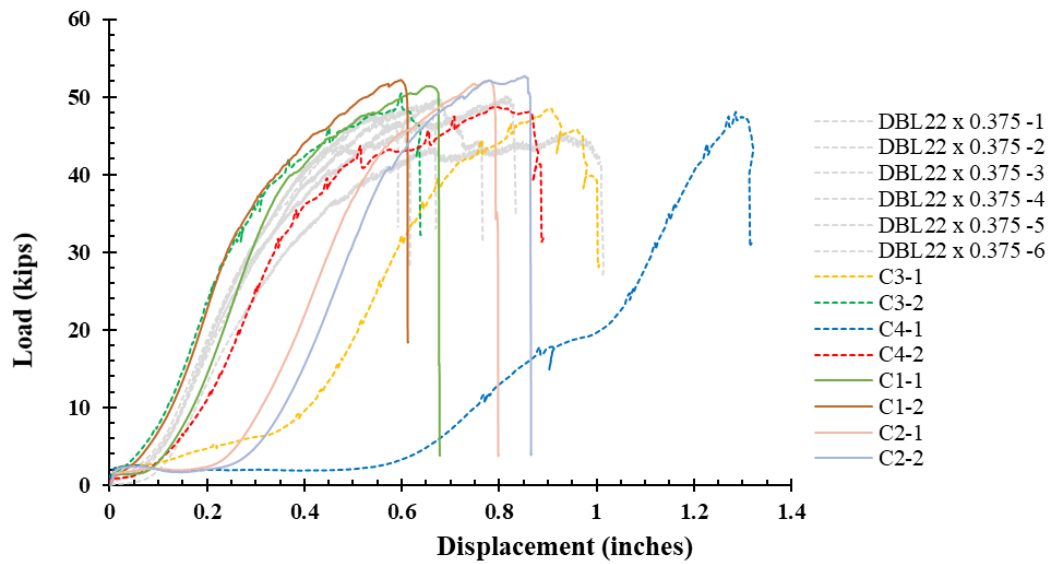
For 0.5 in. diameter bolts, the behavior very closely matches that of the static tests for both loading period groups. Focusing on the peak loads achieved by each specimen, there is virtually no loss of capacity in the sustained loading specimens compared to material tested conducted in

Chapter 3. This is not surprising, considering the small amount of damage noted visually. There is also no noticeable loss of stiffness, indicated by the consistent slopes of the curves. The key difference is the higher initial slip for the sustained load specimens, which gives the “shift” to the right. This initial slip can be directly related to creep, as it represents the displacement that takes place before the bolts are engaged by making contact with the edges of the holes, which in this case is the 0.07 in. for 30 months sustained loading. The mean creep is calculated in Table 4.2.

Similarly, for 0.375 in. bolts, the initial slip for each tested specimen is consistent with its respective level of creep from the displacement-over-time results. The significant variance in displacement results for this bolt size is even more evident in this case. Specimens C3-2 and C4-2 fit reasonably well with material tests. Specimen C3-1 exhibits a different loading progression, although it still fits well with the material tests in terms of ultimate displacement. Specimen C4-1, C2-1 and C2-2 do not fit with the material tests, with a much higher ultimate displacement and a different loading progression. That being said, focusing on the peak loads achieved, there is no noticeable loss in capacity for the sustained loading specimens. Table 4.3 presents the result of the uniaxial tension tests of all specimens.



(a) 0.5 in. diameter bolts



(b) 0.375 in. diameter bolts

Figure 4.15: Residual capacity after 6 and 30 months of sustained loading.

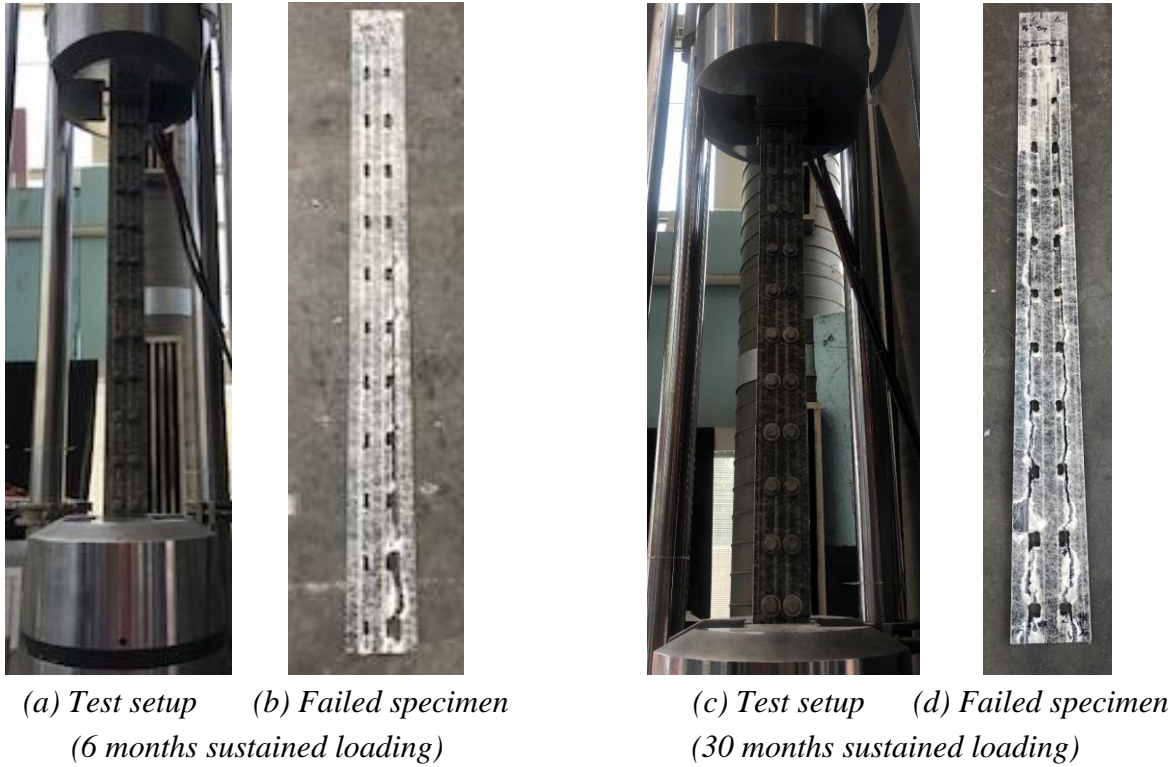


Figure 4.16: Residual capacity test after 6 and 30 months of sustained loading.

Table 4.3: Results of residual capacity of sustained loading specimens.

Bolt Diameter (in)	Specimen ID	Sustained Loading Time (Months)	Max. Force (kips)	Disp. at Max. Force (in.)	Mean Max. Force (kips.)	Design Capacity (kips)
0.5	C1-1	30	48.9	0.436	49.8	46.4
	C1-2		50.5	0.479		
	C2-1		51.0	0.491		
	C2-2		48.7	0.465		
	C3-1	6	46.8	0.454	45.8	
	C3-2		44.0	0.409		
	C4-1		45.5	0.461		
	C4-2		46.8	0.420		
0.375	C1-1	30	51.4	0.652	52.0	48.5
	C1-2		52.2	0.598		
	C2-1		52.1	0.778		
	C2-2		52.1	0.781		
	C3-1	6	48.5	0.905	48.9	
	C3-2		50.4	0.598		
	C4-1		48.1	1.286		
	C4-2		48.7	0.792		

4.1.8 – Observations

Conclusions from the creep test results obtained after 30 months of sustained loading can be summarized as follows:

- On average, specimens fastened with 0.5 in. diameter bolts reached 0.07 in. of creep displacement with minor variation.
- On average, specimens fastened with 0.375 in. diameter bolts reached 0.152 in. of creep displacement with some variation.
- Measurements remain stable and no indications of damage accumulation observed after the first 10 days of initial loading.
- It is recommended that creep be measured within two weeks of applying the prestress force in the retrofit. If the total tensile elongation exceeds 0.25 in. for 0.5 in. bolts, or 0.5 in. for 0.375 in. bolts due to the bearing stresses, then the FRP plate should be replaced.
- The prestress losses in the retrofit after 30 months of loading are comparable to those of relaxation of prestressing steel (~2 kips).
- Ultimate tensile capacity is unaffected.

4.2 – Cyclic Loading

Fatigue refers to the long-term degradation of material properties as a result of cyclic loading. Repeated loading and unloading of a bridge following traffic patterns makes this a crucial consideration for the retrofit used in this research. While some works exist on the cyclic behavior of MF-FRP strengthened structures, the experiments conducted are not extensive, and each presents results for a handful of tests at best. This is because these were concerned with the global behavior of the structure under cyclic loading, which makes for a cumbersome test reliant on the ability to procure or produce reinforced concrete beams, and on a large-scale setup. Consequently, the

results of these experiments are useful as an assurance of the adequacy of MF-FRP as a short-term strengthening solution but provide little information on how to assess fatigue effects. Furthermore, these results are not valid for the retrofit used in this study, because they are representative of different MF-FRP connections in terms of fastener type, size, and length of connection.

Fitting with the overall objective of this research to address gaps in MF-FRP literature and to form the basis of a design guide, the experimental program of this research opted for a small-scale approach that lends itself to repeatability and practicality, to explore a suite of design options. The same setup for the static tests for creep residual capacity is used to test the same 22-bolt MF-FRP plate arrangement, but the loading configuration is changed to a cyclic pattern with a frequency of 1 Hz. Again, both 0.5 in. and 0.375 in. diameter bolts are considered as fastening options. Results were in the form of displacement measurements at each cycle, from which observations can be made about stiffness degradation over time. It was of interest to also obtain a failure envelope for each bolt size, in order to quantify the loss of capacity as a function of the number of cycles. As such, two types of fatigue tests were conducted: ones that went all the way to fatigue failure; and others that were suspended at pre-determined numbers of cycles and then tested statically to obtain residual capacity. Conclusions on displacement, stiffness, and fatigue lifetime were drawn from the results of the former, while those of the latter formed the failure envelope.

This section presents the experimental program, results, and conclusions of the cyclic loading phase of this research. It starts with a discussion on the stress range selected, followed by a chronological exposition of the experiments conducted with results that informed how to proceed at each step. Indeed, the test matrix was modified throughout the program based on the findings

made after certain tests and is understood best with the chronological context provided by this section.

4.2.1 – Cycling Range

The common way of treating the stress range of a cyclic loading experiment is by defining levels of loading as a percentage of yield or ultimate capacity. Though somewhat arbitrary, this approach can be used to determine the fatigue life at different levels of loading. However, given that the operating condition of the retrofit system is well-defined, it is not necessary to consider different stress levels. Hence, the goal is to define a stress range that is representative of a realistic worst-case scenario.

The retrofit constitutes a flexural strengthening application, and therefore is applied on the tension side of a deteriorated beam. As such, the fatigue investigated by this experiment is caused by repeated elongation of the MF-FRP under traffic loading, and so the stress range must replicate this increase in tensile strain. As the MF-FRP is prestressed, in order to improve both inventory and operating load rating of the beams according to AASHTO, the lower bound of the stress should be equal to the level of prestress. A force of 22 kips was selected, which is equivalent to the jacking force of typical 7-wire prestressing steel strands that this retrofit aims to replace.

Determining the upper bound force is less straightforward and may be done in various ways. The approach developed in this research considers a candidate bridge for the application of the MF-FRP retrofit and identifies the maximum live load moment it can be subjected to. Load distribution is neglected across beams in a span, and so it is assumed that a given beam in the bridge carries 50% of that moment, corresponding to a single wheel line. The bottom face of the beam is considered, and the change in strain is calculated based on the change in stresses there due to the addition of the live load moment to stresses from the self-weight and prestressing. Figure 4.17 shows the individual stress profiles of the stresses considered. The reference point is taken as

the instance when the stress at the bottom face of the concrete ($\sigma_{bottom,i}$) is equal to the sum of the axial compressive stress induced by the prestressing forces ($\sigma_{a,ps}$), the compressive flexural stress from the eccentricity of the prestressing forces ($\sigma_{b,ps}$), and the tensile flexural stress from the self-weight of the beam ($\sigma_{a,DL}$). These stresses are summed per Equation 4.4, where compression is positive, and tension is negative.

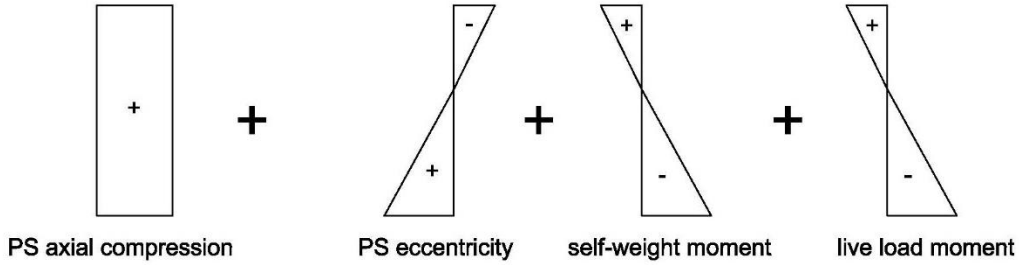


Figure 4.17: Individual stress profiles considered.

$$\sigma_{bottom,i} = \sigma_{a,ps} + \sigma_{b,ps} - \sigma_{b,DL} \quad (4.4)$$

The flexural stress from the live load moment ($\sigma_{b,LL}$) is added in order to obtain the stress under maximum traffic loading ($\sigma_{bottom,f}$), per Equation 4.5:

$$\sigma_{bottom,f} = \sigma_{a,ps} + \sigma_{b,ps} - \sigma_{b,DL} - \sigma_{b,LL} \quad (4.5)$$

Each stress component is calculated based on Equation 4.6 through 4.9:

$$\sigma_{a,ps} = \frac{f_{ps} A_{ps}}{A_c} \quad (4.6)$$

where f_{ps} is equal to 270 ksi for 7-wire prestressing strands, A_{ps} is 0.116 in.² multiplied by the number of prestressing strands in the cross-section, and A_c is the concrete area in the cross-section.

$$\sigma_{b,ps} = \frac{f_{ps} A_{ps} e_{ps} y_c}{I} \quad (4.7)$$

where e_{ps} is the prestressing steel eccentricity, calculated as the difference between the depths to the centroid of the prestressing strands and the centroid of the beam, y_c , and I is the uncracked moment of inertia of the concrete section,

$$\sigma_{b,DL} = \frac{M_{DL} y_c}{I} \quad (4.8)$$

where M_{DL} is the moment from the self-weight of the beam,

$$\sigma_{b,LL} = \frac{M_{LL} y_c}{I} \quad (4.9)$$

where M_{LL} is the maximum live load moment generated from traffic.

The candidate bridge selected was Bridge No. 790152 in Rowan County, for which access to structural analysis documents was given by NCDOT. The superstructure is composed of nine beams. The cross-section of each beam can be seen in Figure 4.18 and shows all the necessary dimensions to calculate A_{ps} (2.415 in.²), e_{ps} (4 in.), A_c (404 in.²), y_c (8.5 in.) and I (12,529 in.⁴). An NCDOT bridge maintenance analysis report was consulted to get the maximum live load moment this bridge is rated for, which is 684 kip-ft., corresponding to a truck of designation TNAGT5B (aggregate truck). This moment was divided by two to get the moment corresponding to a single wheel line, as load distribution is neglected, giving a live load moment M_{LL} of 342 kip-ft. per beam. With a span of 45 ft., M_{DL} can be estimated at 103 kip-ft. assuming a concrete density of 145 lbs./ft.³. The initial stress at the bottom face of the concrete, $\sigma_{bottom,i}$, is therefore equal to +2.55 ksi, and the final stress at the same location, $\sigma_{bottom,f}$, is equal to -0.24 ksi.

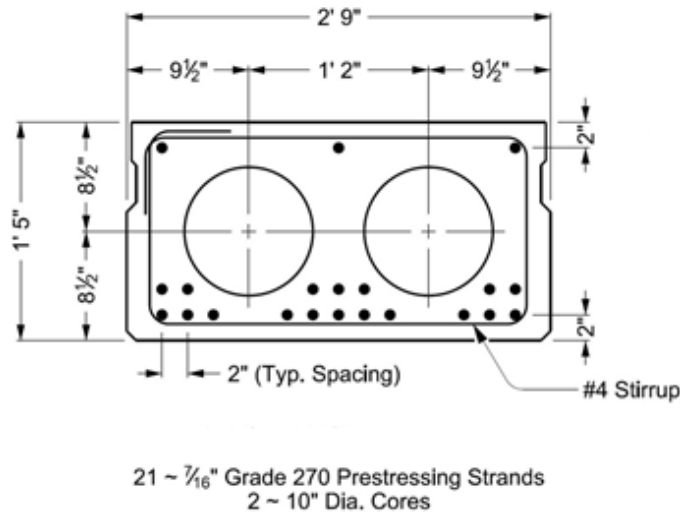


Figure 4.18: Candidate bridge cross-section information and geometry.

These stresses can be used to estimate the change in strain using the linear stress-strain relationship in Equation 4.10, as the stresses are compressive and within 50% of 5 ksi, the design concrete compressive strength (f'_c) of the concrete.

$$\varepsilon_b = \frac{\sigma_{bottom}}{E_c} \quad (4.10)$$

The design concrete compressive strength is used to estimate the elastic modulus, E_c , per Equation 4.11 from ACI 318 (2014):

$$E_c = 57000\sqrt{f'_c} \text{ (psi)} \quad (4.11)$$

The initial and final strains were found to be 0.00063 and -0.00006, respectively, equating to a change in strain, $\Delta\varepsilon$, of nearly 0.0007. This value is used as a representation of the elongation the FRP might be subjected to during each cycle by adding it to the initial prestressing strain, thereby obtaining the upper-bound strain in the FRP, ε_{FRP} , as given by

$$\varepsilon_{FRP} = \frac{\sigma_{pt}}{E_{FRP}} + \Delta\varepsilon \quad (4.12)$$

where E_{FRP} is the elastic modulus of the MF-FRP plate, and is equal to 9,020 ksi, and σ_{pt} is the stress from the 22 kips of post-tensioning,

$$\sigma_{pt} = \frac{22 \text{ kips}}{A_{FRP}} \quad (4.13)$$

where A_{FRP} is the cross-sectional area of the MF-FRP (0.5 in.²). The upper-bound strain ε_{FRP} was found to be approximately 0.0058, which then gives an upper-bound force of approximately 26.2 kips, as given by:

$$P_{upperbound} = E_t \varepsilon_{FRP} A_{FRP} \quad (4.14)$$

These calculations are largely dependent on the bridge studied and the maximum live load moment considered for that particular bridge. So, to be conservative, and in acknowledgement of

the possibility of cases where the upper-bound force might be higher than the one calculated, a factor of 1.1 is applied to the 26.2 kips, giving an upper-bound force of approximately 29 kips.

The final cycling range for the cyclic loading experiment was therefore determined to be from 22 kips to 29 kips.

4.2.2 – Experimental Program and Results

The testing program followed the matrix shown in Table 4.6, where tests are presented in the order in which they were conducted. Immediately noticeable from the table is the variation in fastener torque. This section follows the order of Table 4.4 to explain the progression in understanding achieved with each test and how the torque parameter was affected at certain steps. Also noticeable are the two failures modes encountered: ultimate; and fatigue. The former refers to tests controlled by a set number of cycles, after which the specimens were tested monotonically to measure the residual capacity, while the latter refers to specimens that failed due to fatigue during the cycling loading test.

Table 4.4: Cyclic loading experiment test matrix.

Bolt Diameter	Specimen ID	Failure Mode	No. Cycles Reached	Fastener Torque
0.375 in.	F1-1	Ultimate	40,000	30 in.-lb.
	F1-2	Ultimate	200,000	
	F1-3	Ultimate	400,000	
	F1-4	Ultimate	600,000	
	F1-5	Fatigue	820,000	
	F1-6	Fatigue	1,250,000	30 ft.-lb.
0.5 in.	F2-1	Fatigue	159,000	
	F2-2	Ultimate	250,000	
	F2-3	Fatigue	454,000	

Starting with 0.375 in. bolt diameter tests, specimen F1-1 was subjected to 40000 cycles. At this point, the torque parameter was set at 30 in.-lbs., which is equivalent to the “finger tight + ¼ turn” used in their static tests. Bolts were tightened with a torque-wrench for consistency and

precision. Visually, after 40000 cycles, the damage consisted of some minor longitudinal cracking at the first two rows of bolts only. The specimen was then tested monotonically up to 46.8 kips, at which point longitudinal cracks had spread along the MF-FRP plate, which failed instantly. Specimens F1-2, F1-3, and F1-4 followed the same testing procedure, only at increasingly higher numbers of cycles (200000, 400000, and 600000, respectively). The level of visual damage again consisted only of longitudinal shear cracking, the length of which increased incrementally with increasing number of cycles. Figure 4.19 shows specimen F1-4 near 600000 cycles, the most severe cracking level of the first 4 tests.



Figure 4.19: Fatigue cracking near 600000 cycles.

When loaded monotonically, specimens F1-2, F1-3, and F1-4 reached failure loads of 46.8 kips, 43.4 kips, and 38.5 kips, respectively. One more test was conducted at the 30 in.-lbs. torque, and since the level of degradation was more significant after 600000 cycles, it was decided that F1-5 would be tested cyclically to fatigue failure, which was reached at 820000 cycles. The failure mode was also longitudinal shear cracking (Figure 4.20).



Figure 4.20: Fatigue failure by longitudinal shear crack spreading at 820000 cycles.

Enough data was available at that instant to develop a failure envelope, which is shown in Figure 4.21. The first point at 48.6 kips (intersecting the y-axis) is taken from Chapter 3 results and represents the mean ultimate capacity of the same 22-bolt MF-FRP connection using 0.375 in. bolts. Some key observations can be made about the rate of capacity loss as a function of number of cycles. Prior to 200000 cycles, there is a plateau region at a capacity of 46.8 kips, which, compared to 48.6 kips, indicates virtually no capacity loss. Beyond 200000 cycles, significant decreases in capacity occur, with the rate of degradation increasing at each increment of cycling. The point of fatigue failure at 820000 cycles marks the limit of this failure envelope.

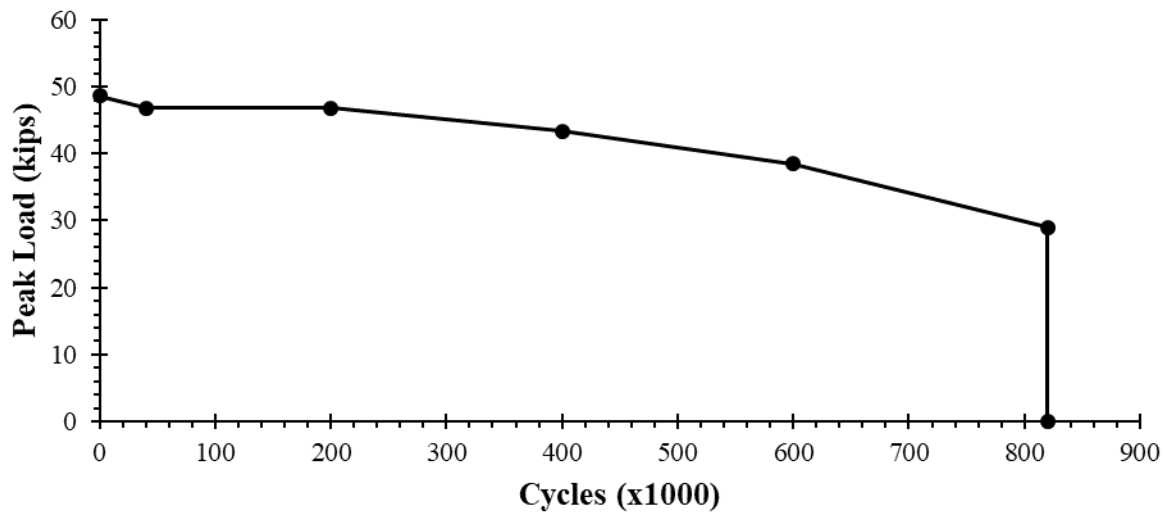


Figure 4.21: Fatigue failure envelope for 0.375 in. bolts at 30 in.-lbs. of torque.

The importance of having a consistent and precise tightening for all bolts goes without saying. However, interest in investigating the effects of torque grew during fatigue testing, specifically with the goal of obtaining the best possible fatigue behavior out of the retrofit. Therefore, one more 0.375 in. specimen was tested up to fatigue failure, this time using a torque of 30 ft.-lbs. instead of 30 in.-lbs. The torque of 30 ft.-lbs. is based on a safe limit for tightening the 0.375 in. diameter bolts used in this study. Specimen F1-6 reached 1250000 cycles before it failed due to fatigue. It was clear then that higher torque levels yield a better fatigue behavior. Time constraints prevented further testing to get an independent failure envelope for the higher torque level, but a conservative prediction is achieved as shown in Figure 4.22 by linearly interpolating between 200000 and 1250000 cycles.

As mentioned previously, the data was collected in the form of displacement measurements at each cycle. The displacement is a measure of the elongation of the plate and extension of holes due to bearing of bolts against the edges. The hysteretic load-displacement data is presented in Figure 4.23, which gives another visual comparison of the cyclic performance at each torque level.

It can be seen that it takes 400000 to 500000 more cycles for the FRP tightened at 30 ft.-lbs. of torque to reach the same displacement as the 30 in.-lbs. torque level.

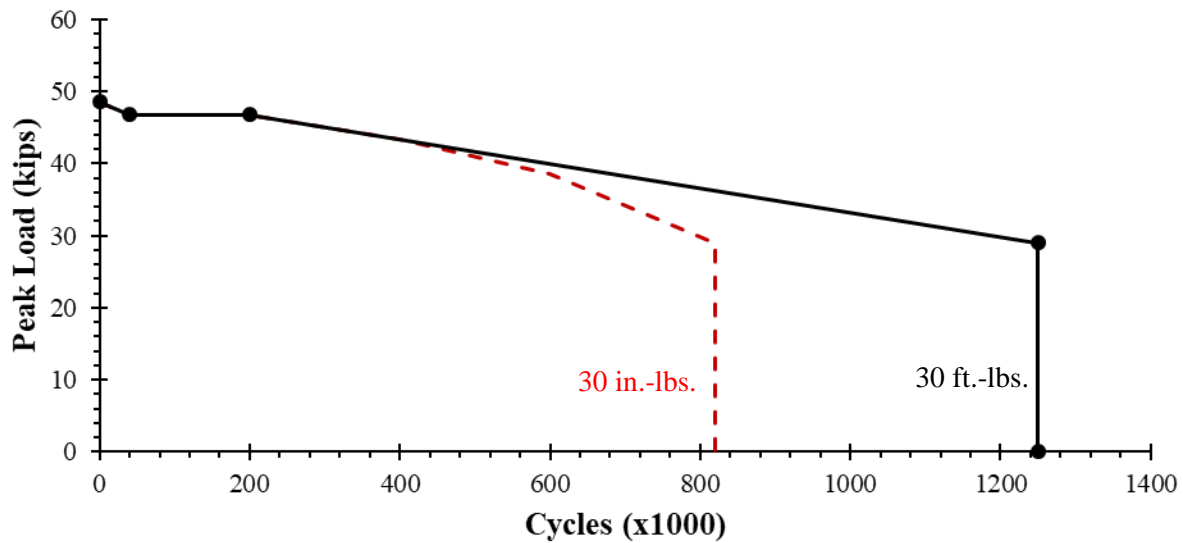


Figure 4.22: Estimate of fatigue failure envelope for 0.375 in. bolts at 30 ft.-lbs. of torque.

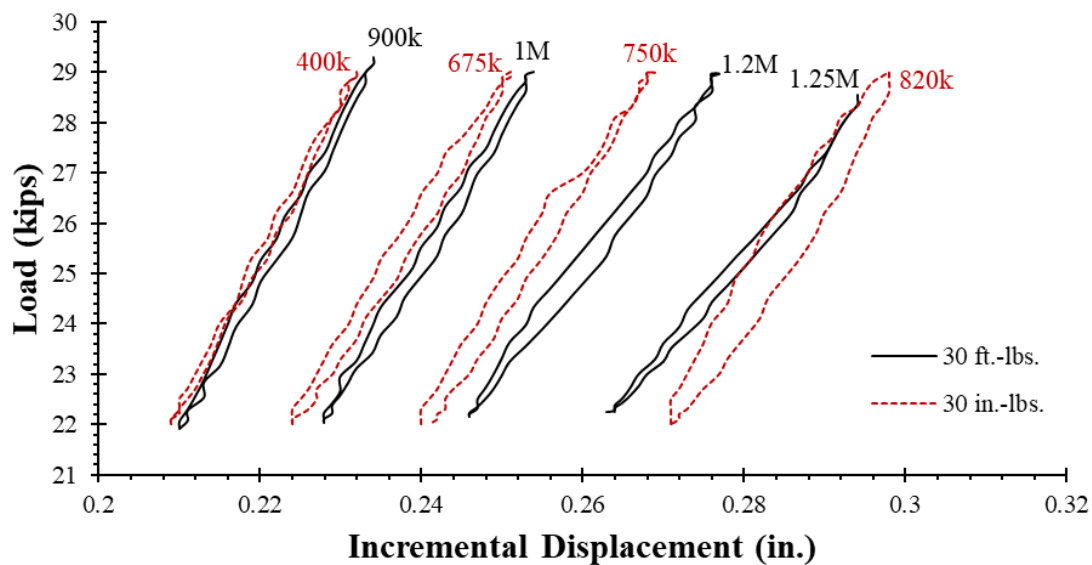


Figure 4.23: Hysteretic load-displacement plots for 0.375 in. bolts.

Figure 4.23 is the source of subsequent plots showing stiffness degradation and incremental displacement per number of cycles. By calculating the secant stiffness at each hysteretic loop, the curves in Figure 4.24 can be plotted. Further comparisons can be drawn between the two torque levels by inspecting the stiffness degradation over time from this graph. Major improvements can be observed for the higher torque level, with a higher initial stiffness (370 kips/in. vs. 310 kips/in.) and a much slower rate of degradation.

For field inspection purposes, an increment displacement per number of cycles graph like that shown in Figure 4.25 will be informative to visually assess damage and stiffness losses based on incremental displacements at each hysteretic loop. At 30 in.-lbs. of torque, slow damage accumulation is exhibited up to 600000 cycles, after which the rate increases rapidly. The incremental displacement measured at 600000 cycles is approximately 0.23 in. For 60 ft.-lbs., this increase in rate occurs at approximately 900000 cycles, also at 0.23 in. So, if 0.375 in. bolts are used the FRP plates should be replaced once 0.23 in. of incremental displacement is measured.

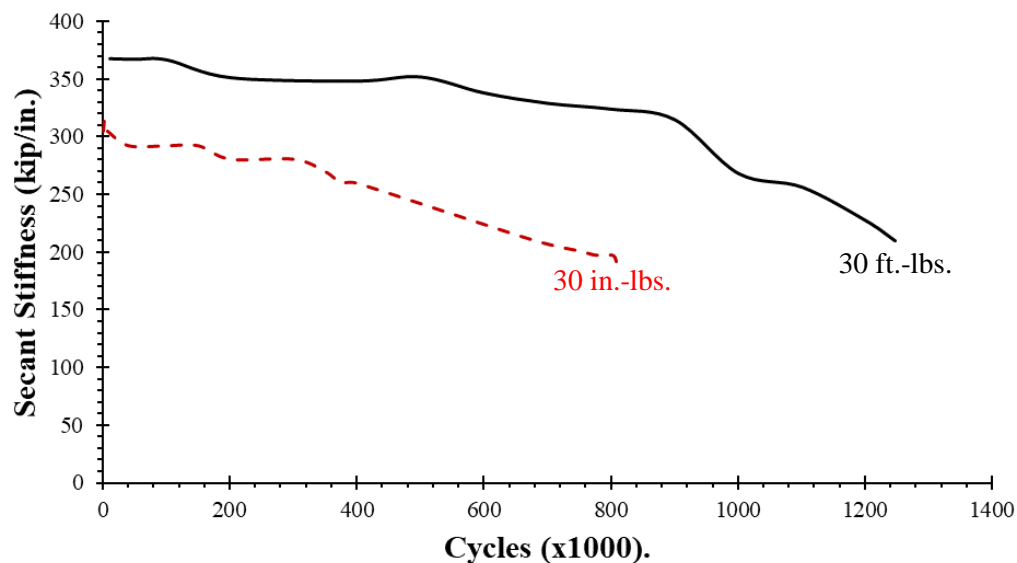


Figure 4.24: Hysteretic secant stiffness per cycle for 0.375 in. bolts.

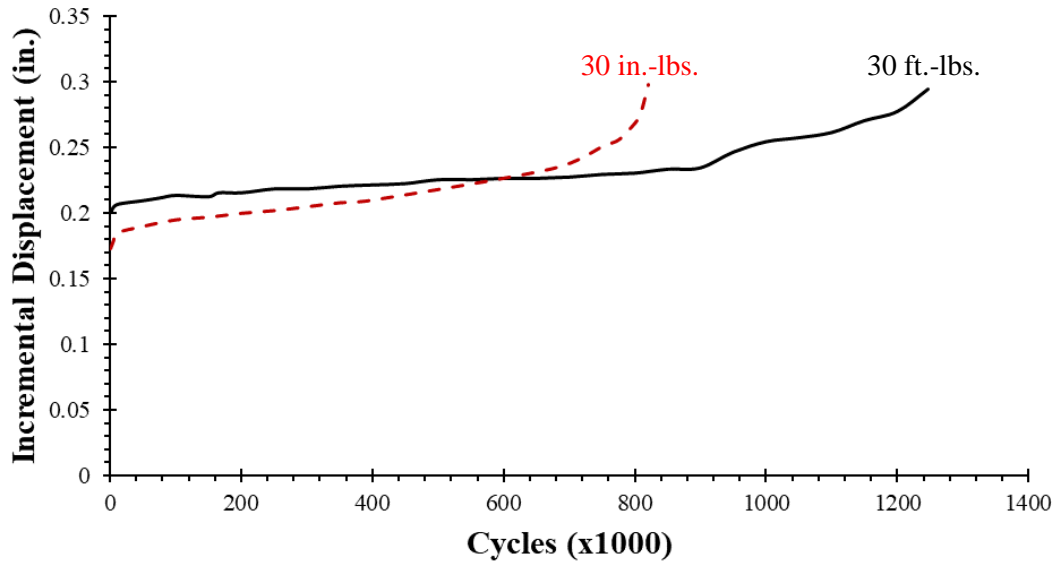


Figure 4.25: Displacement per number of cycles for 0.375 in. bolts.

It is worth mentioning that torque level is also based on the capacity of the bolts. In contrast with 0.5 in. bolts, the 0.375 in. bolts used in this research are not structural bolts and are therefore weaker. As a result, and to accommodate a conservative factor of safety, the upper torque level for 0.375 in. bolts was set at 30 ft.-lbs. For 0.5 in. bolts, the upper torque limit was set at 60 ft.-lbs. based on the bolt stress limit.

Cyclic testing for 0.5 in. was carried out for both 30 ft.-lbs. (to compare directly with 0.375 in. results) and 60 ft.-lbs. (to determine the effect on fatigue behavior). Starting with specimen F2-1, tightened at 30 ft.-lbs., the specimen failed at close to 159000 cycles due to fatigue. Immediately, it can be concluded that fatigue endurance experiences a significant decline going from 0.375 in. to 0.5 in. bolts; the fatigue lifetime for 0.5 in. bolts is approximately 13% that of 0.375 in. bolts. The decision was made therefore to proceed with the higher torque level, 60 ft.-lbs.

Specimens F2-2 was tightened at 60 ft.-lbs., and tested cyclically up to 250000 cycles, which it survived. It was then loaded monotonically to failure at 44.6 kips. Compared to 46.4 kips, the mean for the same 22-bolt MF-FRP connection from Chapter 3, this constitutes a negligible

loss in capacity. This indicates that the failure envelope will be close to a plateau up to 250000 cycles.

It was decided that specimen F2-3 would be tested all the way to fatigue failure, which occurred at 454000 cycles. The failure modes for 0.5 in. bolts were identical to those of 0.375 in. bolts. With such a short fatigue lifetime compared to 0.375 in. bolts, the results of F2-2 and F2-3 were deemed sufficient to form the failure envelope in Figure 4.26 for 0.5 in. bolts.

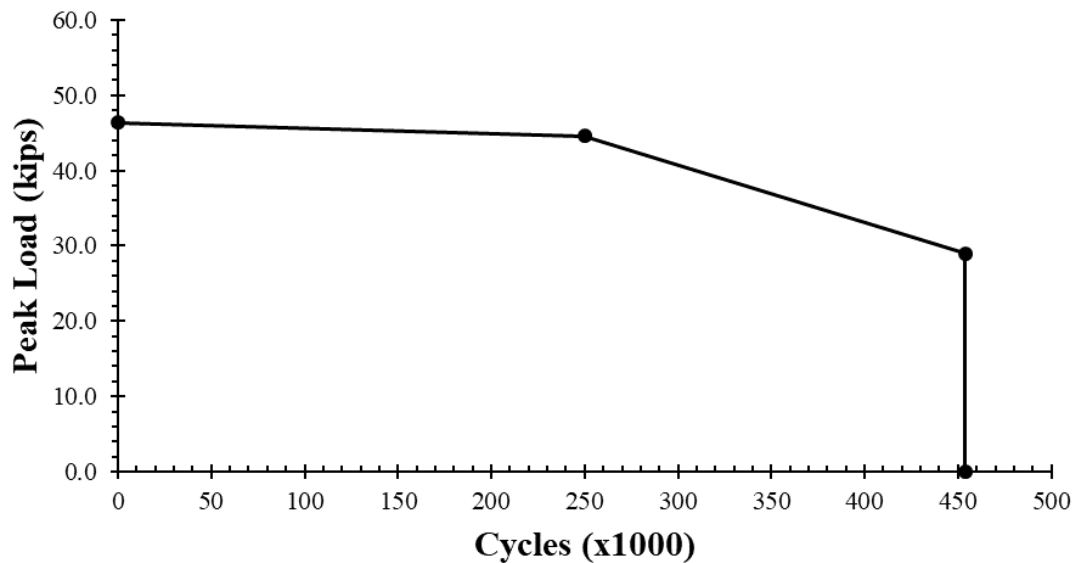


Figure 4.26: Fatigue failure envelope for 0.5 in. bolts at 60 ft.-lbs. of torque.

Figure 4.27 displays the load-displacement plot, highlighting the hysteretic behavior of 0.5 in. diameter bolts at 60 ft.-lbs. of torque. From this plot, the secant stiffness degradation per number of cycles can be obtained, and is shown in Figure 4.28.

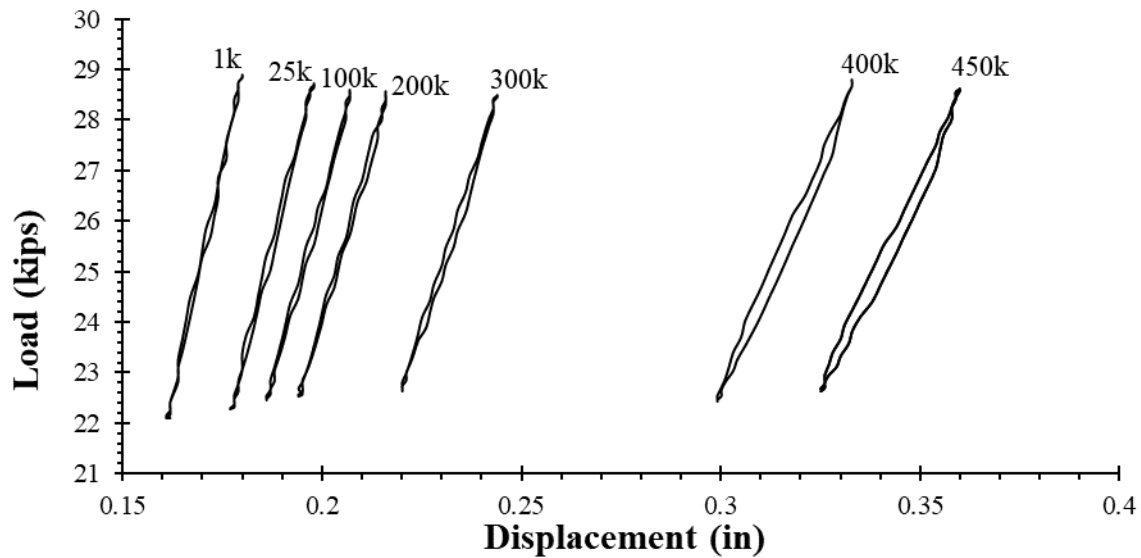


Figure 4.27: Hysteretic load-displacement plot for 0.5 in. bolts at 60 ft.-lbs. of torque.

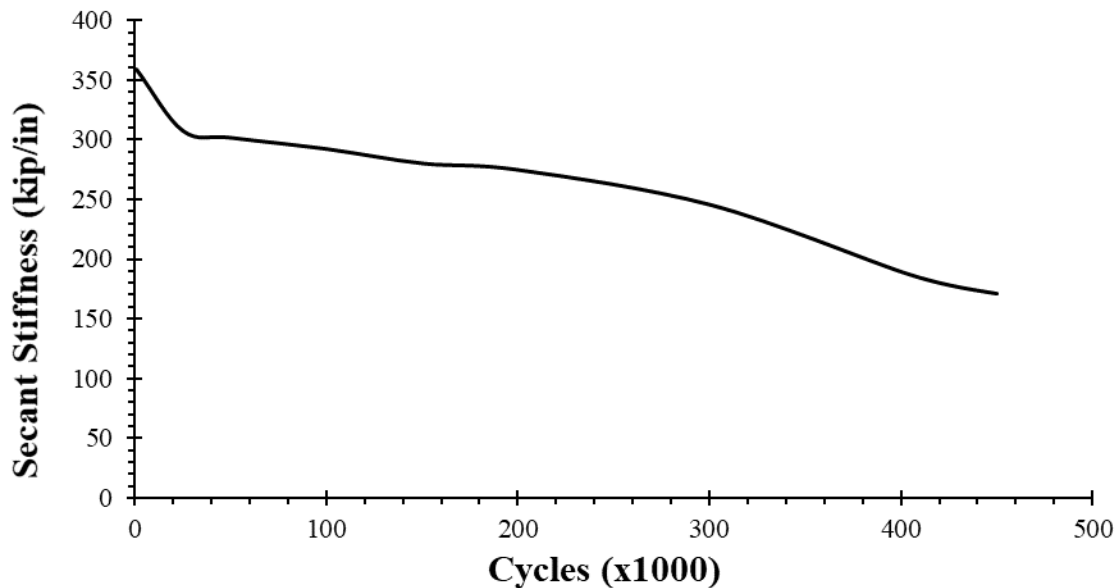


Figure 4.28: Hysteretic secant stiffness per cycle for 0.5 in. bolts at 60 ft.-lbs. of torque.

The incremental displacement per number of cycles for 0.5 in. bolts is shown in Figure 4.29. Damage accumulation can again be seen to slowly and steadily increase up to nearly 300,000 cycles, at 0.24 in., after which it grows rapidly up to failure. Similar to 0.375 in. bolts, a design recommendation for 0.5 in. bolts is to periodically monitor installed retrofits, and if measured incremental displacements exceed 0.24 in., the FRP plate should be replaced.

It is clear from comparing the results that the 0.5 in. bolt diameter connections have a shorter fatigue life compared to that of the 0.375 in. bolt diameter connections. Nonetheless, the 0.5 in. bolts are recommended as they are the smallest diameter structural bolt currently specified by the NCDOT, and the expected service life of the retrofit can be calculated according to the tested fatigue life of the bolted connection, as is illustrated in the next Section.

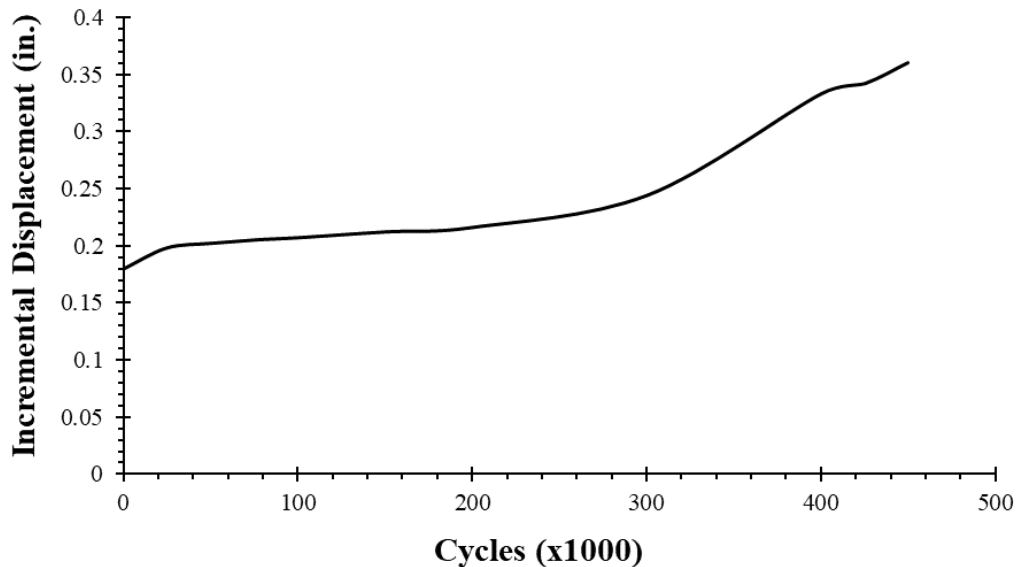


Figure 4.29: Displacement per number of cycles for 0.5 in. bolts at 60 ft.-lbs. of torque.

The retrofits expected service life depends on the traffic patterns of the bridge considered. Using average daily traffic (ADT) data, a breakdown of the number of vehicles per type can be extracted. Each vehicle corresponds to a certain stress range imposed on the retrofit, starting from the 22 kips lower limit (or whatever the designer has selected as the post-tensioning force), and increasing by the stress imposed by the live-load moment from that vehicle. With a full failure envelope curve, the cumulative fatigue damage could be estimated using appropriate laws for fatigue crack growth. The failure envelopes developed in this study, are limited in that they only consider a range of 22 to 29 kips. In reality, for lower stress ranges and peak load, the envelope continues, such that the fatigue lifetime increases. More experimental work needs to be conducted

at lower stress ranges and peak loads to obtain the full S-N curves, and to find the maximum possible fatigue limit.

It is worth noting however that the stress range considered is conservative, as it neglects load distribution and is multiplied by a factor of 1.1. A procedure is proposed in the next section which calculates the number of cycles the retrofit will experience based on ADT data. It assumes that all detoured vehicles will impose the stress range used on the retrofit, which is again, conservative. The cumulative damage incurred due to the traffic considered is likely over-estimated by this procedure.

4.2.3 – Case Study

A wealth of traffic data for North Carolina bridges can be found in NCDOT AADT Web Map Application (n.d.). Bridge 810003 located in Sampson County, NC, was chosen for this example because it was repaired with the proposed prestressed MF-FRP system as part of this project. Details of the bridge and the repair may be found in Chapter 8. The bridge was load-posted at 16 tons for a single vehicle (SV) and 22 tons for a truck tractor semi-trailer (TTST), and was closed in May 2020 after the biannual inspection. The proposed prestressed MF-FRP system was installed with the aim of reopening the bridge to extend its service life until superstructure replacement can be scheduled. Of relevance to this example, the website provides the Annual Average Daily Traffic (AADT) for the selected bridge, including the percent of AADT that are Single Unit trucks (SU_{PCT}) and the percent of AADT that are Multi Unit trucks (MU_{PCT}). This information is provided by the NCDOT Traffic Survey Unit and can be used for calculating the expected fatigue life of the proposed prestressed MF-FRP repair system installed on the selected bridge. Unfortunately, Bridge 810003 is located on a local functional class road that does not include SU_{PCT} and MU_{PCT} data. So, for the purposes of this example, the SU_{PCT} and MU_{PCT} data from NCDOT AADT Station: 082000123, located on NC Hwy 24 approximately 3.5 miles from

Bridge 810003, will be used. In the following example, the $AADT_{2020}$ for Bridge 810003 is 900 vehicles/day, and from NCDOT AADT Station: 082000123 the SU_{PCT} and MU_{PCT} is 5% and 9%, respectively. Therefore, the estimated annual average daily Single Unit trucks (SU_{AADT}) and estimated annual average daily Multi Unit trucks (MU_{AADT}) is given by:

$$SU_{AADT} = 5\% \times AADT_{2020} \quad (4.15)$$

$$MU_{AADT} = 9\% \times AADT_{2020} \quad (4.16)$$

Such that the estimated annual average daily total trucks (AADTT) for Bridge 810003 according to 2020 data is:

$$AADTT_{2020} = 14\% \times 900 = 126 \text{ vehicles/day} \quad (4.17)$$

$AADTT_{2020}$, in the context of this example, is a measure of the number of fatigue cycles per day experienced by the installed retrofit. For the prestressed MF-FRP repair system applied on Bridge 810003, the fatigue life is estimated to be:

$$\frac{820,000 \text{ cycles}}{(126 \text{ cycles/day})} = 6500 \text{ days} \times \frac{1 \text{ year}}{365 \text{ days}} \approx 17.8 \text{ years (0.375 in. bolts)} \quad (4.18)$$

$$\frac{454,000 \text{ cycles}}{(126 \text{ cycles/day})} = 3600 \text{ days} \times \frac{1 \text{ year}}{365 \text{ days}} \approx 9.8 \text{ years (0.5 in. bolts)} \quad (4.19)$$

Conversely, for a target service life of the retrofit, the corresponding number of cycles can be calculated. Assuming a target service life of five years, the retrofit in this example would be subjected to

$$\left(5 \text{ years} \times \frac{365 \text{ days}}{1 \text{ year}}\right) \times 126 \frac{\text{cycles}}{\text{day}} = 229,950 \text{ cycles} \quad (4.20)$$

Based on the experimentally obtained failure envelopes, at 229950 cycles the residual capacity is approximately 46.5 kips and 44.6 kips for 0.375 and 0.5 in. bolts, respectively. This indicates that for the bridge considered and the assumed service life of the retrofit, both bolt sizes are satisfactory. In the same manner, the expected service life in cycles of the retrofit can be

calculated and evaluated by the failure envelopes in Figure 4.21 and Figure 4.24 to determine residual capacity, and by extension, the expected losses in capacity from fatigue for any other bridge.

4.2.4 – Observations

The results of the fatigue experiments can be summarized as follows:

- The behavior of MF-FRP under cyclic loading is highly sensitive to torque and bolt size.
- For the bolts used in this study, and for the same level of torque, 0.375 in. bolts outperform 0.5 in. bolts under cyclic loading.
- Damage accumulates with each cycle through the slow and steady spread of longitudinal shear cracks.
- Periodic measurements of displacement (as a result of plate elongation and bolt bearing) can be used to assess fatigue damage. It is recommended that FRP plates be replaced for installed retrofits when displacements exceed 0.23 in. and 0.24 in. for 0.375 in. bolts and 0.5 in. bolts, respectively.

4.3 – Assessment of Long-Term Performance by Bridge Inspection

The assessment of the long-term performance (including sustained loading and fatigue) of the installed MF-FRP retrofit system is in the form of displacement limits. These limits can be distinguished based on their time-scales. The sustained loading limit is concerned with displacements during the early-ages phase, when hardly any fatigue damage will have occurred. After this phase, fatigue will be the primary concern for the remainder of the retrofit's service life, based on the stable behavior observed under sustained loading. Using this distinction, and to avoid confusion on how to assess damage from each of sustained loading and fatigue, the following procedure is recommended to measure displacements:

1. Before prestressing, but after tensioning to remove the slack out of the system, create a witness mark by placing a mark (point A) on the concrete stem and a mark (point B) on the FRP plate, 1 ft. from the edge of the FRP connector plate (refer to Figure 4.30). The witness mark (point A) can also serve the dual role of monitoring the level of prestress force in the MF-FRP during the prestressing operation.

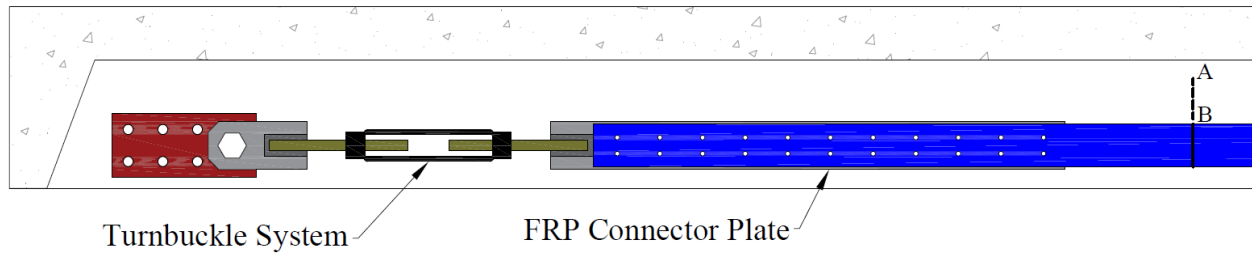


Figure 4.30: Witness mark before prestressing the MF-FRP system.

2. During prestressing of the repair system, the distance between points A and B is the total axial displacement to achieve the desired prestressing force level (ΔL_{TOT}). Upon achieving the desired prestress force level, place a mark (point C) on the MF-FRP aligned with the edge of the FRP connector plate for the creep effect measurement. Figure 4.31 shows the MF-FRP repair system labeling after prestressing.

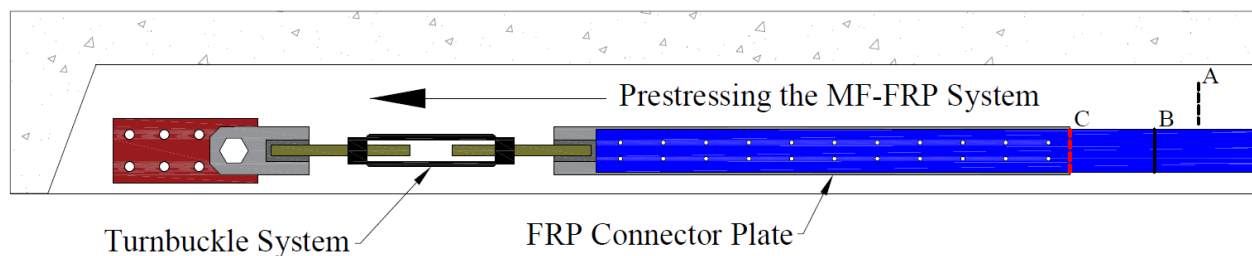


Figure 4.31: MF-FRP repair system labeling after prestressing.

3. Approximately two weeks after the initial prestressing operation, the distance between point C and the edge of the FRP connector plate corresponds to the creep displacement, ΔL_{creep} . If the measured displacement at this point in time (ΔL_{creep}) exceeds 0.15 in. for 0.5 in. bolts (or 0.375 in. for 0.375 in. bolts), then the FRP plate has experienced an excessive

amount of bearing creep deformation and should be replaced. If ΔL_{creep} is within allowable limits, then place a mark (point F) on the MF-FRP plate aligned with the edge of the FRP connector plate as the reference mark for the fatigue effect measurement. Figure 4.32 shows the MF-FRP repair system labeling at this time.

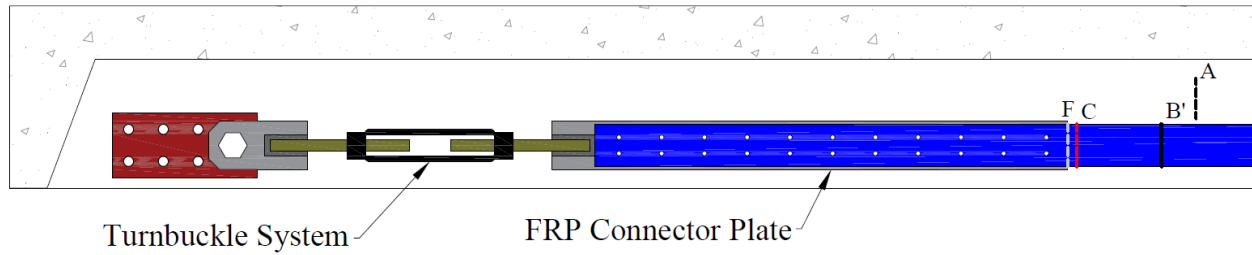


Figure 4.32: MF-FRP repair system labeling 14 days after prestressing.

4. At least as part of the bi-annual bridge inspection, measure the distance between point F and the edge of the FRP connector plate. This measurement corresponds to the fatigue displacement, $\Delta L_{fatigue}$. Figure 4.33 shows the MF-FRP repair system labeling condition during the bi-annual bridge inspection. IF $\Delta L_{fatigue}$ exceeds 0.25 in. (for either bolt size), then the FRP plate is approaching the end of its fatigue life and should be replaced.

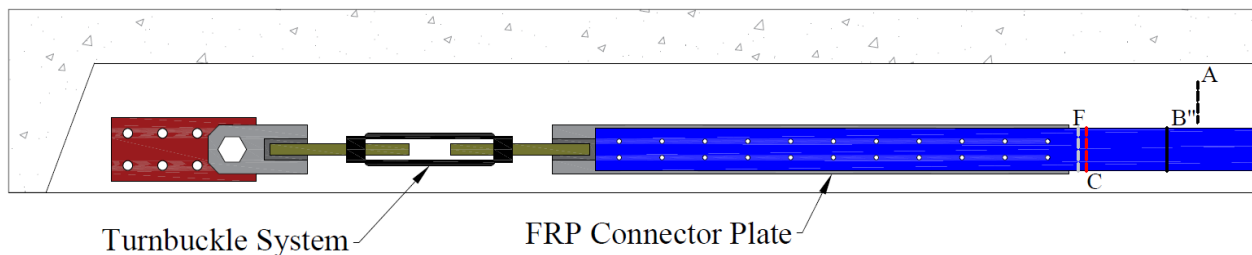


Figure 4.33: MF-FRP repair system labeling condition during the bi-annual bridge inspection.

Measured displacements can be equated to prestress losses in the MF-FRP plates using the measured distance between points A and B'' (see Figure 4.33), following the procedure using Hooke's Law as described in Section 4.1.7.1. For the retrofit used in this study, these losses can be predicted at the design stage, and can be restored by twisting the turnbuckle to stretch the MF-FRP plates to compensate for the lost elongation observed.

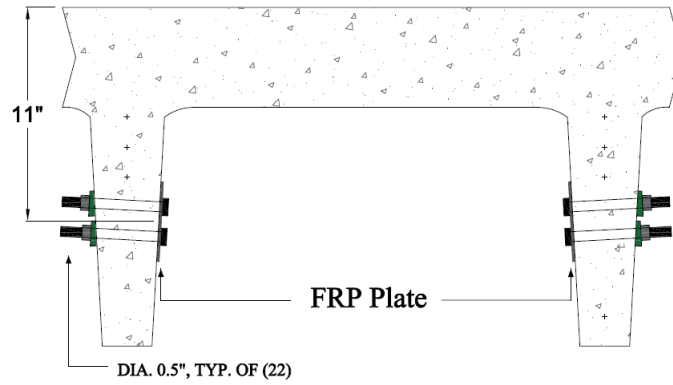
CHAPTER 5 – FULL-SCALE FLEXURAL EXPERIMENTS

This chapter presents design and installation details and full-scale test results for a prestressed mechanically fastened fiber reinforced polymer (MF-FRP) retrofit solution that restores the original operating and inventory rating of prestressed concrete C-channel and cored slab bridge superstructures with prestress losses due to concrete deterioration and steel corrosion. A retrofit solution that can be installed rapidly and immediately restores prestress losses is desired to minimize impacts on commerce, public transportation, and emergency services. The behavior of beams strengthened with the proposed MF-FRP retrofit are presented for damaged (deteriorated) and undamaged C-channel sections and are useful for the ongoing development of a field-ready MF-FRP retrofit solution for DOTs to address prestress loss in deteriorated C-channel beams. Two experimental programs are presented in this report using previously in-service C-channel beams and cored slabs. Six 30 ft. long C-channel beams and five 40 ft. long cored slabs were tested in three-point bending and four-point bending to failure, respectively. The MF-FRP retrofit solution examined in this study was post-tensioned to restore prestress losses and satisfy both inventory and operating rating requirements. The test results are then presented and discussed in the context of the AASHTO load limits of concern.

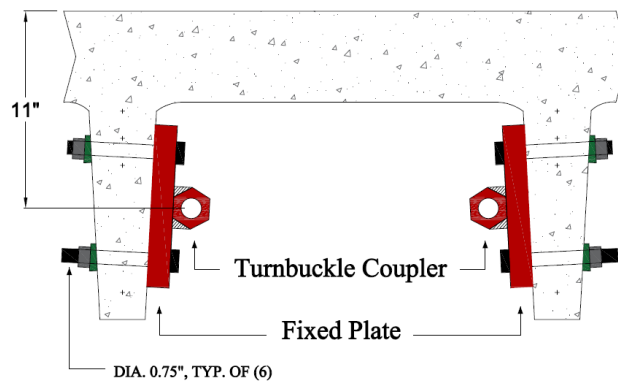
5.1 – MF-FRP Retrofit Design

5.1.1 – MF-FRP 1.0

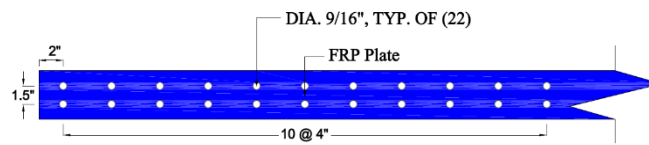
Chapter 3 presented a 22-bolt anchor pattern, indicated in Figure 5.1(c and d), using 0.5 in. diameter bolts arranged in two aligned 11-bolt rows with 1.5 in. transverse spacing between rows. This pattern was proven sufficient to develop approximately 90% of the full capacity of the FRP plate with holes and is sufficiently optimized with respect to the number of bolts and peak bearing stresses in the FRP plate. The capacity of the 22-bolt anchor pattern presented in Chapter 3 is 46.4 kips.



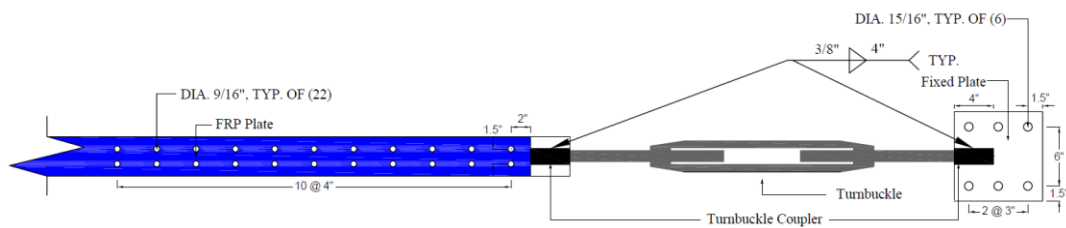
(a) Dead-end cross-section detail



(b) Live-end cross-section detail



(c) Dead-end elevation detail



(d) Live-end elevation detail

Figure 5.1: MF-FRP 1.0 design details.

The initial MF-FRP retrofit design (MF-FRP 1.0) indicated in Figure 5.1 and Figure 4.2 incorporates the 22-bolt anchor pattern by attaching the FRP plate directly to the concrete on the interior of each C-channel stem at one end (dead-end) (Figure 5.1(a and c) and Figure 5.2(a)). The MF-FRP retrofit was attached to the interior only because adjacent beams in the field prevent access to the stem exteriors. The FRP plate was attached to a steel connector plate at the opposite end (live-end) (Figure 5.1(b and d) and Figure 5.2(b)) using the same 22-bolt anchor pattern. The steel connector plate at the live-end was joined to a steel fixed plate through a welded coupler and turnbuckle system (Figure 5.1(b)), and the fixed plate was connected to the interior of the C-channel stem through six 0.75 in. diameter bolts (Figure 5.1(b)). All components of the MF-FRP 1.0 connection were designed in accordance with AISC design guidelines (AISC, 2017) such that the design strength exceeds the 46.4 kips capacity of the 22-bolt FRP connection. Hence, the connection between the FRP plate and steel connector plate is the controlling design element.

MF-FRP 1.0 required 28 holes drilled per stem for the 22-bolt FRP connection at the dead-end, and the six-bolt steel connection at the live-end. A pachometer (rebar detector) was used to locate the high-strength (HS) strands and shear reinforcement prior to drilling, and the placement of the MF-FRP system was adjusted to avoid the HS strands and shear reinforcement in the C-channel stems. All holes were drilled using a commercially available hammer drill. A portable dust collection system with a snorkel attachment in accordance with Occupational Safety and Health Administration (OSHA, 2018) requirements was used to mitigate the effects of respirable crystalline silica dust during drilling operations. Although care was taken to minimize spalling due to drilling, moderate concrete spalling occurred at each hole during drilling. This spalling was repaired at the dead-end with high-strength grout to create a flat surface for the 22-bolt FRP-to-concrete connection (Figure 5.2(a)). At the live-end, the spalling was not repaired because it was

determined that sufficient concrete remained at each hole to give the required bearing surface area at each bolt, and the spalled surface did not impact the installation of the steel base plate. All bolts in steel-to-concrete bolted connections extended through the entire stem thickness. Wedge washers were used to provide even force distribution against the tapered side of the C-channel stems (Figure 5.1(a and b)).

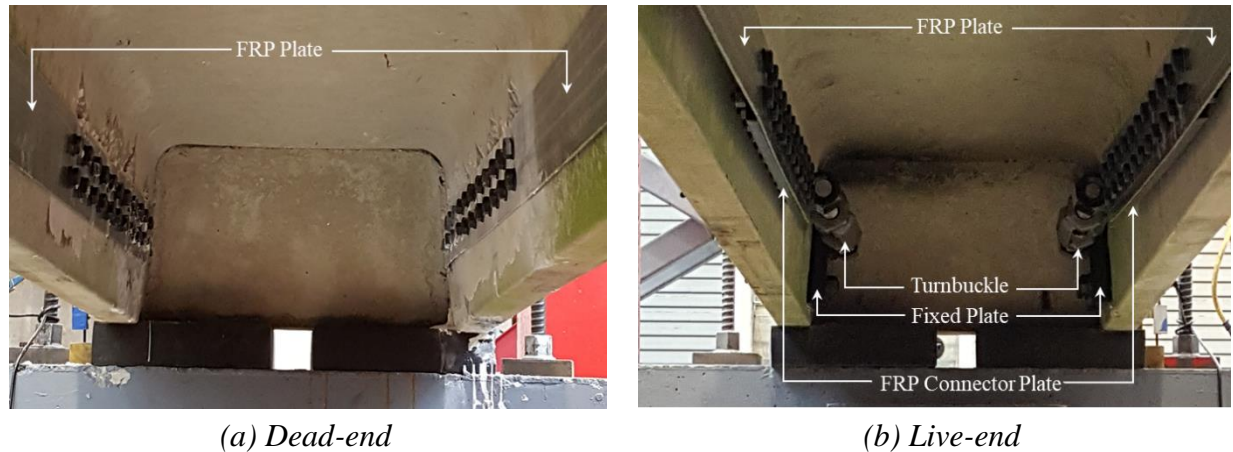
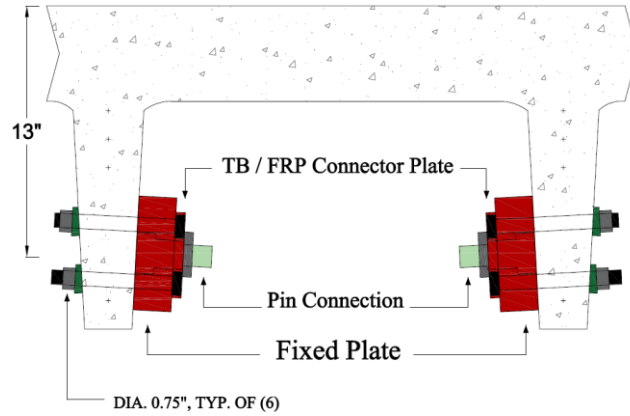


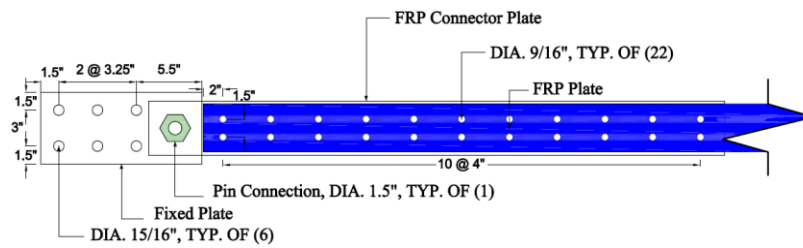
Figure 5.2: MF-FRP 1.0 connection photos.

5.1.2 – MF-FRP 2.0

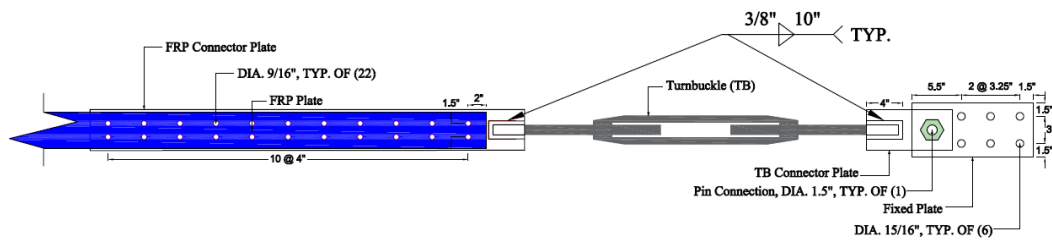
The performance of MF-FRP 1.0 presented the following two critical observations, which are subsequently discussed in greater detail: (1) drilling 28 holes in each stem of the C-channel beam was time and labor intensive, and (2) the 22-bolt dead-end connection created a fixity that resulted in an in-plane moment about the strong-axis of the FRP plate as the beam deflected. This developed transverse stresses in the FRP plate along the bolted connection and reduced the capacity of the MF-FRP system. Therefore, a second MF-FRP retrofit design (MF-FRP 2.0) was developed to reduce field drilling requirements and to allow the FRP plate to remain in uniaxial tension throughout the test. Holes were drilled using the procedures described previously. Details of MF-FRP 2.0 are presented in Figure 5.3 and Figure 5.4.



(a) Dead- and live-end cross-section detail

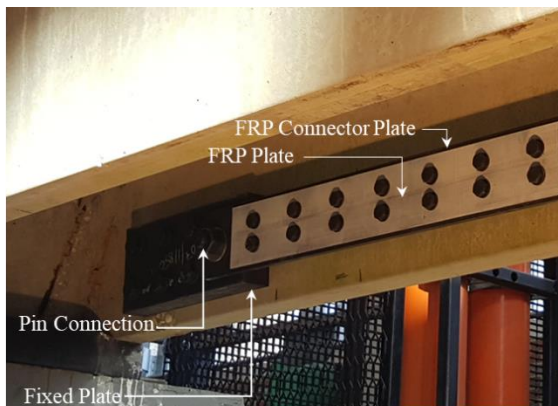


(b) Dead-end elevation detail

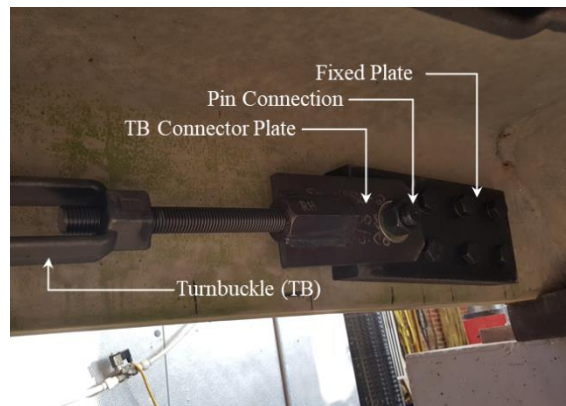


(c) Live-end elevation detail

Figure 5.3: MF-FRP 2.0 design details.



(a) Dead-end



(b) Live-end

Figure 5.4: MF-FRP 2.0 connection photos.

MF-FRP 2.0 used a fixed plate connection at each end of the C-channel beam to transfer the forces between the MF-FRP system and the beam. Forces were transferred through six 0.75 in. diameter bolts at each end of the C-channel beam (Figure 5.3 and Figure 5.4), similar to the live-end of MF-FRP 1.0. The transverse spacing between the fixed plate bolts was reduced to 3.0 in. (Figure 5.3) to optimize the design with respect to concrete splitting behavior and to reduce the weight of the 2 in. fixed plate such that one worker can lift the plate into place during installation. The fixed plate was connected to an FRP connector plate at the dead-end (Figure 5.4(a)) and a turnbuckle (TB) connector plate at the live-end (Figure 5.4(b)) through a pin connection to allow rotation and prevent internal moment in the FRP plate as the beam deflected under applied loads. The TB connector plate connected to the turnbuckle and FRP connector plates at the live-end through a welded connection (Figure 5.3(c) and Figure 5.4(b)) configured such that the centerline of the turnbuckle and connector plates were aligned to minimize internal moment due to eccentricity. Additionally, the effective depth of the FRP centroid from the top compression surface of the C-channel was 11 in. in MF-FRP 1.0 (Figure 5.1(a and b)) and 13 in. in MF-FRP 2.0 (Figure 5.3(a)). This 18% increase in effective depth increased the effectiveness of the FRP, reducing the FRP tensile force required for the same level of strengthening compared with MF-FRP 1.0.

MF-FRP 2.0 was optimized in accordance with AISC (2017) design guidelines with a design strength of 50 kips for the steel connection components—11% greater than the ultimate strength of the FRP plate in uniaxial tension. Therefore, similar to MF-FRP 1.0, the controlling limit state of MF-FRP 2.0 is the connection between the FRP plate and the steel connector plate.

Factors other than design strength influence the thickness of the fixed plate in both connection designs. The thickness of the fixed plate for MF-FRP 1.0 was 1.25 in. to provide

clearance between the concrete stem and turnbuckle such that the body of the turnbuckle could be rotated. The thickness of the fixed plate for MF-FRP 2.0 was controlled by the shoulder length (1.5 in.) and head thickness (1 in.) of the commercially available shoulder bolt that was used as the pin connection in Figure 5.3 and Figure 5.4. A custom turnbuckle or pin connection could be designed to further reduce the thickness of the fixed plate.

5.1.3 – Concrete Splitting

Design guides that model concrete splitting behavior due to mechanical fasteners can be used to check the capacity of the concrete at each bolt. Equation 5.1 is a model presented by Oehlers and Bradford (1995) that determines the minimum concrete splitting force for shear studs and bolted connections in composite steel and concrete elements, for which the length of the fastener is greater than $1.8d_{bolt}$:

$$P_{split} \approx 7\pi c d_{bolt} f_t \left(1 - \frac{d_{bolt}}{2c}\right)^{-2} \quad (5.1)$$

where P_{split} = minimum force at which splitting occurs; d_{bolt} = diameter of the bolt; c = concrete cover to the side of the bolt; and f_t = splitting tensile strength of the concrete in the strengthened member. Using 0.5 in. diameter bolts, a minimum concrete cover of 0.75 in., and concrete splitting tensile strength of 425 psi, P_{split} for a typical C-channel section with the retrofit installed is 7.9 kips per bolt at the dead-end of MF-FRP 1.0. Assuming a uniform distribution of force in the FRP plate at ultimate load conditions, the maximum force per bolt is 2.3 kips, which is below the splitting force. Therefore, force transfer between the FRP plate and the concrete substrate at the dead-end of MF-FRP 1.0 will not result in concrete splitting.

Using Equation 5.1 to check concrete splitting at the live-end of MF-FRP 1.0, the minimum P_{split} is 19.7 kips per bolt, and the maximum force per bolt—assuming uniform distribution at

ultimate load conditions - is 8.3 kips per bolt. Therefore, the bearing force at the bolts on the live-end of MF-FRP 1.0 and both ends of MF-FRP 2.0 will not result in concrete splitting.

The 3 in. transverse spacing and 3.25 in. longitudinal spacing of bolts at the dead- and live-ends of MF-FRP 2.0 (Figure 5.3) are designed using the followings:

$$s_L \geq 1.4b_{eff} \quad (5.2)$$

and

$$s_T \geq b_{eff} \quad (5.3)$$

where s_L = center-to-center longitudinal spacing of bolts; s_T = edge-to-edge transverse spacing of bolts; and b_{eff} = effective width of the connection. The calculated connection width was 2.25 in. (center-to-center spacing minus d_{bolt}) such that the minimum s_L was 3.15 in. and the minimum s_T was 2.25 in. according to Equations 5.2 and 5.3. For convenience of design and installation, s_L was rounded up to 3.25 in.

5.1.4 – Post-Tensioning

Restoration of prestress losses due to deterioration of the C-channel beam was achieved through post-tensioning of the FRP plate. The post-tensioning was delivered through the turnbuckle system at the live-end of the MF-FRP system (Figure 5.1(d) and Figure 5.3(c)). To simulate field applications, the applied prestressing force in each FRP plate was determined through an application of Hooke's Law using as follow:

$$P_{FRP} = \frac{(\Delta L_p)(A_{FRP})(E_{FRP})}{L_g} \quad (5.4)$$

and

$$\Delta L_{TOT} = \Delta L_p + \Delta L_{slip} \quad (5.5)$$

where ΔL_p = change in length of the FRP plate due to the applied prestress force; L_g = gauge length over which ΔL_p is measured; A_{FRP} = cross-sectional area of the FRP; E_{FRP} = elastic

modulus of the FRP; P_{FRP} = prestress force in the FRP; ΔL_{slip} = axial displacement of the FRP plate to account for bolt slip in the connections; and ΔL_{TOT} = total axial displacement required to achieve the desired P_{FRP} . For the FRP plate used in this study, A_{FRP} was 0.5 in.², E_{FRP} was provided by the manufacturer as 9.02×10^6 psi, and the design strength was 92,900 psi (Strongwell, 2016). During post-tensioning, the MF-FRP system remains within 41% of the 46.4 kip capacity of the MF-FRP connection and is well within the elastic limit. Therefore, Hooke's Law is an appropriate application at prestress load levels based on the linear behavior of the MF-FRP shown in Chapter 3.

Prior to post-tensioning, an indicator was affixed to the FRP, and a mark was placed on the interior of the stem near the live-end. A second mark was placed on the stem at the desired ΔL_{TOT} distance from the first mark (Figure 5.5). The gauge length, L_g , was measured on each test specimen from the midpoint of the 22-bolt anchor zone at the dead-end to the indicator affixed to the FRP plate. The midpoint of the anchor zone was used because the elongation of the FRP plate through the 22-bolt anchor region was assumed to linearly decrease through the anchor region toward the end of the FRP plate. The measured L_g for each MF-FRP 1.0 specimen was 149 in., and the desired P_{FRP} was 18.5 kips to restore P_e for the HS strand that was cut to simulate moderate deterioration. Therefore, using Equation 5.4, the desired ΔL_p was 0.61 in. The effect of a bolt slip between the FRP and steel plate, and the fixed plate and the concrete, was also included. ΔL_{slip} was taken as the difference between the hole and bolt diameters. Therefore, ΔL_{slip} for MF-FRP 1.0 was 0.375 in. Using Equation 5.5, ΔL_{TOT} for the MF-FRP 1.0 specimens was approximately 1 in. The measured L_g for the MF-FRP 2.0 specimens was 200 in., and the desired P_{FRP} remained 18.5 kips. ΔL_{slip} for MF-FRP 2.0 was 0.406 in. and, using Equation 5.4, ΔL_p was 0.958 in. Thus,

ΔL_{TOT} for MF-FRP 2.0 was approximately 1.38 in. The marks for the ΔL_{TOT} measurement for MF-FRP 2.0 are provided in Figure 5.5.

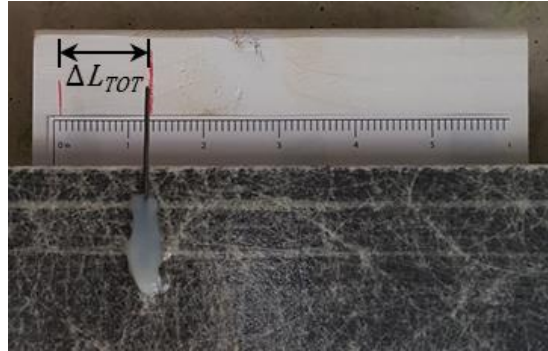


Figure 5.5: ΔL_{TOT} measurement marks for MF-FRP 2.0 at $P_{FRP} = 18.5$ kips.

Throughout the post-tensioning process for all test specimens, FRP strain at midspan was monitored using electric resistance strain gauges. The strain gauge measurement was used to maintain consistency between test specimens and to confirm the application of Hooke's Law to determine PFRP in the field in which strain gauges are not normally practical as a method for measuring the level of applied prestress force. Post-tensioning of the FRP was stopped when the measured strain in the FRP, ϵ_{FRP} , reached 4,100 $\mu\epsilon$, the FRP strain which corresponds to $P_{FRP} = 18.5$ kips, at which point ΔL_{TOT} was confirmed with the marks on the FRP and concrete stem (Figure 5.5).

MF-FRP 1.0 and MF-FRP 2.0 were installed on the side of the C-channel stem between the bottom prestressing strand and the three harped strands to deconflict the bolted connections and the prestressing strands (Figure 5.1 and Figure 5.3). Ideally, the MF-FRP retrofit solution would be installed on the bottom of the section, as is typical of flexural strengthening applications. However, the C-channel stem thickness at the bottom was 2.5 in., and the concrete cover for the bottom strand was 1.5 in. (Figure 5.4). Therefore, it was determined that insufficient concrete cover existed to install the MF-FRP retrofit solution on the bottom of each stem.

For the repair applied on cored slabs, unlike C-channel beams, the repair systems can be installed on the bottom face of the section.

5.2 – Experimental Program – C-Channel Beams

The six C-channel beams tested in this program were removed from North Carolina Bridge 380093, which carries State Route 1156 (SR1156) across Owen Creek in Granville County, North Carolina. All beams selected for testing were interior undamaged girders in serviceable condition. These nominally identical beams allowed for controlling the damage of selected specimens to be implemented in the lab such that the results could be compared across all test specimens. Figure 5.6 provides the cross-section of the 30 ft. long C-channel beams. The beams were prestressed with 7/16 in. diameter HS, stress-relieved strands with an ultimate tension capacity of 270 ksi. The bottom HS strand in each stem was oriented parallel to the bottom of the stem; however, the three HS strands near the mid-height of each stem were harped 3.6 in. at the mid-span.

Two C-channel beams were tested without the MF-FRP retrofit installed, one undamaged (U) and one damaged (D), to determine a control baseline prior to strengthening for each condition. Four C-channel beams were tested with the MF-FRP retrofit installed on the interior face of each stem, two undamaged (MF-FRP-U1 and MF-FRP-U2) and two damaged (MF-FRP-D1 and MF-FRP-D2). Damage was induced in the lab by cutting the bottom prestressing strand in each stem at mid-span (Figure 5.7). The induced damage at mid-span was used to simulate field deterioration with moderate prestress loss at the point of maximum internal moment in the C-channel beam loaded at the mid-span.

Specimens MF-FRP-U1 and MF-FRP-D1 were tested with MF-FRP 1.0, and MF-FRP-U2 and MF-FRP-D2 were tested with MF-FRP 2.0. Table 5.1 presents a summary of the test matrix for the six tested C-channel beams.

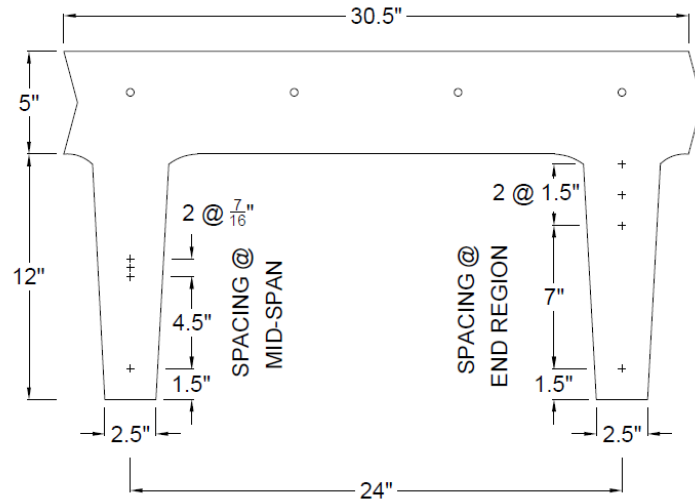


Figure 5.6: C-channel cross-section details. (data from NCDOT, 1966).



(a) cutting bottom strand



(b) damage in both stems at mid-span

Figure 5.7: Damaged C-channel beam.

Table 5.1: Test matrix of C-channel beam flexural test.

Specimen ID	Specimen Description
U	Undamaged Control
D	Damaged (deteriorated) Control
MF-FRP-U1	Undamaged with first version retrofit (MF-FRP 1.0) installed on both stems
MF-FRP-U2	Undamaged with improved retrofit (MF-FRP 2.0) installed on both stems
MF-FRP-D1	Damaged with MF-FRP 1.0 installed on both stems
MF-FRP-D2	Damaged with MF-FRP 2.0 installed on both stems

5.2.1 – Test Setup, Instrumentation, and Procedure

The test setup, indicated in Figure 5.8, was modeled after a previous study that examined the behavior of similar C-channel beams strengthened with EB-FRP (Rosenboom and Rizkalla, 2008). All C-channel beams were loaded in three-point bending with a 220 kip \pm 0.25% capacity load cell and hydraulic actuator mounted on a steel frame at the beam mid-span. The load was applied with a 10 \times 20 in. steel bearing plate in accordance with AASHTO (2017) bearing area requirements for wheel loading. Neoprene bearing pads on concrete blocks were used at the supports to simulate field conditions. The bearing width of each neoprene pad was 7.5 in., creating a span length of 29.4 ft. (Figure 5.8). Prior to testing, all specimens were instrumented with string potentiometers at each quarter-span point and mid-span point of the front stem, and at the mid-span point of the rear stem. Additionally, two linear potentiometers were used to measure vertical displacement due to deformation of the neoprene bearing pads at the supports. Electric resistance strain gauges were attached to all FRP plates at mid-span along the centroidal axis of the FRP plate to measure axial strain throughout the test.

All specimens were tested to failure under displacement-controlled conditions at a rate of 0.25 in. per minute from 0 to 16.0 kips of applied load, after which the rate was increased to 0.5 in. per minute through failure. The 16.0 kips applied load corresponds to an internal moment of 120 kip-ft. at mid-span, which is the live load moment generated by the HS-15 vehicle loading condition, including impact, along a single wheel line for a 30 ft. span length (AASHTO, 2018). The HS-15 is the original operating rating for the C-channel beams examined in this study (North Carolina DOT, 1966), and the HS-15 live load moment assumes that no load transfer occurs between adjacent beams in accordance with the AASHTO (2018) load rating analysis guidelines.

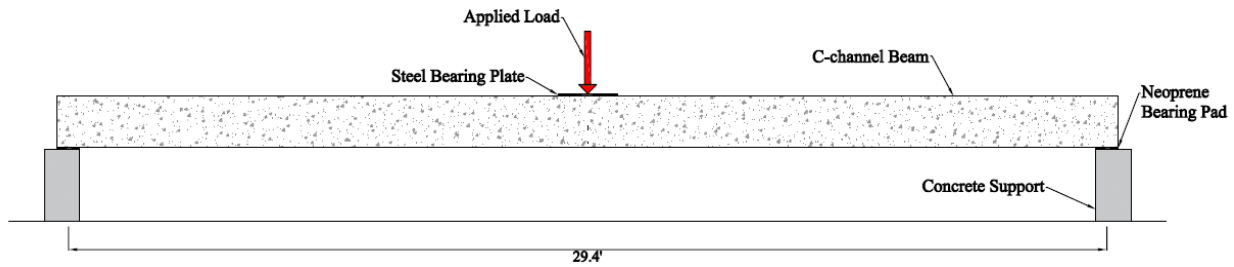


Figure 5.8: Test setup of C-channel beam flexural test.

5.2.2 – Experimental Results

Table 5.2 provides a summary of test results, including ultimate load capacity and failure mode for all C-channel test specimens. Specimen U failed by concrete crushing (CC) at an applied load of 29.6 kips. This ultimate capacity is 185% of the HS-15 internal live load moment and serves as a benchmark for the MF-FRP-D1 and MF-FRP-D2 test specimens.

Specimen D also failed by concrete crushing at an applied load of 18.7 kips. The induced damage to simulate moderate deterioration in the field resulted in a 37% reduction in capacity compared with Specimen U.

MF-FRP-U1 experienced an 18% increase in flexural capacity over U and failed by FRP longitudinal splitting (LS) and rupture (R), followed by concrete crushing. MF-FRP-D1 experienced a 47% increase in flexural capacity over D but failed to reach the full undamaged capacity, achieving 93% of the capacity of Specimen U. MF-FRP-D1 also failed by FRP longitudinal splitting and rupture followed by concrete crushing. Although the MF-FRP 1.0 retrofit system did not restore the full undamaged capacity of the C-channel beam, the system did increase the capacity of the damaged beam such that it exceeded the HS-15 live load by approximately 12 kips—a factor of safety of 1.7; however, Specimen D failed at 3 kips higher than the HS-15 live load—a factor of safety of 1.2.

Table 5.2: C-channel test results summary.

Specimen ID	U	D	MF-FRP-U1	MF-FRP-U2	MF-FRP-D1	MF-FRP-D2
HS-15 Live Load, kips	16.0	16.0	16.0	16.0	16.0	16.0
Ultimate Load, kips	29.6	18.8	35.1	37.3	27.6	26.1
Percent increase from U (%)	--	-36.6	18.1	25.8	-6.85	-12.1
Percent capacity of HS-15 (%)	185	117	219	233	172	163
Maximum measured FRP tensile strain, ($\mu\epsilon$)	--	--	7380	6425	7980	6712
Maximum FRP tensile force ^a kips	--	--	33.2	29.0	36.0	30.3
Failure Mode ^b	CC	CC	LS/R, CC	CC	LS/R, CC	CC

^aObtained from strain gauge and application of Hooke's law.

^bLS = longitudinal splitting; R = rupture; and CC = concrete crushing.

The mid-span load-deflection behavior for all tests is provided in Figure 5.9. Mid-span deflection was determined by averaging the deflection at each stem measured by the two string potentiometers and subtracting the average vertical displacement at the supports measured by the linear potentiometers. The progressive FRP longitudinal splitting and rupture failure of MF-FRP-D1 is visualized in the load-deflection curves (Figure 5.9) with a “stepwise” decrease after ultimate load due to progressive loss in the FRP cross-sectional area. MF-FRP-U1 did not experience incremental FRP rupture but, rather, instantaneous longitudinal splitting and rupture failure just before concrete crushing, which is visualized as an instantaneous drop in load at approximately 7.87 in. of mid-span deflection. The slight drop in load experienced by MF-FRP-D2 at approximately 2 in. of mid-span deflection is likely due slip of the bolted connection between the FRP plate and the FRP connector plate, or the fixed plate and the concrete.

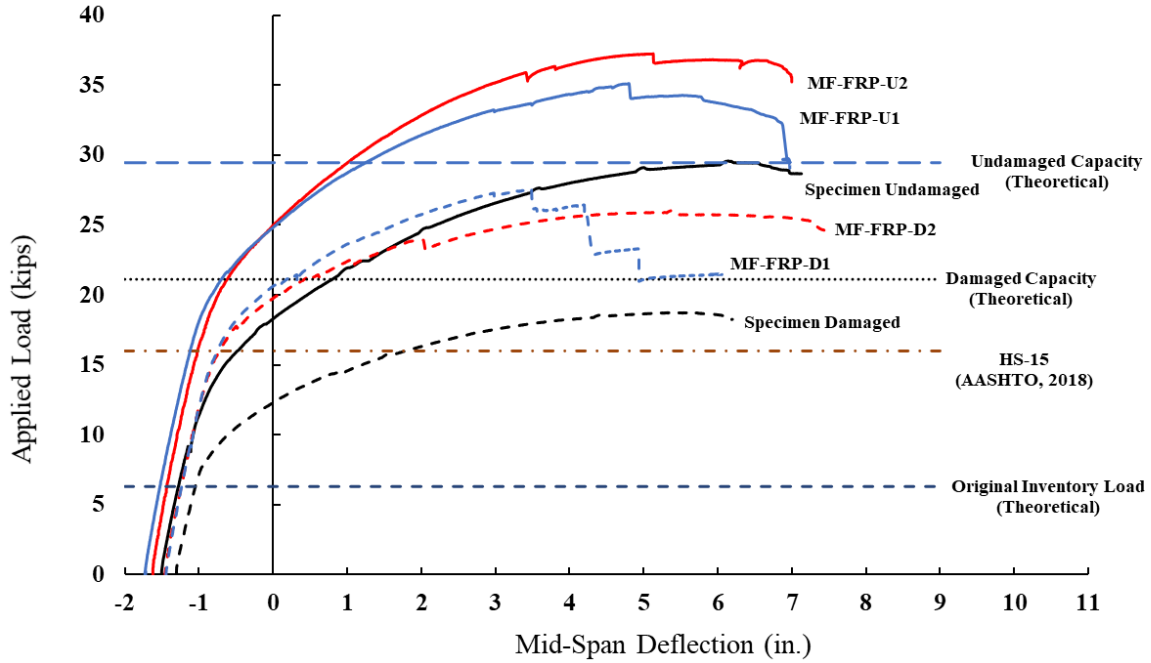


Figure 5.9: Full-scale C-channel beam load-deflection results.

The load-deflection behavior in Figure 5.9 is also compared with the theoretical inventory load, undamaged capacity, and damaged capacity. The theoretical inventory load is determined by calculating the internal moment at which the concrete tensile stress is 0 for an undamaged C-channel beam. Therefore, an internal live load moment, including impact, of 47.3 kips-ft. is considered the inventory load for a candidate bridge in a coastal region (the most conservative inventory load situation), which corresponds to an applied load of 6.3 kips. This is provided in Figure 5.9 and lies well within the elastic region of the load-deflection curves for all test specimens, which indicates that the beam would experience no damage from continued loading over an extended period at this inventory load. The theoretical undamaged nominal moment capacity, $M_{n,undamaged}$, is 221 kips-ft., and the theoretical damaged nominal moment capacity, $M_{n,damaged}$, is 151 kips-ft. which corresponds to an applied load of 29.5 kips and 20.1 kips respectively (Figure 5.9). The maximum applied load for Specimen U is within 1% of the calculated load corresponding to the theoretical undamaged flexural capacity, $M_{n,undamaged}$, and the maximum applied load for

Specimen D is within 6% of the calculated load corresponding to the theoretical damaged flexural capacity, $M_{n,damaged}$ (see Table 5.2 and Figure 5.9).

The applied load that generates the HS-15 live load moment, including impact, (AASHTO, 2018) is also shown in Figure 5.9. For Specimen U, the load-deflection curve intersects with the HS-15 live load just beyond the elastic region at approximately 1 in. of midspan deflection. This indicates that incremental damage may occur at this load, which corresponds to the definition of the operating rating (AASHTO, 2018). Although the maximum load for MF-FRP-D1 is 93% of the maximum load for Specimen U, the load-deflection curve for MF-FRP-D1 intersects with the HS-15 live load at approximately 0.4 in., which is less than 50% of the HS-15 live load deflection for Specimen U and is within the elastic region of the strengthened damaged section. This indicates that the MF-FRP 1.0 system is capable of restoring the HS-15 live load capacity of the beam despite the premature longitudinal splitting failure of the FRP. This led to the development of the MF-FRP 2.0 system described previously, which was designed to prevent the premature FRP failure, enabling the beam to fail by concrete crushing.

During the MF-FRP-U1 and MF-FRP-D1 tests, bending of the FRP plate about its strong axis at the dead-end was observed, as can be seen in Figure 5.10(a). This was due to the fixed condition of the 22-bolt dead-end connection and the side-stem application of the FRP, resulting in the combination of flexural and axial tensile stresses in the FRP, causing longitudinal splitting failure of the FRP plate (Figure 5.10(b and c)). Chapter 3 determined that the capacity of the 22-bolt connection in uniaxial tension is 46.4 kips; however, the FRP plates on MF-FRP-U1 and MF-FRP-D1 ruptured at 33 kips and 36 kips, respectively, well below the expected capacity for the connection. The longitudinal splitting behavior resulted from the shear failure of the transverse glass fibers in the FRP plate and is discussed in detail in Chapter 3. To reduce this increased stress

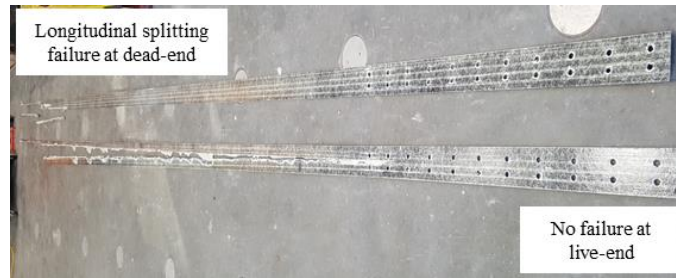
due to flexure in the FRP plate, the MF-FRP 2.0 connection design used a pin connection (Figure 5.3 and Figure 5.4) to allow rotation at each end of the C-channel such that the FRP plate remained in uniaxial tension throughout the loading of the C-channel, eliminating the development of flexural stresses in the FRP. This prevents longitudinal splitting rupture of the FRP and increases the efficiency of the MF-FRP system.



(a) flexural region



(b) longitudinal splitting due to flexure



(c) failed FRP

Figure 5.10: FRP failure mode for MF-FRP 1.0.

MF-FRP-U2 experienced a 26% increase in capacity compared with control Specimen U, and the ultimate load capacity for MF-FRP-D2 was 88% of the capacity for control Specimen U and 94% of the ultimate capacity of MF-FRP-D1. The reduction in the capacity of MF-FRP-D2 compared with MF-FRP-D1 was due to the greater reduction in the effective depth of the MF-FRP as the beam deflects under increasing applied load and the lack of moment developed in the FRP plate. The reduced effective depth of the MF-FRP is discussed subsequently. Although the capacity of MF-FRP-D2 was less than MF-FRP-D1, the MF-FRP 2.0 system increased the damaged

stiffness and capacity of the C-channel such that the HS-15 operating load was within the elastic region of the load-deflection curve; therefore, the MF-FRP 2.0 system restored both the inventory and operating ratings of the damaged C-channel to pre-damaged levels, enabling posted load restrictions and detours to be removed.

Both MF-FRP-U2 and MF-FRP-D2 failed by concrete crushing only. The FRP in MF-FRP-U2 and MF-FRP-D2 did not experience longitudinal splitting or rupture, as in MF-FRP-U1 and MF-FRP-D1. Consequently, a more ductile failure of MF-FRP-D2 was observed compared with that of MF-FRP-D1. This ductile failure of the MF-FRP 2.0 system design, visualized in the extended load plateau of MF-FRP-D2, is similar to that of Specimen U and is a more desirable failure than the brittle failure of MF-FRP-D1. Additionally, the FRP in MF-FRP 2.0 achieved a maximum tensile force of 29.0 kips and 30.3 kips for MF-FRP-U2 and MF-FRP-D2, respectively, leaving an FRP reserve capacity of approximately 15 kips for the MF-FRP 2.0 system, or 33% of the 46.4 kips capacity. This reserve capacity in the FRP allows for a higher prestress force to be applied if necessary, up to 22 kips based on the behavior presented by Chapter 3, to achieve restoration of inventory and operating ratings of the deteriorated C-channel.

The MF-FRP 1.0 and MF-FRP 2.0 systems experienced some minor local concrete splitting near the fixed plate connection. The local splitting occurred in line with the bottom prestressing strand in the stem and was due to the reduced concrete cover at the location of the prestressing strand. In all cases, the local splitting allowed for the prestressing strand to debond from the concrete but did not impact the overall performance of the MF-FRP retrofit solution. The debonding of the bottom prestressing strand is not of concern because the purpose of the MF-FRP retrofit solution is to restore the prestressing effects that would be lost due to deterioration in the

field. In many field cases, the bottom prestressing strand is not present, and the concrete section is restored with a plain concrete patch.

5.3 – Experimental Program – Cored Slabs

Five 40 ft.-long hollow-core beams were obtained from Bridge No. 090014 in Brunswick County, NC. This bridge was built in 1972 and replaced in late 2018. All five beams were in a similar condition from visual inspection, with no degradation beyond some concrete spalling at the ends. This allowed for controlled levels of damage to be applied on the beams in the lab, and for results to be compared across all specimens. The specimens were stored in an NCDOT yard and transported to the Constructed Facilities Laboratory (CFL) one at a time for each test (Figure 5.11).



Figure 5.11: Specimens delivered to the lab.

The cross-section depicted in Figure 5.12 shows dimensions, as well as the location of the cores and prestressing strands. This information is important, because it dictated where the retrofit could be anchored across the width of the section. The 6 in. spacing between the bottom prestressing strands below the cores is the best location to anchor the fixed steel plate components of the retrofit, to minimize chances of hitting steel during drilling. As such, two MF-FRP systems could be applied on each beam. Flexural reinforcement consisted solely of 7/16 in. diameter 7-

wire low-relaxation prestressing strands with an ultimate tensile stress of 270 ksi. According to bridge documents, each strand was initially jacked at 21.7 kips.

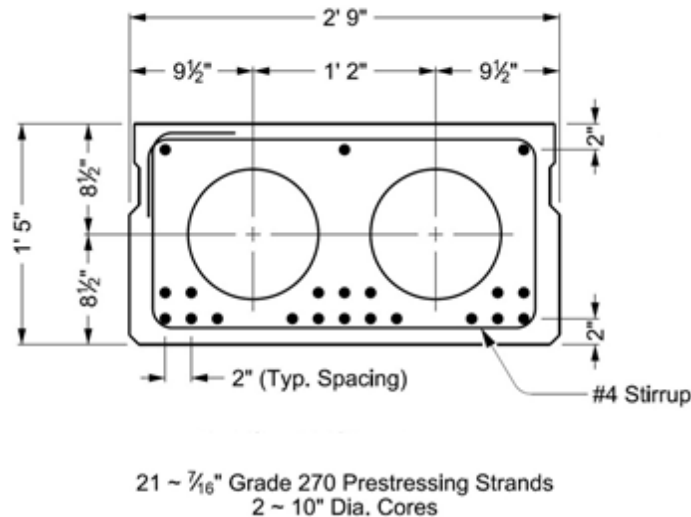


Figure 5.12: Specimens cross-section.

5.3.1 – Test Setup and Test Matrix

A four-point bending setup was followed for this experimental program (Figure 5.13). The loading configuration used for the C-channel beams and cored slabs were based on previous experimental program test setups of the same beam shape. This is not expected to affect the behavior of interest. The load was applied with a 220 kip hydraulic actuator mounted on a steel frame at mid-span. A steel spreader beam was used to transfer the load from the actuator to the third points of the beam (13.3 ft. from each end). A pin and a roller were placed at the loading points between the spreader beam and the specimen. The specimens were supported by concrete blocks with neoprene pads. The photos in Figure 5.14 show different views of this setup.

To measure deflections, four strings potentiometers were placed on each specimen: two at midspan (one on each side), and one at each third point. A linear potentiometer was placed at each support to measure vertical displacement of the beam as the neoprene pads deformed. Additional instrumentation was used for the strengthened specimens in the form of electric resistance strain

gauges. One of these was placed concentrically and longitudinally on each FRP plate at mid-span to measure axial strain throughout the experiments. Tests were conducted in displacement-control, with a load rate of 0.25 in./minute.

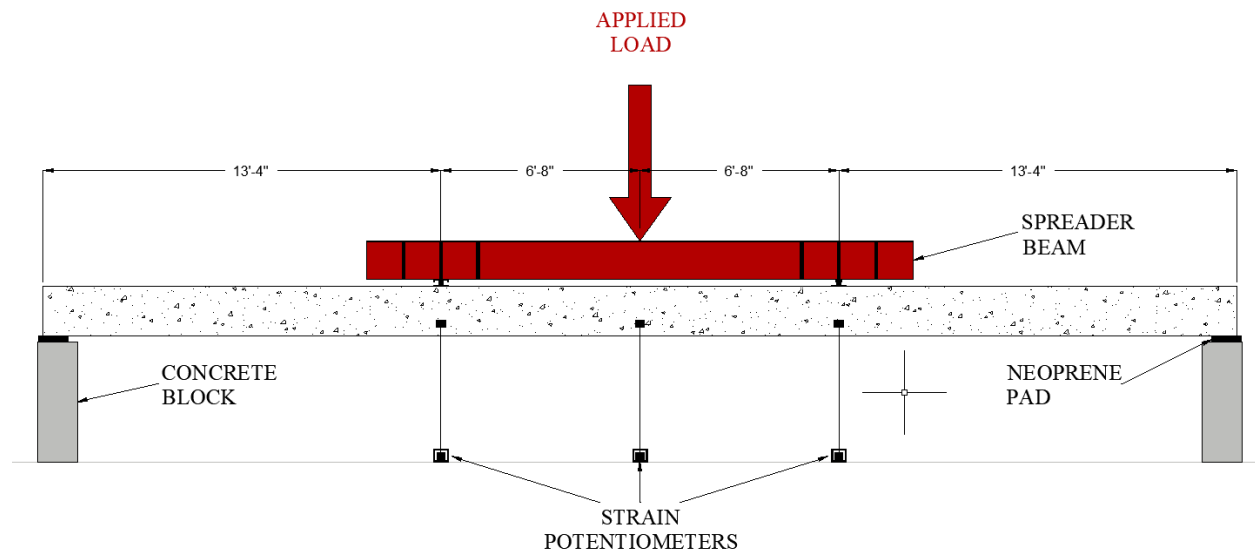


Figure 5.13: Full-scale test setup and instrumentation.



Figure 5.14: Full-scale test setup.

As mentioned previously, five beams were tested in total, following the test matrix in Table 5.3. The first beam was a control specimen (U-U) with no damage applied, serving as a benchmark that dictated the minimum behavior that needed to be reinstated by the retrofit solution, in order to comply with AASHTO load limits. The presence of multiple strands at the bottom prestressing layer allowed for the opportunity to investigate the contribution of the retrofit at different levels of deterioration. For this experimental program, the first level of damage was set at two fully lost prestressing strands, while the second was set at four fully lost prestressing strands. As the MF-FRP retrofit serves to address losses caused by corrosion of prestressing strands, investigation of these two levels of damage was deemed sufficient, and damage beyond four fully lost strands was considered beyond the strengthening expectations for this retrofit. As such, the remaining four beams were divided into two groups based on degradation level. Each level of degradation included one unstrengthened (D-U1 and D-U2) and one strengthened beam (D-S1 and D-S2) in order to quantify the contribution of the retrofit.

Table 5.3: Test matrix of cored slab flexural test.

Specimen ID	Specimen Description
U-U	Undamaged and unstrengthened control
D-U1	Damaged (two strands cut) and unstrengthened
D-S1	Damaged (two strands cut) and strengthened
D-U2	Damaged (four strands cut) and unstrengthened
D-S2	Damaged (four strands cut) and strengthened

5.3.2 – Retrofit Application Procedure

The MF-FRP retrofit was applied on each strengthened specimen prior to instrumentation and after damage was applied. To apply the damage, strands were exposed using a hammer drill on the bottom corner of each side at mid-span and cut (Figure 5.15). The strengthening procedure started with the use of a pachometer to locate the steel reinforcement near the supports. Based on the reinforcement layout uncovered, the anchorage zone of the fixed steel plates was selected, in a

way that prevents contact with steel during the drilling process. Drilling was accomplished with a commercially available hammer drill. Wedge anchors (0.75 in. diameter) were chosen to fasten the steel plates to the beam, and so care was taken not to reach the cores while drilling. This limited the drilling depth to 3.88 in., since the cores were a little over 4 in. away from the bottom face of the beam. After the holes were drilled, the steel plates were attached to the beam with ratchet straps, aligned with the holes drilled. The wedge anchors were then inserted and engaged by hammering them all the way into the drilled holes. With the steel plates in place, the intermediate steel components and turnbuckle were mounted. Two FRP plates were then cut according to the required length, dictated by the placement of the fixed steel plates, and 22-9/16 in. diameter holes were drilled at each end of each plate. The FRP plates were then attached to the intermediate steel plates using 0.5 in. ASTM A325 bolts and tightened at 30 ft.-lbs. The selected torque of 30 ft.-lbs. is different than the recommended 60 ft.-lbs. torque of the long-term fatigue experiment to be consistent with the full-scale experiments conducted on the C-channel beam tests, which was completed before the end of the long-term fatigue experiments. Concrete splitting and ultimate expected force in the FRP plates were the controlling factors in selecting the appropriate wedge anchors, following the procedure detailed by Chapter 5.2.



Figure 5.15: Exposed and cut prestressing strands.

The plates were then post-tensioned by twisting each turnbuckle using wrenches with extender sleeves, in order to bring the rods closer together, thereby stretching the plates. The post-tensioning procedure using a displacement indicator and Hooke's Law was followed exactly and validated through continuous readings from the strain gauges. 22 kips was the target post-tensioning force for these beams, which corresponded to a total elongation of 1.52 in. for each plate. The camber restored for both specimens D-S1 and D-S2 was 0.11 in. per FRP plate, for a total of 0.22 in. Figure 5.16 shows photos of the final MF-FRP retrofit setup before testing. As can be seen, the extra length of the threaded anchor bolts was not cut off prior to installation for convenience. The extra length beyond the nuts does not affect the performance of the system as tested, and in a field application anchors bolts of an appropriate length would be used.

5.3.3 – Experimental Results

Two failure modes were encountered during testing. All unstrengthened specimens in addition to specimen D-S2 failed by concrete crushing (CC), an example of this failure can be seen in Figure 5.17.

The remaining failure mode is concerned with the FRP plates and was observed only with specimen D-S1. Longitudinal shear cracks developed on each side at the bolts furthest from the supports and spread. As the load was monotonically applied on the beam, the 2.5 in. clearance between the plates, which remained horizontal, and the bottom face of the beam was decreasing in proportion to the beam deflection. The eventual contact of the beam with the plates at mid-span (where the deflection was greatest) exerted a point load at the middle of the plates, introducing additional stresses which precipitated their failure. Mid-span beam contact with the top edge of the FRP plate occurred at a total applied load of 66 kips for specimen D-S1, and 62 kips for D-S2. The failure of the FRP came in the form of a combined longitudinal shear (LS) and rupture (R) failure, such that the observed behavior was initiated with rapid spread of longitudinal shear cracks and

splitting on one side of each plate, followed by rupture on the opposite side. Figure 5.18 shows each side of one failed FRP specimen.



Figure 5.16: MF-FRP retrofit applied on PC cored slab.



Figure 5.17: Concrete crushing failure.



Figure 5.18: FRP LS (bottom) and R (top) failures (Specimen D-S1).

For all specimens, no prestressing steel strands ruptured. In fact, these had to be cut manually after each test in order to discard the failed beams in two halves.

The retrofit's concrete-to-fixed steel plate connections behavior was favorable such that the wedge anchors remained firmly in place. The photo in Figure 5.19 shows the anchors embedded in concrete after the strengthened tests were conducted and the fixed steel plates extracted. Beyond minor surface spalling caused by the hammer drilling, no damage can be observed.



Figure 5.19: Condition of wedge anchors after full-scale test.

A summary of the full-scale results is presented in Table 5.4, divided into three portions. The first portion (first five rows) is directly extracted from the experimental data, accompanied by the appropriate failure modes. The percent increase in ultimate capacity relative to the control specimen (U-U) is also given for the sake of comparison. The second portion focuses on the operating load limit. Bridge No. 090014, from which these specimens were extracted, is rated at HS-20, which corresponds to a live load moment of 292.4 kip-ft. (AASHTO, 2016). This is equivalent to a total load of 44.0 kips based on the test setup. Identifying the level of deflection

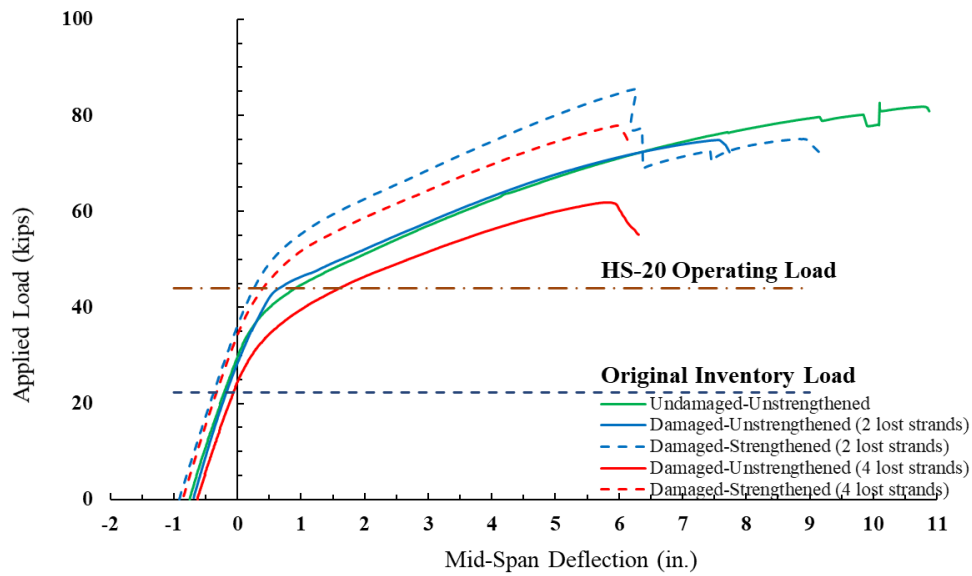
achieved by each specimen at this load provides a straightforward means to compare performance at the operating level relative to the control specimen, with positive values designating to downward deflection and negative values designating to upward camber. The third section does the same thing for inventory rating. The inventory load was calculated using Equation 4.5. The live load stress ($\sigma_{b,LL}$) was of interest this time, so the stress at the bottom concrete layer ($\sigma_{bottom,f}$) was taken as zero, consistent with the definition of the inventory limit in Chapter 1. The procedure and values used to calculate independent stress components were the same except for the prestressing force, which was here taken as the initial jacking force of 21.7 kips per strand, instead of calculating it from the ultimate tensile stress capacity (270 ksi). The live load stress was found to be -1.6 ksi, which corresponds to a moment of 197 kip-ft. and an applied load of 30.0 kips. An impact factor of 33% is included per AASHTO rating requirements, resulting in a live load moment of 148 kip-ft. and an applied force of 22.3 kips.

Figure 5.20 is a graphical summary of the results and complements Table 5.4 by providing visual comparison of the results. The camber was measured prior to and following infliction of damage and post-tensioning of the FRP plates. This is a crucial consideration in the graphical results, as the effect of post-tensioning comes in the form of added camber (0.22 in.) and an elongated elastic portion of the curves, both of which contribute to the enhancement of the behavior of the deteriorated beams. This is also accurately depicted in Table 5.4, where negative values of deflection refer to camber.

Table 5.4: Cored slab test results summary.

Specimen ID	U-U	D-U1	D-S1	D-U2	D-S2
Ultimate load (kips)	82.3	74.9	85.5	61.9	77.9
Percent increase from U-U (%)	0	-9.0	+3.90	-24.8	-5.35
Maximum FRP axial strain ($\mu\epsilon$)	-	-	7231	-	7444
Maximum FRP axial force ¹ (kips)	-	-	32.6	-	33.6
Percent of FRP tensile capacity (%)	-	-	70.3	-	72.4
Failure Mode ²	CC	CC	LS/R, CC	CC	CC
Operating load (kips)	44.0	44.0	44.0	44.0	44.0
Operating deflection (in.)	0.66	0.36	0.17	1.23	0.25
Change in operating deflection (in.)	0	-0.3	-0.49	+0.57	-0.41
Original inventory load (kips)	22.3	22.3	22.3	22.3	22.3
Original inventory deflection (in.)	-0.21	-0.17	-0.37	-0.06	-0.33
Change in inventory deflection (in.)	0	+0.04	-0.16	+0.15	-0.12

Notes: 1) calculated using Hooke's Law ($E_{FRP} = 9020$ ksi); 2) LS=longitudinal splitting, R=FRP rupture, CC=concrete crushing

**Figure 5.20:** Full-scale experimental results.

Specimen U-U achieved an ultimate load of 82.3 kips at an ultimate deflection of 10.9 in. and sets the benchmark for the operating and inventory responses. The deflections reached at the operating and inventory limits were +0.66 in. and -0.21 in., respectively. The operating load line intersects the curve for U-U just past the elastic portion, which is consistent with the definition given in Chapter 1; at this level of loading, some incremental damage will be incurred by the beam.

The inventory limit was defined as the point on the load-deflection curve where tensile stresses develop on the bottom concrete layer. For prestressed concrete members, the intersection of the curve with the vertical axis corresponds to the “balanced condition”, where the section is in uniform compression. Some downward deflection needs to occur to “overcome” this compression and before tension is generated at the extreme concrete layers. So, the inventory limit should fall slightly to the right of the vertical axis, at a small positive deflection. This would be the case if the impact factor were to be neglected; consideration of impact shifts the inventory limit down, resulting in it intersecting the load-deflection curve to the left of the vertical axis, at a region of camber. So, in this respect, the limit may seem inconsistent with the definition, but it must be understood that this is due to the impact factor. The most important consideration is that this limit falls well within the elastic region, such that no incremental damage can be incurred by the structure, which is clearly the case here. To facilitate comparison, the graph in Figure 5.20 is separated into two graphs based on level of damage applied (Figure 5.21 and Figure 5.22), each including the control specimen U-U.

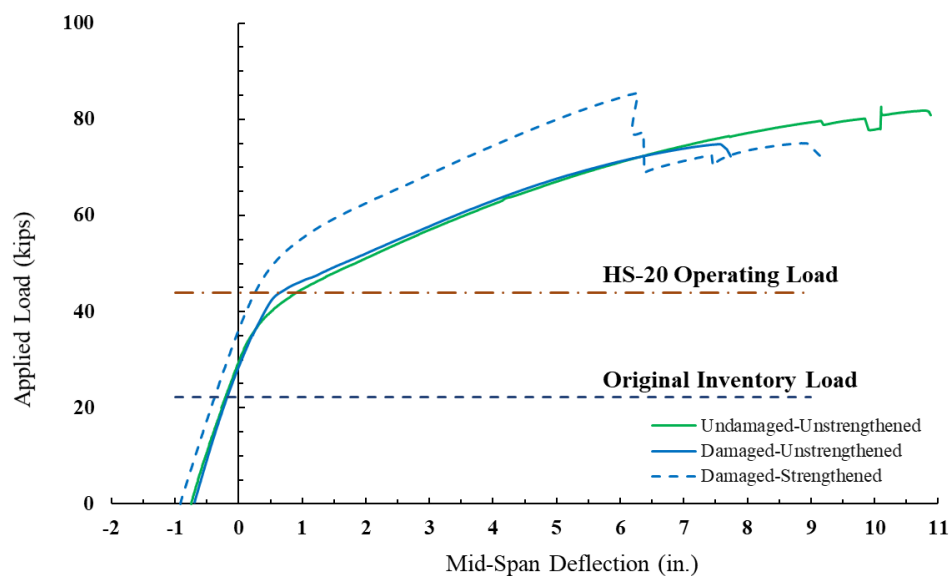


Figure 5.21: Full-scale results for 2 lost strands.

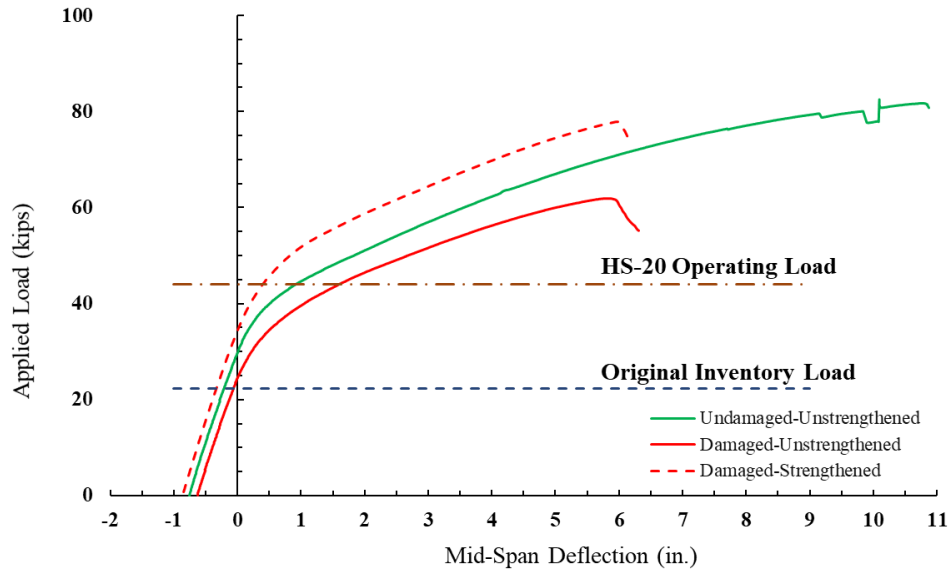


Figure 5.22: Full-scale results for 4 lost strands.

Specimens D-U1 and D-S1 were damaged by cutting two of the bottom prestressing strands. The ultimate capacity achieved by D-U1 was 74.9 kips (91.0% of U-U) at a deflection of 7.57 in. (a decrease of 3.33 in. compared to U-U). Concrete crushing was the controlling failure. Some camber was lost, resulting in a minor increase in the inventory deflection (+0.04 in.). This is not a concern, as it remains well within the elastic region, signaling no incremental damage occurring even for the damaged section. There was virtually no change in behavior other than the 3.33 in. decrease in ultimate deflection, and so the operating limit was unaffected. Therefore, the main concern at this level of damage is the loss of capacity. Judging from Figure 5.21, it seems that the loss of two strands did not significantly change the behavior of the beam. However, a more plausible explanation is that specimen U-U contained internal damage, which would explain why it underperformed, as indicated by its overlap with the curve for D-U1. This is confirmed by the analytical prediction performed in Chapter 6, which shows that the experimental capacity is lower than expected. It will be shown that the predicted undamaged-unstrengthened capacity is 88.4 kips, which is also used from this point on in quantifying the retrofit's contribution to flexural capacity.

The experimental total applied load of 74.9 kips achieved by D-U1 was therefore 84.7% of the predicted capacity.

D-S1 failed first by combined FRP longitudinal splitting and rupture at capacity total applied load of 85.5 kips and was able to achieve 104% of U-U's capacity, corresponding to an increase of 12.9% in ultimate capacity from D-U1. Significant camber was added (0.22 in.), and so the inventory deflection was 0.16 in. lower than that of U-U. The improvement in behavior can also be seen from the elongated elastic portion, such that the operating load line can now be seen intersecting the D-S1 curve just past the upper limit of the elastic region and just before the softening (large decrease in stiffness) occurs. As a result, even less damage would be incurred by the structure at the original operating limit. The ultimate capacity of D-S1 is 96.7% of the predicted undamaged-unstrengthened capacity, which corresponds to a 12.0% increase in flexural capacity compared to D-U1. The FRP plates reached 70.3% of their tensile capacity before failing prematurely as a result of added stress from their contact with the deflecting beam at mid-span, as discussed previously.

Specimens D-U2 and D-S2 were subject to more damage with four of the bottom prestressing strands cut. The ultimate capacity reached by D-U2 was 61.9 kips (75.2% of U-U) at a deflection of 5.87 in. (a decrease of 5.03 in. compared to U-U), with a failure controlled by concrete crushing. This capacity was also 70.0% of the predicted undamaged-unstrengthened capacity. The deterioration in behavior is much more noticeable at this level of damage. Going from U-U to D-U2, the elastic portion shortens, and the softening occurs earlier. As a result, the original operating limit intersects the D-U2 curve at a deflection of 1.23 in., which is 0.57 in. higher than the operating deflection of U-U. This means that a lot more incremental damage would be incurred by the structure at the original operating limit. The shortened elastic portion combined

with the lost camber results in the inventory limit intersecting the curve at the beginning of softening. This means that small incremental damage would be incurred by the structure at the original inventory rating, accelerating the rate of damage accumulation.

In practice, as a result of this level of degradation, a load restriction would have to be placed to reduce the load rating of the bridge. Alternatively, the MF-FRP retrofit can be applied to the structure to enhance its behavior, resulting in the behavior obtained by specimen D-S2. It achieved a peak load of 77.9 kips (94.7% of U-U) at a deflection of 5.99 in., approximately the same as D-U2. Compared to U-U, the curve for D-S2 has a longer elastic portion, and the softening occurs at a higher load. Thus, the operating deflection is 0.41 in. lower than that of U-U, and even smaller incremental damage will result from the original operating load rating. Thanks to the longer elastic portion and the 0.22 in. of added camber, the inventory limit intersects the D-S2 curve to the left of the vertical axis (on the camber side) and within the linear portion, so no incremental damage will result from the original inventory load rating. The capacity of D-S2 is 88.1% of the predicted undamaged-unstrengthened capacity, which corresponds to an increase in flexural capacity of 18.1% compared to D-U2. The FRP plates reached 72.4% of their tensile capacity before the beam failed by concrete crushing.

5.4 – Observations

The following observations may be made based on the full-scale experimental program of the C-channel beams and cored slabs:

5.4.1 – C-channel Beams

- MF-FRP 1.0 and MF-FRP 2.0 retrofit designs sufficiently restore a damaged C-channel with moderate deterioration at the maximum moment location such that the retrofitted C-channel is capable of supporting the original operating and inventory ratings. However, MF-FRP 1.0 allows an in-plane moment in the FRP plate to develop near the dead-end

anchor zone, which introduces flexural stresses not present in uniaxial tension loading and should be avoided. This in-plane moment causes longitudinal splitting and rupture of the FRP plate at 69% of the uniaxial tension capacity.

- MF-FRP 2.0 retrofit design resulted in failure by concrete crushing and a more ductile behavior compared with that of MF-FRP 1.0. The residual capacity of the FRP plate at concrete crushing is 33% of the FRP tensile capacity. This residual capacity in the FRP plate gives engineers the flexibility to increase the prestress force beyond the 18.5 kips applied in this investigation, up to 22 kips. This would further increase the inventory and operating ratings of retrofitted C-channel beams.

5.4.2 – Cored Slabs

- For damage of up to two fully lost strands, the retrofit is able to increase the ultimate capacity to a level higher than the original design capacity. For damage of up to four fully lost strands, the retrofit is able to restore the ultimate capacity to approximately 95% of the original undamaged section.
- The camber added from post-tensioning two FRP plates to 22 kips each was 0.22 in. for both levels of damage.
- For both levels of damage, the sections strengthened with the retrofit showed a longer elastic portion and softening occurred at a higher load compared to the original undamaged section.
- As a result of the above points, the levels of damage incurred by the structure at the original load ratings (operating and inventory) are lower for the strengthened sections than for the undamaged section. This means that for sections damaged by loss of up to four fully-lost

prestressing strands, the enhancement provided by the retrofit is more than enough to be in compliance with original AAHSTO load limits.

- For the strengthened tests (D-S1 and D-S2), the FRP plates reached 70.3 to 72.4% of their tensile capacity, respectively.

CHAPTER 6 – ANALYTICAL FLEXURAL MODELING OF RETROFITTED C-CHANNEL BEAMS AND CORED SLABS

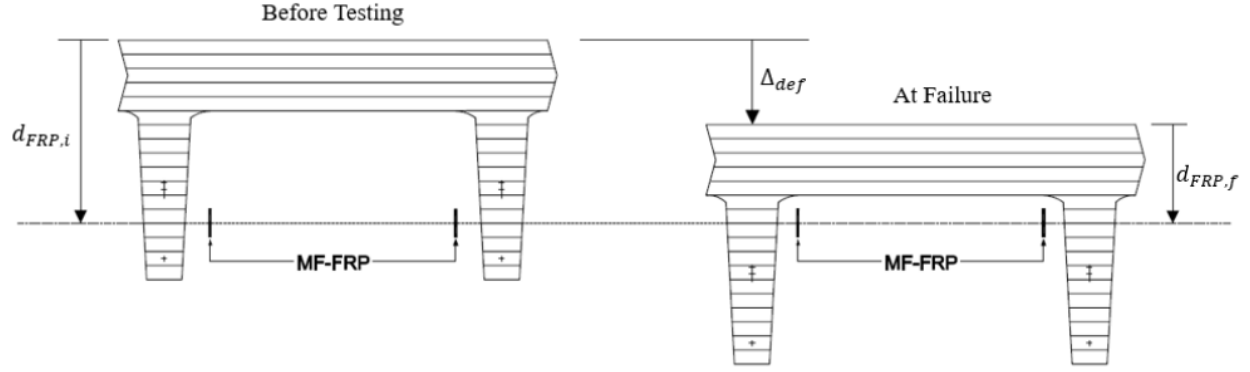
This chapter presents the development of an analytical procedure to model PC C-channel beams and cored slabs retrofitted with prestressed MF-FRP and compares the analytical predictions with experimental results from Chapter 5. A layered-sectional analysis (LSA) approach (Collins and Mitchell, 1997) was chosen to predict the full moment-curvature response in this research. The LSA approach is conducted by discretizing the section into multiple layers with a selected thickness. The stress in each layer can be found using appropriate constitutive material models, assuming plane sections remain plane. Sectional moment and curvature can then be calculated by achieving force equilibrium with an iterative procedure on the strain profile. The LSA can easily simulate nonlinear material behavior and provides a good prediction tool. A detailed analytical procedure of the MF-FRP retrofitted C-channel beams is explained. The full moment-deflection response under a specific applied load pattern can then be determined using the first moment of area theorem and the moment-curvature response from the LSA. Material properties used and modeling challenges are also explained in this chapter. The moment-deflection responses are compared to the experimental results from Chapter 5 to validate the proposed analytical procedure.

6.1 – Modeling of Repaired C-Channel Beams

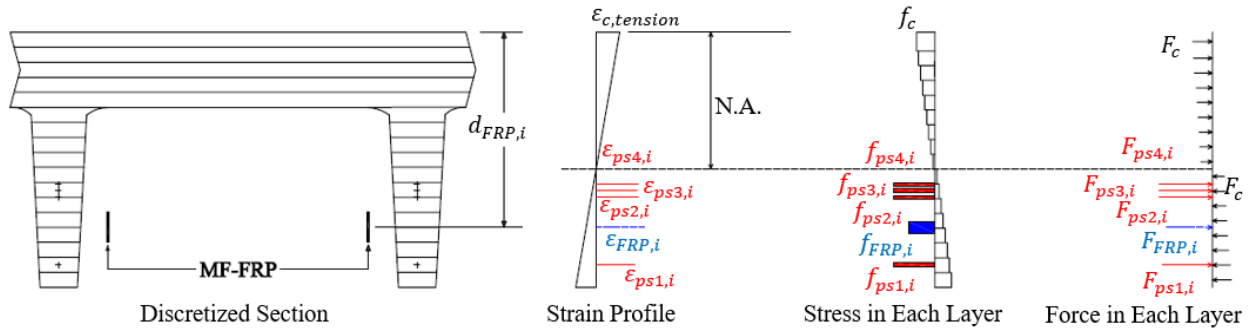
Appropriate constitutive models and material test results were considered in the nonlinear analysis of the section to obtain reasonable predictions. Concrete compressive stress was calculated using the Jensen et al. (1988) relationship. The concrete compressive strength used in the analysis was 10 ksi from the concrete core data obtained by C-channel beams tested in Chapter 5.2. Stress was assumed to be linear for concrete in tension until cracking, and then considered to be zero post-cracking. The tension stiffening effect was not applied to simplify the analysis. The

Mattock (1979) relationship based on the modified Ramberg-Osgood model (Ramberg and Osgood, 1943) was used to model the stress in the high-strength prestressing strands. The stress-strain relationship of the prestressing strands was assumed the same in both tension and compression. A linear-elastic relationship was used to obtain the FRP stress, following Hooke's Law. A detailed discussion of the materials used in the analysis is presented in Section 6.1.1.

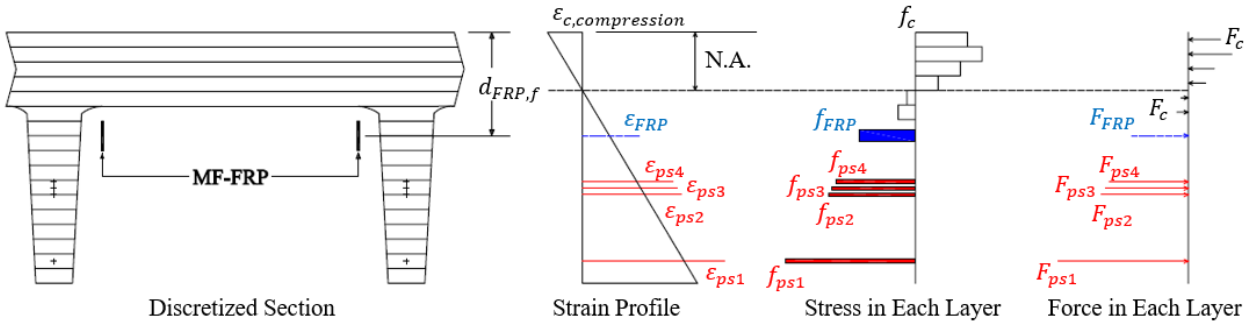
In most cases, full strain compatibility and plane sections remain plane are assumed to conduct the strain-based iterations to achieve axial force equilibrium and calculate the corresponding moment and curvature. However, the prestressed MF-FRP system applied on the C-channel beam was not bonded to the concrete structure and is similar to external unbonded prestressed strands. Therefore, full strain compatibility cannot be assumed in the analysis. According to the literature, the second-order effect and unbonded tendon strain behavior needs to be considered in the LSA approach. Figure 6.1(a) presents the discretized beam cross-section at mid-span considering the second-order effects at different loading stages; initial and ultimate applied loads. It can be seen that the global position of the MF-FRP remains the same while the beam deflects with increasing applied load, accompanied by a reduction of the FRP effective depth. Figure 6.1 (b) and (c) show the LSA approach considering the second-order effects. In Figure 6.1 (a), $d_{FRP,i}$ and $d_{FRP,f}$ represent the initial and final MF-FRP effective depth at a deflection, Δ_{def} , respectively.



(a) Global position of the MF-FRP at different loading stages



(b) Initial stage



(c) Ultimate stage

Figure 6.1: LSA approach.

A full moment-deflection response can be obtained using the first moment of area theorem, starting by discretizing the beam into 1 ft. long segments. A moment diagram along the beam can be obtained for any applied load and then the corresponding section curvature determined from an appropriate LSA. The member deflection can be calculated by integrating the curvature diagram at each segment along the length of the beam. Figure 6.2 shows the discretized member and

curvature diagram under three-point bending used for the first moment area method. However, due to the second-order effect and the harped tendon profile, additional modifications need to be considered.

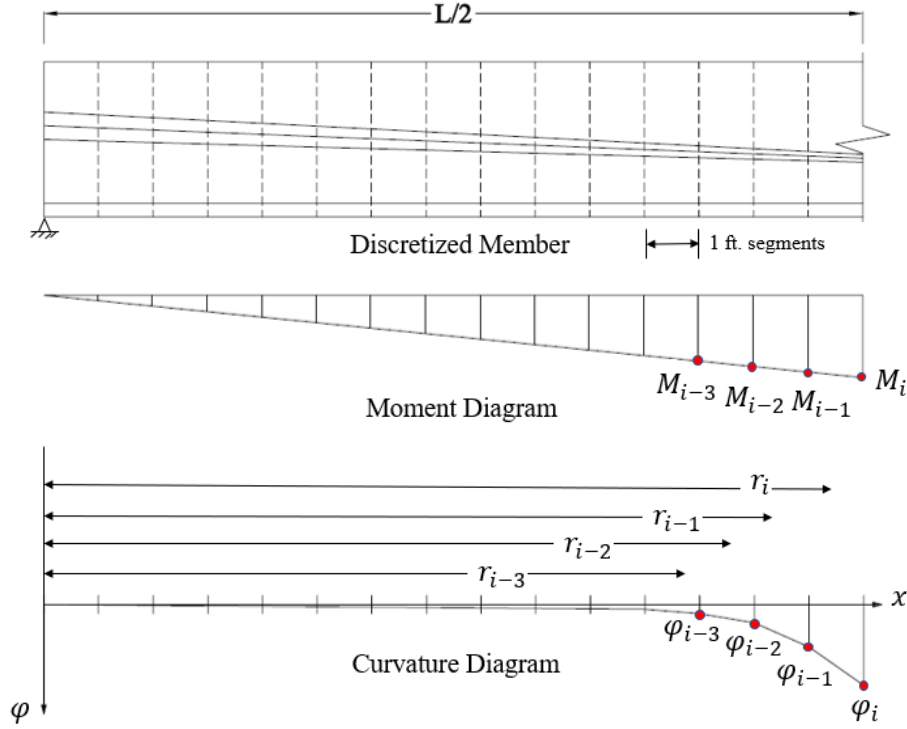


Figure 6.2: First moment of area theorem to calculate member deflection (three-point bending).

The most important factor in this analysis is to find the relationship between the external FRP strain to the concrete strain affected by the second-order effect. This factor can be divided into two steps: transfer the external FRP strain with the changing effective depth to the virtual *internal* unbonded FRP strain with variable effective depth and convert the virtual internal unbonded FRP strain to the concrete strain using a bond reduction factor. An idealized right triangle shape was used to transfer the external FRP strain to the internal unbonded FRP strain to simplify the calculation, as can be seen in Figure 6.3. The analysis is considered in two parts, the linear and nonlinear regions. For the beams and spans considered in this research, a member

deflection of 0.5 in. is used as the transition between regions. The second-order effect is not considered in the linear region to simplify the calculation.

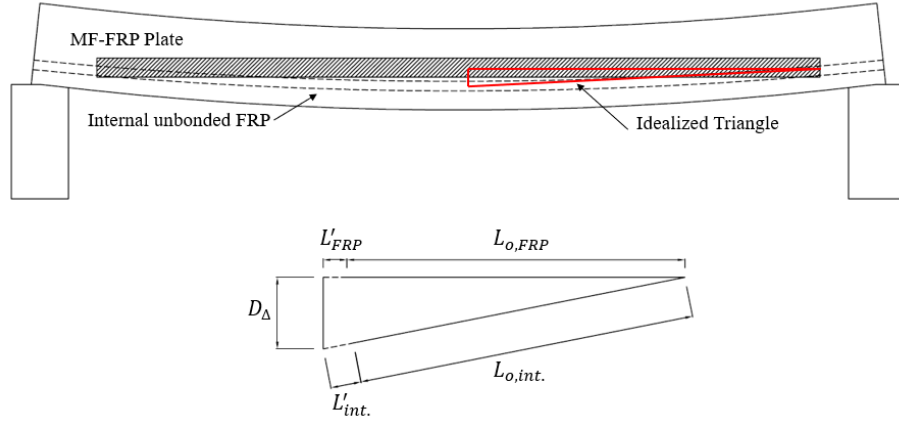


Figure 6.3: Idealized relationship to consider second-order effect.

The effective depth of the external MF-FRP varies with the applied load due to the second-order effect, resulting in a varying the changing distance between the new effective depth to the original effective depth. The total length of the virtual FRP internal unbonded FRP can be calculated by the hypotenuse of the right triangle using the distance between the external FRP plate and virtual internal FRP plate and the total length of the FRP plate. The parameters are given by

$$L_{Tot,FRP} = L'_{FRP} + L_{o,FRP} \quad (6.1)$$

$$D_{\Delta} = d_{frp,o} - d_{frp,i} \quad (6.2)$$

$$L'_{Tot,int} = L'_{int} + L_{o,int} = \sqrt{D_{\Delta}^2 + L_{Tot,FRP}^2} \quad (6.3)$$

$$\varepsilon_{FRP,int} = \frac{L'_{int}}{L_{o,int}} \quad (6.4)$$

where $L_{Tot,FRP}$, is the total length of the FRP plate from mid-span to the end of the repair system, L'_{FRP} , is the change in length of the MF-FRP plate, $L_{o,FRP}$ is the original length of the FPR plate from mid-span to the end of the repair system, D_{Δ} is the distance between the original FRP

effective depth to the MF-FRP effective depth at any deflection, $d_{frp,o}$ is the original MF-FRP effective depth, $d_{frp,i}$ is the MF-FRP effective depth at any deflection, $L'_{Tot,int}$ is the total length of the virtual internal unbonded FRP tendon, L'_{int} is the change in length of the virtual internal unbonded FRP tendon, $L_{o,int}$ is the initial length of the virtual internal unbonded FRP tendon and is assumed equal to $L_{o,FRP}$, and $\varepsilon_{FRP,int}$ is the virtual internal unbonded FRP strain.

The most important procedure in the LSA approach is using an iteration process to find a neutral axis resulting in equilibrium for a control strain value on the cross-section to meet the assumption of full strain compatibility and plane sections remain plane. Therefore, a bond reduction coefficient, Ω , is required to convert the strain from the internal unbonded tendon to the concrete strain at the same level. The bond reduction coefficient used in this research is from Tan and Ng (1997) and is given by the following:

$$\Omega = \frac{5.4}{\left(\frac{L}{d_{ps}}\right)} \quad (6.5)$$

where Ω is the bond reduction coefficient, L is the beam length, and d_{ps} is the effective depth of internal unbonded tendon which is equal to $d_{frp,o}$. Therefore, by transferring the strain from the MF-FRP plate to the concrete at the level of the original effective depth, the regular LSA approach can be conducted to find the sectional moment capacity at the corresponding condition.

The analysis can be briefly described as choosing an MF-FRP strain and guessing the corresponding beam deflection. The LSA approach is then used to determine the corresponding moment. Moment and curvature at each segment along the beam can be calculated using the moment-curvature response determined for each segment. Beam deflection can then be obtained using the first moment area theorem with the assumed MF-FRP strain and beam deflection. A

single point of moment-deflection can be obtained once the calculated deflection converges with the assumed deflection.

The detailed analysis procedure for the prestressed MF-FRP retrofitted C-channel beam is presented below:

- 1 Define the cross-sectional geometry and material properties.
- 2 Discretize the cross-section into layers with a constant thickness.
- 3 Calculate the area and centroid location for each layer.

Note: Steps 1 to 3 set up the cross-section prior to the start of the iterative analysis in Step 7.

- 4 Make initial assumptions.
 - 4.1 Assume a strain, ϵ_{FRP} , in the MF-FRP.
 - 4.2 Assume a central beam deflection, $\Delta_{def,o}$, to determine the MF-FRP effective depth, $d_{frp,i}$ at the assumed deflection.
- 5 Calculate the virtual internal unbonded tendon strain at the original MF-FRP effective depth from the assumed MF-FRP strain value at assumed deflection using the idealized right triangle relationship described by Figure 6.3.
- 6 Calculate the concrete strain at the level of the original MF-FRP effective depth using the bond reduction coefficient.
- 7 Open the first iterative loop by assuming the neutral axis depth for the calculated strain from step 6.
 - 7.1 Calculate the strain at each layer assuming a linear strain distribution, and that the concrete and prestressing strands are perfectly bonded with each other. The MF-FRP is treated as external prestressing strands.

- 7.2 Calculate the material stress at each layer according to the appropriate constitutive models.
 - 7.3 Calculate the axial force in each layer.
 - 7.4 Sum the axial forces. If not in equilibrium, repeat step 7 by assuming a new neutral axis depth.
 - 7.5 When axial force equilibrium is reached, calculate the moment of each force at each layer.
 - 8 Sum moments and calculate curvature at the critical section.
- Note:** Steps 4 to 8 are used to obtain one point on the moment-curvature response.
- 9 Divide the beam into segments and determine the moment at each beam segment based on the applied loading.
 - 10 Calculate the neutral axis depth and curvature for each segment for the external moment using the moment-curvature response.
 - 11 Calculate the central beam deflection, Δ_{def} , using the first moment of area theorem with the curvature obtained at the end of each segment by assuming a linear variation of curvature along the segment.
 - 12 If $\Delta_{def} \neq \Delta_{def,o}$, update $\Delta'_{def} = \Delta_{def}$ and repeat steps 4.2 to 11.
 - 13 If $\Delta'_{def} = \Delta_{def}$, one point of moment-deflection response is determined.
 - 14 Update a new MF-FRP strain, ε_{FRP} , and repeat the procedure from steps 4 to 13 until the full moment-deflection response of the beam is developed.
 - 15 The analysis stops when one of the two failure conditions is first achieved.
 - 15.1 The concrete strain reaches the crushing strain based on the selected concrete model. This limit is based on the experimental failure modes observed by

Chapter 5.2. The assumed ultimate concrete compression strain, 0.003, is based on ACI 318-19.

15.2 The beam deflection reaches the C-channel beam cross-sectional limitation, Δ_{allow} , in terms of the C-channel flange height, H_{flange} , MF-FRP width, W_{FRP} , and initial effective depth, $d_{FRP,i}$. Figure 6.4 shows the concept of obtaining the beam deflection limit, given by the following expression.

$$\Delta_{allow} = d_{FRP,i} - H_{flange} - \frac{W_{FRP}}{2} \quad (6.6)$$

The full moment-deflection response of a retrofitted C-channel beam can be obtained considering the second-order effect. With the complete response, the AASHTO inventory and operating load limit of the original undamaged beam can be applied to the moment-deflection diagram to capture the MF-FRP repaired beam behavior.

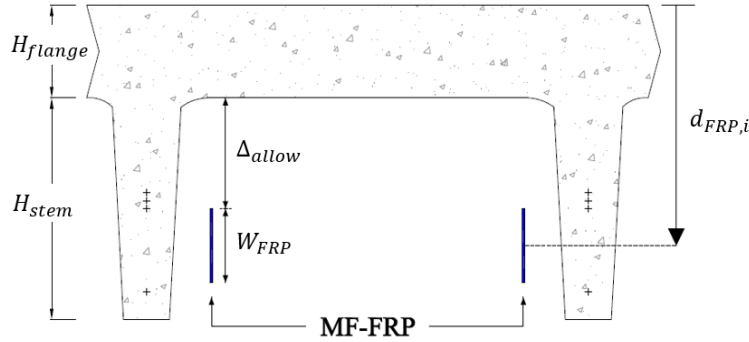


Figure 6.4: Concept of beam deflection limit.

6.1.1 – Constitutive Models

This section provides detailed discussions of the constitutive models used in the analysis, for the concrete, prestressing strand, steel reinforcement, and MF-FRP.

6.1.1.1 – Concrete

The Jensen et al. (1988) relationship was used to calculate the concrete compressive stress, f_c , based on the strain, ϵ_c , in each concrete layer using the following:

$$f_c = f'_c \left[\frac{n \left(\frac{\varepsilon_c}{\varepsilon'_c} \right)}{n-1 + \left(\frac{\varepsilon_c}{\varepsilon'_c} \right)^{nk}} \right] \quad (psi) \quad (6.7)$$

where f_c is the calculated concrete compressive stress in each layer, f'_c is the peak compressive stress obtained from concrete core cylinder tests, ε'_c is the strain at f'_c , n is a curve-fitting factor, and k is a factor to increase the post-peak decay in stress. Factors n and k can be calculated using

$$n = 0.8 + \frac{f'_c}{2500} \quad (psi) \quad (6.8)$$

$$k = 0.67 + \frac{f'_c}{9000} \geq 1.0 \quad (psi) \quad (6.9)$$

With n calculated, ε'_c can be obtained using

$$\varepsilon'_c = \frac{f'_c}{E_c} \frac{n}{n-1} \quad (6.10)$$

where E_c is the tangent stiffness for concrete strength greater than 6000 psi, given by

$$E_c = 40000\sqrt{f'_c} + 10^6 \quad (psi) \quad (6.11)$$

Concrete ultimate crushing strain is assumed to be 0.003 and was used to control the end point in Step 15 of the LSA. In tension, concrete stress, f_c , is assumed as linear up to flexural cracking and taken zero after that, given by

$$f_c = E_c \varepsilon_c, \quad \text{if } \varepsilon_c < \varepsilon_r \quad (6.12)$$

$$f_c = 0, \quad \text{if } \varepsilon_c \geq \varepsilon_r$$

where the rupture strain, ε_r , corresponds to the cracking moment and is calculated as

$$\varepsilon_r = \frac{7.5\lambda\sqrt{f'_c}}{E_c} \quad (psi) \quad (6.13)$$

where λ is 1.0 for normal-weight concrete.

It can be found that concrete compressive strength, f'_c , plays an important role in calculating the concrete stress in each layer. Therefore, it is desirable to use the actual concrete

strength to obtain a more accurate prediction. Two methods were considered to obtain the concrete strength; the Schmidt-Hammer and drilling concrete cores to conduct compression cylinder tests.

The Schmidt-Hammer is nondestructive test (NDT) equipment that can be easily used on-site by measuring the rebound value of a spring-loaded mass impacting against the concrete surface. Concrete strength can be obtained by converting the rebound value using the chart from the device, shown in Figure 6.5. Figure 6.6 shows the measurement being taken on a C-channel beam flange and stem, and the measured results from four beams tested in this research program are shown in Table 6.1.

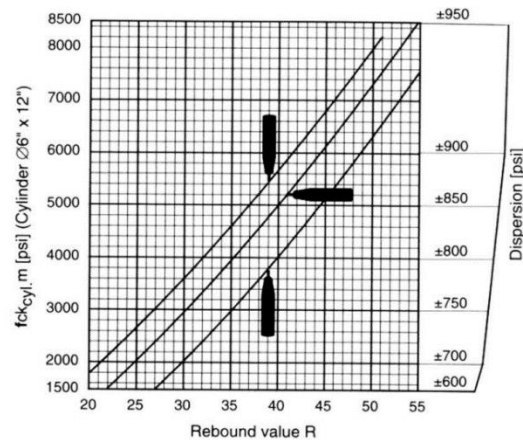


Figure 6.5: Schmidt-Hammer conversion curves (adapted from Schmidt-Hammer user's manual).



(a) *Horizontal measurement*



(b) *Vertical measurement (downward)*

Figure 6.6: Application of Schmidt-Hammer.

Table 6.1: Schmidt-Hammer measured results.

Beam No.	Location	Average Rebound Value	Predicted Concrete Strength (psi)
1	Flange	53	>8200
	Stem	58	>8500
2	Flange	54	>8200
	Stem	56	>8500
3	Flange	48	7500
	Stem	58	>8500
4	Flange	51	8200
	Stem	53	8000

The results presented in Table 6.1 show that the Schmidt-Hammer can reasonably obtain concrete strength compared to the 10 ksi concrete strength obtained by McCoy (2019); however, the measured strength is limited by the conversion curves and measuring direction, to 8200 and 8500 psi for C-channel beam flange and stem, respectively. Therefore, drilling concrete cores from the beams was considered the best solution to obtain more accurate measurements of concrete strength. Cores were initially obtained using a 2.5 in. diameter core drill using equipment available in the lab, as seen in Figure 6.7. The core drill diameter was then switched to 2 in. due to accidental damage of the drill bit. The actual diameters of the 2.5 and 2 in. cores were measured to be 2.25 and 1.96 in., respectively. A total of four concrete cores were drilled on each specimen. The ends of each core were cut using a wet tile saw to provide flat parallel surfaces (Figure 6.8). Concrete cores were capped using hydro stone at each end due to the specimen diameter and tested according to ASTM C39-18 and ASTM C42-18, shown in Figure 6.9(a). Figure 6.9(b) and (c) show the expected cylinder failure mode and a premature failure mode due to uneven loading, respectively. Concrete strength was then calculated in accordance with ACI 214.4 (2010). Table 6.2 presents the results of the C-channel concrete core data. There was a learning curve in the coring process and preparation of the first set of cylinders from Beam No. 1 resulting in premature concrete splitting failure. This data was not considered in the average core compressive strength calculation.



Figure 6.7: Coring a tested C-channel beam.



Figure 6.8: Cutting cores using a wet tile saw.

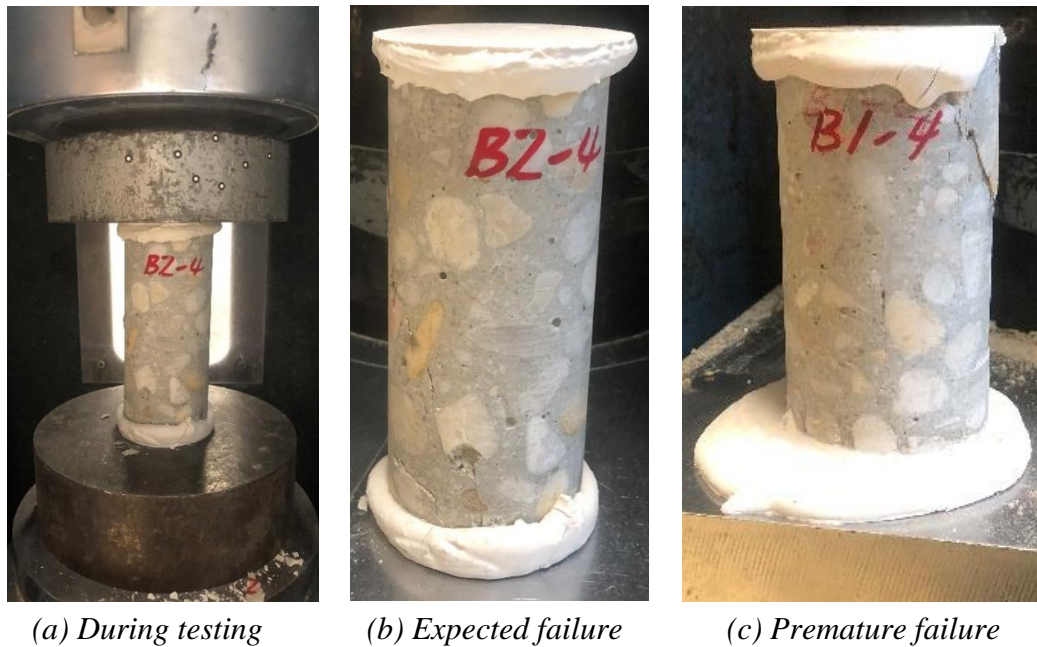


Figure 6.9: Concrete core compression test.

Table 6.2: Concrete core data.

Beam No.	Core ID	$f_{core,peak}$ (psi)	$F_{l/d}^a$	F_{dia}^b	F_{mc}^c	F_d^d	Adjusted f_{core} (psi)
1	B1-1	4464	1.00	1.06	0.96	1.06	4790 ^e
	B1-2	6163	0.99	1.06	0.96	1.06	6600 ^e
	B1-3	8007	1.00	1.06	0.96	1.06	8590
	B1-4	5071	0.99	1.06	0.96	1.06	5430 ^e
	Average						8590
2	B2-1	7793	1.00	1.00	0.96	1.06	8390
	B2-2	6077	1.00	1.00	0.96	1.06	6550 ^e
	B2-3	9426	1.00	1.00	0.96	1.06	10160
	B2-4	9323	1.00	1.00	0.96	1.06	10050
	Average						9500
3	B3-1	7372	1.00	1.00	0.96	1.06	7940
	B3-2	7268	1.00	1.00	0.96	1.06	7830
	B3-3	8568	1.00	1.00	0.96	1.06	9240
	B3-4	7771	1.00	1.00	0.96	1.06	8380
	Average						8350
4	B4-1	8793	1.00	1.00	0.96	1.06	9470
	B4-2	8501	1.00	1.00	0.96	1.06	9160
	B4-3	8663	1.00	1.00	0.96	1.06	9340
	B4-4	8952	1.00	1.00	0.96	1.06	9650
	Average						9400

^aLength-to-diameter ratio; ^bCore diameter; ^cMoisture content; ^dDamage during coring

^eEliminated from f_{core} calculation due to premature failure

According to Table 6.2, it can be found that the average measured concrete strength obtained from the cores was higher than the predictions from the Schmidt-Hammer. This was expected and results from the Schmidt-Hammer can be used as a lower bound concrete strength for the targeted beams on-site if they cannot be cored. The concrete cores could only be obtained from the flange due to the limitation of core size (cylinder height to diameter ratio of 2:1) and the C-channel stem dimension. Therefore, concrete strength results from concrete cores obtained from the flange were taken to apply to the entire beam. The measured concrete strength for each beam was used to calculate the shear capacity in Chapter 7. In general, the concrete strength obtained from this experimental program is close to the concrete core data by from C-channel beams tested in Chapter 5.2. Figure 6.10 shows the concrete stress-strain response used in the analysis according to the concrete core testing based on the 10 ksi concrete strength in Chapter 5.2.

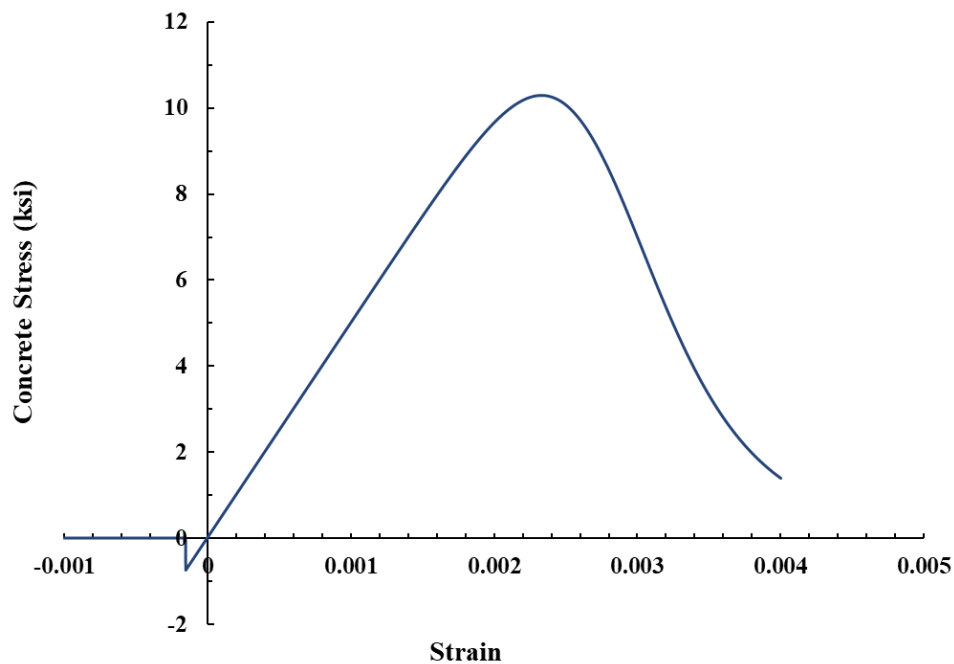


Figure 6.10: Stress-strain relationship for concrete.

6.1.1.2 – Prestressing Strand

Figure 6.11 shows the section detail of the standard C-channel beam cross-sections used by NCDOT, including three different strand patterns. Type A pattern was the cross-section used in this research. The section includes eight 7/16 in. prestressing strands located in two stems with a harped tendon profile and four No. 3 steel reinforcement in the flange.

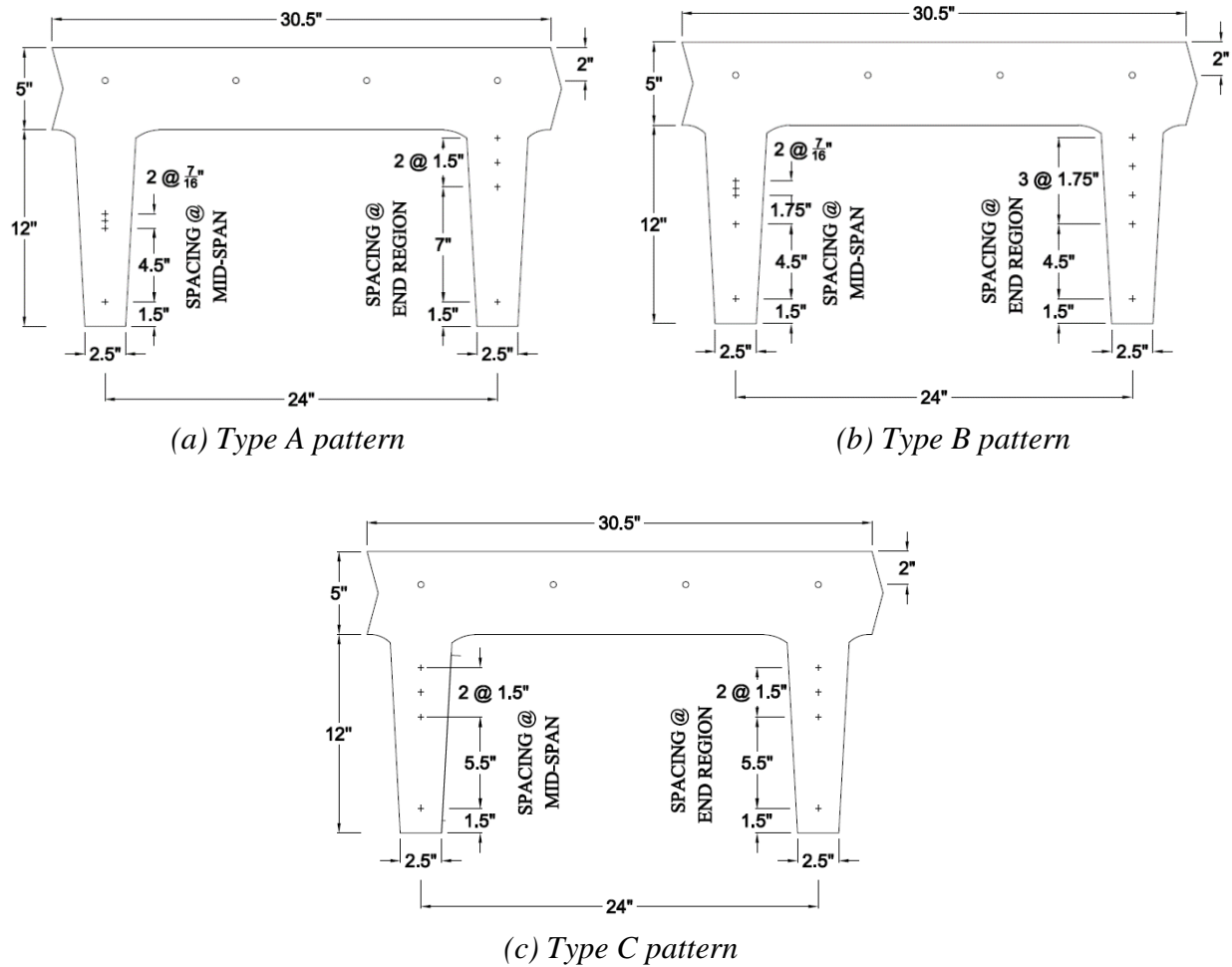


Figure 6.11: C-channel beam cross-section (adapted from NCDOT, 1966).

Five prestressing strands were cut from the tested specimens and tested in a 220 kips servo-hydraulic universal testing machine (UTM) in accordance with ASTM A1061 (2020) to obtain the material properties. A 3D non-contact measurement system, OPTOTRAK Certus, was used to measure the prestressing strand strain using the relative displacement of LED targets. The LED

targets were placed evenly along with the length of prestressing strand with a 2 in. center-to-center spacing to be consistent with the 2 in. gauge length extensometer. An OPTOTRAK camera was used to track the 3D position of each LED target during testing. The first three prestressing strands tested included additional instrumentation (extensometer, weldable strain gauge (AWC-8B-11-3LT), and normal glueable strain gauge (FLA-5-11-3LJCT-F)) to provide extra information on the data collected by different instrumentation. This was done to decide what instrumentation would be best to obtain the total prestress losses from the full-scale beams.

Figure 6.12 shows the test setup of the prestressing strand tension test and typical failure mode with necking and rupture of the wires. Figure 6.13 presents the test results of one prestressing strand from the different instruments and the schematic diagram of instruments located along the prestressing strand. It is observed that only OPTOTRAK was able to capture the complete stress-strain response compared to the other instruments. The extensometer was removed from the strand after reaching 80% of its ultimate capacity to avoid damaging the device during testing. Both weldable and normal strain gauges were damaged during testing at higher strain levels. The results presented in Figure 6.13 are not intended to serve as a direct comparison between each instrument due to their different location along the prestressing strand and gauge length. Rather, the purpose was to provide additional information to select the best instrument to use for the remaining tension tests and future small-scale experiments to measure the remaining prestress level. Therefore, it was determined that only the OPTOTRAK system would be used to conduct the remaining material tests. By comparing the experimental results and relative cost of weldable and normal strain gauges, the normal strain gauge was selected to obtain the remaining prestress level, which will be discussed later.



(a) Test setup



(b) Typical failure mode

Figure 6.12: Prestressing strand tension test and failure mode.

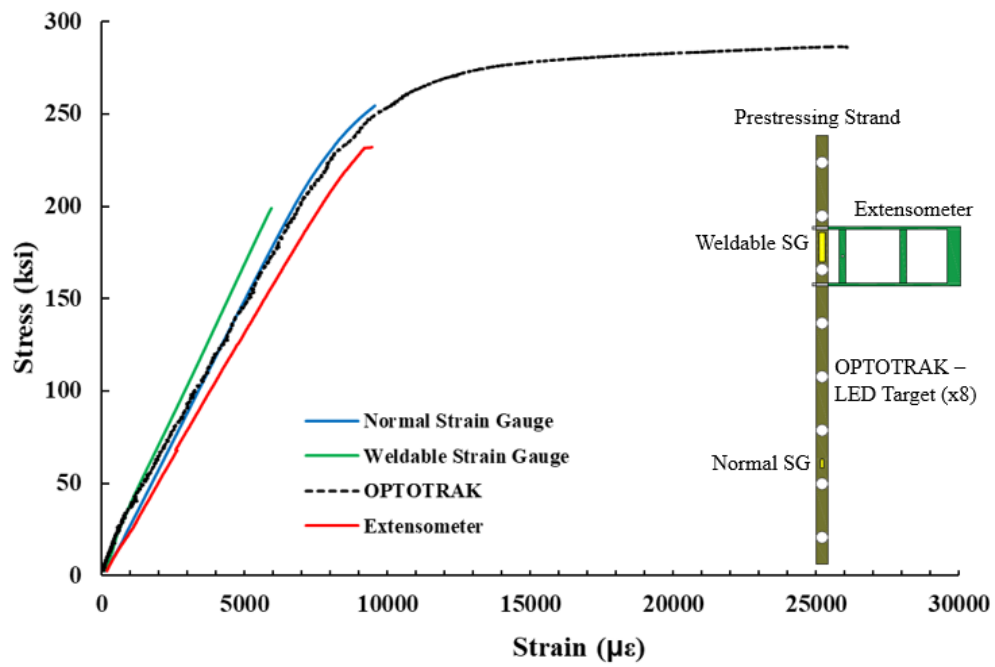


Figure 6.13: Experimental results of one tension test.

Figure 6.14 shows the OPTOTRAK test results for all five specimens as well as the stress-strain curve using the Mattock (1979) relationship

$$f_{ps} = E_p \varepsilon_{ps} \left\{ A + \frac{1-A}{[1+(B\varepsilon_{ps})^C]^{1/C}} \right\} \leq f_{pu} \quad (psi) \quad (6.14)$$

where E_p is the elastic modulus of the prestressing strand, taken as 29000 ksi based on ACI 318 (2019), ε_{ps} is the prestressing strain, f_{pu} is the ultimate stress of the prestressing strand, and A , B , and C are factors that can be adjusted to obtain the best fit curve. Figure 6.14 shows the stress-strain relationship of the Mattock (1979) model with A , B , and C equal to 0.017, 105, 6, respectively.

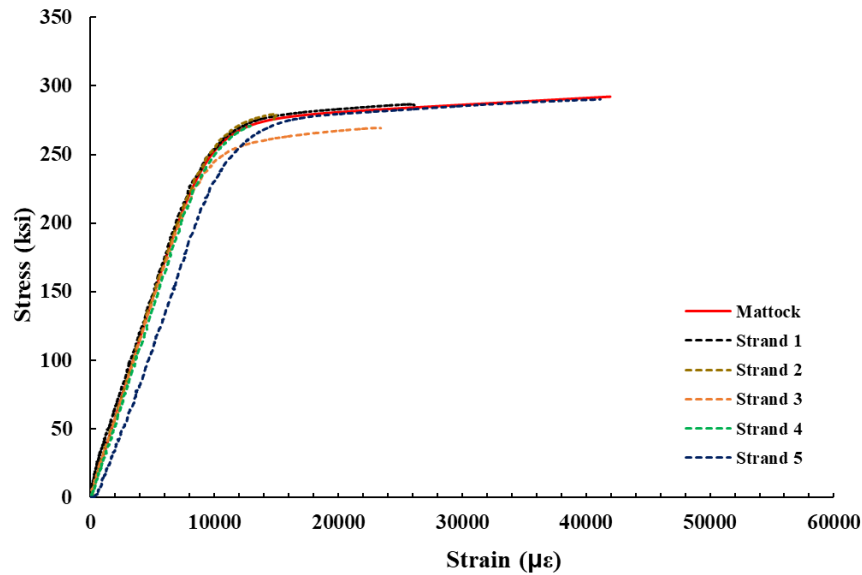


Figure 6.14: Stress-strain relationship of prestressing strand from experiments and Mattock (1979).

6.1.1.3 – Reinforcement Steel

Four No. 3 Grade 60 reinforcing bars are located in the C-channel flange. However, unlike the prestressing strands that can be easily obtained and tested, it was difficult to access the reinforcing bar from the C-channel flange. Therefore, the reinforcing steel was modeled using the common idealized elastic-perfectly plastic stress-strain relationship (see Figure 6.15). No strain

hardening was considered in the analysis and the same response in both tension and compression was used. Given the location of the reinforcing bars in the cross-section, the predicted flexural response would not be sensitive to the material model used.

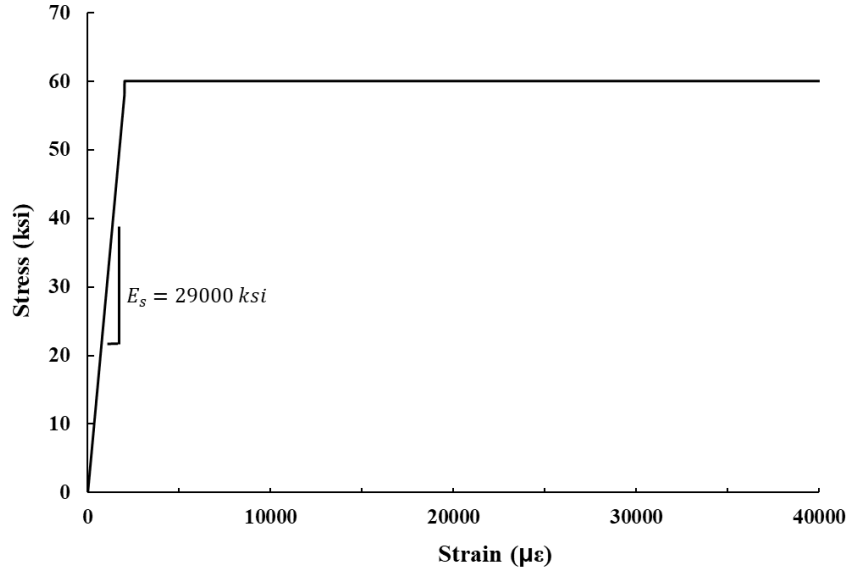


Figure 6.15: Idealized elastic-perfectly plastic stress-strain relationship for reinforcing bar.

6.1.1.4 – MF-FRP

As discussed in Chapter 3, both 0.5 and 0.375 in. bolt diameters with the 22-bolt pattern were studied and have similar ultimate capacity. However, according to the general practice for structural bolts used by NCDOT, 0.5 in. diameter is the smallest size allowed for the fastening application. Therefore, to be consistent in repair applications for both lab testing and field application, the 0.5 in. diameter bolt was considered.

The linear-elastic model used in the analysis to calculate the force in the MF-FRP plate, with an ultimate capacity of 46.4 kips based on the small-scale material testing from Chapter 3, is given by the following.

$$\begin{aligned}
 F_{FRP} &= E_{FRP} \varepsilon_{FRP} A_{FRP} & \text{if } F_{FRP} \leq 46.4 \text{ kips} \\
 F_{FRP} &= 0 & \text{if } F_{FRP} > 46.4 \text{ kips}
 \end{aligned}
 \tag{6.15}$$

where E_{FRP} is the FRP elastic modulus provided by the manufacturer (Strongwell, 2016), 9020 ksi, ϵ_{FRP} is the FRP strain, and A_{FRP} is the cross-sectional area of the FRP plate, 0.5 in². Hence, the target prestress strain can be calculated using the following application of Hooke's Law.

$$\epsilon_{FRP} = \frac{F_{PT}}{E_{FRP}A_{FRP}} \quad (6.16)$$

where F_{PT} is the target prestress force. An 18.5 kips effective force is the design prestress force giving prestress strain value of a 4100 $\mu\epsilon$. This prestressing force is consistent throughout the experiments conducted in Chapter 5.2 and the repair applications conducted in Chapters 7 and 8.

6.1.2 – Modeling Challenges

In addition to the second-order effect of the MF-FRP and failure condition of the retrofitted beam behavior mentioned in the analysis procedure, a few modeling challenges made the analysis even more complex. These challenges are discussed in the following sections to increase the accuracy of the LSA approach. From the NCDOT perspective, it is essential to obtain accurate behavior in the transition region between elastic and inelastic behavior of damaged and retrofitted PC C-channel beams compared to the original AASHTO inventory and operating limits.

6.1.2.1 – Prestressing Strand Profile

As mentioned in the previous section, the C-channel beam cross-section tested in this research was the type A pattern, consisting of four prestressing strands at each stem with one straight strand and three harped strands. With the harped strand profile, sections along the span have their own moment-curvature response according to the strand geometry. Figure 6.16 shows the different moment-curvature responses at mid-span and quarter span, in which the same applied moment results in a different curvature response. This difference will affect the first moment of area theorem to obtain the beam deflection at any given load stage, especially at large deflections. A unique moment-curvature response is generated for each segment to conduct the first moment

of area theorem. Therefore, it is important to be certain of the strand profile of the C-channel beam before conducting the analysis.

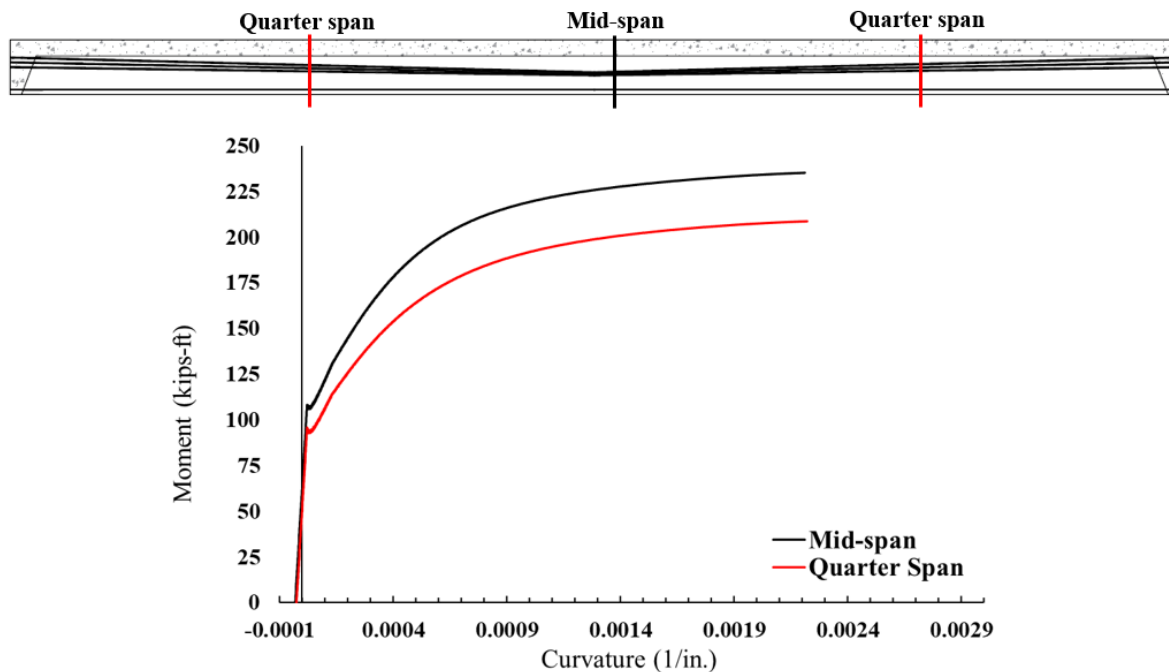


Figure 6.16: Moment-curvature response of cross-section at different locations.

6.1.2.2 – Total Prestress Losses

The prediction of the total prestress losses of the C-channel beam is an important parameter for the LSA approach. Figure 6.17 and Figure 6.18 show moment-curvature responses at mid-span and moment-deflection curves of a C-channel beam for different levels of total prestress losses. It can be observed that different prestress losses do not affect the ultimate flexural capacity; however, it affects the behavior at the location where the inventory and operating limits are of most interest in this research. The accuracy of the load rating assessment is related to the accuracy of the total prestress losses calculation. In this research, two methods were used to obtain the actual prestress losses of the beams tested. First, by measuring the remaining stress in the strand at the mid-span after cutting the strand, and second, by applying load using an actuator in a flexural test to obtain

the cracking moment experimentally from which the total prestress losses can be calculated. Both methods and results are presented in the following sections.

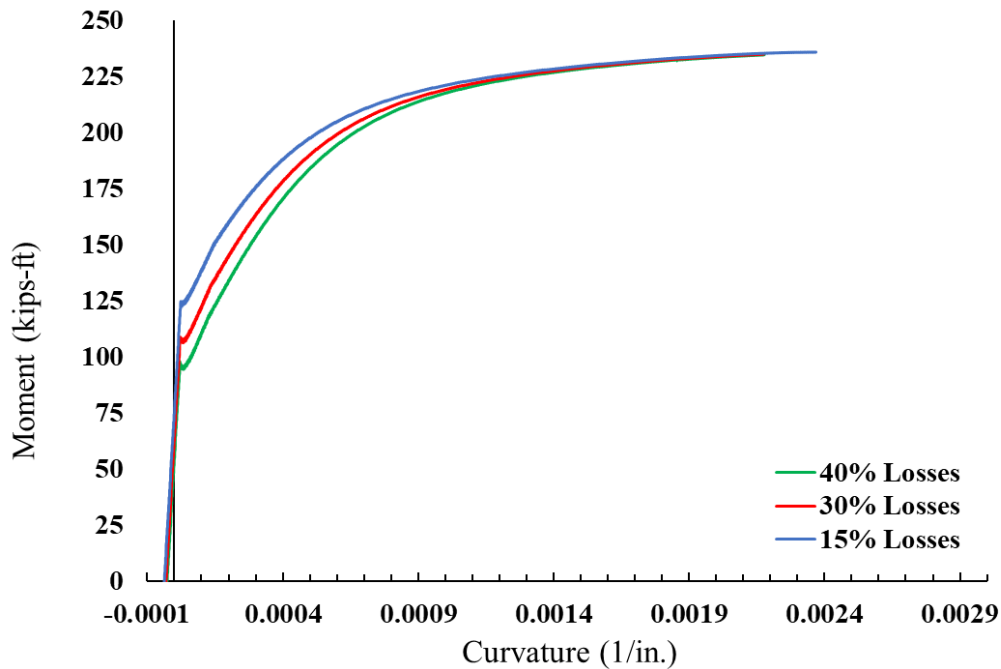


Figure 6.17: Moment-curvature response of mid-span cross-section at different total prestress losses.

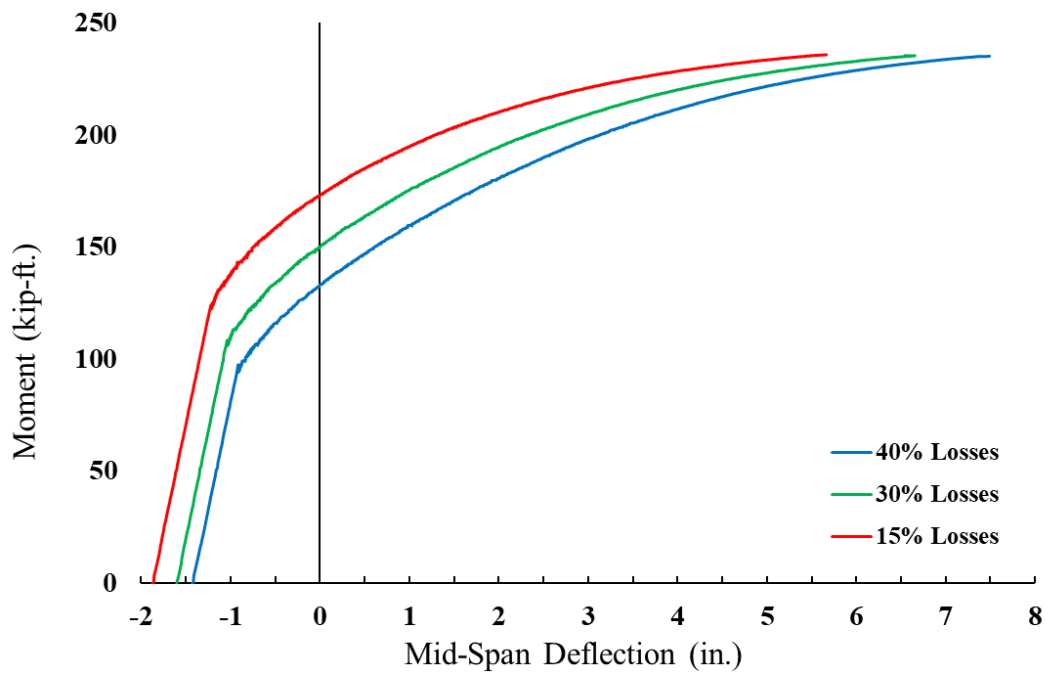
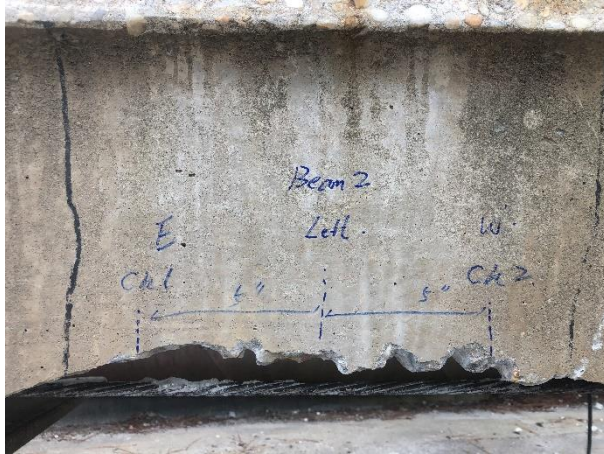


Figure 6.18: Moment-deflection response of a member at different total prestress losses.

6.1.2.2.1 – Measuring Total Prestress Losses using Strand Cutting Method

A comprehensive procedure to obtain the total prestress losses and results are presented in this section. The application was conducted using tested specimens from the full-scale shear experiments, which will be presented in Chapter 7. The procedure starts by selecting a location of interest where the prestressing strand can be fully developed and then the surrounding concrete section chipped away exposing the prestressing strand. The strand is then cleaned using a wire brush, sandpaper, and degreaser to remove all remaining debris. The mid-point of the exposed strand needs to be identified, and the locations to attach strain gauges determined. Based on the material testing results presented in Section 6.1.1.2, normal glueable strain gauges were selected for this application. Strain gauges are attached at the same distance from the mid-point on the same wire and connected to a P3 strain indicator and recorder. Strain gauge values are tared to set an initial reference point before cutting the strand. The strand is cut using a hand-cutting wheel at the mid-point of the exposed strand. Due to the large energy release during cutting, the strand wires unravel and affect the strain measurement. Therefore, the strand wires need to be restored to the original spiral condition to record the correct strain value. Strain values obtained after cutting the strand are used to calculate the stress in the strand at the time of cutting. The measured stress value is then compared with the initial jacking stress to obtain the total prestress losses. Some strain gauges were damaged due to the substantial energy released during the cutting process. This procedure is illustrated in Figure 6.19. Table 6.3 shows the strain measurement data and calculated remaining stress obtained from the experiments using a modulus of elasticity of 29000 ksi. Remaining stress was then compared to the initiated jacking stress (186 ksi). Table 6.4 presents the calculated total prestress losses compared to the initial jacking stress using this method.



(a) Chip away concrete around strand



(b) Clean strand with a wire brush



(c) Attach strain gauge at the selected locations



(d) Cut strand with a hand cutting wheel



(e) Strand condition after cutting



(f) Restore the original strand condition

Figure 6.19: Procedure of obtaining the total prestress losses.

Table 6.3: Strain measurement data and remaining stress.

Beam ID	Location	Measured Strain ($\mu\epsilon$)				Calculated Remaining Stress (ksi)		Jacking Stress (ksi)	Remaining Stress $f_{mea.}/f_{jack.}$	
		East	West	Average	Peak	Average	Peak		Average	Peak
1	Mid-span	3054	3178	3116	3178	90.36	92.16	186	0.49	0.50
1	2 ft. from mid-span ^a	2525	3103	2814	3103	81.61	89.99		0.44	0.48
2	Mid-span	3161	4189	3675	4189	106.6	121.5		0.57	0.65
2	Mid-span	3262	3843	3553	3843	103.0	111.4		0.55	0.60
3	Mid-span	-- ^b	3942	3942	3942	114.3	114.3		0.61	0.61
3	Mid-span	3181	2823	3002	3181	87.1	92.2		0.47	0.50

^a Prestressing strand ruptured during testing.
^b Strain gauge damaged during strand cutting.

Table 6.4: Measured total prestress losses.

Beam ID	Measured Total Prestress Losses (%)	
	Average	Minimum
1	51	50
1	56	52
2	43	35
2	45	40
3	39	39
3	53	50
Average	47.8	45.2

Based on Table 6.4, the average value of the minimum total prestress losses is 45%. The measured strain value from strain gauges may be considered slightly lower than the actual value due to the specimen condition after the shear testing. However, the applied moment at mid-span during the shear test was lower than its operating limit. Therefore, this impact can be neglected from the results.

6.1.2.2.2 – Measuring Total Prestress Losses using the Cracking Moment Method

The cracking moment method was performed using a full-scale flexural test to determine the remaining prestress force, following the test procedure conducted by Higgs et al. (2015) where the applied load has to exceed the predicted cracking moment by at least 25% to ensure concrete

cracking is initiated at the location of interest. The specimen was tested under three-point bending using an actuator with three loading stages based on the predicted sectional cracking moment. This method was applied prior to destructive testing of the beam. The applied load at each loading stage was 8.5, 12, and 15 kips, representing before cracking, at cracking, and after cracking conditions, respectively. Three cycles were applied at each loading stage. The predicted sectional cracking moment was 90 kips-ft. based on the concrete strength and prestress losses from the previous experiments, which were 9.5 ksi and 45% losses, respectively.

Two techniques were used to measure concrete strain during testing: bonded concrete strain gauges; and Digital Image Correlation (DIC). The Correlated Solutions DIC system uses a series of high-resolution photos to measure the displacement on the specimen surface of interest through a random speckle pattern field. Images are captured at a specified frequency during testing. By comparing the images captured during testing, strain maps can be obtained over the surface of interest using the Correlated Solutions software.

A strain gauge was attached on the bottom side of a stem to obtain the concrete strain. The DIC was focused on the opposite stem to which the strain gauge was installed. The DIC results were analyzed at the same location of the strain gauge to enable a comparison. Figure 6.20 shows the strain map at the maximum applied moment of the third loading stage during the cracking moment test. The location of high strain can be seen in the image. Figure 6.21 presents the applied moment and strain response at the side of the bottom stem from the strain gauge and DIC results using a similar gauge length. The results presented in Figure 6.21 show that the strain value from the strain gauge did not capture the behavior well compared to the DIC. This is due to the location where the strain gauge was installed, which happened to be between two primary flexural cracks (refer to Figure 6.21). By finding the intersection point of the two slopes at the first cycle of each

loading stage (before and after cracking) from Figure 6.21 using the same procedure from Higgs et al. (2015), the cracking moment is determined to be 95 kips-ft., which is close to the predicted cracking moment of 90 kips-ft., assuming 45% of total prestress losses.

Therefore, according to the experimental results from Sections 6.1.2.2.1 and 6.1.2.2.2, the total prestress losses of the C-channel beams used in the analyses presented herein is taken as 45%.

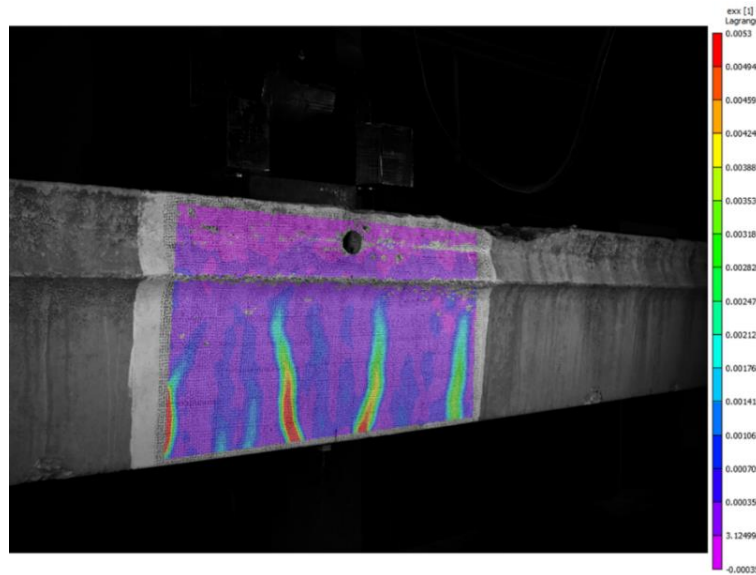


Figure 6.20: Strain map obtained from DIC at third load stage after cracking.

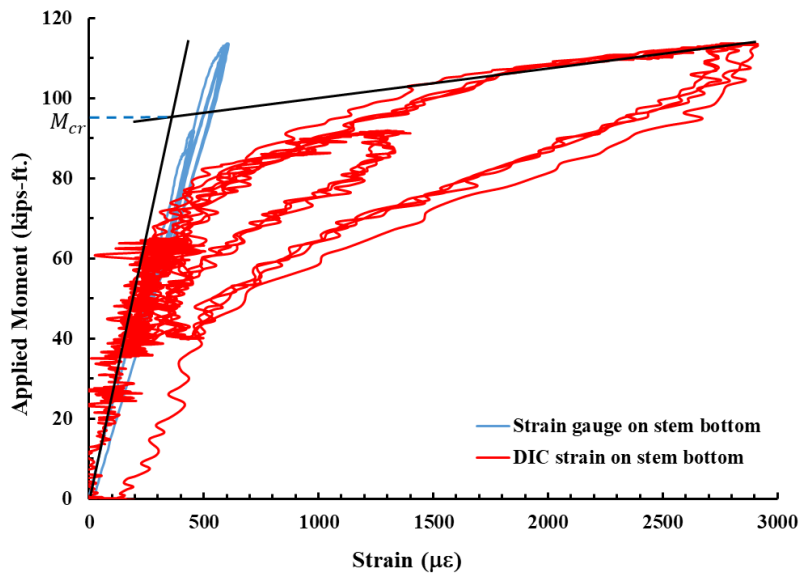


Figure 6.21: Strain response from strain gauge and DIC.

6.1.2.2.3 – Calculated Prestress Losses using Design Guide

The measured total prestress losses were obtained experimentally using the strand cutting method and the cracking moment method. However, it is worth checking the calculated prestress losses for comparison to the experimentally measured value. The calculated prestress losses of the pretensioned C-channel beam used in this experimental program is presented in this Section using simple expressions from PCI (2017). For pretensioned concrete members, total prestress losses, $\Delta f_{P, TL}$, are due to elastic shortening, $\Delta f_{P, ES}$, creep of concrete, $\Delta f_{P, CR}$, shrinkage of concrete, $\Delta f_{P, SH}$, and relaxation of tendons, $\Delta f_{P, RE}$. The relationship is shown as follows:

$$\Delta f_{P, TL} = \Delta f_{P, ES} + \Delta f_{P, CR} + \Delta f_{P, SH} + \Delta f_{P, RE} \quad (6.17)$$

A detailed explanation of each term is presented in the following, starting from the elastic shortening,

$$\Delta f_{P, ES} = \frac{K_{es} E_{ps} f_{cir}}{E_{ci}} \quad (psi) \quad (6.18)$$

where K_{es} is the coefficient of the elastic shortening and taken as 1.0 for pretensioned components, E_{ps} is the modulus of elasticity of prestressing tendons, E_{ci} is the modulus of elasticity of concrete at time prestress is applied, and f_{cir} is the net compressive stress in the concrete at the center of gravity of the prestressing force immediately after the prestress has been applied to the concrete given by

$$f_{cir} = K_{cir} \left(\frac{P_i}{A_g} + \frac{P_i e^2}{I_g} \right) - \frac{M_g e}{I_g} \quad (psi) \quad (6.18a)$$

where K_{cir} is the compressive stress coefficient and taken as 0.9 for pretensioned components, P_i is initial prestress force (jacking force after anchorage loss), e is the eccentricity of the center of gravity of the tendons with respect to center of gravity of the concrete at the cross-section considered, A_g is the area of the gross concrete section at the cross-section considered, I_g is the

moment of inertia of the gross concrete section at the cross-section considered, and M_g is the bending moment due to dead load of the prestressed component and any other permanent loads in place at time of prestressing.

The prestress losses due to creep of concrete are calculated as:

$$\Delta f_{P, CR} = \frac{K_{cr} E_{ps}}{E_c} (f_{cir} - f_{cds}) \quad (psi) \quad (6.19)$$

where K_{cr} is the creep coefficient and is taken as 2.0 for normal-weight concrete, E_c is the modulus of elasticity of concrete at 28 days, and f_{cds} is stress in the concrete at the center of gravity of the prestressing force due to all superimposed, permanent dead loads that are applied to the member after it has been prestressed and is given by:

$$f_{cds} = \frac{M_{sde}}{I_g} \quad (psi) \quad (6.19a)$$

where M_{sd} is the moment due to all superimposed, permanent dead load and sustained load applied after prestressing.

Losses due to shrinkage of concrete are calculated as:

$$\Delta f_{P, SH} = (8.2 \times 10^{-6}) K_{sh} E_{ps} \left(1 - 0.06 \frac{V}{S}\right) (100 - RH) \quad (psi) \quad (6.20)$$

where K_{sh} is the coefficient of shrinkage and is taken as 1.0 for pretensioned components, $\frac{V}{S}$ is the volume-to-surface ratio after removing the formwork, and RH is the average ambient relative humidity which is taken as 75 for a bridge located in the coastal area of North Carolina.

The prestressing strands located in the C-channel beams tested are stress-relieved but not low-relaxation strands due to the technology at the time of the construction. Therefore, the prestress losses due to relaxation are likely to be significant and can be calculated as:

$$\Delta f_{P, RE} = [K_{re} - J(\Delta f_{P, SH} + \Delta f_{P, CR} + \Delta f_{P, ES})] C \quad (psi) \quad (6.21)$$

where K_{re} and J are the relaxation coefficients and taken as 20000 and 0.15 for grade 270 stress-relieved strand, respectively, and C is the coefficient related to the initial jacking stress.

Alternatively, the prestress losses due to relaxation of tendons can also be calculated using Equation 6.21a by considering the time effect (Nawy, 2010).

$$\Delta f_{P, RE} = f'_{pi} \frac{\log t}{10} \left(\frac{f'_{pi}}{f_{py}} - 0.55 \right) \quad (psi) \text{ (stress-relieved strand)} \quad (6.21a)$$

where f'_{pi} is the transfer stress, t is the time in hours that the PC member has been in service, and f_{py} is the yield strength of the prestressing strand.

Table 6.5 shows the calculated prestress losses using the expressions mentioned above and considering different relaxation calculations.

Table 6.5: Calculated prestress losses.

$\Delta f_{P, ES}$ (psi)	$\Delta f_{P, CR}$ (psi)	$\Delta f_{P, SH}$ (psi)	$\Delta f_{P, RE}$ (psi)	$\Delta f_{P, TL}$ (psi)	$\Delta f_{P, TL}/f_{pi}$ (%)
9435	17398	4893	13946 ^a	45672	25
			28086 ^b	59812	32

^aPrestress losses due to relaxation according to the Equation 3.21
^bPrestress losses due to relaxation according to the Equation 3.21a at 45 years since construction

The calculated prestress losses compared to the initial jacking stress presented in Table 6.5 show that the use of the expression for obtaining prestress losses from the relaxation of prestressing tendon results in an 8% difference of calculated prestress losses. However, 25% to 32% of calculated total prestress losses is substantially lower than the 45% total prestress losses obtained from the experimental methods. Therefore, additional factors need to be considered in the calculated prestress losses based on the experimental results.

The calculated remaining prestress in the prestressing strand using the cutting strand method is less than the remaining prestress obtained using the same method on an in-service bridge due to the different dead load (wearing surface) and support conditions. The remaining prestress

can be better examined using the following equation, resulting in an increased stress value in the bottom strand so that the calculated remaining stress better represents the condition on-site

$$f_{bot,strand} = \frac{M'_d e_{bot,strand}}{I_g} \quad (psi) \quad (6.22)$$

where $f_{bot,strand}$ is the calculated stress on the bottom strand, M'_d is the applied moment from the wearing surface or self-weight for the span length considered, and $e_{bot,strand}$ is the eccentricity of bottom strand. Further, the C-channel beam span between supports while conducting the cutting strand method was reduced due to the failure mode from the full-scale testing compared to the in-service condition. The increased calculated prestress due to the wearing surface, and support condition is predicted to be approximately 440 psi. This discrepancy is negligible compared to the magnitude of prestress losses calculated in Table 6.5.

The difference in total prestress losses between the experimental methods and the empirical code based expressions is approximately 13% to 20%, even when the additional dead load and different support conditions are considered in the calculation. The difference may be explained due to the corrosion of the prestressing strands, resulting in reduced bond stress and causing slip between the concrete and the prestressing strand. Many conditions observed in real bridges in service for more than 45 years may result in additional prestress losses, which are not accounted for in the empirical expressions.

6.1.2.3 – Development Length

The effect of prestressing strand development length is another factor that affects the predicted member deflection. Sections can only achieve their full flexural capacity when the strands are fully developed. Prestressing strand development can be calculated using the following expression from Nawy (2010)

$$l_d = l_t + l_f = \frac{f_{pe}}{3} d_b + (f_{ps} - f_{pe}) d_b \quad (in.) \quad (6.23)$$

where l_t is the transfer length for the strand to develop its effective stress, l_f is the flexural bond length that enables the strand to develop its ultimate stress, d_b is the prestressing strand diameter, f_{pe} is effective prestress stress, and f_{ps} is the stress in the prestressing strand at the sections nominal strength.

The effective prestress stress, f_{pe} , based on the total prestress loss value obtained from Section 6.1.2.2, is 101.8 ksi, the prestressing strand used in the C-channel beam is 7/16 in. diameter, and f_{ps} is taken as 243 ksi assuming $0.9f_{pu}$. Using Equation 6.11, the calculated development length, l_d , is 76.6 in. (14.8 in. for l_t and 61.8 in. for l_f). Figure 6.22(a) shows the prestressing strand stress development over the full development length from Nawy (2010). For analysis purposes, a simplified bi-linear model, as shown in Figure 6.22(b) was used in the analysis.

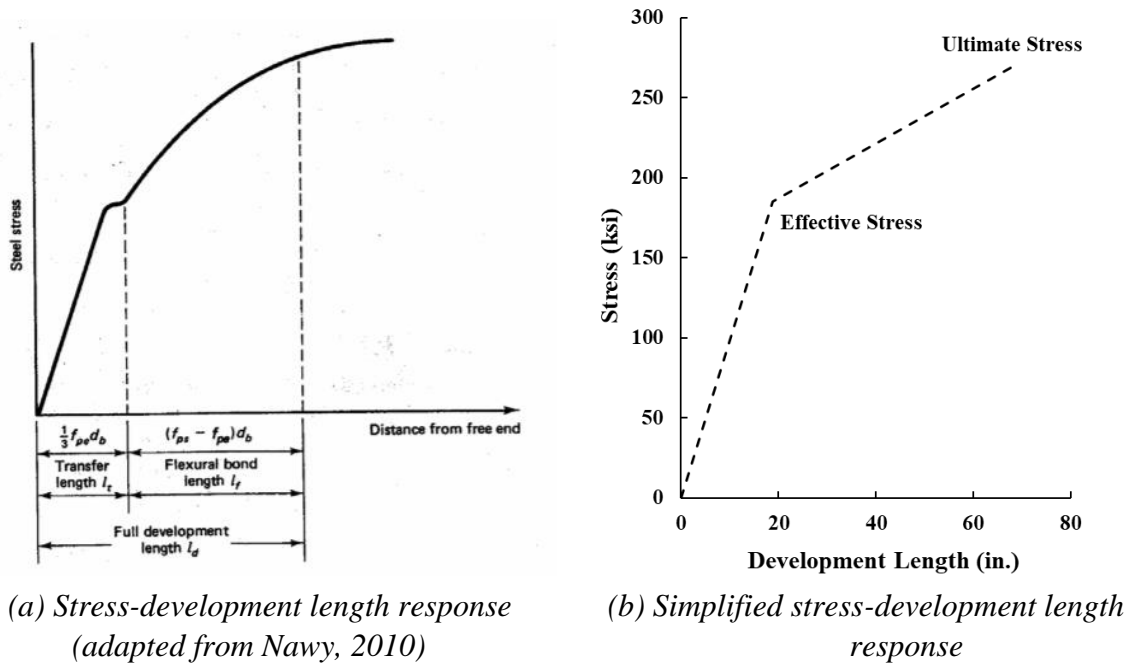


Figure 6.22: Stress-development length response.

Figure 6.23 shows the variation of flexural capacity along the length of a C-channel beam by considering the development length effect and the harped strand profile.

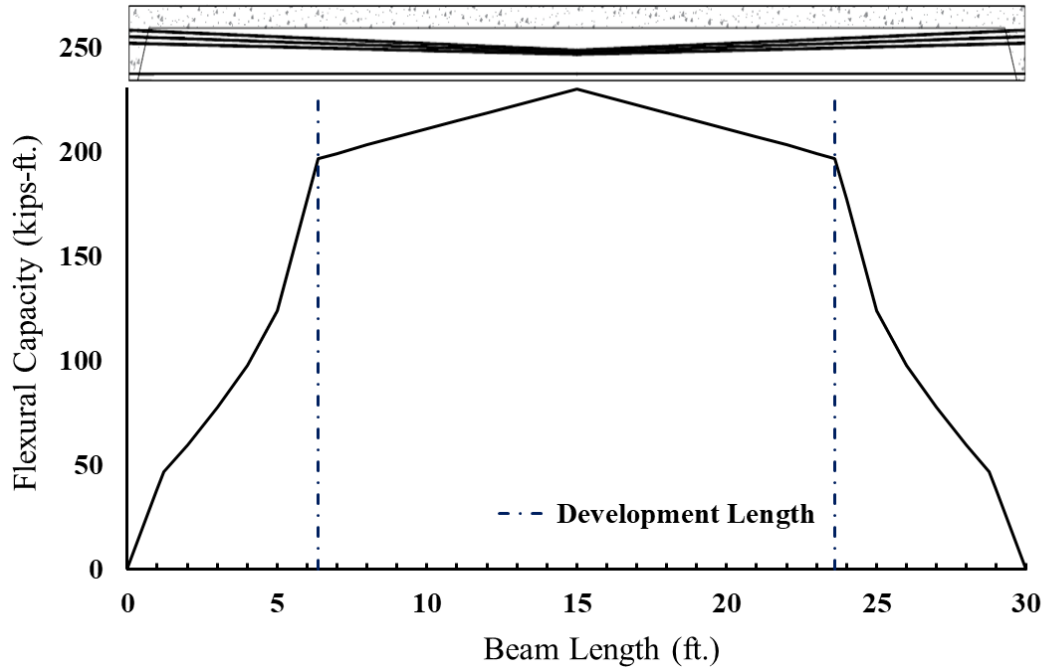


Figure 6.23: Variation of flexural capacity.

6.1.2.4 – Modeling Damage Condition

Modeling the damage condition is the last challenge to be considered in the analysis, which affects the predicted initial beam camber. The damage condition created in the lab was achieved by cutting the bottom strand at each stem at mid-span using a hand cutting wheel. However, the damage observed in the field includes exposure of prestressing strands along the span resulting in the loss of cross-section at random locations due to corrosion. There will be less loss of camber for the damage created in the lab as the prestressing strands can be developed stress away from the cut area. However, as for the damage observed on-site, due to the exposed prestressing strand and losses of cross-section, prestressing strand stress will not be able to develop due to the bond condition and can be considered as the loss of the entire strand along the span. Figure 6.24 illustrates the moment-deflection response of beams with different damage conditions. It can be observed that there is a substantial difference in the predicted response at the early stages of loading for the two damage conditions considered. The predicted moment-deflection response considering

the cut bottom strands at mid-span is similar to the experimental result for the same damaged condition.

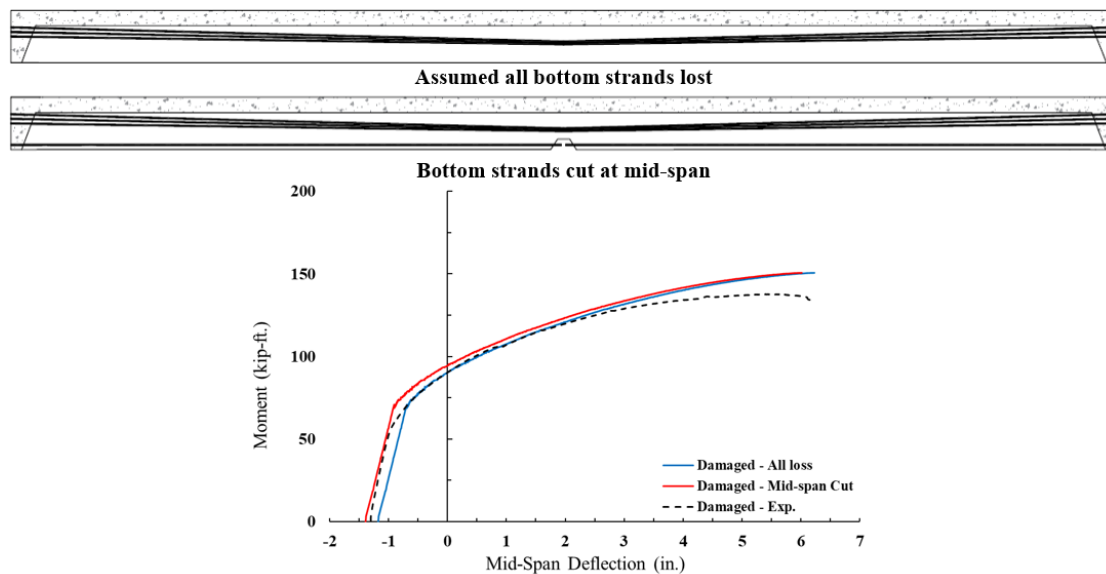
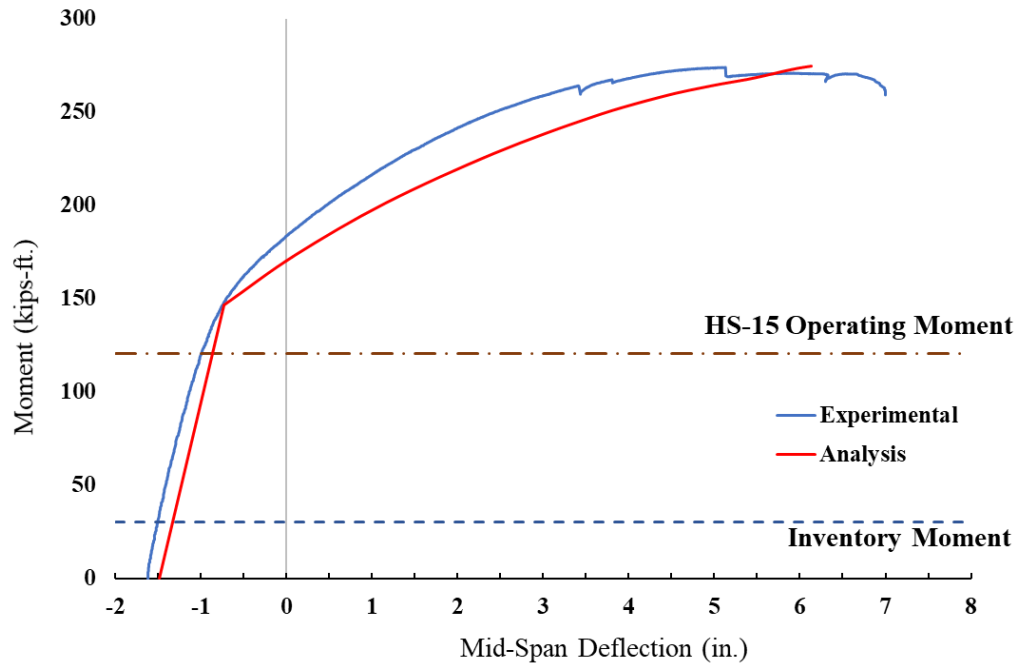


Figure 6.24: Moment-deflection response with different damage conditions.

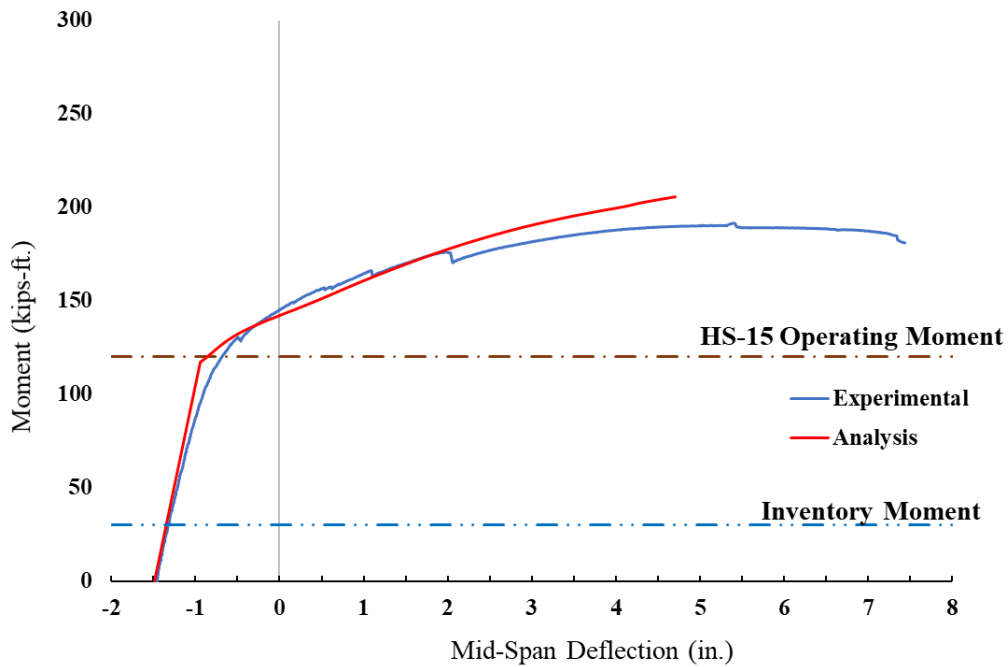
6.1.3 – Results and Comparison of Repaired C-channel Beams

Figure 6.25 shows the analytical prediction compared with the experimental results from Chapter 5.2. A reasonable moment-deflection response was obtained compared to the experimental results. In the analytical prediction, beam deflection was predicted less than the experimental result likely due to the assumed ultimate concrete compression strain limit. Table 6.6 presents a comparison of the flexural capacity between the analytical results conducted in this research to the experimental results and the results from a LSA using experimental data obtained from Chapter 5.2 such as initial camber, deflection at maximum load, and average FRP strain at maximum load. The results show that the LSA predictions for the retrofitted C-channel beams are approximately 5% of the experimental results and provide a conservative prediction. The analytical results of the flexural capacity presented in this research are very similar to the results calculated from the LSA approach using the experimental data, demonstrating that the assumptions used in the analysis are correct and reasonable. Figure 6.26 shows the MF-FRP strain and member deflection relationship

for the analytical and experimental results. The result was obtained from Chapter 5.2, using the current design detailing, identified as specimens MF-FRP-U2 and MF-FRP-D2. An additional experimental result was provided from the retrofitted C-channel beam tested in flexure in this research and presented in Chapter 4. The flexural experiment had similar damage and repair conditions as the MF-FRP-D2 specimen tested in Chapter 5.2, with an additional shear strengthening system applied at the beam end-region, shown as MF-FRP-D2-1 in Figure 6.26. A linear behavior was observed in the experimental results of MF-FRP strain-to-beam deflection. The LSA approach results present a similar MF-FRP strain-to-beam deflection behavior compared to the experimental data. This relation may be used as a method to simplify the analysis. The results show that a similar slope was observed on the MF-FRP strain-to-beam deflection response for both MF-FRP-D2 and MF-FRP-D2-1. It is said that the same strain deflection response can be obtained from the MF-FRP repair system applied on the same cross-section and repair details. The relation between MF-FRP strain and beam deflection can be obtained from the slope of the relationship, decreasing the number of iterations required in the LSA approach.



(a) MF-FRP-U2 (repaired, undamaged)



(b) MF-FRP-D2 (repaired, damaged)

Figure 6.25: Comparison of moment-deflection results.

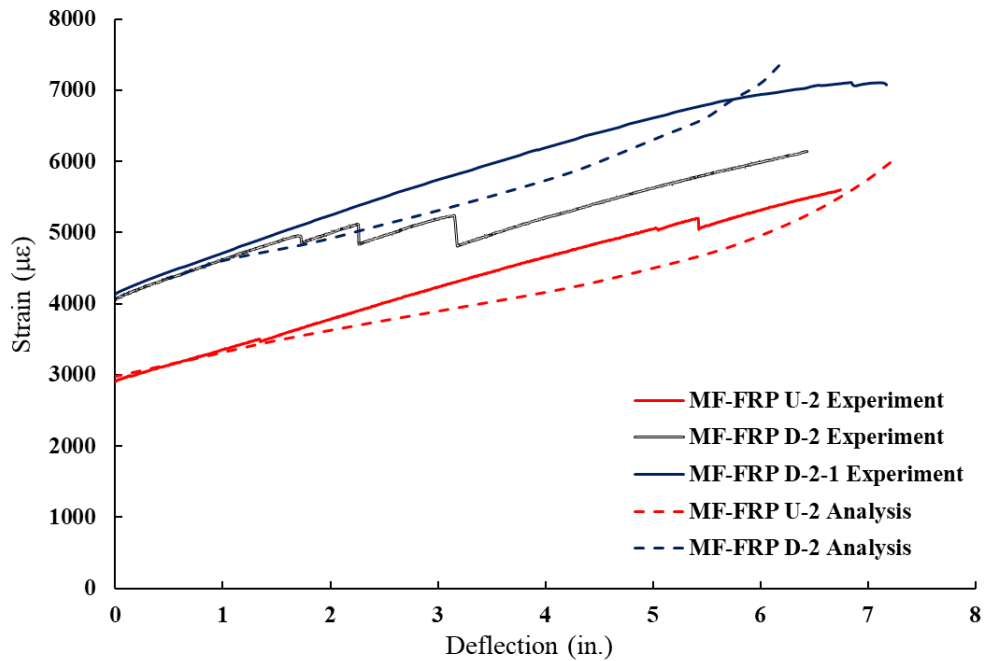


Figure 6.26: MF-FRP strain-to-member deflection relationship of the experimental and analytical results.

Table 6.6: Comparison of experimental and analytical results of ultimate capacity.

Specimen ID	Experimental moment ^a (kips-ft.)	LSA moment ^b (kips-ft.)	Predicted moment ^c (kips-ft.)	Pred. ^c / Exp.	Pred. ^c / LSA. ^b
MF-FRP-U2	274	267	274	1.00	1.03
MF-FRP-D2	192	193	205	1.07	1.06

^a Ultimate moment obtained from three-point bending

^b LSA approach using experimental data

^c Predicted ultimate moment from current research

6.2 – Modeling of Repaired Cored Slabs

This section presents a procedure to model prestressed concrete cored slabs repaired with the MF-FRP repair system using the LSA approach. The analytical procedure is similar to the modeling procedure used for repaired C-channel beams but is generally easier to apply. The second-order effect is minimal on the repaired cored slab due to the location of the MF-FRP system, which is installed on the bottom face of the slab. Considering the global behavior of repaired cored slabs, the second-order effect initiates at the early stages of loading due to the gap between the MF-FRP plate and the bottom of the slab because of the thickness of the fixed anchor plate. The second-order effect no longer exists when the slab engages the MF-FRP plates once the slab deflection closes the gap between the MF-FRP plate and the bottom of the slab. Therefore, to simplify the modeling procedure the second-order effect is neglected in the prediction of repaired cored slabs using the MF-FRP system, and the MF-FRP plate is assumed to be located at the bottom face of the cored slab and perfectly bonded to the concrete so that the increased strain in the MF-FRP plate and concrete will be the same at that level. An overview of the procedure is explained, followed by a discussion of the constitutive models and a comparison of analytical results with experimental results. A simplified analytical procedure is presented at the end of this section, allowing quick predictions of the strengthened section capacity.

6.2.1 – Modeling Procedure

The general analytical approach using LSA and the first moment of area theorem is similar to that used to model the repaired C-channel beams, which is described in Section 6.1.

The detail analysis procedure for the prestressed MF-FRP retrofitted cored slab is shown below:

- 1 Define the cross-sectional geometry and material properties.
- 2 Discretize the cross-section into layers with a constant thickness.

- 3 Calculate the area and centroid location for each layer.

Note: Steps 1 to 3 set up the cross-section prior to the start of the iterative analysis in Step 4.

- 4 Open first iterative loop by selecting a bottom strain value (strain at the extreme bottom layer).

- 4.1 Open second iterative loop by assuming top strain value (strain at top extreme layer).

- 4.1.1 Calculate the strain at each layer assuming a linear strain profile bounded by the bottom and top strain assumed.

- 4.1.2 Calculate the stress at each layer for each constituent material (concrete, steel, FRP) based on the appropriate stress-strain constitutive models.

- 4.1.3 Calculate the resultant axial forces in each layer.

- 4.1.4 Check that the sum of forces is equal to zero. If not, go back to step 4.1 and assume a new top strain.

- 4.1.5 With equilibrium satisfied, calculate the moment contribution of each layer.

- 4.2 Sum moments and calculate curvature to get the corresponding point on moment-curvature response plot.

- 5 Repeat step 4 selecting new bottom strain value until sufficient moment-curvature points are obtained to model the full sectional response.

- 6 Plot the moment-curvature response

- 7 The full moment-deflection response of the repaired cored slab can be generated using the first moment of area theorem.

Figure 6.27 gives a visualization of the LSA procedure. The concrete is discretized into 0.1 in. deep layers. The prestressing strands at each layer are lumped into a total area of steel proportional to the number of strands present in that layer. The same is done with FRP, which is lumped into a total FRP area proportional to the number of plates used.

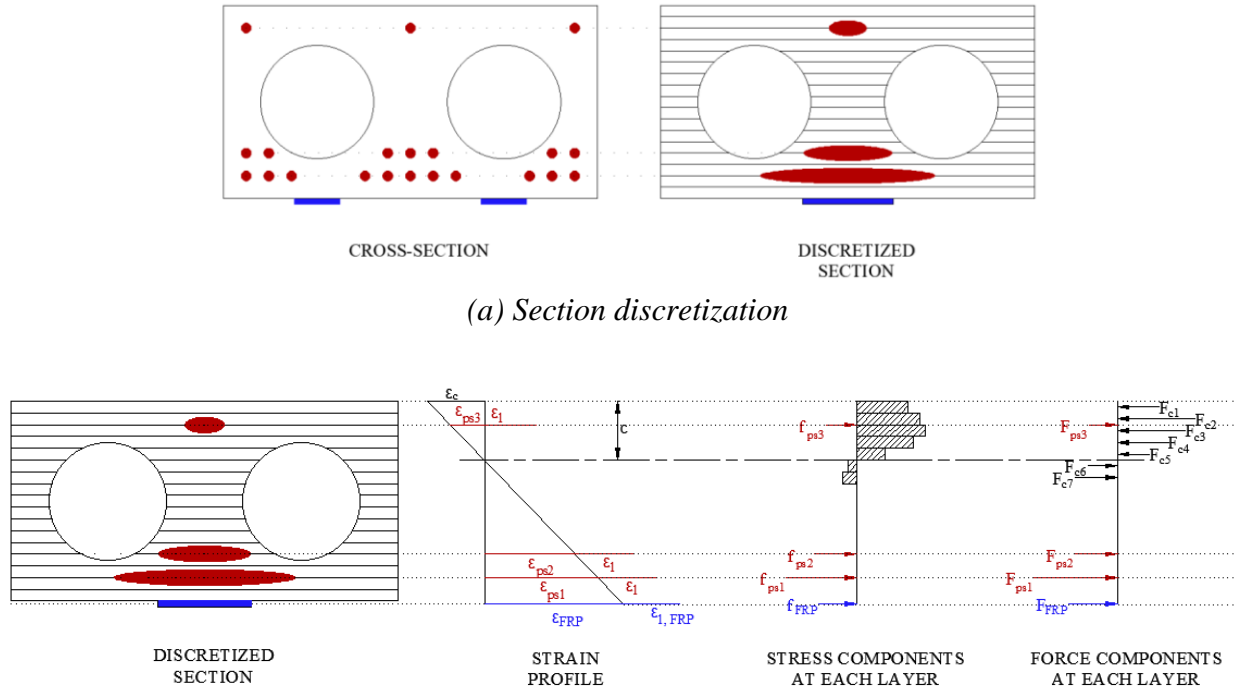


Figure 6.27: Visualization of LSA procedure.

The concrete strain at each layer is directly extracted from the profile shown (a linear interpolation from the selected bottom strain to the assumed top strain). Prestressing steel strains however are the sum of the strain of the surrounding concrete layer from the linear profile, $\epsilon_{ps,i}$, and the “locked in” strain from the jacking force, ϵ_1 . Similarly, the FRP strain is the sum of the corresponding strain at the depth of the plates along the linear strain profile, assuming full strain compatibility, ϵ_{FRP} , and the “locked in” strain from the post-tensioning force. Full strain compatibility is assumed in this analysis, noting that the initial slip is overcome by the post-tensioning.

The strains calculated can be used to obtain the corresponding stress at each layer, using stress-strain relations from appropriate constitutive material models, which already described in Section 6.1.1. The stresses can in turn be used to calculate the resultant axial forces in the section; the stress of each component at a given layer is multiplied by its area in that layer. A reference point can be selected, and the moment contributions of each layer can be calculated and summed to obtain the total moment in the section. For instance, if the top of the section is chosen as the reference point, the moment at each layer can be calculated by multiplying the force at each layer by the distance from the top of the section to the centroid of the layer, and the sum of these moments gives the total moment in the section. An approximate moment-deflection plot can in turn be extracted from the moment-curvature response using numerical integration. For a given applied load, the moment distribution can be calculated, and the corresponding curvature can be obtained from the previously generated moment-curvature response.

The LSA method is especially useful in this research considering the need to evaluate the load limits set by AASHTO. Of most interest is the ability to capture the behavior of an MF-FRP strengthened PC beam in and around the elastic portion, where the inventory and operating ratings are defined.

6.2.2 – Modeling Challenges

Based on the experimental results obtained for cored slabs, a few modelling complexities arose. Certain aspects of the moment-deflection results stem from behaviors that are beyond the capabilities of a typical LSA program. These are discussed below to set expectations for the levels of accuracy to be achieved by the LSA program. As a result, the shortcomings discussed in the following section do not detract from the quality of predictions subsequently presented.

6.2.2.1 – Prediction of Failure Point

For the unstrengthened specimens, the LSA performs well in capturing the behavior of all experiments but fails to predict the failure load and corresponding deflection well. Figure 6.28 shows an example of a comparison between an experimental result and a prediction and highlights the discrepancy in capacity (ΔP) and deflection (Δd). This can be due to the assumption that the compressive strength of concrete (f'_c) is the same for all specimens, which is most likely incorrect; specimens tested may have been cast using different batches of a given concrete mix, or subjected to different loading and exposure conditions depending on their specific location within the bridge superstructure, resulting in material variability after more than 40 years of service. Therefore, the compressive strength assumed (10.5 ksi) may be higher than the actual strength of some of the specimens. Another reason for this is tied to the first moment area method used to obtain the load-deflection curve by discretizing the member into 1 ft. segments. The procedure finds the curvature at each boundary for each segment along the discretized member, corresponding to the moment from the applied load assumed. Along each segment, the behavior is interpolated between the boundaries, and so is assumed to share their properties; if, for instance, cracking has occurred at one boundary, then it is assumed to have occurred on each side of that boundary. Consequently, the stiffness of uncracked concrete between cracks is not captured, and instead, a more flexible behavior will be predicted.

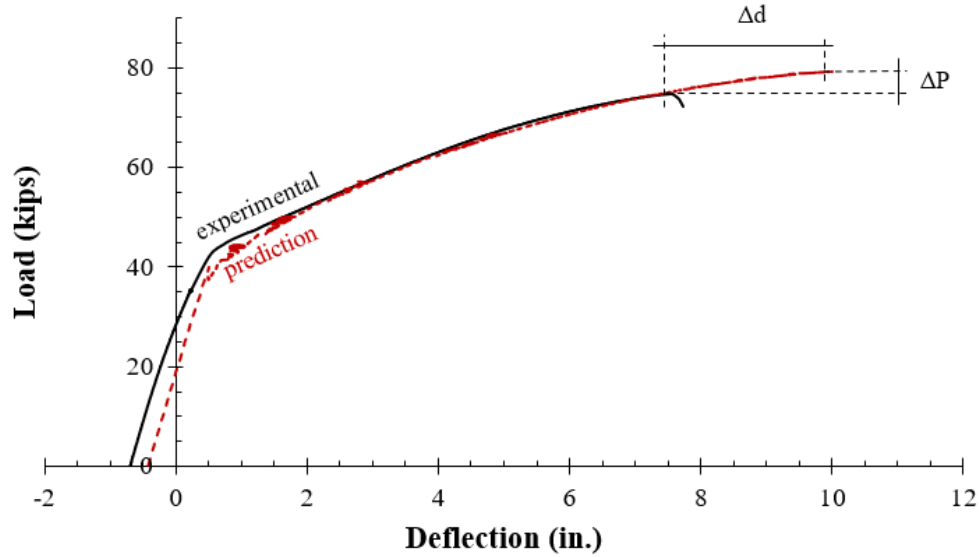


Figure 6.28: Example comparison of experimental result and prediction.

6.2.2.2 – Contact at Midspan

In the discussion on the failure modes observed with the hollow-cores, it was mentioned that as the load was monotonically applied on D-S1, the clearance between the FRP plates, which remained horizontal, and the bottom face of the beam was decreasing in proportion to the beam deflection. The eventual contact of the beam with the plates at mid-span (where the deflection is greatest) exerted a point load at the middle of the plates, introducing bending stresses which precipitated their failure. This presents a complex state of stress unaccounted for by the linear-elastic idealization of the MF-FRP connections, and so is not captured by the LSA predictions.

6.2.2.3 – Prediction of Camber

The hollow-cores tested all exhibited camber, even prior to strengthening and after cutting strands. These beams were retrieved from a bridge that had been in service for over 40 years, and so it is likely that excess camber accumulated over time as a result of creep. The predictions of the LSA do not account for creep, as consideration of long-term effects drastically changes the behavior predicted and is not consistent with the short-term monotonic loading applied during the experiments. Prediction of initial camber from creep also heavily relies on assumed values of the

concrete compressive strength and prestress losses, and so is fraught with uncertainties. It is therefore neglected in this LSA, and all predictions consistently underpredicted camber, such that the predicted response is shifted to the right. As a result, predictions will produce slightly higher levels of deflection (and by extension, damage) at the inventory and operating load limits, offering reasonable conservatism.

6.2.3 – Comparison to Experimental Results

6.2.3.1 – Undamaged-Unstrengthened

As mentioned in the full-scale experimental results discussion, specimen U-U may have contained some internal damage unidentified visibly prior to testing or could have had a lower concrete compressive strength than the one assumed. This is evidenced by its load-deflection curve overlapping with that of specimen D-U1 (Figure 5.21), indicating virtually no change in stiffness. The analytical prediction in Figure 6.29 confirms this. The model, the accuracy of which will be supported by subsequent predictions for damaged specimens, follows the same overall trend of the U-U curve, but exhibits an ultimate moment that is 8% higher.

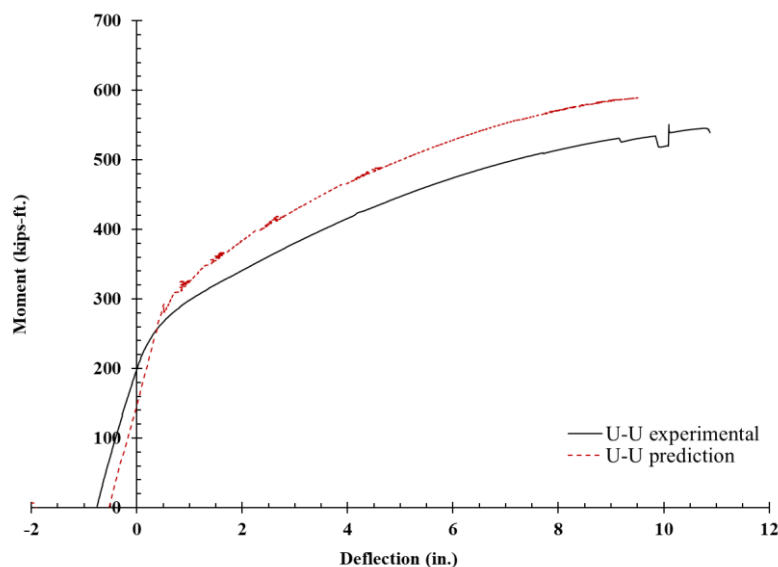


Figure 6.29: Comparison of analytical prediction to experimental result (U-U).

6.2.3.2 – Damaged-Unstrengthened 1

Besides the slight discrepancy in initial camber (due most likely to creep), the prediction matches the experimental load-deflection curve very well (Figure 6.30). The prediction goes beyond the point of experimental failure, which was previously mentioned in the discussion on the modelling challenges. It is most likely a consequence of variability in concrete compressive strength across specimens and of the first moment area method used to develop the load-deflection curve. The AASHTO load limits are the biggest concern however, and as the slope and extent of the elastic portion are accurately modeled, the assessment of behavior at the inventory and operating limits will be appropriate and conservative (due to unaccounted for camber from creep).

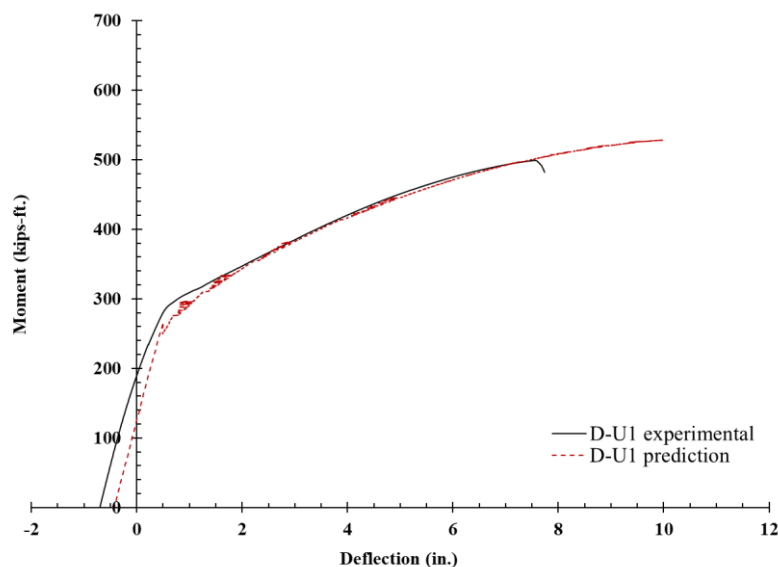


Figure 6.30: Comparison of analytical prediction to experimental result (D-U1).

6.2.3.3 – Damaged-Unstrengthened 2

Similarly, the prediction for D-U2 matches the experimental load-deflection curve very well, as can be seen in Figure 6.31, but over predicts the failure point. Again, the region around the elastic portion where the inventory and operating limits are defined is of most interest and is accurately depicted aside from the slight shift to the right due to the additional camber from creep

not accounted for in the analysis. Therefore, for the purposes of NCDOT, this LSA method is appropriate.

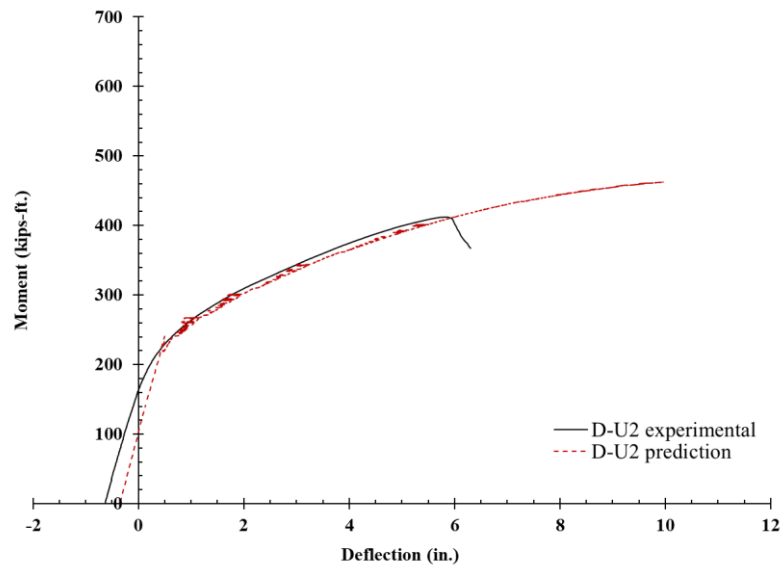


Figure 6.31: Comparison of analytical prediction to experimental result (D-U2).

6.2.3.4 – Damaged-Strengthened 1

The LSA program predicts the ultimate capacity of specimen D-S1 within 4.2% of the experimental results (Figure 6.32). The overall trend of the strengthened section is also accurately modelled. The largest discrepancy is the deflection at which the FRP fails, where the prediction is lagging by approximately 1.5 in. The model can therefore be said to offer conservative predictions of the strengthened capacity. Considering the modeling challenges previously discussed, namely the complex state of stress from the contact of the beam with the FRP at midspan and the different sources of variability in the system, this prediction is satisfactory. Furthermore, and consistent with the unstrengthened predictions, the behavior in and around the elastic region where the load limits are defined is very well depicted.

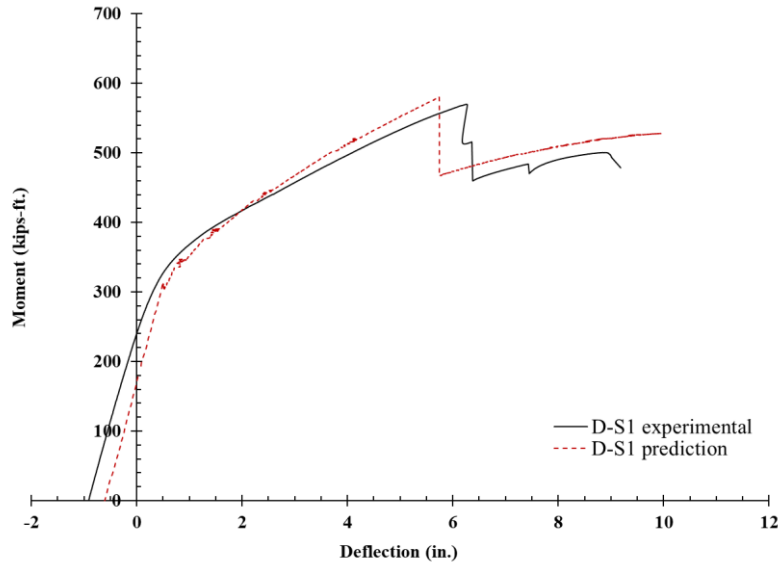


Figure 6.32: Comparison of analytical prediction to experimental result (D-S1).

6.2.3.5 – Damaged-Strengthened 2

The LSA program predicts the ultimate capacity of specimen D-S2 within 5.39% of the experimental results (Figure 6.33). The same points made in comparing the prediction of D-S1 to experimental results can be made here. The only difference is that the program predicts an early FRP failure, while the results indicate a concrete crushing failure. It is worth noting that for D-S2, the concrete crushing failure occurs at nearly 6 in. of deflection, which is very close to the deflection reached when the FRP failed for specimen D-S1. Considering this and the model's inability to predict ultimate deflections for damaged specimens, the FRP failure predicted for D-S2 is not entirely inappropriate, although it is lagging by nearly 1.5 in. of the actual deflection corresponding to FRP failure. This prediction is therefore conservative and reasonable enough for the evaluation of compliance with AASHTO load limits.

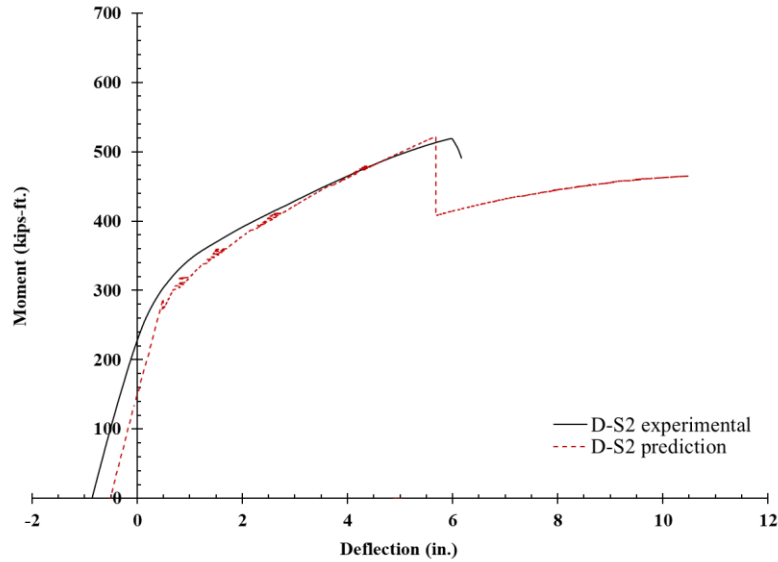


Figure 6.33: Comparison of analytical prediction to experimental result (D-U2).

6.2.4 – Ultimate Strength Analysis

A simplified procedure to calculate the flexural capacity of a strengthened section may be of interest to the designer. This section presents such a procedure, using the case of the tested hollow-cores as an example.

An equivalent rectangular stress block is considered for the concrete stress distribution. Figure 6.34 shows this idealized stress block model, as well as the linear strain profile assumed along the cross-section. FRP failure is assumed to control the behavior of the strengthened section, in which case the Whitney stress block is not appropriate, as concrete strain (ϵ_c) will be less than 0.003 (the assumed crushing strain of concrete). The strain at which the peak compressive stress occurs (ϵ'_c) is taken as 0.002. The parameters α and β can be calculated using Equations 6.24 and 6.25.

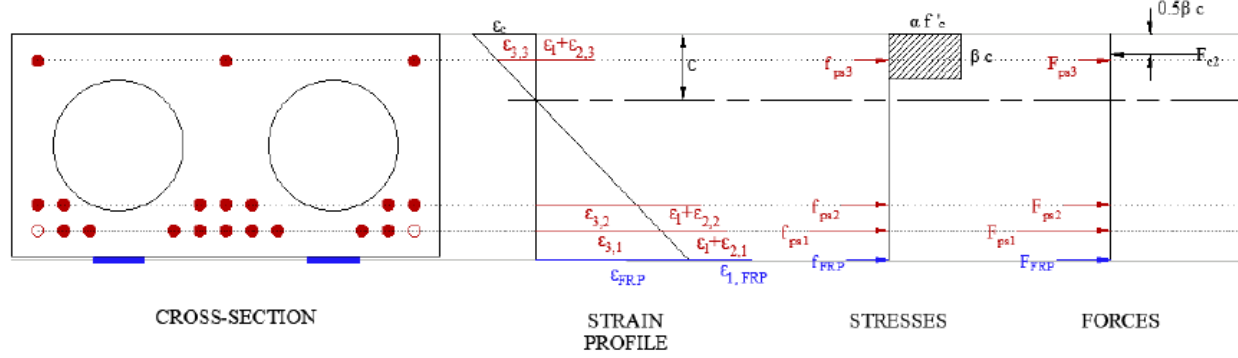


Figure 6.34: Equivalent stress block model.

$$\alpha\beta = \frac{\varepsilon_c}{\varepsilon'_{fc}} - \frac{1}{3} \left(\frac{\varepsilon_c}{\varepsilon'_{fc}} \right)^2 \quad (6.24)$$

$$\beta = \frac{4 - \frac{\varepsilon_c}{\varepsilon'_{fc}}}{6 - \frac{2\varepsilon_c}{\varepsilon'_{fc}}} \quad (6.25)$$

This equivalent stress block is appropriate provided that c , the neutral axis depth, is less than 4 in. away from the top face of the beam, so that the width of the compression zone is constant at $b = 33$ in. The concrete force can then be calculated as

$$F_c = (\alpha f'_c)(\beta c)b \quad (6.26)$$

The prestressing steel strain for each layer is the sum of three terms (Equation 6.27): ε_1 , the initial jacking strain (Equation 6.28); $\varepsilon_{2,i}$, the section decompression strain (Equation 6.29); and $\varepsilon_{3,i}$, the compatibility strain (Equation 6.31).

$$\varepsilon_{ps,i} = \varepsilon_1 + \varepsilon_{2,i} + \varepsilon_{3,i} \quad (6.27)$$

$$\varepsilon_1 = \frac{\frac{P_j}{A_{ps}} \times l}{E_{ps}} \quad (6.28)$$

where P_j is the jacking force (21.7 kips), A_{ps} is the area of each prestressing strand (0.115 in.²), E_{ps} is the elastic modulus of the prestressing steel (29000 ksi), and l is the percentage of remaining prestressing force after losses assumed (70%), which is based on trial and error to obtain the best fit response.

$$\varepsilon_{2,i} = \frac{f_{c,i}}{E_c} \quad (6.29)$$

where $f_{c,i}$ is calculated as

$$f_{c,i} = \frac{P_j n_{ps,i}}{A_c} + \frac{(P_j n_{ps,i})(e - \frac{h}{2})^2}{I_c} \quad (6.30)$$

where A_c is the area of the concrete cross section (404 in.²), $n_{ps,i}$ is the number of strands per layer, e is the eccentricity of strands at each layer, h is the depth of the section (17 in.), and I_c is the uncracked moment of inertia of the section (12529 in.⁴).

$$\varepsilon_{3,i} = \frac{\varepsilon_{FRP}(d_i - c)}{d_{FRP} - c} \quad (6.31)$$

where d_{FRP} and d_i are the depths of the FRP plates and the layer of prestressing strand considered, respectively. ε_{FRP} , is the FRP failure strain calculated as the ratio of the ultimate slip over E_{FRP} (9020 ksi) and is equal to 0.0103 for 0.5 in. diameter bolts, per the constitutive MF-FRP model presented earlier in this chapter.

As the ultimate FRP strain controls the failure of the section, the force in each plate, F_{FRP} , is taken as the ultimate capacity from the MF-FRP constitutive model (46.4 kips for 0.5 in. bolts). The prestressing steel force at each layer, $F_{ps,i}$, is simply the area of steel multiplied by the stress, calculated using the Ramberg-Osgood fit in Equation 6.14, with the same A, B, and C constants (0.015, 113, and 4, respectively).

The procedure is a simple iterative process to achieve force equilibrium. This is done by trial and error of different values for the neutral axis depth c . After assuming a neutral axis depth value, all the calculations can be carried from Equation 6.24 to 6.31, and the assumption can be verified by summing all the forces in the section:

$$\sum F = F_c + \sum F_{ps,i} + \sum F_{FRP,i} \quad (6.32)$$

When the assumed c yields a sum of forces close to zero, the moment capacity of the section can be calculated as follows

$$M_n = F_c \left(\frac{\beta c}{2} \right) + \sum F_{ps,i} d_i + \sum F_{FRP,i} d_{FRP,i} \quad (6.33)$$

The cross-section in Figure 6.34 strengthened with two FRP plates is considered. The number of prestressing strands in the bottom layer is reduced by two, simulating damage amounting to two fully-lost strands. As such, the procedure can be carried out and compared with the experimental result for D-S1. The nominal moment M_n is found to be 626 kip-ft. This equates to 94.2 kips of total applied load based on the experimental setup (four-point bending with load distributed to third points). D-S1 had a measured capacity of 85.5 kips, and so the procedure yielded a result that overestimates capacity by 10%.

The process is repeated for a damage amounting to four fully-lost prestressing strands. The nominal moment is found to be 562 kip-ft., equating to an applied load of 84.5 kips. D-S2 had a measured capacity of 77.9 kips, and so this procedure over predicts capacity by 8.5%. An over prediction within 10% of the experimentally obtained capacity is within reason for such assessments and is in part due to material and geometric variability of specimens taken from previously in-service bridges.

6.3 – Observations

6.3.1 – Repaired C-Channel Beams

The developed analytical modeling procedure of retrofitted C-channel beams can be summarized as follows:

- By considering the second-order effect from the MF-FRP system, the analytical procedure presented in this chapter shows a good predicted behavior and conservative ultimate prediction within a 5% difference compared of the experimental results.

- The predicted member behavior can be improved substantially by using good quality input data, including concrete strength, prestress strand properties, prestressing strand profile, prestress losses, development length, and damage condition.
- Both the applied strain gauges on the prestressing strand and the cracking moment methods resulted in similar total prestress losses for the beams tested.
- Total prestress losses obtained from the experimental methods are 13% to 20 % higher than that of empirical code based models, which may be due to corrosion on the prestressing strand, resulting in additional prestress losses due to reduced bond and slip between the concrete and the strand. This phenomenon for deteriorated in-service bridges is not considered by the empirical calculations.

6.3.2 – *Repaired Cored Slabs*

The comparison of analytical predictions to experimental results can be summarized as follows:

- The analytical procedure presented constitutes a modeling attempt using a simple linear-elastic idealization of the MF-FRP behavior, and shows very good agreement with experimental results, which validates the LSA procedure devised for this research.
- The LSA procedure comes short in predicting the exact failure point and the initial camber, due to variability in the concrete compressive strength, assumptions inherent to the first moment area method used to extrapolate the load-deflection curve, and neglect of additional camber from creep. This is not a concern however, as the region around which the AASHTO inventory and operating limits are defined is consistently predicted very well.

- Strengthened predictions of ultimate capacity are conservative, with predicted capacities that are with 4.2 to 5.4% of the experimental results.
- The moment capacity of repaired cored slab can be calculated using ultimate strength analysis and the calculated capacity are overestimated with 10 and 8.5% of experimental results.

CHAPTER 7 – DESIGN AND VALDATON OF A SHEAR STRENGTHENING SYSTEM FOR C-CHANNEL BEAMS

The previously developed flexural MF-FRP retrofit system can provide a successful flexural capacity and AASHTO load rating improvement of deteriorated beams as demonstrated in Chapter 5 by testing C-channel beams and cored slabs from out-of-service bridges. Although previous studies considered flexural deterioration only as seen by the example of Bridge 340080 (refer to Figure 1.1(a)), shear deterioration can also occur at the ends of beams that need additional attention. The deterioration at the end regions of beams include loss of concrete stem section and exposure of prestressing strands and stirrups due to overloaded traffic and corrosion from water leakage. The purpose of this full-scale experimental program is to study the beam shear behavior by simulating damage similar to that observed on-site in Bridge 810003 in Sampson County, NC (Figure 7.1). Additional flexural testing was also undertaken to provide information that was not previously collected. This includes beam prestress losses and restored camber from the repair system to improve the analytical modeling.



Figure 7.1: Shear deterioration at beam end-region observed on Bridge 810003.

This Chapter presents the experimental testing and results of C-channel beams with different levels of shear deterioration, and with different repair systems tested in shear. Additional flexural testing with both shear and flexural deterioration repaired with the combined shear and flexural repair system was also conducted to compare with the repaired flexural deteriorated C-channel beams tested in Chapter 5.2. The detailed experimental program is presented, including specimen descriptions, test setup, test matrix, and repair procedure. The experimental results and discussions are then presented in this chapter. The last section provides analytical predictions of the unstrengthened C-channel beams using ACI 318 (2019) to validate the experimental results.

7.1 – Design of the Shear Strengthening System

The design flexural MF-FRP system presented in Chapter 3 is only for flexural deterioration. However, to address the shear concern, a shear strengthening system was designed for the shear deterioration at the end regions of C-channel beams. The design aims to improve the deteriorated beam shear behavior and integrate the original flexural MF-FRP system. A steel plate was used for the shear strengthening due to the simplicity of design, availability, and ease of integration with the existing MF-FRP system. The shear strengthening plate was optimized based on AISC (2017) design guidelines with a minimum shear design strength of 20 kips using Grade 50 steel to provide sufficiently increased shear capacity of the shear deteriorated beam back to its original shear capacity. Six 5/8 in. diameter bolts were used to attach the shear strengthening plate to the concrete stem after checking bolt shear, bearing capacity, and concrete splitting in both vertical and longitudinal directions. Figure 7.2 shows the designed shear strengthening plate. The dimensions of the shear strengthening plate are 38 in. long, 10 in. deep, and 0.25 in. thick with a slope at one end to fit the inside of the C-channel stem. A 0.25 in. plate thickness not only provides enough shear strength and ease of handling on-site by the installation crew, but avoids the potential

bending issue during loading. The weight of this shear strengthening plate is 27 lbs. and can be handled by one person on-site.

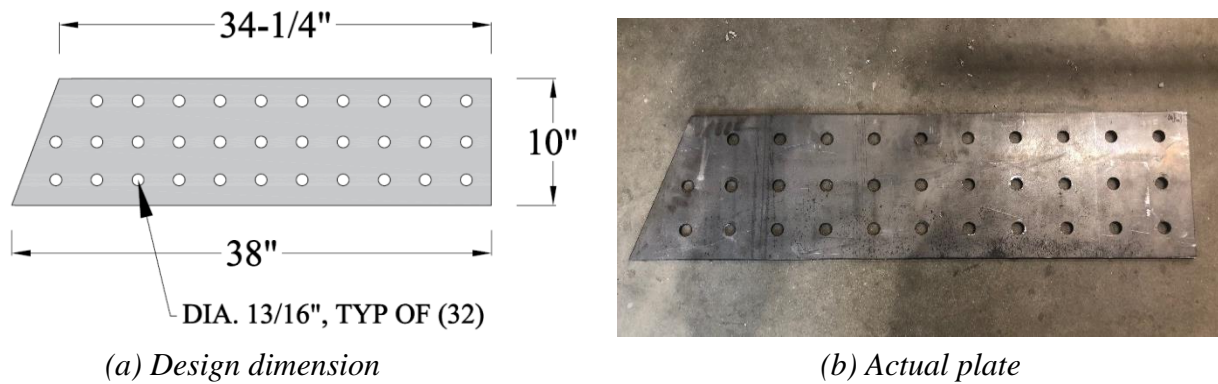


Figure 7.2: Shear strengthening plate.

The shear strengthening plate is designed to be located between the fixed anchor plate and the concrete stem through the hole pattern, as shown in Figure 7.3. The bolt hole grid of the bottom two rows on the shear strengthening plate follows the same pattern as the fixed anchor plate to provide flexibility of locating the anchor plate while installing the flexural repair system. Shear strengthening bolts were anchored to the top and bottom two rows to anchor the maximum possible depth of the shear strengthening plate. Combining the flexural MF-FRP system with the shear strengthening plate, the proposed flexural/shear repair can be used to address both flexural and shear deterioration. Spalled concrete associated with end-region deterioration requiring shear strengthening must be adequately patched to restore the original concrete cross-section. The quality of the patch, as well as its bond to the existing concrete, must be sufficient to withstand the effects of drilling the bolt holes and to resist the forces applied by the bolts while the retrofit is in service.

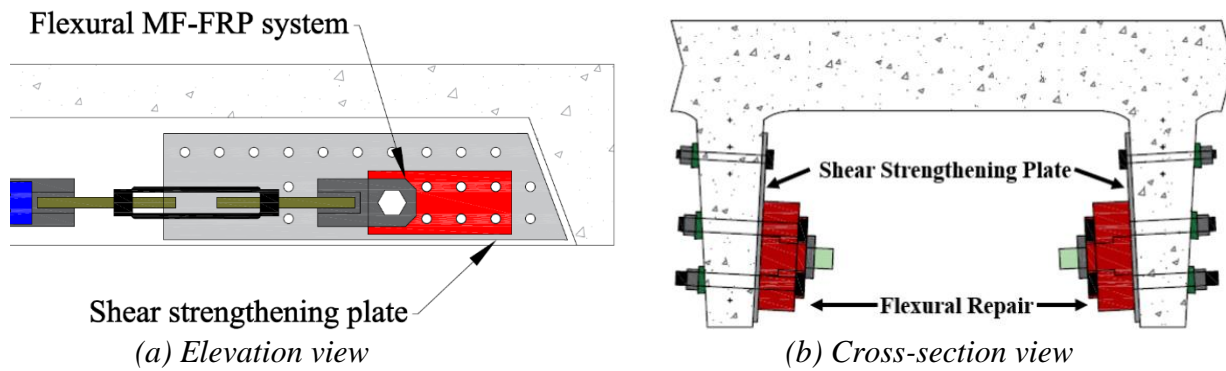


Figure 7.3: Flexural/shear repair system.

7.2 – Experimental Program

7.2.1 – C-channel Beams

Four 30 ft.-long C-channel beams were obtained from Bridge 380093 in Granville County, NC, the same C-channel bridge as the beams tested in Chapter 5.2 tested. All four C-channel beams were in relatively good condition based on visual inspection with no concrete spalling or exposed prestressing strands. The good quality of the beams enabled the research team to control the damage level to achieve the goal of the experimental program. All beams were stored at the NCDOT Division 5 yard and shipped to the Constructed Facilities Laboratory (CFL) on March 10th, 2021. Figure 7.4 shows the beams as stored at the NCDOT Division 5 yard and the delivery by truck to the CFL.



(a) C-channel beams stored at NCDOT yard



(b) C-channel beams delivered to the CFL

Figure 7.4: C-channel beams used in this test program.

As mentioned in Chapter 6, the cross-section of the C-channel beam used in this research was a type A pattern with a 13 in. stirrup spacing based on NCDOT (1966). The design detail of the C-channel beam can provide stirrup spacing information that minimizes the chance of cutting steel during drilling. As for the beams repaired with the MF-FRP system, the same detail can be applied to beams tested in Chapter 5.2 to enable a direct comparison.

7.2.2 – Failure Envelope of the PC C-channel Beam

The failure envelope along the beam for both flexure and shear needed to be determined before finalizing the test setup. The failure envelopes were developed by discretizing the beam into 1 ft. long segments and the flexural and shear capacity calculated at each segment.

7.2.2.1 – Moment Envelope

The moment envelope was calculated in both undamaged and damaged unstrengthened conditions using the LSA approach discussed in Chapter 6 by considering the strand profile and development length of the prestressing strands. Figure 7.5 shows the moment envelope for the undamaged and damaged condition. The assumed damaged condition was the loss of the bottom strand at each stem, which is considered as the worst case scenario. By considering the effect of the prestressing development length and the harped profile of the prestressing strand, the beam flexural capacity starts at zero at the ends and increases toward the mid-span as the prestressing stress develops.

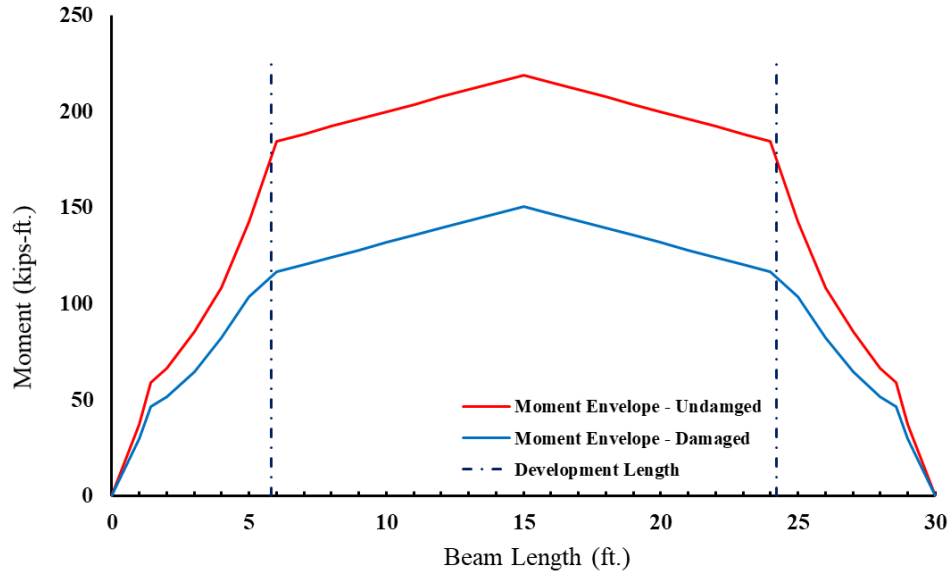
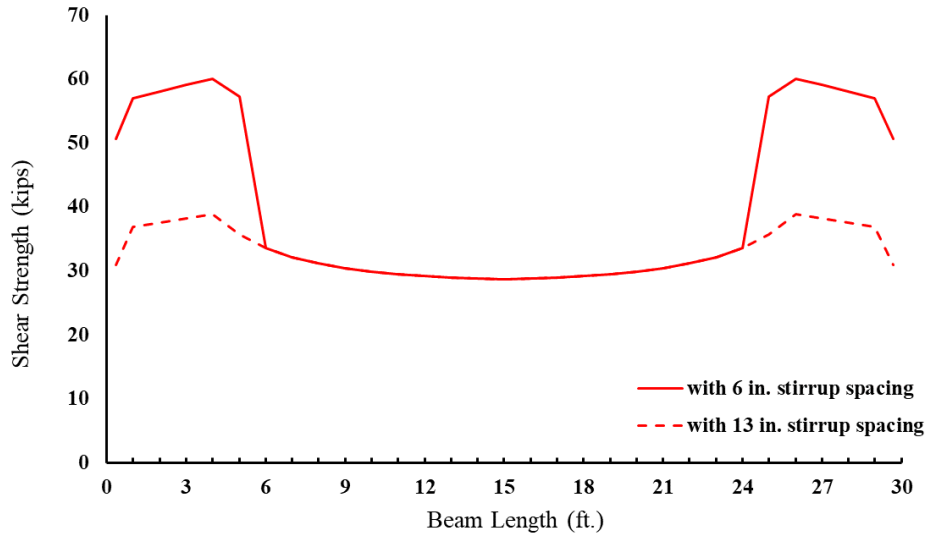


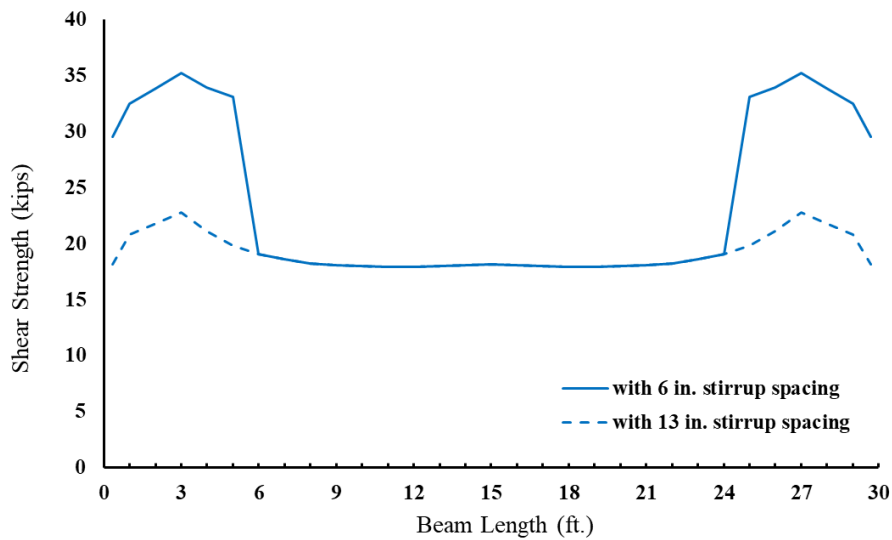
Figure 7.5: Moment envelope of undamaged and damaged C-channel beams.

7.2.2.2 – Shear Envelope

The shear capacity at each segment was calculated using the method from ACI 318 (2019) for prestressed concrete members. The actual effective depth of the prestressing strand was applied to the calculation to obtain the concrete shear strength. Concrete shear strength of the damaged section was calculated assuming the loss of the bottom strands, which is the same damaged condition created in the full-scale experiments. The stirrup shear strength was initially calculated using the spacing obtained from the NCDOT standard C-channel beam drawings and site measurements obtained from Bridge 810003 in Sampson County, NC, which were 13 and 6 in., respectively. The prestressing strand effective depth used in the ACI method was the actual effective depth of the section instead of using the suggested 80% of the cross-sectional height. Due to the slope along the height of the concrete stems (refer to Figure 5.1), the bottom web width was selected to calculate the concrete shear strength. These modifications aim to obtain the best estimates of concrete shear strength. Figure 7.6 presents the calculated shear capacity envelope of the undamaged and damaged section considering the two different stirrup spacing.



(a) Undamaged

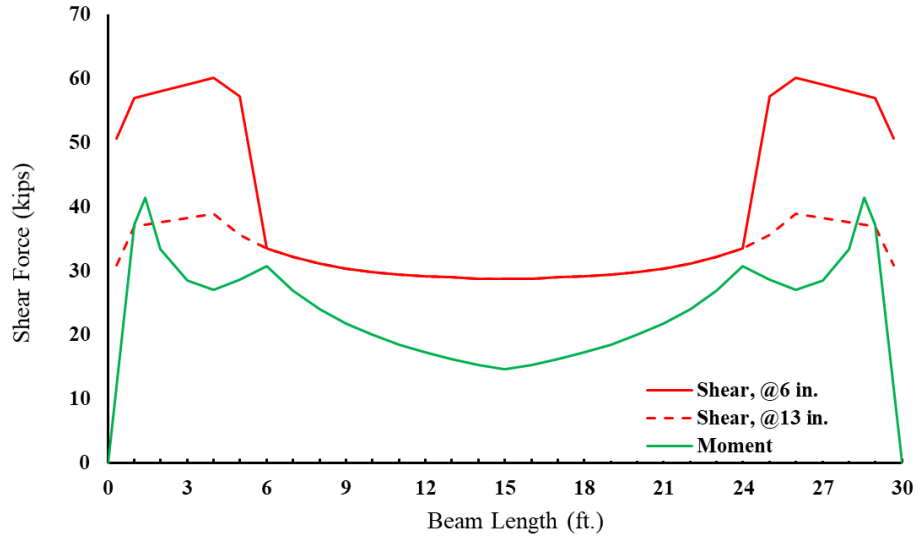


(b) Damaged

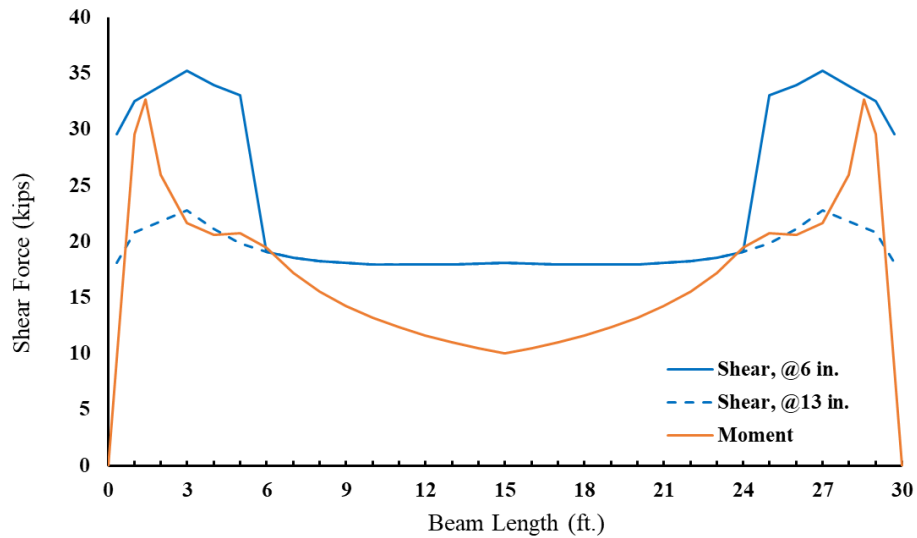
Figure 7.6: Shear envelope along the C-channel beams.

7.2.2.3 – Failure Envelope

Figure 7.7 shows the moment and shear failure envelope for undamaged and damaged beams. The envelopes are presented in terms of shear force to allow a direct comparison. The objective is to observe a shear failure by avoiding a premature flexural failure so that the shear behavior of the deteriorated beam may be determined.



(a) Undamaged



(b) Damaged

Figure 7.7: Failure envelope along the length of C-channel beams.

According to the result presented in Figure 7.7, shear failure can occur before flexural failure at the region around 1 to 3 ft. from the end of the beam for the undamaged and damaged conditions. Therefore, the test setup was designed using a four-point loading system located near the end of the beam considering with the truck axle spacing and anchor hole pattern on the lab strong-floor.

7.2.3 – *Test Setup and Instrumentation*

Four beams and seven tests were conducted to understand the shear behavior of deteriorated C-channel beams. Shear testing was conducted on both ends of the beam to use the specimens efficiently. A reduced span length was required for the second test on the untested end due to the damage condition after testing the first end. All PC C-channel beams tested in shear were supported by concrete blocks with neoprene pads and loaded to failure using hydraulic jacks close to the beam end region with a selected shear span. The load was applied to the beam with four-point loading system using hydraulic jacks. All jacks were connected to an electric pump with a closed hydraulic loop to share the same pressure source and ensure equal applied load.

The North Carolina non-interstate legal vehicles category, shown in Figure 7.8, is used by NCDOT to analyze the operating rating limit of bridges considered in this research. It can be seen that the minimum truck axle spacing is 4 ft. for the different types of trucks in this category. Due to the arrangement of the anchor holes on the CFL strong-floor, hydraulic jacks can be connected to two HSS loading tubes 3 ft. apart located on the top of the beam. Therefore, the first two jacks were located 40 in. from the support to create a shear span of four times the average prestressing strands' effective depth. The selected shear span is considered to avoid the deep-beam effect and arching action and enable the beam to experience flexural behavior. The average prestressing strand effective depth is calculated based on the harped strand profile along the beam (11.8 in. at the midspan and 9.1 in. at the ends of the beam). The remaining two jacks were placed 3 ft. away from the first two jacks. The layout was used to simulate the minimum truck axle spacing and apply a reasonable loading configuration.

However, an unexpected flexural failure occurred after testing the first undamaged specimen in shear, resulting in rupture of a prestressing strand due to the moment at the second loading point. Subsequently, the test setup was changed to a single point load using two hydraulic

jacks to reduce the applied moment at the loading point relative to the shear in the shear span. Therefore, the remaining shear experiments were conducted using an one-point load test setup.


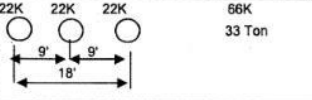

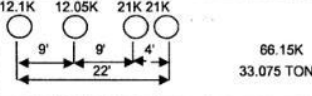

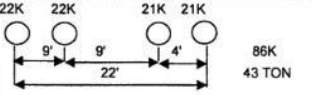
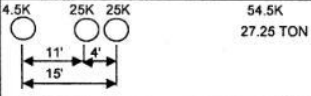
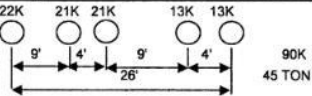
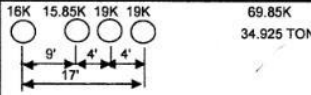
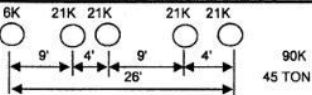
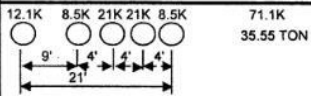
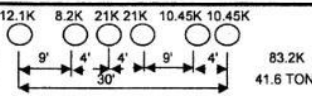
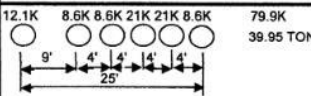
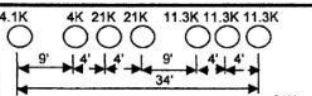
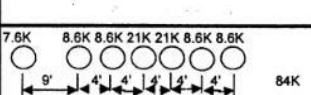
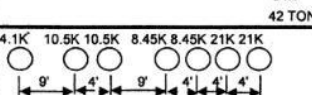
SINGLE VEHICLE (SV)			TRUCK TRACTOR SEMI-TRAILER (TTST)		
REF. #	SCHEMATIC		REF. #	SCHEMATIC	
SNSH			TNAGRIT3		
SNGARBS2			TNT4A		
SNAGRIS2			TNAGRIT4		
SNCOTTS3			TNAGT5A		
SNAGGRS4			TNAGT5B		
SNS5A			TNT6A		
SNS6A			TNT7A		
SNS7B			TNT7B		

Figure 7.8: North Carolina non-interstate legal vehicles (adapted from Weiger, 2017).

A three-point bending setup was used for the specimen with both flexural and shear deterioration and the combined flexural and shear retrofit system. This specimen was tested in flexure with the same configuration as tested in Chapter 5.2. The load was applied using a 440 kip hydraulic actuator attached to a steel frame located at the mid-span. A 10 x 20 in. steel bearing plate was used to transfer the actuator force to the specimen in accordance with the AASHTO (2017) bearing area for wheel loading. The specimen was tested under displacement-control, with a load rate of 0.25 in./minute. All three test setups are presented in Figure 7.9.



(a) Initial shear test with two-point loads



(b) Subsequent shear tests with one-point load



(c) Flexural test with 1-point loading at midspan

Figure 7.9: Test setups for different loading conditions.

The applied load was measured using load cells placed on the hydraulic jacks or from the actuator for the shear and flexural experiments, respectively. String potentiometers were used to obtain the member deflection during testing. For the shear tests, string potentiometers were

attached at the applied load points and mid-span. For the flexural test, string potentiometers were attached to the mid-span and quarter-spans. Linear variable differential transducers (LVDT) were installed at each support to measure the relative deformation of the neoprene pads during loading. Electrical resistance strain gauges were installed on the MF-FRP to measure the FRP axial strain while applying the prestressing force and during testing, as can be seen in Figure 7.10.

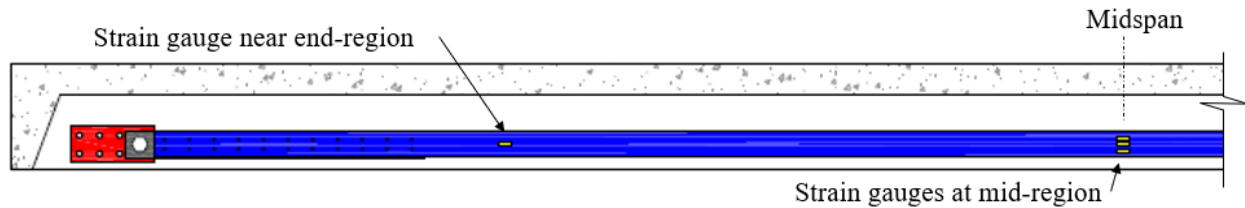


Figure 7.10: Strain gauges installed on the FRP plate.

7.2.4 – Test Matrix

7.2.4.1 – Specimen ID Nomenclature

All test specimens have been uniquely labeled and identified for quality and traceability using the format:

X-PPP-NN-MM

where X is the repair condition, PPP is the damage type, NN is the test type, and MM is the repair system. The detailed nomenclature is summarized in Table 7.1.

Table 7.1: Specimen identification for full-scale testing.

Parameter Description	Detail	ID
Repair condition	Control specimen	C
	Repair specimen	S
Damage type	Undamaged	U
	Severe shear damage	DS
	Intermediate shear damage	IDS
	Flexural damage and severe shear damage	DFS
Testing type	Shear test with two-point load	S2
	Shear test with one-point load	S1
	Flexural test with one-point load	F
Repair system	Flexural repair system	F
	Flexural/shear repair system	FS

7.2.4.2 – Test Description

Table 7.2 presents the test matrix for the four beams and seven tests completed to investigate C-channel beam shear behavior. The first test on beam No. 1 was an undamaged shear control specimen under a two-point loading condition (C-U-S2). The test setup was changed to one-point loading after experiencing flexural failure. The second test on beam No. 1 served as a severe shear damage control specimen (C-DS-S1) by chipping away a 1 ft. length of concrete with a 2 in. height from the bottom of stem starting 8 in. from the end of the beam with a reduced beam span of 23 ft. The same volume of concrete was removed for all shear deteriorated specimens to simulate the damage region. The bottom prestressing strand on both stems were cut using a cutting torch or hand cutting wheel to simulate the severe shear damage that can occur on-site. Test three on beam No. 2 was the undamaged shear control specimen (C-U-S1), serving as a benchmark to compare the behavior with the other shear experiments. Test four on beam No. 2 was the intermediate shear damage specimen (C-IDS-S1) with a similar shear deterioration observed on-site and a reduced beam span of 24 ft. Intermediate shear damage was achieved by only chipping away the concrete and exposing the prestressing strand as described previously. This application was achieved carefully to ensure that only the bottom part of the prestressing strand was not bonded to the concrete. However, the top part of the prestressing strand was still in contact with the concrete section. The bottom strand on each stem was not cut. Figure 7.11 presents the sketch of the intermediate shear damage and severe shear damage cases created in the lab. The intermediate damage condition created in the lab compared to the damage condition observed on-site is presented in Figure 7.12.

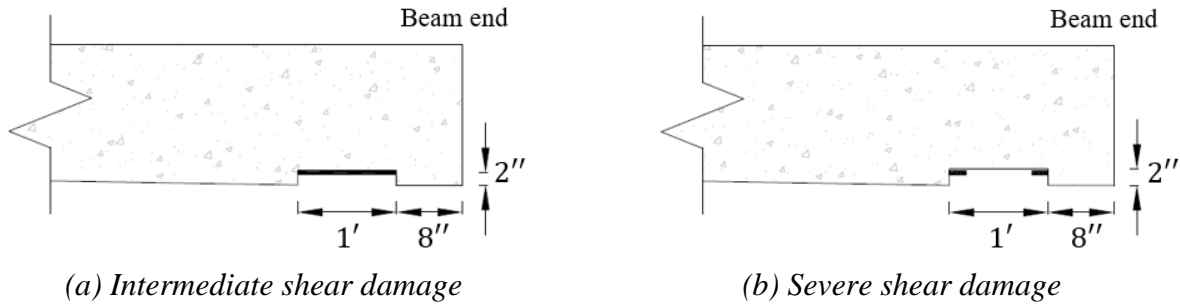


Figure 7.11: Shear damage conditions.



Figure 7.12: Shear damage comparison.

Tests five and six on beam No.3 were the shear tests using the proposed repair system. Both tests five and six included the severe shear damage case. All severe shear damaged regions were patched to restore the concrete prior to the repair installation. Test five was repaired with only a flexural MF-FRP system (S-DS-S1-F), and test six was repaired locally with the proposed flexural/shear system (S-DS-S1-FS) under a reduced beam span of 24 ft. The difference between tests five and six was to compare the contribution of the different repair systems. However, both MF-FRP plates were removed prior to test six due to the loss of the concrete section at the other end of member where the fixed anchor plated was attached for test five. Test seven (S-DFS-F-FS) on beam No. 4 was the last and only flexural test conducted in this research. Both the flexural and severe shear damage was created by cutting the bottom prestressing strands at mid-span and both

end-regions of each stem. Figure 7.13 shows the flexural deterioration created in the lab. The specimen was then repaired with the flexural/shear repair system. Figure 7.14 to Figure 7.20 show the full-scale test setup and instrumentation of all seven tests.

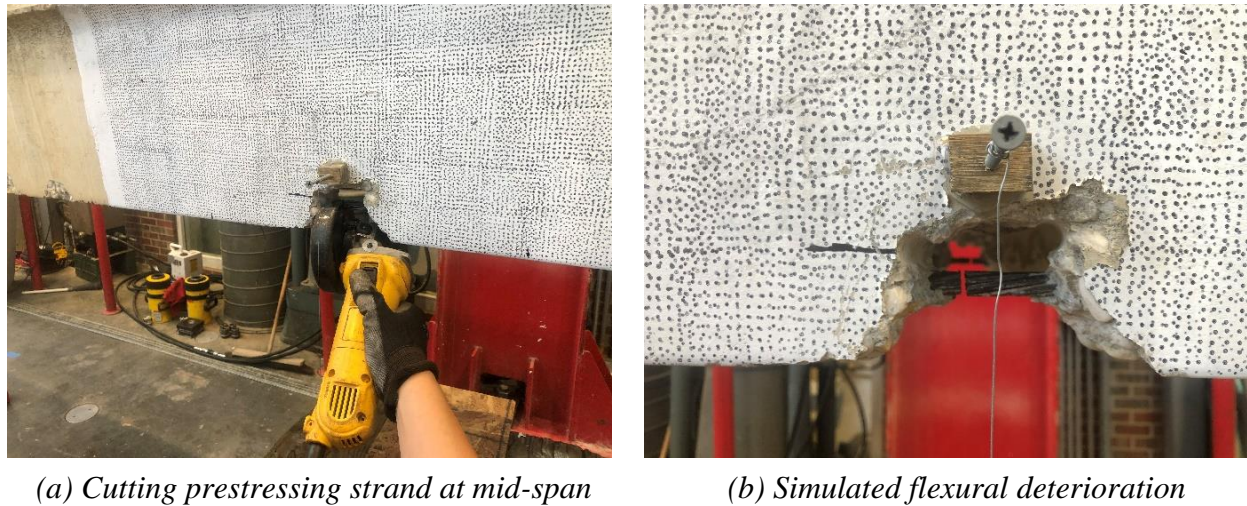


Figure 7.13: Flexural deterioration at midspan.

Table 7.2: Test matrix.

Test No.	Beam No.	Specimen ID	Description	a/d ^b	Testing Type
1	1	C-U-S2 ^a	Undamaged shear control – two-point load	4	Shear
2		C-DS-S1	Severe damaged shear control		
3	2	C-U-S1	Undamaged shear control		
4		C-IDS-S1	Intermediate damaged shear control		
5	3	S-DS-S1-F	Severe damaged shear with flexural repair	17.6	Flexure
6		S-DS-S1-FS	Severe damaged shear with flexural and shear plates only		
7	4	S-DFS-F-FS	Damaged flexure and shear with flexural and shear repair		

Note:

^a Only specimen tested in two-point loading.

^b *a* is the 40 in. shear span for shear tests and 176 in. for the flexural test; *b* is the average effective depth taken as 10 in.

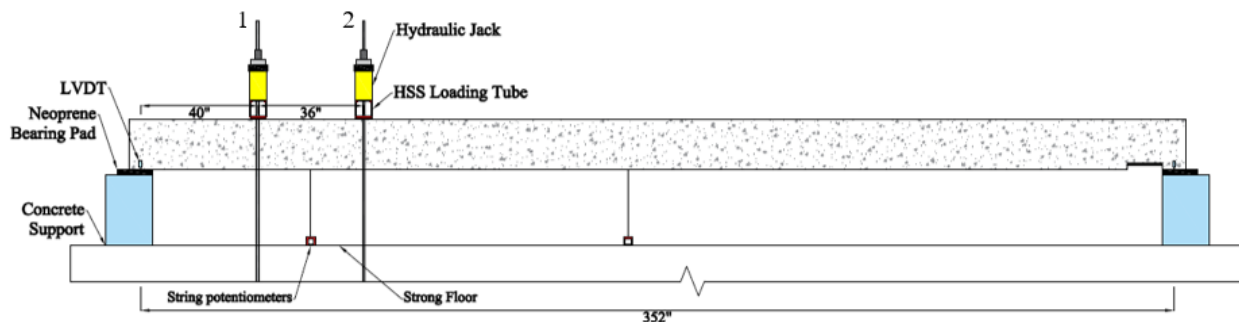


Figure 7.14: C-U-S2 (Test 1 on Beam 1).

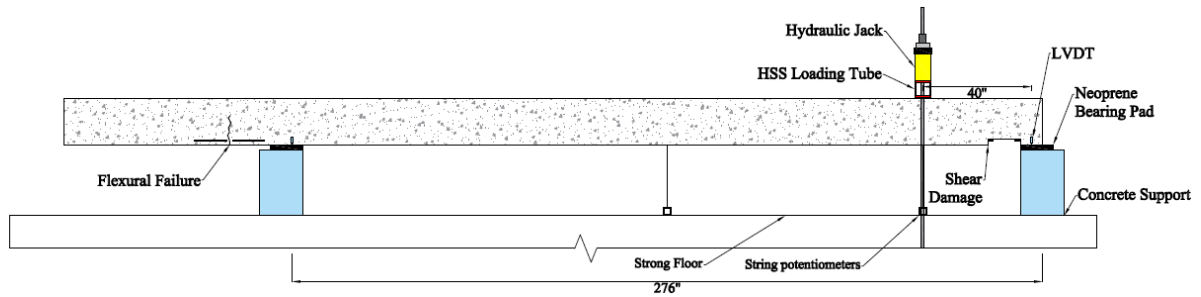


Figure 7.15: C-DS-S1 (Test 2 on Beam 1).

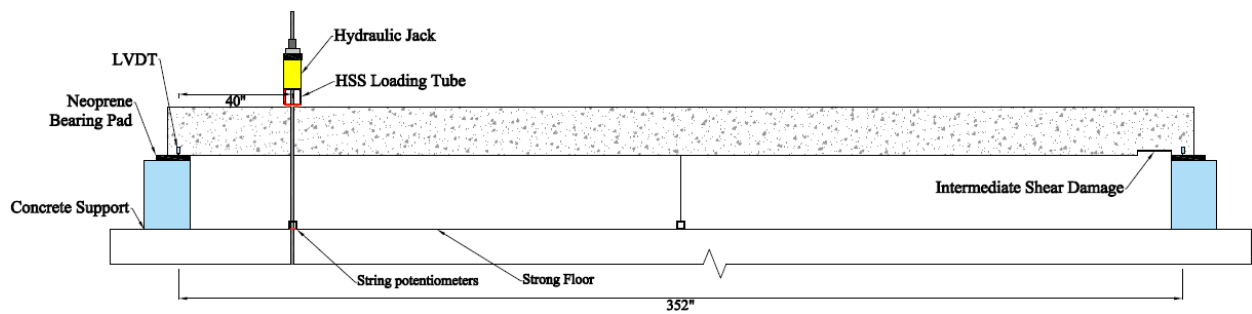


Figure 7.16: C-U-S1 (Test 3 on Beam 2).

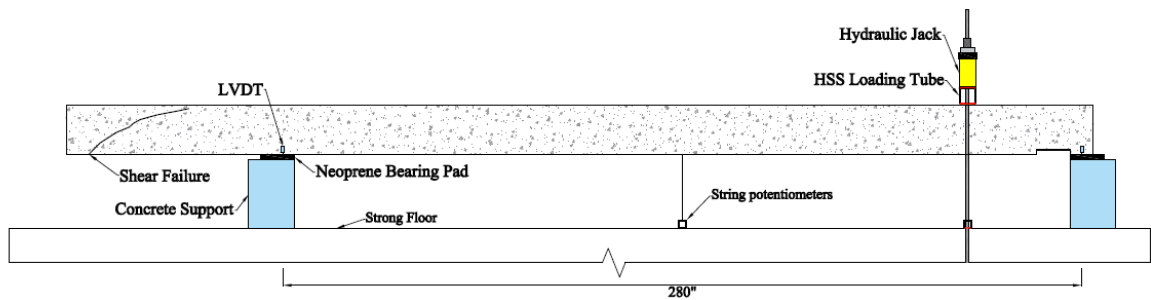


Figure 7.17: C-IDS-S1 (Test 4 on Beam 2).

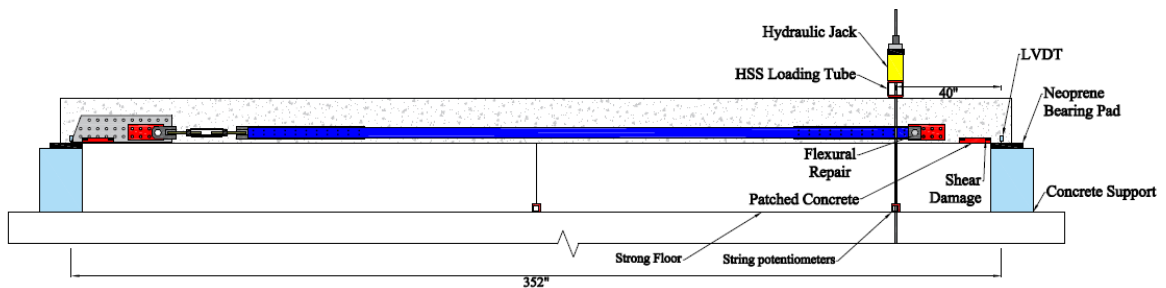


Figure 7.18: S-DS-S1-F (Test 5 on Beam 3).

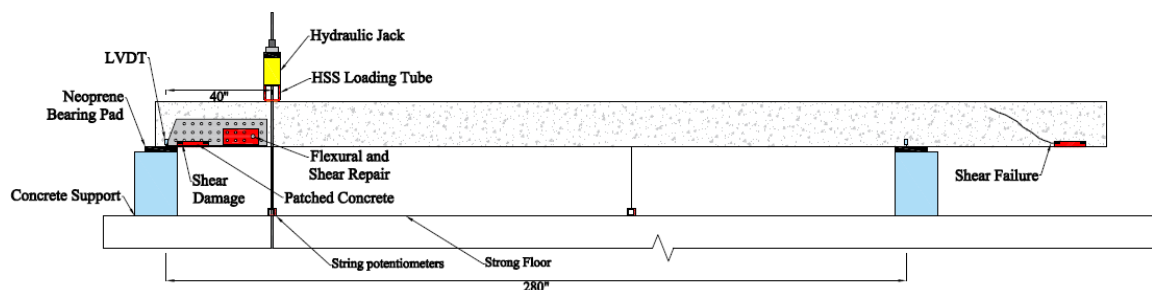


Figure 7.19: S-DS-S1-FS (Test 6 on Beam 3).

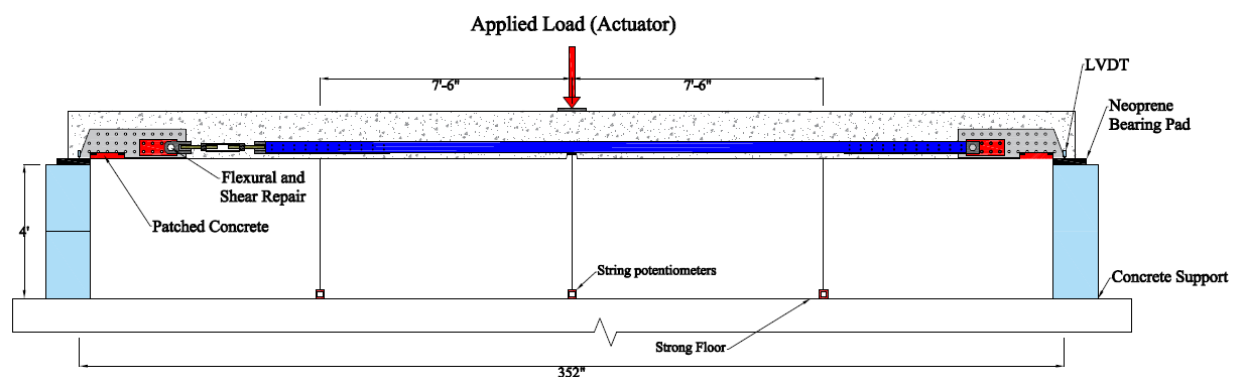


Figure 7.20: S-DFS-F-FS (Test 7 on Beam 4).

7.2.5 – Specimen Preparation

7.2.5.1 – Control Specimens

Three control specimens were tested in this program, including the undamaged control, intermediate shear damage, and severe shear damage. These control specimens enable the experimental quantification of the C-channel beam shear behavior under different levels of shear damage without applying any retrofit system, as shown in Figure 7.14 to Figure 7.17. The intermediate shear damage control was achieved by chipping away the concrete and exposing the prestressing strand. It is worth noting that even though the stem concrete appeared to be in good condition, corrosion was observed on the strands after chipping away the concrete, as can be seen in Figure 7.21(b). Unlike the intermediate shear damage, the severe damage condition simulates the worst condition that can occur on-site. Total loss of the prestressing strand cross-section due

to corrosion was simulated by cutting the strand as seen in Figure 7.21(c). Minor tensile stress-energy was released during the cutting process due to the short development length at the end regions.



(a) Undamaged control



(b) Intermediate shear damage control



(c) Severe shear damage control

Figure 7.21: Different shear damage levels.

7.2.5.2 – Retrofitted Specimens

Two retrofit systems were applied on the deteriorated C-channel beams. To simulate a field application, the chipped concrete was patched using fast setting cement before installing the repair system. The purpose was to create a flat surface for the shear repair system and decrease the corrosion rate of the prestressing strands, which is typical of current repair methods DOTs use on-

site. An additional shear strengthening plate was added to serve as the primary shear strengthening component applied on the C-channel stem, located between the fixed anchor plate of the MF-FRP system and the stem (refer to Figure 7.3(b)).

The MF-FRP repair was applied on beams No. 3 and No. 4. After determining the retrofit design, the repair started by locating the stirrups and prestressing strands with a pachometer. This step reduces the installation time as the stirrup spacing and orientation are not the same as provided by the NCDOT (1966) design drawings. The location of the fixed anchor plates and shear strengthening plates were then selected after the steel positions were defined. Holes were drilled using a hammer drill from outside the C-channel beam for convenience (Figure 7.22). On-site, drilling would need to be from the inside of the C-channel beam. All drilling processes were completed outside the lab for dust control. The steel plates (fixed anchor plate and shear strengthening plate) were bolted to the C-channel stem after the holes were drilled and the shear deterioration patched (Figure 7.23). Knowing the location of the fixed anchor plate, the FRP plates were cut according to the required length. The 22-bolt pattern was drilled at each end of the FRP plates. The FRP plates were then fastened to the FRP connector plates using 0.5 in. diameter A325 bolts and tightened with 30 ft.-lbs. torque, to be consistent with the previous full-scale testing. The FRP elements and turnbuckle system were then mounted to the fixed anchor plate after the flexural deterioration was created.



(a) Locating the anchor plate template



(b) Drilling holes for the shear strengthening plate

Figure 7.22: Drilling holes for the MF-FRP system.



Figure 7.23: Shear deterioration patched with fast setting cement.

The FRP plates were prestressed by rotating the turnbuckle body using regular wrenches to achieve the designed prestressing force. In this case, 18.5 kips was the target prestressing force at an FRP strain of $4100 \mu\epsilon$, the same value used by specimens tested in Chapter 5.2. A detailed installation procedure is presented in Chapter 5.8, and Appendix A. Strain gauges were installed on the FRP plates at mid-span and the near end regions to observe the FRP strain variation along the length and width of the plate during prestressing and testing. Although the MF-FRP repair system was applied on beams No. 3 and No. 4, only beam No. 4 experienced flexural deterioration.

Flexural deterioration was excluded in beam No. 3 to avoid any possible flexural failure outside the shear critical region during the shear test. Beam camber was carefully measured during the MF-FRP prestressing process using the string potentiometers.

Prestressing of the MF-FRP was stopped at 15.8 kips of force due to unexpected concrete splitting at the anchor plate bolts along the bottom of the stem, as shown in Figure 7.24. The concrete splitting is likely related to the damage of the C-channel stem due to the drilling process where the anchor bolts are located, or the aggregate size used in the concrete. Concrete spalling inside the stem was observed while drilling from the outside, which reduced the concrete area available to resist the force transferred by the MF-FRP system to the concrete stem. A different drilling procedure was used for the MF-FRP retrofit system on beam No. 4. Leading holes were drilled from inside the stem with plywood clamped to the outside face of the stem using a smaller bit to minimize concrete spalling on the stem. The final hole diameter was then achieved by drilling from both sides of the stem. Figure 7.25 shows the stem condition for beam No. 3 and beam No. 4. After changing the drilling procedure, much less concrete spalling was observed during the drilling process on beam No. 4. Little concrete spalling was observed in the field application (presented in Chapter 8), but nonetheless, care should be taken.

Besides concrete spalling caused by drilling, another problem was observed related to the location of the fixed anchor plates after testing beam No. 3. To minimize repair time, the fixed anchor plate should be placed away from the internal steel reinforcement to avoid hitting them during drilling. In this beam, the fixed anchor plates were located between two widely spaced stirrups. This arrangement resulted in only pure concrete resisting the force transferred by the MF-FRP system, leading to a premature failure. Therefore, the fixed anchor plate locations were adjusted to have a stirrup passing between the two columns of anchor bolts on beam No. 4. This

adjustment might increase the chance of hitting steel reinforcement during drilling. However, it will help avoid premature splitting failure at a higher MF-FRP force.

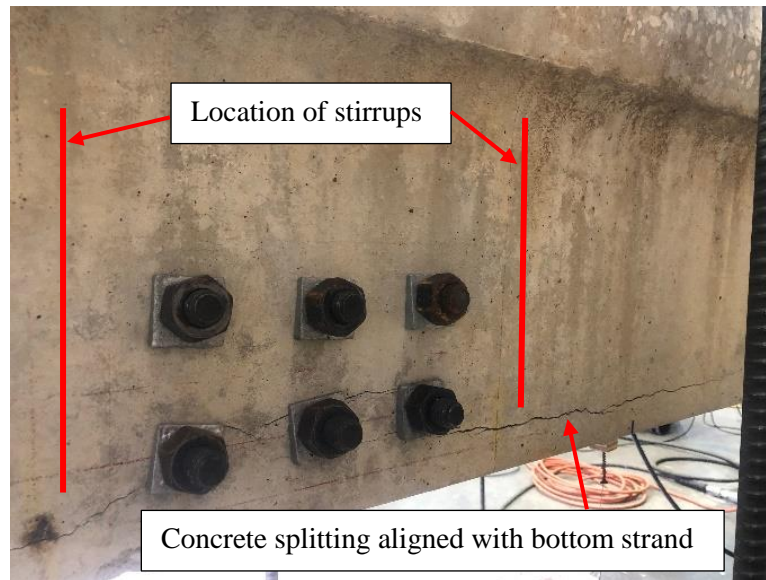


Figure 7.24: Concrete splitting during prestressing of the MF-FRP system in beam No. 3.



(a) Beam No. 3



(b) Beam No. 4

Figure 7.25: Stem condition after drilling fixed anchor plate bolt holes.

The camber restored in beams No. 3 and No. 4 was 0.137 and 0.177 in. with 15.8 and 18.5 kips prestressing force applied by each MF-FRP plate, respectively. The lower prestress force applied in beam No. 3 was due to the observation of concrete splitting at the anchor bolts during

the prestressing FRP procedure. Figure 7.26 and Figure 7.27 show both ends of the final MF-FRP system applied on beams 3 and 4, respectively.



(a) Live-end



(b) Dead-end

Figure 7.26: MF-FRP repair system applied on beam No. 3.



(a) Live-end



(b) Dead-end

Figure 7.27: MF-FRP repair system applied on beam No. 4.

7.2 – Experimental Results

Table 7.3 summarizes the full-scale experimental results, including the maximum applied force, measured displacement at the maximum applied force, total span and shear span length, applied shear force at shear span, and observed failure mode. Member deflection was measured

using the string potentiometers located under the applied load accounting for the deformation of the neoprene pads during testing. The applied shear force in the shear span was calculated using static equilibrium and taken to be the shear capacity. The detailed discussion and the observed behavior of each test is presented in the following sections. Measured FRP strain at different positions along the FRP length and width is discussed later in this Chapter. Figure 7.28 shows the applied shear–deflection response of all the shear tests conducted with one-point load. Due to the different loading conditions and test type, C-U-S2 and S-DFS-F-FS are not included in Figure 7.28. The maximum measured applied shear is compared to the shear demand of the HS-15 load limit for the corresponding total beam span lengths.

The applied shear force of the HS-15 truck type for any beam length can be calculated using the relationship shown in Figure 7.29. Due to the different reduced total beam span for some tests, the calculated applied shear force from HS-15 was 30.9, 28.0, and 27.5 kips for C-U-S1, C-IDS-S1, and C-DS-S1, respectively.

Table 7.3: C-channel test results summary.

Test No.	Beam No.	Specimen ID	Max. Applied Load (kips)	Measured Disp. at Max. Load Location (in.)	Total Span (in.)	Shear Span (in)	Applied Shear Force at Shear Span (kips)	Failure Mode
1	1	C-U-S2	57.0	4.72	352	40	50.5	Flexure and Shear
2		C-DS-S1	45.4	2.71	268		38.7	Shear
3	2	C-U-S1	58.4	1.51	352		51.8	Shear
4		C-IDS-S1	57.4	0.90	280		49.2	Shear
5	3	S-DS-S1-F	37.3	0.52	352		33.0	Shear
6		S-DS-S1-FS	45.0	2.33	280		38.6	Flexure
7	4	S-DFS-F-FS	27.1	5.66	352	176	13.6	Flexure

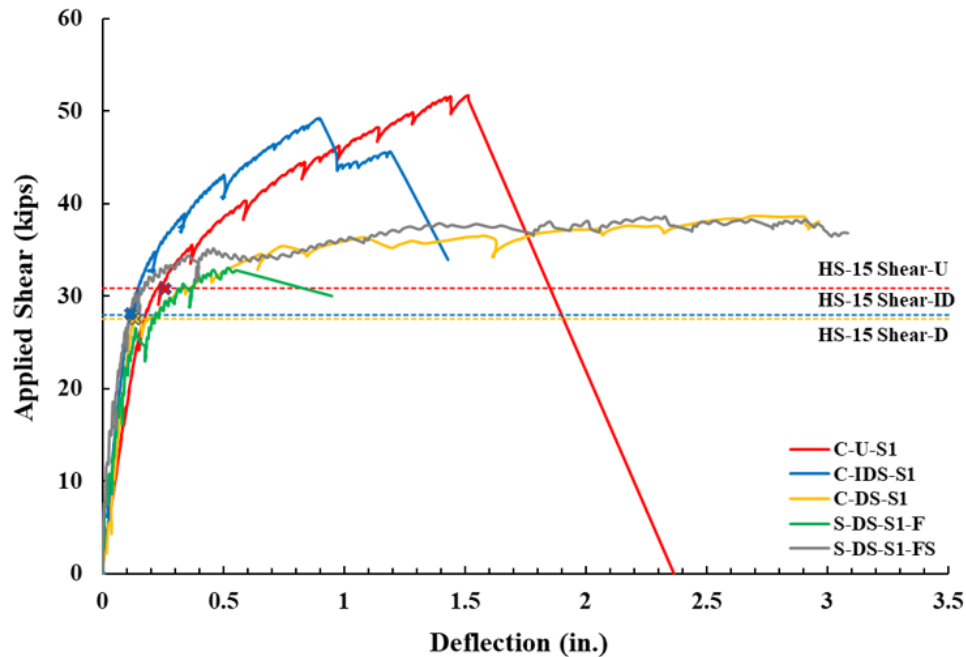


Figure 7.28: Full-scale experimental results (1- point load shear tests).

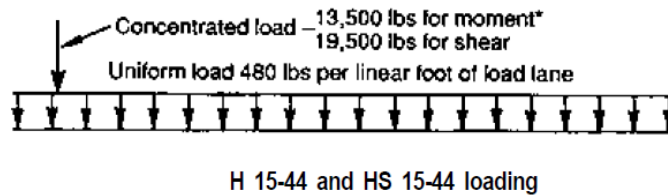


Figure 7.29: Load combination for calculating HS-15 applied shear force (adapted from AASHTO, 2018).

7.2.1 – C-U-S2

Specimen C-U-S2 is the undamaged specimen tested with two-point loading on beam No. 1 and was the first full-scale shear test conducted in this program. Figure 7.30 shows the total applied load and beam deflection response. First flexural crack was observed at the 25 kips load stage. When loaded to 40 kips, multiple flexural cracks formed, and the existing flexural cracks elongated and became wider along the span. Two flexural shear cracks were observed at the 45 kips load stage. One of them initiated between one loading point and propagated toward the second loading point, while the other was located next to the first loading point, as can be seen in Figure

7.31. The specimen was loaded to failure after the 50 kip loads stage. As can be seen from Figure 7.30, a flexural behavior was observed with a large member deflection. The C-channel beam experienced rupture of a prestressing strand at 51.4 kips of total applied load. After prestressing strand rupture in one stem, the applied load increased to 57.0 kips at an ultimate deflection of 4.72 in. at which time a shear failure was observed. Therefore, the failure mode of C-U-S1 is defined as flexural/shear failure, as seen in Figure 7.32. With the flexural failure and rupture of a prestressing strand, the test setup was changed to one-point load to reduce the maximum moment for a given shear for all subsequent shear tests. The revised test setup avoided premature flexural failures during testing (refer to Figure 7.15 to Figure 7.19).

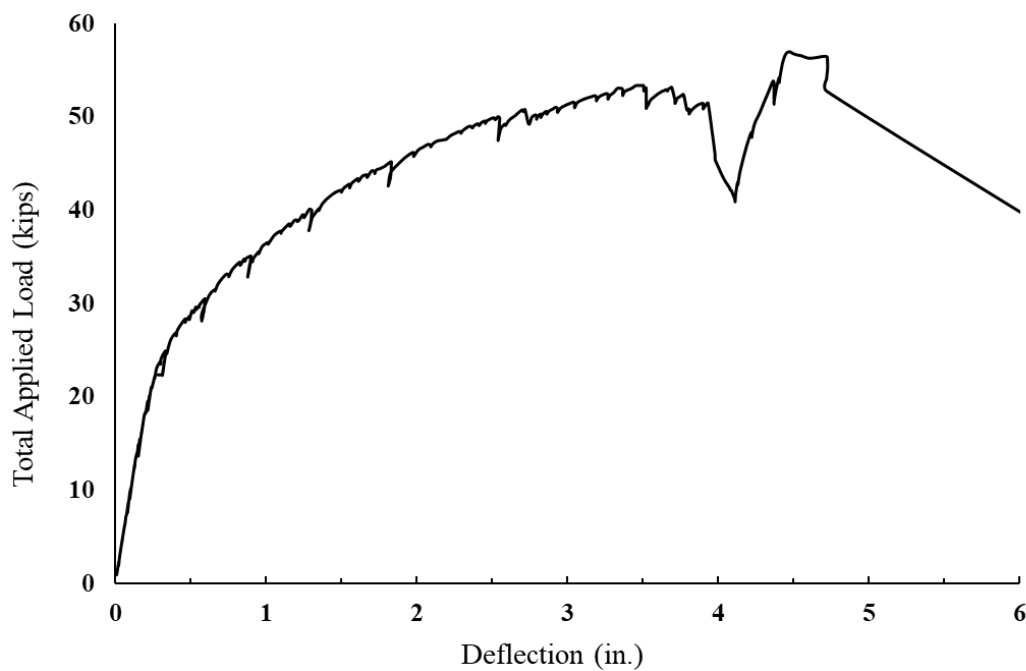


Figure 7.30: Experimental result of C-U-S2.

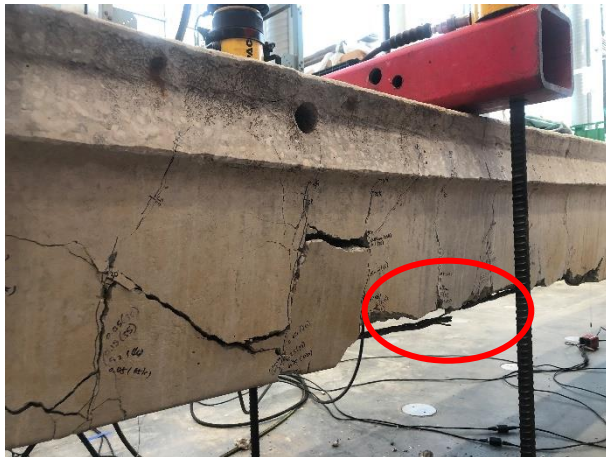


(a) Flexural-shear crack at first loading point



(b) Flexural-shear crack between two loading points

Figure 7.31: First flexural-shear crack occurred at the 45 kips load stage (C-U-S2).



(a) Prestressing strand rupture at 51.4 kips



(b) Shear failure at 57 kips

Figure 7.32: Failure mode of C-U-S2.

7.2.2 – C-U-S1

Specimen C-U-S1 was the first test on beam No. 2 and served as a benchmark for the shear strength of an undamaged specimen to allow a direct comparison for the other specimens. Flexural cracks initiated at the 35 kips load stage under the applied load. More flexural cracks occurred and propagated until 52 kips when the first flexural-shear crack was formed. A new shear crack initiated suddenly from the support and propagating toward the applied load point while load was paused at the 58 kips load stage, shown in Figure 7.33. Shear failure occurred immediately after

reloading from the 58 kips load stage with an ultimate load of 58.4 kips at a maximum deflection of 1.51 in. Figure 7.34 illustrates the failure mode of C-U-S1. It was observed that the failure mode was slightly different on the left stem with a short longitudinal crack along the bottom strand from the support, which might be due to internal corrosion of the prestressing strand. The shear crack was measured to be approximately 45 degrees, as shown in Figure 7.35.

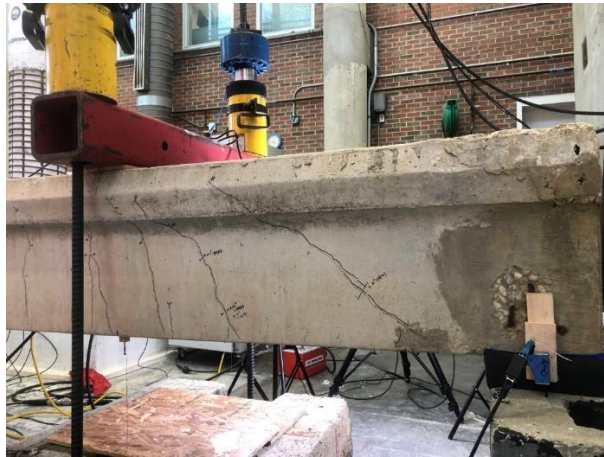
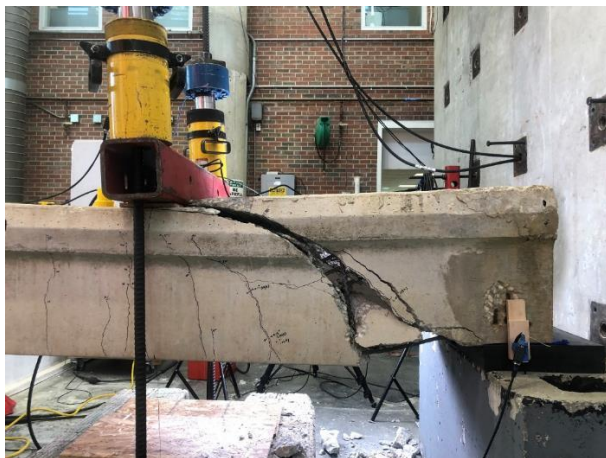


Figure 7.33: Formation of first shear crack at 58 kips (C-U-S1).



(a) Left stem



(b) Right stem

Figure 7.34: Failure mode of C-U-S1 at 58.4 kips.



Figure 7.35: Crack angle of C-U-S1 at failure.

7.2.3 – C-IDS-S1

Specimen C-IDS-S1 was tested at the opposite end of C-U-S1 from beam No. 2 with a reduced total span. C-IDS-S1 was damaged by chipping away the concrete and exposing the prestressing strand on both stems to serve as the closest deterioration observed on-site. No newly formed cracks were observed up to the 30 kips load stage except for a longitudinal crack under the left stem outside the shear critical region from the original deterioration. Flexural cracks initiated at the 35 kips load stage under the applied load point. The first inclined shear crack occurred at the 40 kips load stage at the end of shear deterioration and propagated to the loading point at the 45 kips load stage, shown in Figure 7.36. An additional shear crack was observed at the 50 kips load stage. Specimen C-IDS-S1 experienced shear failure at an ultimate load of 57.4 kips at a deflection of 0.90 in. (a decrease of 0.61 in. compared to C-U-S1). Figure 7.37 shows the shear failure mode of C-IDS-S1. Specimen C-IDS-S1 had resisted 98% of the applied load compared to C-U-S1 but at a lesser deformation at failure. The internal deterioration level of the prestressing strand between the two stems resulted in different crack patterns but that did not appear to affect the member's general behavior.



Figure 7.36: Shear crack at 45 kips (C-IDS-S1).



(a) Left stem



(b) Right stem

Figure 7.37: Failure mode of C-IDS-S1 at 57.4 kips.

Specimen C-IDS-S1 was carefully examined after the test was completed and moved outside of the lab. Corrosion was observed on the prestressing strands after chipping away the concrete, as can be seen in Figure 7.38. The prestressing strands pulled-out 0.25 in. at the end of both stems due to the large shear force applied on the beam and low bond stress with the concrete (Figure 7.39). The stirrup spacing was measured after the removal of the damaged concrete. Figure 7.40 shows the measured stirrup spacing using an edge ruler and a tape measure. The measured spacing was 10 in., instead of 13 in. as given by NCDOT (1966). This information is important so that the beam shear capacity can be predicted more accurately. The measurement of stirrup spacing

was also conducted for beam No. 1 and 3 using a tape measure. An average 10 in. spacing was measured for stirrups located at the end regions. Moreover, the orientation of the stirrups was not perpendicular to the beam's longitudinal direction (refer to Figure 7.40(a)). This will increase the possibility of cutting stirrups during drilling. With the different stirrup spacing and orientation observed from the tested beams and on-site compared to the standard drawing provided by NCDOT (1966), it is hard to provide a consistent repair design to locate the fixed anchor plate and the required FRP length. Therefore, careful field measurements of the target beams to be repaired is required to assist the design and installation process.



Figure 7.38: Corrosion on the prestressing strand after chipping away the concrete.



(a) Left stem

(b) Right stem

Figure 7.39: Pull-out of strand after testing (C-IDS-S1).

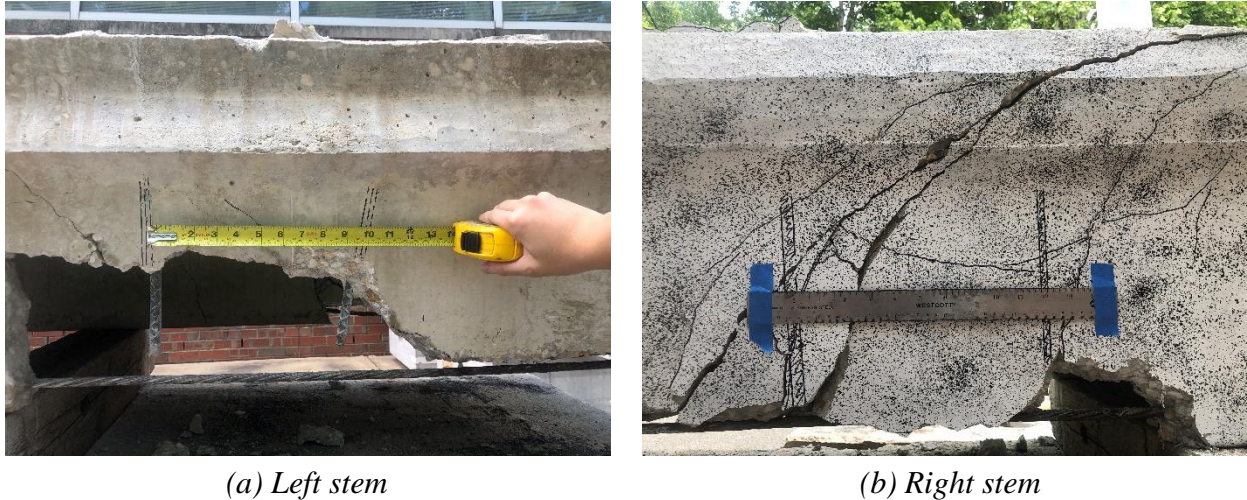


Figure 7.40: Measuring stirrup spacing and orientation (C-IDS-S1).

7.2.4 – C-DS-S1

Specimen C-DS-S1 was tested at the opposite end of C-U-S2 on beam No. 1 with a reduced total span due to the ruptured prestressing strand from the previous test on Specimen C-U-S2. C-DS-S1 was damaged by chipping away the concrete and cutting the exposed prestressing strand on both stems to serve as the most severe shear damage case that can be observed on-site. The total applied shear to beam deflection response can be seen in Figure 7.28. No cracks were observed until 26 kips of total load. A longitudinal splitting crack initiated at 30 kips starting from the end of the cut prestressing strand due to the debonding of the prestressing strand. At 33.2 kips, a shear crack formed resulting in a drop of applied load, as can be seen in Figure 7.41. However, the load continued to increase to failure. Due to the dowel action of the bottom prestressing strand, additional longitudinal cracks were initiated along the second layer of prestressing strands propagating from the main shear crack. The ultimate load achieved by C-DS-S1 was 45.4 kips at a deflection of 2.71 in (an increase of 1.2 in. compared to C-U-S1). Specimen C-DS-S1 resisted 78% of the applied load compared to C-U-S1. Figure 7.42 shows the failure mode of C-DS-S1. The same failure mode was observed on both stems. The interaction of the cracking with the location of the internal steel stirrups can be seen on the left stem in Figure 7.42(a).

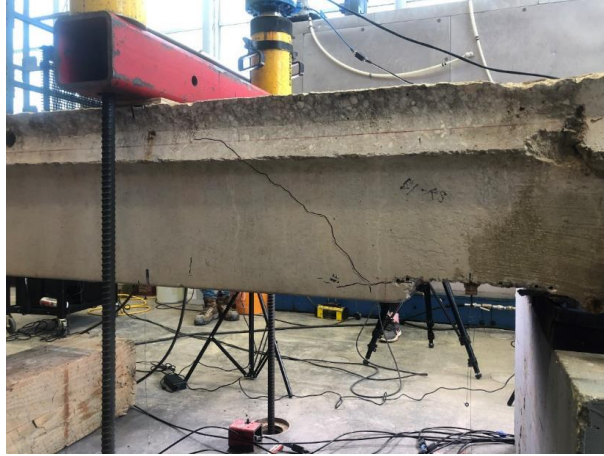


Figure 7.41: Formation of first shear crack at 33.2 kips (C-DS-S1).



(a) Left stem



(b) Right stem

Figure 7.42: Failure mode of C-DS-S1 on both stems.

7.2.5 – S-DS-S1-F

Specimen S-DS-S1-F was tested on beam No. 3 and repaired only with the original flexural MF-FRP system. S-DS-S1-F was repaired with the flexural MF-FRP system to study the effect of the flexural MF-FRP system on the severe shear damage case. Severe shear damage regions were patched to restore the concrete section prior to testing, as would be done prior to installation on-site. Concrete splitting cracks formed during prestressing of the MF-FRP plate, such that some initial damage occurred on the concrete stem. No shear or flexural cracks were observed at the 20 kips load stage. However, the concrete splitting cracks elongated and became wider. The first

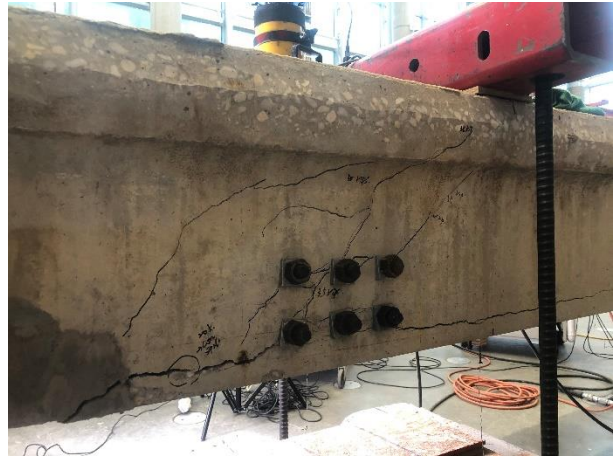
inclined shear crack initiated at the 30 kips load stage, passing through the top row of anchor bolts, shown in Figure 7.43, at which time the applied load dropped to 28 kips sudden. Multiple shear cracks formed at the 35 kips load stage with a random pattern from the support or propagating from the original shear cracks, as shown in Figure 7.44. The specimen failed in shear at an ultimate load of 37.3 kips, lower than the severe shear damage specimen (U-DS-S1), at a deflection of 0.52 in., the smallest deflection of all beams tested; 0.99 in. less compared to C-U-S1. Specimen S-DS-S1-F resisted 64% of the applied load compared to C-U-S1. Figure 7.45 presents the shear failure mode of S-DS-S1-F. An entire concrete section, which the fixed anchor plate was bolted to, spalled off at failure on the right stem. It was observed that the fixed anchor plate was located between two stirrups, and only pure concrete resisted the applied force transferred from the MF-FRP system. On the left stem, shear cracks initiated from the end of the patched region and passed through the anchor bolts. Additional minor concrete splitting cracks were observed after failure, but significantly smaller than the initial concrete splitting cracks that formed during prestressing of the MF-FRP system. For the case of severe shear damage, the presence of only the flexural repair system resulted in a weaker behavior. The shear repair system must be applied together with the flexural repair system to avoid premature failure under severe shear deterioration.



Figure 7.43: Shear crack formed at 28 kips (S-DS-S1-F).



(a) Left stem



(b) Right stem

Figure 7.44: Additional shear cracks initiated at 35 kips load stage (S-DS-S1-F).



(a) Left stem



(b) Right stem

Figure 7.45: Failure mode of S-DS-S1-F at 37.3 kips.

7.2.6 – *S-DS-S1-FS*

Specimen S-DS-S1-FS was tested on the opposite end of S-DS-S1-F on beam No. 3 with a reduced total span. S-DS-S1-FS had severe shear damage repaired with the proposed flexural/shear system to study the effect of the flexural/shear repair system on the severe shear damage case. However, both MF-FRP plates were removed prior to testing due to the loss of the concrete section where the fixed anchor plated was attached (refer to Figure 7.45(b)). Each shear strengthening plate was bolted and sandwiched between the concrete stem and the fixed anchor plate to simulate the condition of both repair systems. During testing, no cracks were observed at the 30 kips load stage. The first inclined shear crack initiated at the 35 kips load stage, shown in Figure 7.46. Figure 7.47 shows the formation of additional shear cracks at the 40 kips load stage, starting from the end of the patched region and propagating toward the load point. Specimen S-DS-S1-FS was loaded to failure after the 40 kips load stage. Unlike the previous shear experiments, specimen S-DS-S1-FS experienced a flexural failure by concrete crushing at the top fiber at an ultimate load of 45.0 kips and a deflection of 2.33 in., an increase of 0.82 in. compared to C-U-S1. Specimen S-DS-S1-FS resisted 77% of the applied load compared to C-U-S1. No prestressing strand rupture was observed at failure. The shear strengthening plates were not utilized efficiently to restore the member shear capacity due to pull-out of the prestressing strands, which dominated the member behavior. However, the presence of the shear strengthening plates did change the member failure mode from the brittle shear failure to a ductile flexural failure by clamping the concrete stem and delaying the propagation of shear cracks. Figure 7.48 and Figure 7.49 present the failure condition observed on the two stems of S-DS-S1-FS, and the flexural failure mode, respectively. Figure 7.49(b) shows clear evidence of flexural failure, where a crack was observed across the section on the bottom of the flange at the maximum moment location. According to the applied shear-deflection response of the tested specimen in Figure 7.28, although the repair system

did not increase the member shear resistance up to undamaged specimen (C-U-S1), the specimen experienced a ductile behavior and failed in flexure. It is worth mentioning that the shear resistance measured is not the shear capacity from the flexural/shear repair system due to the removal of the MF-FRP plate from the previous experimental failure mode at the other end. Therefore, the flexural capacity at the maximum moment location was reduced due to the missing MF-FRP plate.



Figure 7.46: Formation of first inclined shear cracks at 35 kips (S-DS-S1-FS).



Figure 7.47: Additional shear cracks at the 40 kips load stage (S-DS-S1-FS).



(a) Left stem



(b) Right stem

Figure 7.48: Failure mode of S-DS-S1-FS at 45 kips.



(a) Top of the flange



(b) Bottom of the flange

Figure 7.49: Flexural failure by concrete crushing (S-DS-S1-FS).

7.2.7 – S-DFS-F-FS

Specimen S-DFS-F-FS was tested on beam No. 4 in flexure and was damaged by cutting the two bottom prestressing strands at mid-span and at both ends. S-DFS-F-FS was tested to study the flexural behavior of a C-channel beam with flexural and severe shear damage repaired with the developed flexural/shear system. The result of S-DFS-F-FS was directly compared to the C-channel flexural experiments conducted in Chapter 5.2, shown in Figure 7.50. The ultimate capacity achieved by S-DFS-F-FS was 27.1 kips (91.6% of the undamaged specimen tested in

Chapter 5.2) at a deflection of 5.66 in. (0.47 in. less than that of the undamaged specimen), and the maximum measured FRP tensile strain was 6148 $\mu\epsilon$. Specimen S-DFS-F-FS failed by concrete crushing due to flexure, as can be seen in Figure 7.51. The MF-FRP in S-DFS-F-FS did not experience any substantial damage, such as longitudinal splitting or rupture failure. However, minor longitudinal cracking was observed at the first four columns of FRP bolts, shown in Figure 7.52, which is a typical phenomenon observed when the MF-FRP plate experiences high forces. Minor concrete splitting was found at one fixed anchor plate aligned with the bottom row of anchor bolts after testing. Figure 7.53 shows the local concrete splitting at the fixed anchor plate.

A similar moment-deflection response was observed for S-DFS-F-FS compared to MF-FRP-D2. Specimen S-DFS-F-FS had a 4% larger capacity, but at a lower deflection (11% less), compared to MF-FRP-D2 due to the different concrete strength, prestress losses, and beam position even though they came from the same bridge. Specimens repaired with the MF-FRP system (S-DFS-F-FS and MF-FRP-D2) experienced a lower member deflection at the AASHTO operating limit. Although the ultimate capacity of S-DFS-F-FS was less than that of the undamaged specimen, S-DFS-F-FS experienced an increased stiffness and had a better performance at the operating limit compared to the undamaged specimen. The experimental results demonstrate that the specimens repaired with the flexural/shear MF-FRP system have improved inventory and operating load limits, and ultimate capacity compared to the flexural/shear deteriorated specimen.

It is said that severe shear deterioration does not affect the general flexural behavior due to the low shear force applied to the shear span. The maximum applied shear force in the shear span was 13.6 kips, which is 35% of specimen C-DS-S1. Moreover, C-DS-S1 was still in the linear range at 13.6 kips of applied shear force (refer to Figure 7.28). However, with the presence of the

shear strengthening plate, the end region shear capacity can be improved, and the propagation of concrete splitting cracks may be prevented or delayed.

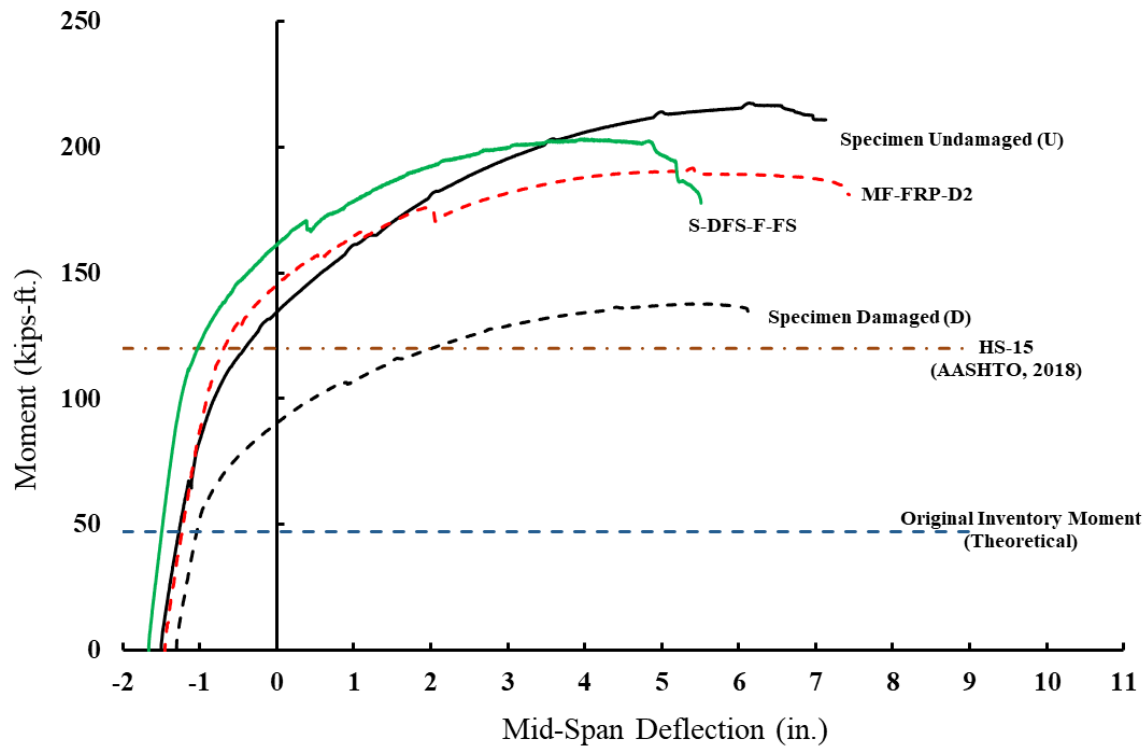


Figure 7.50: Full-scale C-channel beam moment-deflection results.



(a) Left stem



(b) Right stem



(c) Bottom view of flange

Figure 7.51: Flexural failure by concrete crushing at 27.1 kips (S-DFS-F-FS).



(a) FRP plates from dead-end



(b) FRP plates from live-end

Figure 7.52: Minor longitudinal splitting on FRP plates.



(a) Outside of right the stem



(b) Inside of right stem

Figure 7.53: Minor local concrete splitting on concrete stem.

The FRP strain was measured during testing at different locations on the FRP plate. Figure 7.54 shows the location of strain gauges installed on the FRP plates. Of the four strain gauges used per FRP plate, one of them was attached at mid-height 1 ft. away from the FRP connector plate, serving as the end region value. The remaining three strain gauges were installed at the mid-span of the C-channel beam, at the top, middle, and bottom positions of the FRP width, representing the mid-region values. Figure 7.55 shows the FRP strain response with member deflection for the mid-height gauges at the end and mid-regions of the plate during testing. No substantial strain variation is observed between these two locations along the length of the plate, supporting the assumption made in Chapter 6 that the FRP strain is constant along the length of this external prestressing element. Figure 7.56 shows the same response but for the three strain gauges at the mid-region of the plate during testing. The results show that the strain measured by the top and middle gauges is slightly higher than the strain measured by the bottom gauge. In Figure 7.55 and Figure 7.56, the strain value recorded is the changer in strain after prestressing of the MF-FRP. Ideally, the pin connection of the MF-FRP plates would result in pure uniaxial tension of the plate during prestressing or testing. However, according to experimental results from Figure 7.56, minor in-

plane bending is observed due to the slightly different strain across the plate width. This is likely due to the frictional resistance of the pin connection at both ends and is small enough to not affect the axial tension capacity of the MF-FRP plate.



Figure 7.54: Location of strain gauges installed on the FRP plate.

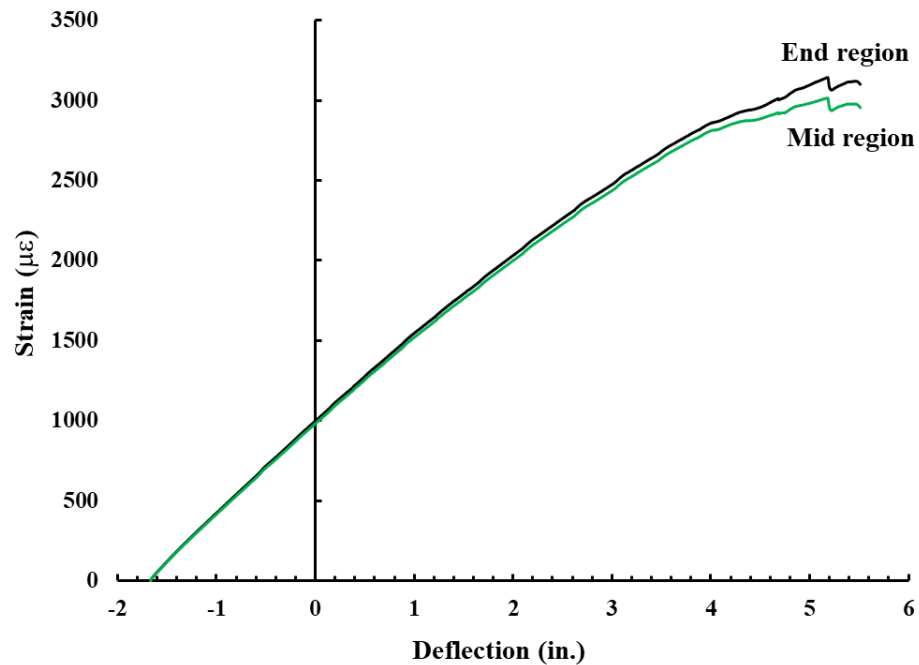


Figure 7.55: FRP strain variation at different locations along length of plate.

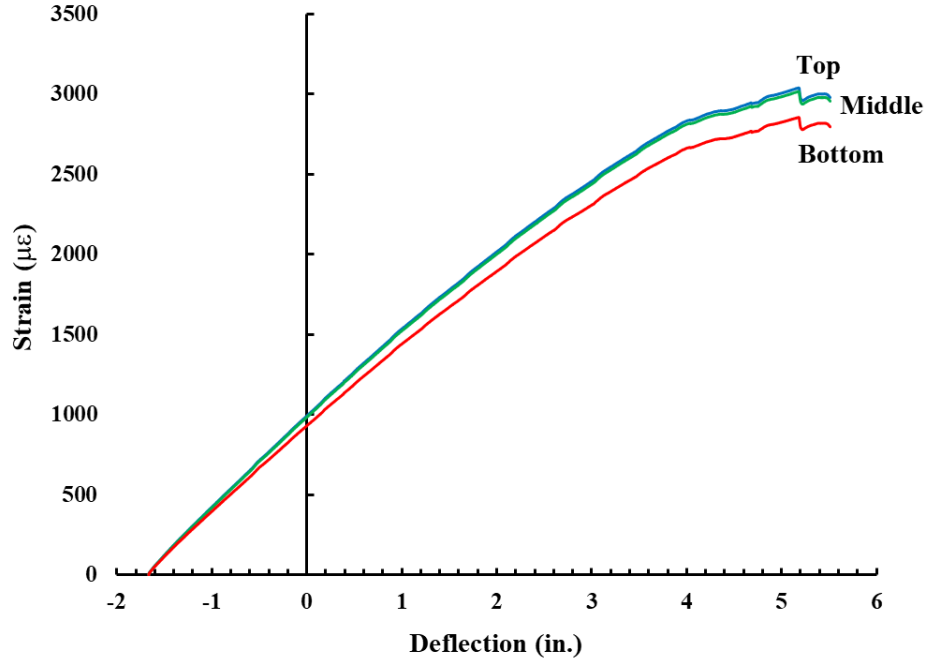


Figure 7.56: FRP strain distribution across plate at mid region.

7.3 – Predicted Shear Capacity of Unstrengthened Specimens

For retrofit applications, it is important to understand the member capacity so that the best repair option can be provided. The shear capacity of undamaged and damaged C-channel beams can be obtained from experiments. However, in practice, it is necessary to calculate the member shear capacity using procedures from design guides or codes. Several expressions are used to calculate shear capacity of a prestressed concrete beam. According to ACI 318 (2019), Equations 7.1 are used to calculate the shear contribution from the concrete for prestressed concrete structures. Equations 7.1(a) and 7.1(b) represent two types of shear strength in concrete beams: web-shear strength, V_{cw} ; and flexure-shear strength, V_{ci} . The nominal shear strength provided by the concrete section is the lesser of the web-shear strength and flexure-shear strength.

$$V_{cw} = (3.5\sqrt{f'_c} + 0.3f_{pc})b_wd_p + V_p \quad (lbs) \quad (7.1a)$$

$$V_{ci} = 0.6\lambda\sqrt{f'_c}b_wd_p + V_d + \frac{V_iM_{cr}}{M_{max}} \quad (lbs) \quad (7.1b)$$

where f'_c is the concrete strength, f_{pc} is the compressive stress in the concrete after considering all prestress losses, b_w is the concrete web width, d_p is the effective depth of the prestressing strand and not to be taken less than $0.8h$ where h is the total depth of the section, V_p is the vertical component of the effective prestress force, V_d is the shear force at the section due to unfactored dead load, V_i is the factored shear force at the section due to externally applied loads occurring simultaneously with M_{max} , M_{cr} is the cracking moment, M_{max} is the maximum factored moment at the section due to externally applied load, and λ is a factor for different types of concrete (e.g. $\lambda = 1$ for normal weight concrete and 0.75 for light weight concrete).

$$M_{cr} = \left(\frac{I}{y_t} \right) (6\lambda\sqrt{f'_c} + f_{pe} - f_d) \quad (7.1c)$$

where I is the moment of inertia of the section about the centroidal axis, y_t is the distance from the centroidal axis of the gross section to tension face, f_{pe} is the compressive stress in concrete due to effective prestress forces, and f_d is the stress due to unfactored dead load.

$$\frac{V_i}{M_{max}} = \left(\frac{1}{a} \right) \quad (7.1d)$$

The ratio of V_i to M_{max} used in calculating V_{ci} at the section of interest can be determined by Equation 7.1(d), where a is the shear span at region of interest.

According to ACI 318 (2019), the following equation is used to calculate the shear contribution from the steel stirrups.

$$V_s = \frac{A_v f_{yt} d_p}{s} \quad (lbs) \quad (7.2)$$

where V_s is the nominal shear strength provided by the shear reinforcement, A_v is the area of shear reinforcement, f_{yt} is the specified yield strength of the shear reinforcement, and s is the spacing of shear reinforcement.

Table 7.4 shows the predicted shear capacity using the ACI 318 (2019) expressions for C-U-S1, C-IDS-S1 and C-DS-S1, compared to the experimental results. The concrete strength used in C-U-S1, C-IDS-S1, and C-DS-S1 was 9.5, 9.5, and 8.5 ksi, respectively, from the concrete core tests (refer to Table 6.2). The spacing of shear reinforcement, s , was taken as 10 in. based on the measurements taken from the tested specimen. The concrete web width was taken as 5 in. given by the summation of each stem width at the bottom fiber. The effective depth of prestressing strand, d_p , used in the calculation was calculated to be 13.6 in. due to the effective depth restriction of $0.8h$. A 45% total prestress loss was used in the calculation based on the experimental results, and the shear reinforcement was taken as No. 4 Grade 60 steel bars.

Table 7.4: Predicted shear capacity using ACI 318 (2019).

ID	f_c (psi)	b_w (in)	d_p (in)	s (in)	V_c (kips)	V_s (kips)	$V_{n,pred.}$ (kips)	$V_{n,exp.}$ (kips)	$V_{n,pred.}/V_{n,exp.}$
C-U-S1	9500	5	13.6	10	31.3	32.6	63.9	51.8	1.23
C-IDS-S1	9500	5	13.6	10	31.3	32.6	63.9	49.2	1.30
C-DS-S1	8500	5	13.6	10	28.2	32.6	60.8	38.7	1.57

Table 7.4 shows that ACI 318 (2019) over-predicted the shear capacity by 23, 30, and 57% for C-U-S1, C-IDS-S1 and C-DS-S1, respectively. The restriction on the prestressing strand effective depth set by ACI 318 (2019) is intended for design. However, it miscalculates the prediction for this analysis, especially for the severe shear damaged condition. The concrete web width is another variable that affects the prediction accuracy for the C-channel beams considered due to the shape of the stems. The width of stems is not constant along the height, making it difficult to decide what width value should be used. Therefore, some modifications are proposed to adjust the current ACI 318 (2019) expressions for the application considered in this research.

The first modification was reconsidering the prestressing strand effective depth for analysis purposes. For a C-channel beam with a harped strand profile, the centroid of all the prestressing strands was used at the section of interest in the analysis. However, the severe shear damage was

created by cutting the bottom strand at both stems in the shear critical regions. Therefore, sections at the shear critical region should be considered with no bottom strands. The second modification was made by adjusting the value of concrete web width. Concrete web width should be selected at the location where concrete can provide shear resistance. Therefore, it was assumed to be at the location of the bottom prestressing strand for the undamaged specimen as concrete cover could not be relied upon to resist the applied shear force. Although the bottom prestressing strands were not considered in calculating the shear capacity of the severe shear damage specimen, the bottom prestressing strands were still bonded to the concrete that enabled the concrete to provide shear resistance at the location of the bottom prestressing strands. Figure 7.57 presents the different concrete web widths used with the ACI 318 (2019) equations. Table 7.5 presents the predicted shear capacity using the modified parameters representing a location 3 ft. from the end of the beam.

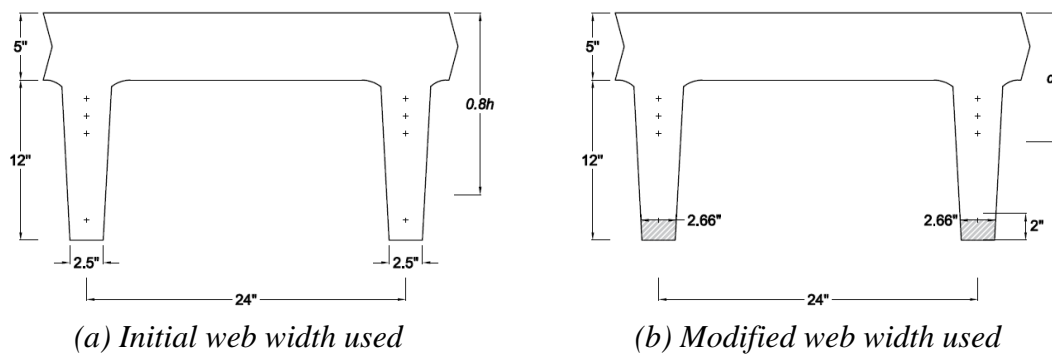


Figure 7.57: Concrete web width used for calculating concrete shear strength.

Table 7.5: ACI 318 (2019) predicted shear capacity using modified parameters.

ID	f_c (psi)	b_w (in)	d_p (in)	s (in)	V_c (kips)	V_s (kips)	$V_{n,pred.}$ (kips)	$V_{n.exp.}$ (kips)	$V_{n,pred.}/V_{n.exp.}$
C-U-S1	9500	5.32	9.66	10	23.8	23.2	47.0	51.8	0.91
C-IDS-S1	9500	5.32	9.66	10	23.8	23.2	47.0	49.2	0.96
C-DS-S1	8500	5.32	7.71	10	16.6	18.5	35.1	38.7	0.91

The results presented in Table 7.5 show a substantial difference in the accuracy of the predicted shear capacity compared to Table 7.4. A better and conservative shear capacity prediction can be obtained using the modified values used in the ACI 318 (2019) expressions.

The member shear capacity of the severe shear damage case repaired with the flexural/shear system can be obtained using the following expression if the shear strengthening can be fully utilized.

$$V_n = V_{c,mod} + V_{s,mod} + V_{plate} \quad (lbs) \quad (7.3)$$

where $V_{c,mod}$ is the concrete strength using the modified parameters, $V_{s,mod}$ is the shear strength using the modified parameters, and V_{plate} is the shear strength provided by shear strengthening plates based on the 20 kips designed capacity of each plate. Therefore, the nominal shear strength of a severe shear damaged C-channel beam repaired with shear strengthening plate is predicted to be 75.1 kips, higher than the shear strength of the undamaged specimen.

7.4 – Observations

The design and implementation of the proposed shear strengthening system integrated with the original flexural MF-FRP system applied to C-channel beams can be summarized as follows:

- Full-scale shear experiments were able to fail the specimens in shear using a one-point load setup, and the shear capacity of the three control specimens was obtained directly through testing.
- The specimen with severe shear damage repaired only with the flexural MF-FRP system experienced the worst behavior among all tests due to the formation of concrete splitting and inclined shear crack passing through the anchor bolts. The additional stresses from the fixed anchor bolts resulted in a premature shear failure.
- The shear strengthening plate increased the shear capacity and the shear test failed in flexure. The measured applied shear resistance is not the shear capacity from the flexural/shear repair system due to the removal of the MF-FRP plate after the test on the

other side of the beam. Furthermore, the shear strengthening plate was not fully utilized due to the pull-out of the prestressing strands.

- Even the severe shear damage condition did not affect the flexural behavior during testing. The repaired flexural and shear deteriorated beam achieved a capacity of 91.6% of the undamaged specimen.
- The repaired system improved the beam moment-deflection response by increasing the stiffness of the elastic portion. Therefore, the retrofitted beam experiences a lower deflection level and therefore, less damage, at the AASHTO operating limit.
- The FRP strain remains constant along the length of the plate. However, minor in-plane bending is likely developing in the FRP plate due to the presence of friction at the pin connections. This does not appear to affect the tensile capacity of the plate.
- Modified values of prestressing strand effective depth and concrete web width for the use with the ACI 318 (2019) design equations provide a good and conservative shear capacity prediction, within 9% of the experimental capacities. The modified values are used to better reflect the actual geometry and conditions of the deteriorate region on site.
- By repairing with the shear strengthening plate, the nominal shear capacity of the severely damaged beam at the end regions can be restored to that of the undamaged beam.
- The designed shear strengthening plate can be used with the original flexural MF-FRP system to address shear deterioration of in-service prestressed concrete C-channel beams.

CHAPTER 8 – RETROFIT OF AN IN-SERVICE DETERIORATED PC C-CHANNEL BRIDGE

This chapter presents the repair of a second in-service deteriorated PC bridge in North Carolina using the prestressed MF-FRP system developed in this research. Initial measurements and long-term monitoring and temperature effects from the retrofitted bridge are also presented. The successful experiments conducted in Chapter 5 showed that the MF-FRP retrofit system could restore the prestress losses and improve inventory and operating load limit for deteriorated PC C-channel beams and cored slabs. The first field demonstration installed on an in-service deteriorated C-channel beam on Bridge 340080 located in Franklin County, NC, in April 2019 only had one stem on one beam repaired with the prestressed MF-FRP system. The retrofit was observed in October 2020 after being in-service for more than 18 months, and it was found to be in good condition, as can be seen in Figure 8.1. The repair system is believed to serve as an ideal method to retrofit deteriorated PC bridges.



Figure 8.1: Condition of retrofit on Bridge 340080 in Franklin County, NC, after 18 months in-service.

Bridge 810003, a three-span C-channel bridge located in Sampson County, NC, built in 1966, was found to have severe deterioration due to natural aging and likely overloaded traffic, resulting in corrosion of the prestressing strands, and concrete spalling. The deteriorated PC bridge

was closed by NCDOT in May 2020, following the biannual inspection where excessive deflection under traffic load was observed. Figure 8.2 shows an overall view of the closed bridge. The closure of the bridge resulted in a 6 mile detour and affected local businesses and farming. Due to the impact of the closure and the replacement schedule, an immediate action to reopen the bridge was required to extend its service life. The prestressed MF-FRP repair system studied in this research was recommended to reopen the bridge based on the good performance of the field demonstration on the Bridge 340080 in Franklin County, NC. The MF-FRP repair system was selected by NCDOT to reopen the bridge, minimize the community and business impact, and connect the research project to practical application. The repair was installed by an NCDOT Division 3 maintenance crew under the supervision of the research team.



Figure 8.2: Overview of Bridge 810003.

8.1 – Condition Assessment of Bridge 810003

Field observation was required to assess the bridge deterioration and provide an appropriate repair system. Figure 8.3 shows the deterioration observed on the bridge, including concrete spalling, corrosion, exposure of the prestressing strands, and loss of prestressing strands, which reduced the beam flexural capacity and violated the AASHTO load rating limits. In addition, the

loss of concrete section and exposed strands at the end-support regions shown in Figure 8.4 raised concern of the beams' shear capacity, which has not been considered in previous research using the MF-FRP system. Sound concrete is required for the prestressed MF-FRP retrofit system to prevent concrete splitting from drilling and the anchorage system. A Schmidt-Hammer was used to estimate the concrete strength resulting in predicted strengths of 7.0 and 8.5 ksi for stem and flange concrete, respectively. Note that the measured value obtained from the Schmidt-Hammer is limited to 8.5 ksi due to limitations of the device itself. Nonetheless, the predicted concrete strength is still higher than the initial design concrete strength of 5.0 ksi. Figure 8.5 shows the retrofit plan of the deteriorated bridge after field inspection. Although most of the target deteriorated C-channel beams had only one stem with severe deterioration, the repair team decided to provide a comprehensive repair plan and retrofit both stems for each deteriorated C-channel beam. It was determined that 6 beams (12 stems) required flexural strengthening, and 7 damaged end regions needed additional treatments to address shear capacity concerns. The end region deterioration observed on this bridge was not considered previously when the MF-FRP system was initially developed. The proposed flexural/shear MF-FRP system presented in this research (Chapter 7) was developed to address the retrofit needs required for this bridge application.



Figure 8.3: Concrete spalling and exposed prestressing strands near mid-span.



Figure 8.4: Loss of concrete section and exposed prestressing strand and stirrup at end regions.

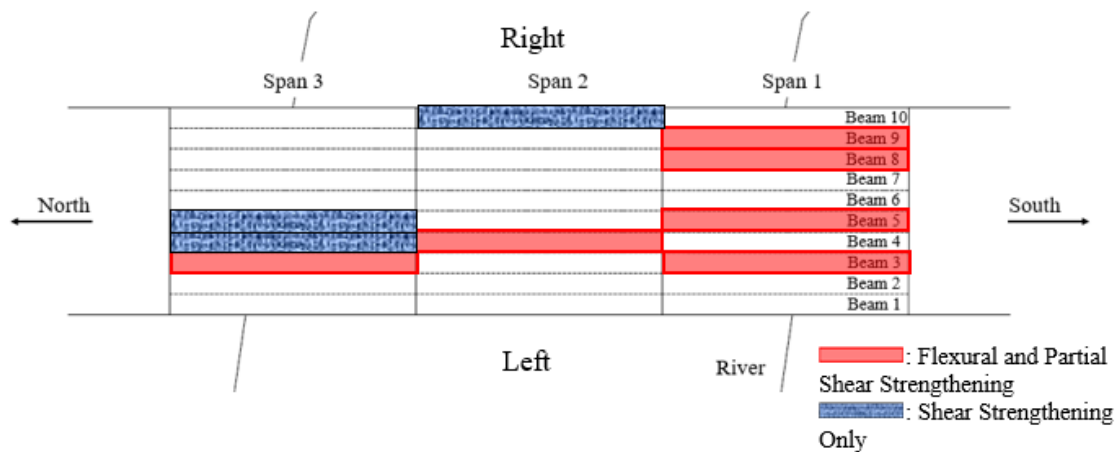
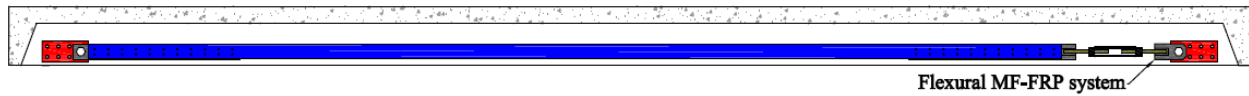


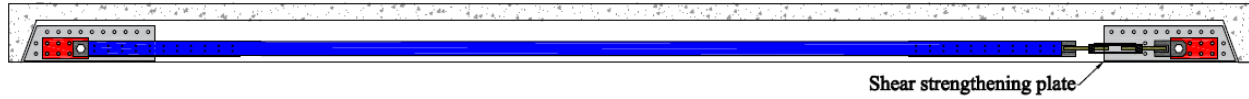
Figure 8.5: Retrofit plan for Bridge 810003.

8.2 – Retrofit Design

The purpose of the retrofit using the prestressed MF-FRP system developed in this research was to reopen the bridge until the replacement can be scheduled, currently scheduled for early 2022. The current version of the MF-FRP design in this research was used for the repair. However, to address the deterioration observed at the end regions, the additional shear strengthening plate that was designed to integrate with the original flexural MF-FRP system and presented in Chapter 7 was used. Figure 8.6 and Figure 8.7 show the elevation and cross-section views of the repair system applied in the application, respectively.

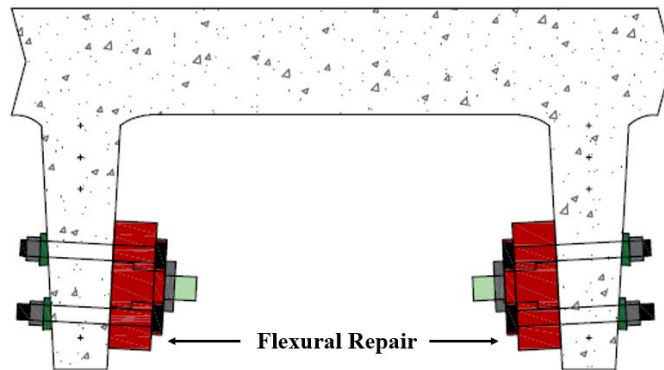


(a) Flexural repair

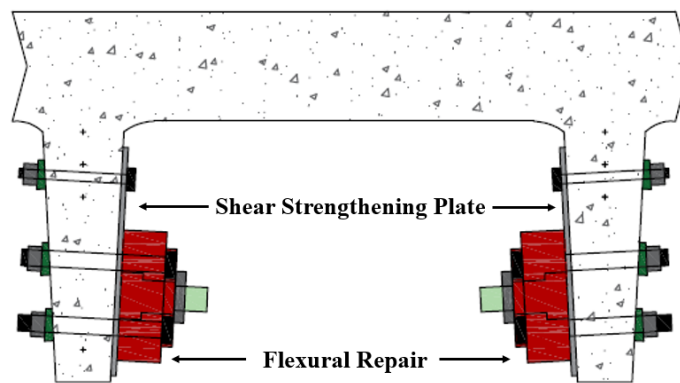


(b) Flexural and shear repair

Figure 8.6: Elevation view of the retrofit system.



(a) Flexural repair only



(b) Flexural and shear repair

Figure 8.7: Cross-section view of the retrofit system.

8.3 – Retrofit Procedure

After determining the extent of damage and completing the retrofit design, the installation procedure started with the FRP preparation. Beam measurements were taken to identify the best location of the fixed anchor plates. For the end with only flexural MF-FRP system, the fixed anchor plate was located as close the end of the beam as possible so that repair system can cover the entire beam as much as possible. Furthermore, for the ends with shear deterioration, the fixed anchor plate was located at least 1 ft. away from the shear deterioration to avoid the chance of developing premature damage during prestressing. Prestressing strands and stirrups were located using a pachometer to avoid hitting them while drilling the anchor holes based on the strand pattern and stirrup spacing provided in NCDOT (1966). However, it was observed that none of the strand patterns and stirrups spacing in NCDOT (1966) matched the details measured on-site. The FRP plates were cut to the appropriate length for the retrofit plan using a wet tile saw to control crystalline S_iO_2 and dust. The designed 22-bolt pattern of the MF-FRP was predrilled in the laboratory to ensure the alignment of the bolts at each row to avoid uneven bearing while the system is tensioned. Wooden templates for the fixed anchor plate and shear strengthening plate were prefabricated to provide a reference while drilling on-site, minimizing labor effort. Damaged concrete sections at the end regions were patched one week prior to installation to provide sound concrete and a flat surface for anchoring the shear strengthening plate, to minimize concrete splitting while prestressing the MF-FRP system. Installation activities on-site started with clamping the wooden templates of the fixed anchor and shear strengthening plates to the previously determined locations. Holes for the dead-end and live-end of the anchor plates and the shear strengthening plate were drilled with a hammer drill. All plates were anchored and tightened using regular wrenches by the repair team. The FRP was mechanically fastened to the FRP connector

plates at both ends with 30 ft.-lbs. torque to be consistent with the previous full-scale testing. Applied torque to prevent premature fatigue failure based on the experimental results from Bourara (2019). The turnbuckle system was attached to the FRP connector plate and turnbuckle plate. The FRP connector plate and turnbuckle plate were then attached to the dead-end and live-end anchor plates, respectively. FRP slack was removed by slightly rotating the turnbuckle body until the system remained straight. Before prestressing, elongation witness marks were aligned on the FRP plate and C-channel stem to indirectly monitor the applied prestress force. Additional strain gauges were attached to the MF-FRP prior to the installation serving as a cross-check of the prestressing operation and for the research purposes, to monitor long-term FRP strain and observe temperature effects. In this retrofit, the MF-FRP was prestressed to 18.5 kips of effective prestress force by rotating the turnbuckle body using a wrench. A second wrench was used to hold the FRP as a brace to prevent the FRP plate from rotating. The strengthening procedure was finished after reaching the desired prestressing force level. Figure 8.8 shows key steps of the installation procedure. An overview of the installed retrofit can be seen in Figure 8.9. A detailed step-by-step installation procedure is provided in Appendix A.



(a) Locating steel using a pachometer



(b) Precutting the FRP plates with a wet tile saw



(c) Drilling holes in the FRP plates



(d) Wooden template on stem



(i)



(ii)

(e) Drilling fixed anchor plate holes (i) and shear strengthening plate holes (ii) conducted by NCDOT personnel



(i)



(ii)

(f) Installing bolts of the fixed anchor plate (i) and shear strengthening plate (ii) by NCDOT personnel



(g) Tightening of FRP bolts to 30 ft.-lbs. torque by NCDOT personnel



(h) FRP prestressing conducted by NCDOT personnel

Figure 8.8: Key steps in retrofit installation.



(i) Dead-end anchor plate with shear strengthening plate



(ii) Live-end anchor plate



(iii) View of live-end



(iv) Overall view of retrofit

Figure 8.9: Overview of installed retrofit.

The entire repair process required five days of fieldwork by an inexperienced 6 person NCDOT maintenance crew with no special equipment to retrofit 6 beams (12 stems) including 7 shear strengthening plates. The installation was completed on November 4th, 2020, and the bridge reopened on November 5th, 2020.

8.4 – Long-term Monitoring

Instrumentation was installed on the retrofit system to conduct short- and long-term monitoring, including beam camber, FRP strain, and FRP elongation. Beam camber was measured before and after prestressing the MF-FRP using a stretched-wire system and a tape measure. The type of string used to measure the camber is important using the stretched-wire method to prevent sagging due to self-weight and relaxation. Kelly et al. (1987) and O'Neill et al. (2012) used piano wire and 80-pound fishing wire for the stretched-wire method, respectively. The reference positions were achieved by drilling anchor bolts or screws into the concrete and attaching the string (O'Neill et al., 2012). An 80-pound fishing wire attached to screws was used in this research to provide flexibility during installation. Beam camber was measured on Span 1 for Beams 7, 8, and 9 (refer to Figure 8.5) before and after prestressing. Beam 7 is an unstrengthened beam, while beams 8 and 9 are repaired deteriorated beams. These beams were selected to study the restored camber from the retrofit system on an individual retrofitted beam and on the adjacent beam. This helps understand the condition of the transverse prestressing. Figure 8.10 shows the camber measurement system installed on a C-channel beam.

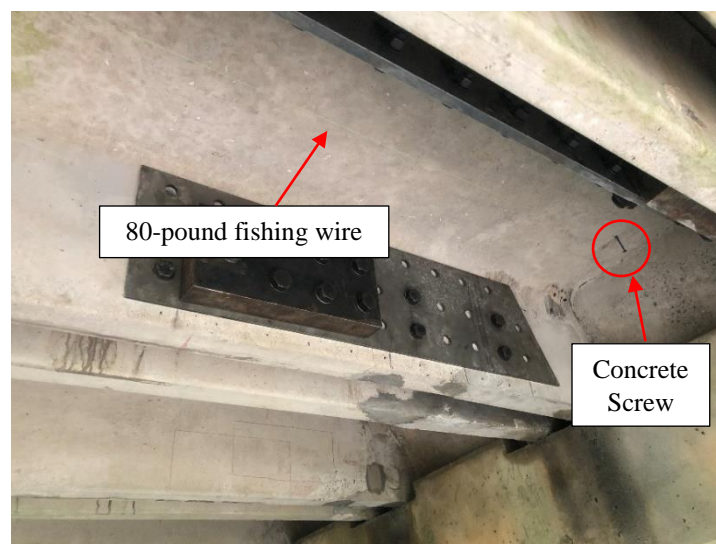


Figure 8.10: Beam camber measurement system.

Measured FRP elongation provides an easy and economical way to obtain and monitor the applied prestressing force using witness marks on the FRP plate and concrete stem, as shown in Figure 8.11. In Figure 8.11, the ruler indicator and tape were temporarily attached to the concrete during prestressing of the MF-FRP to help monitor the FRP prestressing force.

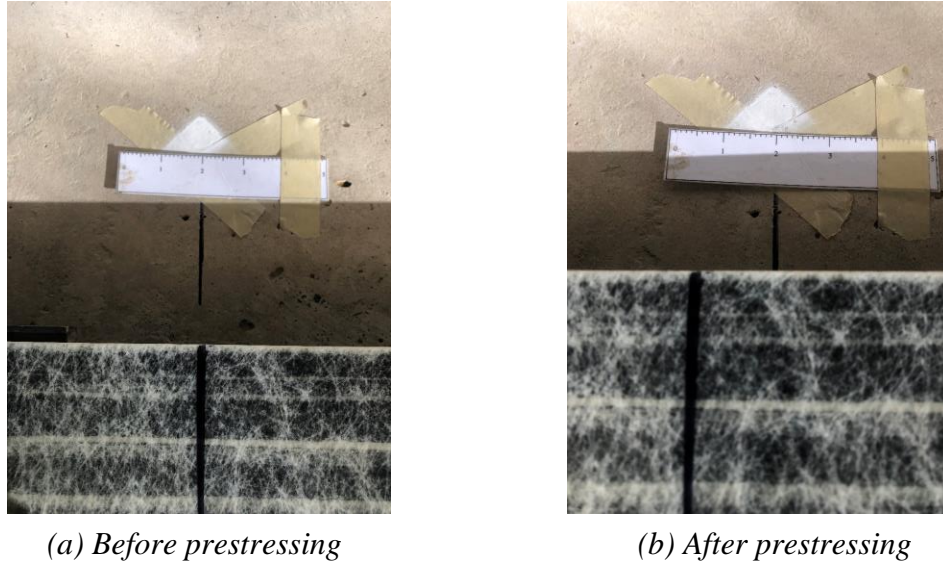


Figure 8.11: Witness mark measurement.

The required elongation can be determined using Equations 8.1 and 8.2 (Equations 5.4 and 5.5 from Chapter 5), which consider the elongation from the applied prestress force and slip between the bolts and connections. The initial measured FRP elongations were between 1.1 to 1.3 in. due to the difference in FRP gauge lengths.

$$\Delta L_p = \frac{P_{FRP} \times L_g}{A_{FRP} \times E_{FRP}} \quad (8.1)$$

and

$$\Delta L_{TOT} = \Delta L_p + \Delta L_{slip} \quad (8.2)$$

where ΔL_p is the elastic elongation of the FRP plate due to the prestressing force, L_g is the gauge length over which ΔL_p is measured, A_{FRP} is the FRP cross-sectional area, E_{FRP} is the FRP elastic modulus, P_{FRP} is the applied prestressing force, ΔL_{slip} is the axial displacement of the FRP

considering bolt slip in all of the connections, which is taken as 0.4375 in., and ΔL_{TOT} is the total axial displacement required to achieve the targeted P_{FRP} which can be measured while applying the prestressing force.

Electrical resistance strain gauges (FLA-5-11-3LJCT-F) were also installed on the FRP plates to measure the FRP strain. FRP strain was measured using a P3 strain indicator and recorder, the same equipment used to obtain the prestress losses described in Section 6.1.2.2.1. The strain gauge served as a check to compare the measured FRP elongation with the same applied prestressing force. The required FRP strain is determined following Hooke's Law given by

$$\varepsilon_{FRP} = \frac{P_{FRP}}{E_{FRP}A_{FRP}} \quad (8.3)$$

where ε_{FRP} is the target FRP strain measured using a strain gauge, E_{FRP} is the FRP elastic modulus (9020 ksi), A_{FRP} is the FRP cross-sectional area (0.5 in^2), and P_{FRP} is the design prestressing force in the FRP. With 18.5 kips of applied prestressing force on the FRP, the target FRP strain was $4100 \mu\varepsilon$. Strain gauges were installed on both sides of the selected FRP plate and used to measure the long-term strain variation and temperature effects on the FRP system. Long-term strain variation readings were taken between 9:30 and 10:00 a.m. to minimize the daily temperature effect. The daily temperature effect on the FRP system was measured on sunny days with a large expected temperature change (at least 10°F) according to the weather forecast with, a one-hour interval between each measurement. All instrumentation applied to this bridge was revised and improved based on the application experience from the Bridge 340080 installation, so that the data can be better collected during installation and beyond the time period of this research.

8.5 – Results and Discussions

The repair process started on October 28th, 2020, and finished on November 4th, 2020, which took five days of fieldwork according to the NCDOT maintenance crew schedule. The retrofit of deteriorated PC beams was successful, and the bridge was reopened on November 5th, 2020, one day after the repair was completed. The short- and long-term measurements taken during and after the repair are presented in the following.

8.5.1 – Beam Camber

Table 8.1 presents the measured beam camber for a period of time covering the first 6 months since the retrofit was installed. The restored beam camber was observed to be 3/16 in. due to the prestressing of the MF-FRP system on beams 8 and 9, with an effective depth of 12 in. However, the restored camber was zero for beam 7, adjacent to beam 8, likely due to the loss of the transverse prestressing force. The beam camber remained constant during the first 6 months of service when measurements were taken.

Table 8.1: Measured beam camber.

ID	Initial Value (in.)	Prestressing First Plate (in.)	Prestressing Second Plate (in.)	Days after installation			
				18	28	75	173
Beam 7	1-3/4	--	--	1-3/4	1-3/4	1-3/4	1-3/4
Beam 8	1-3/4	1-7/8	2	1-15/16	1-15/16	1-15/16	1-15/16
Beam 9	1-3/4	1-7/8	1-15/16	1-15/16	1-15/16	1-15/16	1-15/16

8.5.2 – FRP Elongation

Figure 8.12 presents the measured FRP elongation after installation. The ID nomenclature of the legend shown in Figure 8.12 is the FRP plate where SX represents span number, BX is the beam number, and R and L are the right and left stems, respectively, defined by the direction facing south to north. The results show that the retrofit system experienced a reduction in elongation within the first ten days after installation. However, the loss of elongation stabilized after ten days

of service. As mentioned in Section 8.4, FRP elongation can be used as a convenient method to monitor the applied prestress force. However, the decreased elongation during the first ten days was not from prestress losses but rather from the combined actions of the FRP bolts bearing on the FRP plate under sustained loading (refer to Section 4.1), and beam creep. It is recommended that the initial prestress force used in assessments be the value measured using the witness marks at least ten days after installation to allow the initial losses to take place. FRP elongation measurements from S2B4-R and -L could not be accessed after January 2021 due to the removal of the cross-board, a temporary walking platform set between bridge piles during installation, under the bridge by NCDOT Division 3 personnel. The remainder of the FRP elongation measurements have remained stable after being in-service for at least one year.

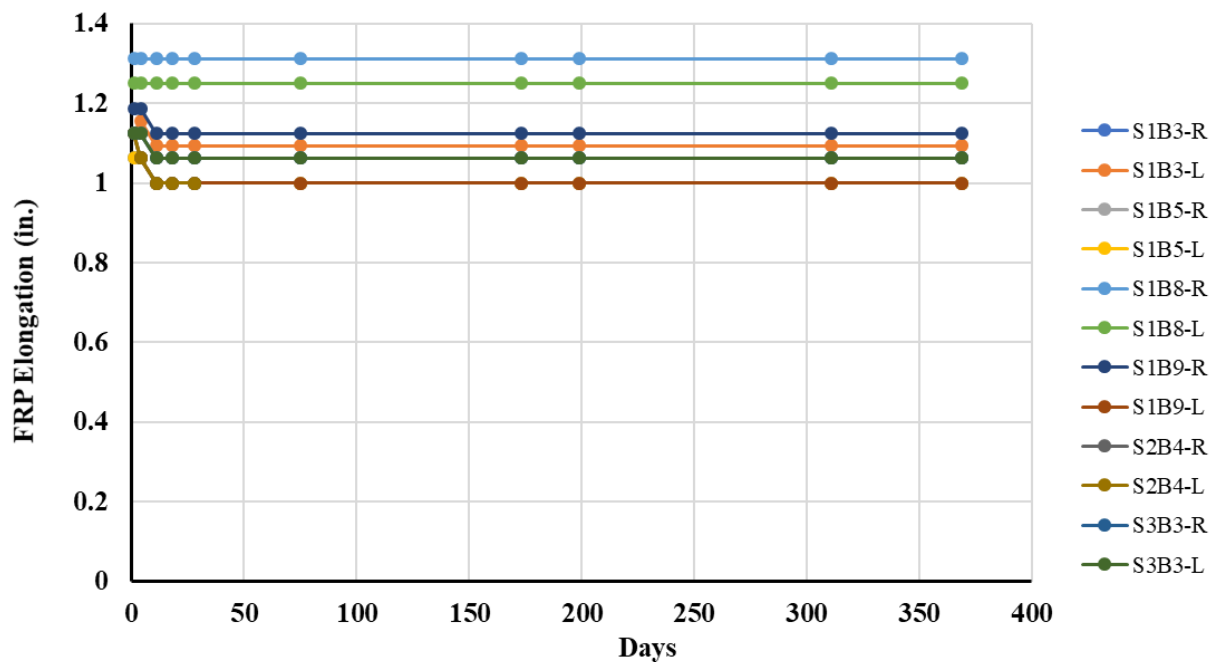


Figure 8.12: Measured FRP elongation after installation.

8.5.3 – FRP Strain – Long-term behavior and Temperature Effect

The variation of FRP strain after installation is shown in Figure 8.13. Similar ID nomenclature used for the FRP elongation was used for the FRP strain gauge data presented in Figure 8.13. SX represents span number, BX is the beam number, R and L are the right and left stems, and S and M show the gauge location, on the concrete stem face of the FRP, or the inward face of the FRP, respectively. The average initial measured prestress strain was $4280 \mu\epsilon$, close to the target strain of $4100 \mu\epsilon$. Similar behavior was observed as for the FRP elongation measurements (refer to Figure 8.12), where the greatest variation of FRP strain occurred during the first ten days after installation and remained stable after that. It was observed that all measured FRP strains decreased slightly between the measurements taken at 75 and 173 days after installation, with an average difference of $180 \mu\epsilon$ (ranging from 100 to $230 \mu\epsilon$). This reduction of FRP strain results in about a 0.034 in. reduction (ranging from 0.0196 to 0.045 in.) in FRP elongation based on Equation 8.1. Such a small change in length is less than the minimum scale reading from the tape measure used for the long-term monitoring. Hence, the FRP elongation measurement remained unchanged even though small differences of MF-FRP strain were recorded by the strain gauges. The measurements conducted at 75 and 173 days was on January 19th and April 27th, 2021, respectively, representing winter and spring seasonal variations. Therefore, the strain difference is more likely a result of the temperature effect due to the seasonal difference, and not from prestress losses. To date, the average initial losses of FRP strain is approximately 3.9 %, and the average losses between seasons is around 3.7 %.

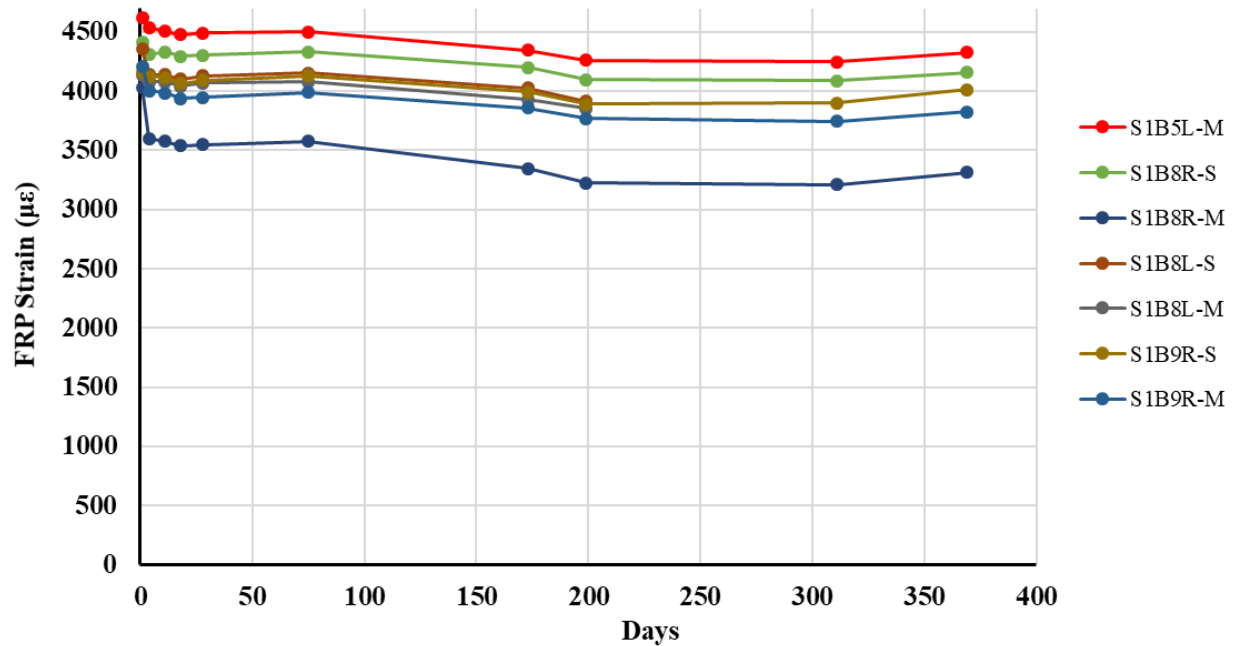


Figure 8.13: Long-term monitoring of FRP strain.

The long-term readings were conducted between 9:30 to 10:00 a.m. for each measurement to avoid potential daily temperature effects on the measured FRP strain. Two set of measurements were performed on December 3rd, 2020, and April 27th, 2021, to investigate daily FRP strain variation due to temperature in different seasons. Figure 8.14 and Figure 8.15 present the measured temperature location and data collected, respectively. Due to the manual process of collecting data, the data was only collected during daylight hours. The measured FRP strain results demonstrate the daily temperature effect on the measured FRP strain. By examining the relationship between FRP strain and air temperature, it is observed that the minimum measured FRP strain occurs at the maximum air temperature. The time lag between FRP strain and air temperature is due to the heat transfer time, enabling member deformation to develop, which is approximately three to four hours. Figure 8.16 illustrates the measured temperature location and the temperature gradient along the height of the section. It was observed that all temperature results measured from the bottom of the beam experienced a similar variation of around 15 °F to the air temperature no matter what

season it is. However, the asphalt surface underwent the highest temperature variation because of the direct sunlight compared to locations under the beam; 33 °F and 63 °F differences in winter and spring seasons, respectively. The high-temperature variation measured on the asphalt surface in spring resulted in a higher FRP strain variation compared to the winter season. The results presented in Figure 8.15 show that the measured FRP strain variations in the data collection period were only 52 and 70 $\mu\epsilon$ in winter and spring, respectively. It can therefore be concluded that the temperature effect on the repair system is minimal and can be ignored, resulting in a change of 0.019 and 0.025 in. in axial deformation for the 30 ft. beam span in the winter and spring season, respectively.

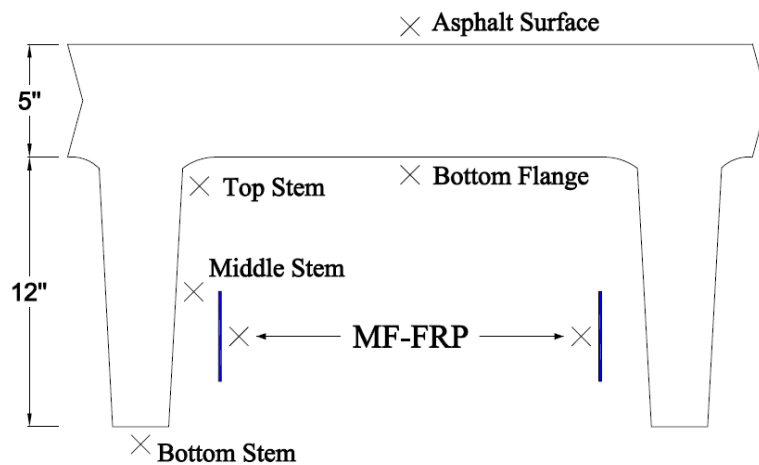
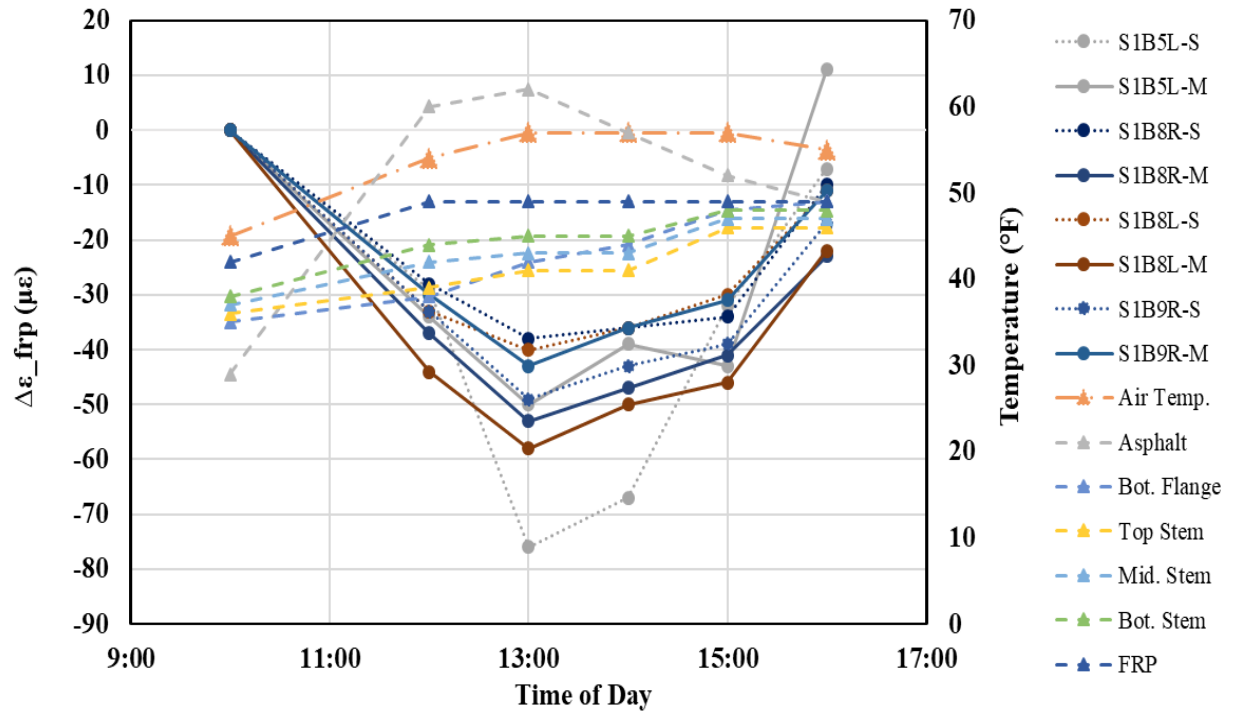
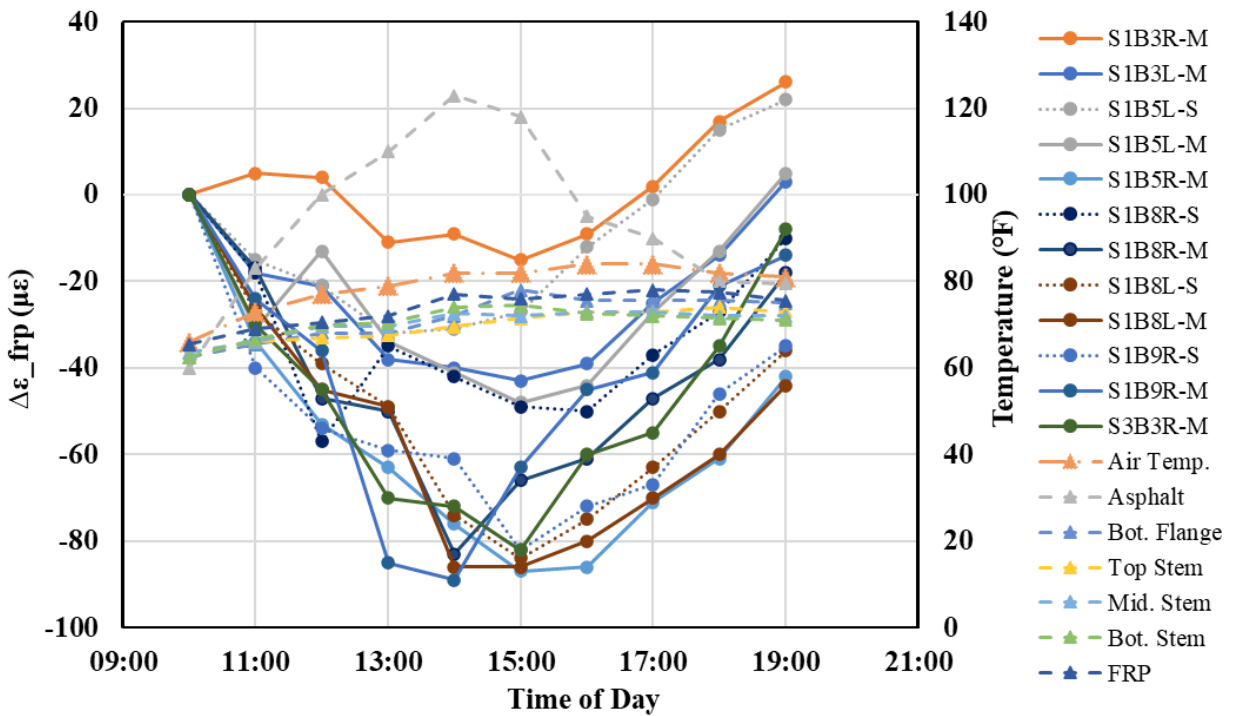


Figure 8.14: Measured temperature location.



(a) December 3rd, 2020



(b) April 27th, 2021

Figure 8.15: Variation of FRP strain and temperature.

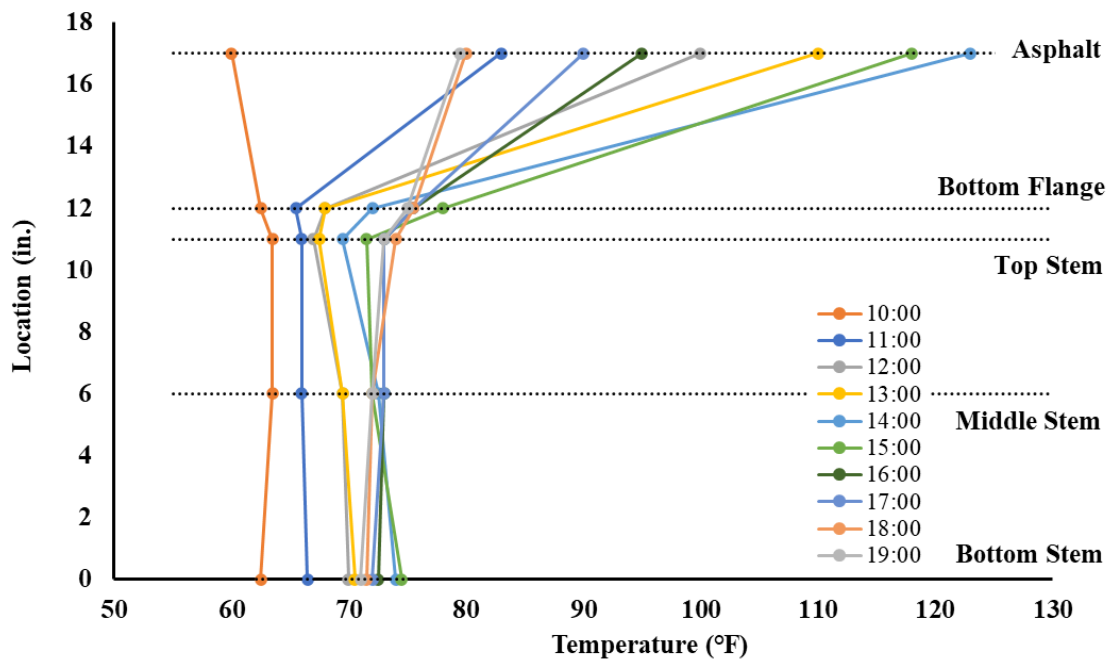
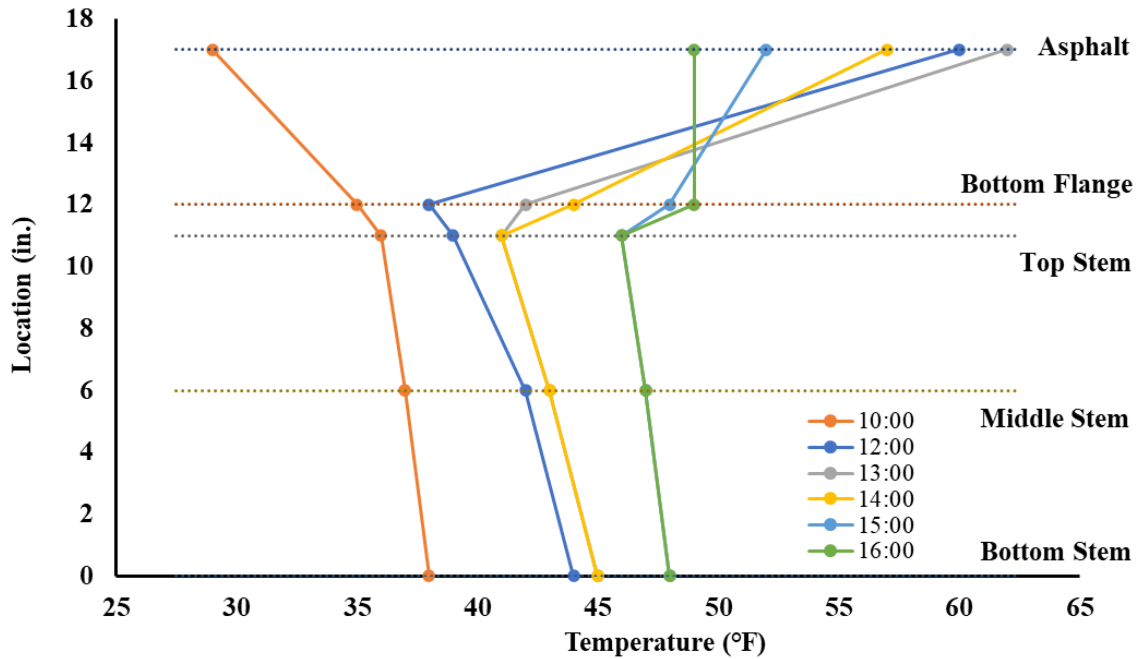


Figure 8.16: Measured temperature gradient over the section height.

8.5.4 – Prestressed MF-FRP Retrofit System

The prestressed MF-FRP retrofit system successfully repaired the deteriorated PC bridge and enabled the bridge to be put back in service under the current load-posting condition. It remains in good condition after being in-service for more than 1 year. Only minor longitudinal cracks were observed on some of the FRP plates, located at the first one or two rows of FRP bolts, which was expected based on the fatigue test results presented in Section 4.2.2. Longitudinal cracking was observed after the bridge reopened but remained unchanged after the initial two weeks of being in-service, shown in Figure 8.17. Besides longitudinal cracking of the FRP plates, no signs of concrete splitting or deterioration of the repair system are observed except for surface rusting of the steel elements. Figure 8.18 shows the condition of the steel elements of the repair system after being in-service for approximately 1 year.

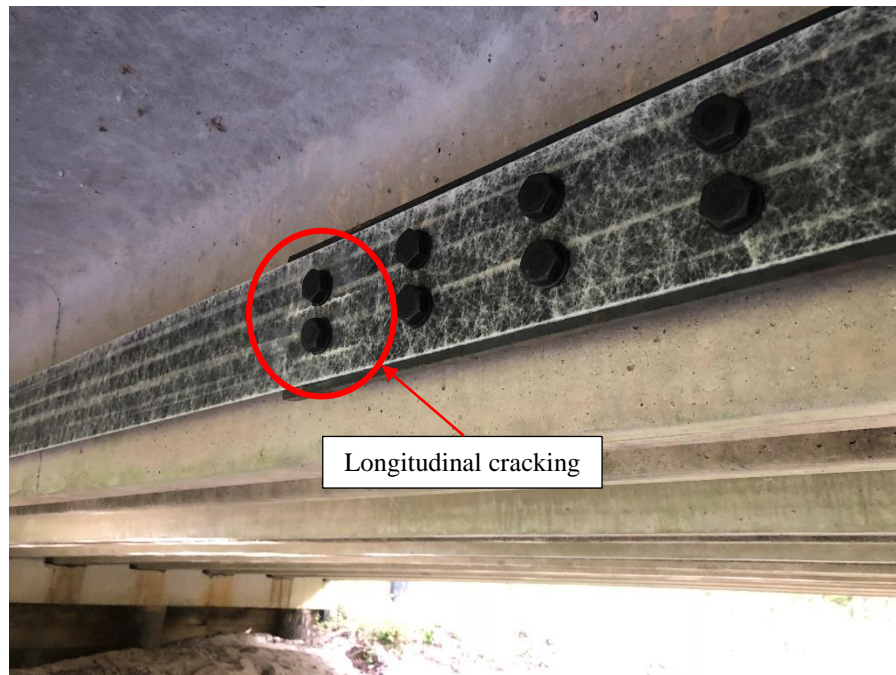


Figure 8.17: Longitudinal cracks on MF-FRP plate.



Figure 8.18: Repair system after 1 year after installation.

8.5.5 – *Cost Benefits*

As mentioned in Chapter 1, one of the repair methods available to DOTs is to replace a deteriorated C-channel beam with a good condition C-channel beam. However, DOTs are no longer using C-channel type beams in new construction. Therefore, there will be a limited stockpile of good quality C-channel beams available to conduct such repairs in the future, making traditional replacement less feasible. In addition, C-channel beam replacement method requires renting a mobile crane to move the C-channels beam on-site. The cost of renting a mobile crane and hiring an operator for 3-4 days is approximately \$50,000, according to the information provided by NCDOT personnel. This adds significant cost to the replacement budget and requires road closure during the replacement process, resulting in a temporary inconvenience for the local community.

McCoy et al. (2021) showed that the optimized field-level installation time was 4.1 labor-hours for the flexural MF-FRP repair system on a deteriorated C-channel beam (2 stems). The MF-FRP repair system can provide a rapid and economical solution with little labor and simple tools and skills required. All components of the MF-FRP system and required installation tools are readily available commercially. For the repair applied on Bridge 810003, the total material cost,

including steel elements, hardware, and FRP plate, for a single beam (2 stems) was approximate \$2,000 with a total of \$12,000 for 6 beams, which is significantly lower than the cost of traditional beam replacement. Material prices are subject to change. Further, the witness marks used during installation allows monitoring of the prestress level in the long term without the need for additional instrumentation. And, as needed, the turnbuckle can be used to adjust the prestress level in the future. Further, most of the elements, except for the FRP plate, can be reused after bridge replacement, which is valuable from a budget perspective.

8.6 – Observations and Repair Application Recommendations

8.6.1 – Observations

The results of the field application can be summarized as follows:

- The retrofit application for 6 C-channel beams (12 stems) using the proposed flexural/shear MF-FRP repair system was successful, and Bridge 810003 was put back in-service after the repair was completed. It took an inexperienced 6 person NCDOT maintenance crew five days to complete the installation.
- The repair system remains in good condition after being in-service for more than 1 year. No signs of damage were observed on the repair system except for minor longitudinal cracking on the FRP plate at the first and second rows of FRP bolts.
- Longitudinal cracking was expected on the repair system after being in-service as was observed in laboratory testing. The longitudinal cracking did not continue to propagate after being in-service for two weeks.
- Measured FRP elongation and beam camber remained constant after the initial two weeks of being in-service when the system became stable.
- Long-term FRP strain measurements demonstrated a noticeable effect due to seasonal temperature variation.

- Daily temperature variations of approximately 15 °F (45 °F to 57 °F in winter and 66 °F to 84 °F in spring) resulted in a 52 - 70 $\mu\epsilon$ variation in FRP strain. In spring, the temperature effect tends to impact the member deformation more compared to winter.
- Seasonal and daily temperature variation has a negligible effect on the FRP plate strain and can be ignored from the perspective of measuring total elongation using the witness marks.
- The MF-FRP repair system can serve not only as an effective method to repair deteriorated PC bridges, it can also save a significant amount of money in terms of labor-hours, material cost, and equipment compared to the traditional repair or replacement alternatives.

8.6.2 – Repair Application Recommendations

Additional installation time can be saved by taking the recommendations mentioned in the following based on the experience on Bridge 810003. The MF-FRP repair system requires drilling 24 holes in the concrete stems (six holes for each fixed anchor plate). It takes approximately five minutes to drill a single hole without hitting a stirrup or prestressing strand. However, the drilling time increases to more than 30 minutes for a single hole once internal reinforcing is hit. Therefore, a good quality and accurate pachometer is recommended to locate internal steel prior to drilling, as the beams are old and lack detailed information. It has been observed that stirrup spacing and orientation and strand patterns on-site are different than those specified on design drawing.

A good quality hammer drill should be used for the installation. The drilling process can only be conducted under the beam, limiting the drilling space to the clear distance between the two stems, approximately 20 in. An angular chuck was installed on a regular hammer drill to provide extra working space during drilling (refer to Figure 8.8 (e)-(h)). However, the angular chuck seemed to decrease the drilling power and experienced over-heating. Therefore, it is recommended to use a regular hammer drill with the length of the drill, including the drill bit, less than 20 in.

The purpose of the MF-FRP flexural/shear repair system is to extend the bridge service life for an additional 3 to 5 years until bridge replacement is scheduled. However, the schedule of bridge replacement is hard to predict due to a lot of variables including budget and construction priority, which may delay the planned schedule. Corrosion of the steel elements of the repair system may become critical due to the time the system is in-service under extreme environmental conditions. Therefore, it is recommended to coat the steel elements before installation to resist or delay corrosion.

CHAPTER 9 – CONCLUSIONS AND RECOMMENDATIONS

This chapter presents the conclusions and findings of this research program. Future research is also recommended based on the outcomes of this project.

9.1 – Conclusions

9.1.1 – Anchor Bolt Pattern for MF-FRP Plate

The following conclusions are drawn from the investigation of anchor bolt pattern presented in this research.

- The 22-bolt pattern using 0.5 in. diameter bolts is sufficiently optimized for the MF-FRP plate with an ultimate tensile capacity of 46.4 kips.
- The 0.375 in. bolt diameter treatment groups have load capacities similar to that of the 0.5 in. treatment groups with the same 22-bolt pattern.
- Longitudinal shear failure controls the ultimate capacity of the open-hole and multibolt treatment conditions with greater than 14 bolts providing a more progressive failure with visual indication of the propagation of longitudinal shear cracks.
- It is recommended to use the 22-bolt pattern with 0.5 in. diameter bolts, and an initial prestress force less than or equal to 22 kips.

9.1.2 – Long-term Behavior

This research investigated the behavior of the 22-bolt MF-FRP connection of the retrofit using 0.5 in. and 0.375 in. diameter bolts. Significant differences were discovered.

- Under sustained loading, the MF-FRP connection experiences creep in the early ages (within the first 5 days for 0.5 in. bolts, and 10 days for 0.375 in. bolts) in the form of bearing-induced displacements.
- Under 22 kips of sustained loading for 30 months, the connection experienced on average 0.07 in. and 0.152 in. of creep for the 0.5 in. and 0.375 in. bolts, respectively.

- Prestress losses from creep are comparable to those of prestressing steel relaxation for both bolt sizes.
- Ultimate tensile capacity is unaffected after 30 months of sustained loading.
- The use of 60 ft.-lbs. torque applied on the 0.5 in. diameter bolts is recommended for the repair application to avoid premature fatigue failure, with up to 450,000 cycles reached for a MF-FRP plate force range of 22 to 29 kips.
- In some cases, the maximum MF-FRP plate force is likely to be less than 29 kips, resulting in a longer fatigue life.
- A maximum fatigue displacement of 0.25 in. is set for both 0.375 in. and 0.5 in. bolts.
- Periodic measurement of fatigue displacement is recommended after installation of the retrofit to examine creep and fatigue damage, following the procedure provided at the end of Section 4.2.
- Prestress losses from creep or fatigue can be restored by using the turnbuckle to re-stretch the MF-FRP plates by a length equivalent to the displacements measured, using Hooke's Law.
- Minor longitudinal cracks at the bolts are expected on the MF-FRP plate from both sustained loading and fatigue. The MF-FRP plate should be replaced if the longitudinal cracks have propagated beyond the first 4 rows of FRP bolts, or bearing displacements greater than 0.4 in. for the 0.5 in. bolts (0.625 in. for the 0.375 in. bolts) between the MF-FRP plate and the bolts is observed by inspection.

9.1.3 – Full-scale Flexural Experiments

This research proves the success of the retrofit with full-scale testing of six PC C-channel beams and five PC cored slabs using the designed MF-FRP system. The following conclusions were drawn:

9.1.3.1 – Repaired C-channel Beams

- The MF-FRP 2.0 retrofit design is recommended as the final version of the MF-FRP repair system considered in this research.
- The MF-FRP 2.0 retrofit design resulted in failure by concrete crushing and a more ductile behavior. The residual capacity of the FRP plate at concrete crushing is 33% of the FRP tensile capacity. This residual capacity in the FRP plate gives engineers the flexibility to increase the prestress force beyond the 18.5 kips applied in this investigation, up to recommended maximum prestress force of 22 kips. This would further increase the inventory and operating ratings of retrofitted C-channel beams.
- The MF-FRP 2.0 retrofit requires the concrete (and patching material, if needed) in the C-channel stems to be of sound quality at the location where the anchor plates are attached to the concrete substrate (fixed plates in MF-FRP 2.0).

9.1.3.2 – Repair Cored Slabs

- For two fully-lost prestressing strands, the strengthened beam's capacity was 14.2% higher than that of the companion unstrengthened damaged beam. For four fully-lost prestressing strands, the strengthened beam's capacity was 25.8% higher than that of the companion unstrengthened damaged beam.
- Using two MF-FRP plates post-tensioned at 22 kips, 0.22 in. of camber was restored to the strengthened beams for both levels of damage.

- The retrofit enhanced the load-deflection behavior of the beams by significantly increasing the length of the elastic portion. As a result, the levels of damage incurred by the structure at the original load ratings (operating and inventory) are lower for the strengthened sections than for the undamaged section.
- For sections damaged by prestress loss of up to four fully-lost strands, the enhancement provided by the retrofit was sufficient to be in compliance with original AAHSTO load limits.

9.1.4 – Analytical Modeling

A layered-sectional analysis (LSA) approach was illustrated in Chapter 6 to generate the complete moment-deflection response of retrofitted C-channel beams and cored slabs. The conclusions are shown as follows:

9.1.4.1 – C-channel Beams

- The LSA approach resulted in a good response prediction compared to the experimental results considering the second-order effect from the MF-FRP system when the FRP plate is treated as an external unbonded tendon.
- The ultimate capacity of the retrofitted C-channel beams predicted by the LSA approach provides a prediction within 5% of the experimental results.
- Predicted member response can be improved by considering the prestressing strand profile (harped or straight), prestresses losses, development length of prestressing strand, concrete strength, and the member damage condition.
- The remaining prestress force in PC C-channel beams can be obtained by cutting a strain gauged prestressing strand, or by testing the cracking moment experimentally. For the C-channel beams tested in this program, it was found that 45% of the prestress was lost relative to the reported jacking stress.

- The difference of total prestress losses between experimental results and empirical calculations may be due to corrosion of the prestressing strand in the deteriorated beams, resulting in reduced bond and increased slip between the concrete and the prestressing strands.

9.1.4.2 – Cored Slabs

- Strengthened capacity predictions were within 5% of the recorded experimental capacities.
- An ultimate strength analysis using the conventional equivalent rectangular stress block sectional method was presented. It over predicted the nominal moment of a strengthened section with two fully-lost strands by 10%, and that of a strengthened section with four fully-lost strands by 8.5%.

9.1.5 – Full-scale Testing and Modeling of Shear Deteriorated C-channel Beams

The shear behavior of C-channel beams with different levels of shear deterioration was obtained through full-scale experiments using a one-point load test setup. Additional flexural testing was conducted to study the influence of severe shear deterioration on the flexural behavior.

The conclusion can be summarized as follows:

- For beams with severe shear deterioration, losing the bottom prestressing strand of each stem at the shear critical region, the measured shear capacity was 25% less than that of the undamaged specimen.
- For intermediate shear deterioration, the shear capacity was 5% less than that of the undamaged specimen. However, at failure it achieved only 60% of the deflection compared to that of the undamaged specimen.

- Severe shear deterioration repaired only with the flexural MF-FRP system had the worst behavior with a premature shear failure due to the formation of inclined shear cracks through the anchor bolts and concrete splitting in the longitudinal direction.
- The designed shear strengthening plate can improve the specimen's shear behavior, resulting in a more desirable flexural failure.
- The retrofitted C-channel beam achieved 91.6% of the ultimate capacity of the undamaged specimen (presented in Section 5.2). Severe shear deterioration did not affect the member flexural behavior.
- The MF-FRP repair system enhanced the beam's moment-deflection response by increasing the stiffness of the elastic portion. As a result, the retrofitted C-channel beam experienced a lower deflection value at the AASHTO operating limit, which indicates less incremental damage is being accumulated.
- Conservative shear capacity was predicted for the undamaged and severe shear damaged beams, within 9% of the experimental results according to ACI 318 (2019) with modified parameters. Removing the restriction on prestressing strand effective depth and defining a modified concrete web width helped improve the prediction accuracy.

9.1.6 – Field Application

A deteriorated PC C-channel bridge located in Sampson County, NC, was repaired successfully using the MF-FRP system by an NCDOT maintenance crew and the NC State research team. Long-term monitoring was conducted during and after the repair was completed.

The following conclusions are made:

- Six C-channel beams with 12 stems were repaired using the proposed flexural/shear MF-FRP system by a 6 person NCDOT maintenance crew and the NC State research team in five days of fieldwork.
- The retrofit on the deteriorated C-channel bridge was conducted successfully, and the bridge was reopened after the repair was completed.
- The repair system remains in good condition after being in-service for more than 1 year. No damage was observed on the repair system except for minor longitudinal cracking on the MF-FRP plate at the first and second rows of bolts, and surface rust on the steel elements. It is recommended to coat the steel elements to help delay, or prevent, corrosion.
- Minor longitudinal cracking of the FRP plate was expected after being in-service based on observations from the fatigue tests presented in Section 4.2.
- The repair system became stable after two weeks of being in-service with constant measured FRP elongation and beam camber.
- The repaired beams experienced a higher temperature effect in spring compared to winter, and a 15 °F difference in daily temperature resulted in a 52 and 70 $\mu\epsilon$ variation in FRP strain during the winter and spring season, respectively.
- The minor variation in FRP strain observed due to daily and seasonal temperature differences is negligible as confirmed by the constant measured FRP elongation.

- The MF-FRP repair system can serve as an ideal repair method to extend the service life more than a year with significant economic benefits.

9.2 – Design Recommendations, and Field Inspection

9.2.1 – Design Recommendations

- The flexural MF-FRP repair system is recommended for C-channel beams with up to two prestressing strands lost (typically the bottom-most strand of each stem). For cored slabs, the repair system can be used with up to four prestressing strands lost due to corrosion.
- The shear strengthening plate is only designed for C-channel beams with deteriorated end-regions including concrete spalling of the stem and with exposed corroded stirrups and prestressing strands. Spalled and damaged concrete must be patched with an appropriate material to restore the cross-section, bond with the existing concrete and resist the forces applied from the bolted connection. The shear strengthening plate is not required if the concrete is sound at the end-region of the stems and there is no local indication of stirrup or strand corrosion.
- There are no restrictions on the use of the proposed prestressed MF-FRP retrofit system for typical cross-sectional geometry, material properties, span length, and steel prestressing strand layout of C-channel beams and cored slab prestressed concrete bridge superstructures.
- All steel elements are required to be Grade 50 steel, and it is recommended that they be coated to prevent, or delay, corrosion. Alternatively, stainless steel equivalent components may be used.

- The fixed anchor plate should be located as close to the ends of the beam as practically possible, typically around 12-20 in.

9.2.2 – Field Inspection

- The current level of prestress force in the MF-FRP plates can be determined by measuring the distance between the witness marks identified at the time of installation to apply the initial prestress force.
- If the total measured displacement two weeks after installation of the MF-FRP retrofit system due to bearing creep, ΔL_{creep} , exceeds 0.15 in. for 0.5 in. bolts (or 0.375 in. for 0.375 in. bolts), then the MF-FRP plate should be replaced. Refer to Section 4.3 for measurement details.
- If, as part of a bi-annual bridge inspection, the displacement measurement corresponding to fatigue damage accumulation, $\Delta L_{fatigue}$, exceeds 0.25 in. for either bolt size, the MF-FRP plate is approaching the end of its fatigue life and should be replaced. Refer to Section 4.3 for measurement details.
- Inspect the concrete condition at the fixed anchor plates. Remove the repair system if concrete splitting has initiated and propagated along a line of bolt holes.
- Inspect the surface condition of the MF-FRP plates for damage. Longitudinal shear cracks along the first 2 rows of bolts are typical and expected. However, if the longitudinal shear cracks have propagated beyond the first 4 rows of bolts, the MF-FRP system should be replaced.
- All bolts should be checked to confirm their tightness. The tightness of the FRP bolts to 60 ft.-lbs. torque should be confirmed.

- If too much prestress force in the MF-FRP plates has been lost, and the retrofit system is otherwise in good condition, the MF-FRP plates may be re-tensioned using the turnbuckle system.

9.3 – Recommendations for Future Work

- Develop an analytical model to predict the tensile capacity and failure mode of FRP plates that can be mechanically fastened. This will allow optimization of the FRP plate in the future and allow more design flexibility.
- Design FRP components that can replace the current steel elements of the MF-FRP system so that the system's weight can be reduced and corrosion of the repair can be eliminated.
- Customize the fixed anchor plate design with a pin connection so that the dimensions and weight of the fixed anchor plate can be reduced.
- Perform shear tests on a beam with intermediate shear damage repaired with (i) only the flexural repair system, and (ii) the flexural/shear repair system.
- Modify the shear strengthening system by enlarging the bolt holes on the plate so that it can be installed more efficiently with more flexibility.

REFERENCES

- AASHTO. (2017). *LRFD bridge design and specifications*. 8th Ed. Washington, DC: AASHTO.
- AASHTO (2018). *The Manual for Bridge Evaluation*, 3rd Ed., 674 Washington, DC: AASHTO.
- ACI 214.4R (2010). Guide for Obtaining Cores and Interpreting Compressive Strength Results. American Concrete Institute, Farmington Hills, MI, 17.
- ACI 318 (2019). Building Code Requirements for Structural Concrete and Commentary, *ACI Manual of Concrete Practice*, American Concrete Institute, Farmington Hills, MI, 520.
- ACI 440.2R (2017). Guide for the Design and Construction of Externally Bonded FRP Systems for Strengthening of Concrete Structure. American Concrete Institute, Farmington Hills, MI, 2017, 116.
- Adhikary, B. B., Mutsuyoshi, H., and Sano, M. (2000). Shear strengthening of reinforced concrete beams using steel plates bonded on beam web: experiments and analysis. *Construct Bldg Mater.* 14(5): 237–44
- Adhikary, B. B., and Mutsuyoshi, H. (2005). Shear strengthening of reinforced concrete beams using various techniques. *Construct Bldg Mater.*, 20 (6): 366–373.
- Adhikary, B. B., and Mutsuyoshi, H. (2006). Shear strengthening of RC beams with web bonded continuous steel plates. *Construct Bldg Mater.*, 20 (5): 296–307.
- AISC (2017). *Steel Construction Manual*, 15th Ed. American Institute of Steel Construction Inc., Chicago, IL, 2192.
- ASTM A1061 (2020). Standard Test Method for Testing Multi-Wire Steel Prestressing Strand. *American Society for Testing and Materials (ASTM)*, West Conshohocken, PA.
- ASTM C39 (2018). Standard Test Method for Compressive Strength of Cylindrical Concrete Specimens. *American Society for Testing and Materials (ASTM)*, West Conshohocken, PA.
- ASTM C42 (2018). Standard Test Method for Obtaining and Testing Drilled Cores and Sawed Beams of Concrete. *American Society for Testing and Materials (ASTM)*, West Conshohocken, PA.
- ASTM D3039/D3039M. (2014c). *Standard test method for tensile properties of polymer matrix composite materials*. West Conshohocken, PA: ASTM.
- ASTM D5766/D5766M-11. (2014a). *Standard test method for open-hole tensile strength of polymer matrix composite laminates*. West Conshohocken, PA: ASTM.

- ASTM D5961/D5961M. (2017). *Standard test method for bearing response of polymer matrix composite laminates*. West Conshohocken, PA: ASTM.
- ASTM D638. (2014b). *Standard test method for tensile properties of plastics*. West Conshohocken, PA: ASTM.
- Bank, L. C. (2004). Mechanically-fastened FRP (MF-FRP) – A Viable Alternative for Strengthening RC Members. *FRP Composites in Civil Engineering - CICE 2004*, (pp. 3–15), London, Taylor and Francis Group.
- Bank, L. C., and Arora, D. (2007). Analysis of RC beams strengthened with mechanically fastened FRP (MF-FRP) strips. *Composite Structures*, 79(2), 180-191.
- Bank, L. C., Lamanna, A. J., Ray, J. C., and Velazquez, G. I. (2002). Rapid strengthening of reinforced concrete beams with mechanically fastened, fiber-reinforced polymeric composite strips. *Rep No. ERDC/GSL TR-02-4*, U.S. Army Corps of Engineers Engineer Research and Development Center, Vicksburg, MS, 99.
- Barnes, R. A., Baglin, P. S., Mays, G. C., and Subedi, N. K. (2000) External steel plate systems for the shear strengthening of reinforced concrete beams. *Eng. Struct.* 23 (9): 1162–1176.
- Bomarito, G. F., Hochhalter, J. D., Ruggles, T. J., and Cannon, A. H. (2017). Increasing accuracy and precision of digital image correlation through pattern optimization. *Opt. Lasers Eng.* 91 (4): 73–85.
- Borowicz, D. T. (2002). *Rapid strengthening of concrete beams with powder-actuated fastening systems and fiber reinforced polymer (FRP) composite materials*. M.S. Thesis, University of Wisconsin-Madison, Madison, WI.
- Bourara, Z. (2019). *Long-Term Behavior and Modeling of Prestressed Mechanically-Fastened Fiber-Reinforced Polymer Retrofit for Prestressed Concrete Bridge Elements* (Master's dissertation). North Carolina State University.
- Cavalline, T., Whelan, M., Tempest, B., Goyal, R., and Ramsey, J. (2015). Determination of Bridge Deterioration Models and Bridge User Costs for the NCDOT Bridge Management System. *Technical Report No. FHWA/NC/2014-07*, North Carolina Department of Transportation, October, 188.
- Chen, J. F., and Teng, J. G. (2003). Shear capacity of FRP-strengthened RC beams: FRP debonding. *Construct Bldg Mater.*, 17(1):27
- Collins, M. P., and Mitchell, D. (1997). *Prestressed Concrete Structures*, 766. Toronto: Response Publications.
- Dempsey, D., D., and Scott, D. W. (2006). Wood Members Strengthened with Mechanically Fastened FRP Strips. *Journal of Composites for Construction*, 10(5), 392-398.

- Devore, J. L. (2015). *Overview and descriptive statistics*. Chap. 1 in *Probability and statistics for engineering and the sciences*. 9th ed. 1–51. Boston: Cengage Learning.
- Diab, H., Wu, Z., and Iwashita, K. (2009). Short and long-term bond performance of prestressed FRP sheet anchorages. *Engineering Structures*, 31(5), 1241-1249.
- Du, G. C., and Tao, X. K., (1985) Ultimate Stress of Unbonded Tendons in Partially Prestressed Concrete Beams. *PCI Journal*, V. 31, No. 6, pp. 72-91.
- Ebead, U. (2011). Hybrid Externally Bonded/Mechanically Fastened Fiber-Reinforced Polymer for RC Beam Strengthening. *ACI Structural Journal*, 108(6), 669-678.
- Ekenel, M., Rizzo, A., Myers, J. J., and Nanni, A. (2006). Flexural Fatigue Behavior of Reinforced Concrete Beams Strengthened with FRP Fabric and Precured Laminate Systems. *Journal of Composites for Construction*, 10(5), 433-442.
- Ebead, U., and Saeed, H. (2014). Flexural and Interfacial Behavior of Externally Bonded/Mechanically Fastened Fiber-Reinforced Polymer-Strengthened Reinforced Concrete Beams. *ACI Structural Journal; Farmington Hills*, 111(4), 741-751.
- Ekenel, M., Rizzo, A., Myers, J. J., & Nanni, A. (2006). Flexural Fatigue Behavior of Reinforced Concrete Beams Strengthened with FRP Fabric and Precured Laminate Systems. *Journal of Composites for Construction*, 10(5), 433–442. [https://doi.org/10.1061/\(ASCE\)1090-0268\(2006\)10](https://doi.org/10.1061/(ASCE)1090-0268(2006)10)
- Elsayed, W. E., Ebead, U. A., and Neale, K. W. (2009). Studies on Mechanically Fastened Fiber-Reinforced Polymer Strengthening Systems. *ACI Structural Journal; Farmington Hills*, 106(1), 49- 59.
- El-Maaddawy, T. A. (2014). Mechanically Fastened Composites for Retrofitting Corrosion-Damaged Reinforced-Concrete Beams: Experimental Investigation. *Journal of Composites for Construction*, 18(2), doi:10.1061/(ASCE)CC.1943-5614.0000447.
- El-Maaddawy, T., Nessabi, A., and El-Dieb, A. (2013). Flexural Response of Corroded Reinforced Concrete Beams Strengthened with Powder-Actuated Fastened Composites. *Journal of Composites for Construction*, 17(6), doi:10.1061/(ASCE)CC.1943-5614.0000395.
- Galati, D., Rizzo, A., and Micelli, F. (2007). Comparison of reinforced concrete beams strengthened with FRP pre-cured laminate systems and tested under flexural loading. In *Proceeding of the FRPRCS-8*, Patras, Greece, 16-18 July.
- Harajli, M. H., Khairallah, N., and Nassif, H. (1997). Externally prestressed members: evaluation of second-order effects. *J. Struct. Eng.*, 125, 1151–1161.

- Higgs, A., Barr, P. J., and Halling, M. W. (2015) Comparison of Measured and AASHTO LRFD-Predicted Residual Prestress Forces, Shear and Flexural Capacities of High-Strength Prestressed-Concrete Bridge Girders. *J. Bridge Eng.* 20, 05014009.
- Hoult, N. A., Take, W. A., Lee, C., and Dutton, M. (2013). Experimental accuracy of two-dimensional strain measurements using digital image correlation. *Eng. Struct.* 46: 718–726.
- Jensen, J., Thorenfeldt, E., and Tomaszewicz, A. (1988). Structural properties of high-strength concrete and applications in design. In Vol. 3 of *Proc., Int. Conf. on Behavior of Offshore Structures*, 1129–1144. Trondheim, Norway: Tapir Publishers.
- Kelly, D.J., Bradberry, T.E., and Breen, J.E. (1987). Time Dependent Deflections of Pretensioned Beams. *Research Report CTR 381-1*, Center for Transportation Research – The University of Texas at Austin.
- Khairallah, N., and Harajli, M. H. (1997). Experimental and analytical evaluation of the behavior of concrete T beams with external prestressing. *Res. Rep.*, Dept. of Civ. and Envir. Engrg., Faculty of Engineering and Architecture, American University of Beirut, Beirut, Lebanon.
- Khalifa, A., and Nanni, A. (2000). Improving shear capacity of existing RC T-section beams using CFRP composites. *Cem Concr Compos.* 22: 165–74.
- Khalifa, A., Gold, W. J., Nanni, A., and Aziz, A. (1998). Contribution of externally bonded FRP to shear capacity of RC flexural members. *ASCE J Compos Constr.* 2(4):195–203.
- Lamanna, A. J., Bank, L. C., and Borowicz, D. T. (2004a). Mechanically Fastened FRP Strengthening of Large Scale RC Bridge T Beams. *Advances in Structural Engineering*, 7(6), 525-538.
- Lamanna, A. J., Bank, L. C., and Scott, D. W. (2001). Flexural strengthening of RC beams using fasteners and FRP strips. *ACI Structural Journal*, 98(3), 368-376.
- Lamanna, A. J., Bank, L. C., and Scott, D. W. (2004b). Flexural Strengthening of Reinforced Concrete Beams by Mechanically Attaching Fiber-Reinforced Polymer Strips. *Journal of Composites for Construction*, 8(3), 203-210.
- Lee, D. K., and Kim, K. S. (2011). Flexural strength of prestressed concrete members with unbonded tendons. *Struct Eng Mech.* 38(5): 675–96
- Lee, H. L., Lopez, M. M., and Bakis, C. E. (2009). Flexural behavior of reinforced concrete beams strengthened with mechanically fastened FRP strips. In *Proceeding of the FRPRCS-8*, Patras, Greece, 16-18 July.
- Lee, J. H., Lopez, M. M., and Bakis, C. E. (2009). Slip effects in reinforced concrete beams with mechanically fastened FRP strip. *Cem. Concr. Compos.* 31 (7): 496–504.

- Lin, S. H. (2021) *Analysis and Design of Deteriorated Prestressed Concrete Bridge Beams in Flexure and Shear Repaired with Prestressed Mechanically-Fastened Fiber-Reinforced Polymer*. (Doctoral dissertation). North Carolina State University.
- Martin, J. A., and Lamanna, A. J. (2008). Performance of Mechanically Fastened FRP Strengthened Concrete Beams in Flexure. *Journal of Composites for Construction*, 12(3), 257-265.
- Martinelli, E., Napoli, A., Nunziata, B., and Realfonzo, R. (2014). A 1D finite element model for the flexural behaviour of RC beams strengthened with MF-FRP strips. *Composite Structures*, 107, 190- 204.
- Mattock, A. H. (1979). Flexural strength of prestressed concrete sections by programmable calculator. *PCI J.* 24 (1): 32–54.
- McCoy, B. C. (2019). *Design and Implementation of a New Retrofit for Prestressed Concrete Bridge Elements Using Mechanically-Fastened Fiber-Reinforced Polymer* (Doctoral dissertation). North Carolina State University.
- McCoy, B. C., Bourara, Z., Lucier, G.W., Seracino, R., and Liu, M., and Lin, S. H. (2021). Prestressed MF-FRP: An Experimental Study of a Rapid Retrofit Concept for Deteriorated Prestressed C-Channel Beams. *ASCE Journal of Performance of Constructed Facilities*, 35(1), 1-10.
- McCoy, B. C., Bourara, Z., Seracino, R., and Lucier, G. W. (2019). Anchor bolt patterns for mechanically-fastened FRP plates. *J. Compos. Constr.*, 23(4): p.04019024.
- Michels, J., Martinelli, E., Czaderski, C., and Motavalli, M. (2014). Prestressed CFRP Strips with Gradient Anchorage for Structural Concrete Retrofitting: Experiments and Numerical Modeling. *Polymers*, 6, 114-131.
- Naaman, A. E., and Alkhairi, F. M. (1991a). Stress at ultimate in unbonded post-tensioning tendons - Part 1: evaluation of the state-of-the-art. *ACI Struct. J.*, 88(5), 641-651.
- Naaman, A. E., and Alkhairi, F. M. (1991b). Stress at ultimate in unbonded post-tensioning tendons - Part 2: proposed methodology. *ACI Struct. J.*, 88(6), 693-692.
- Naaman, A. E., and Breen, J. E., eds. (1990). External prestressing in bridges. *ACI Special Publication SP-120*, American Concrete Institute, Detroit.
- Napoli, A., Matta, F., Martinelli, E., Nanni, A., and Realfonzo, R. (2010). Modelling and verification of response of RC slabs strengthened in flexure with mechanically fastened FRP laminates. *Magazine of Concrete Research*, 62(8), 593-605.
- Nawy, E. G. (2010). *Prestressed Concrete: A Fundamental Approach (5th Ed.)*. Upper Saddle River, New Jersey: Pearson Education, Inc.

- North Carolina DOT. (1966). *Standard prestressed concrete channels 20 ft., 25 ft., and 30 ft.-Spans, 24 ft., 29 ft., and 34 ft.-roadways*. Standard BMD-13. Raleigh, NC: North Carolina DOT.
- NCDOT (North Carolina DOT). (2018). *Stand specifications for roads and structures*. Raleigh, NC: NCDOT.
- NCDOT. (n.d.). NCDOT AADT Mapping Application. Retrieved March 12, 2018, from <http://ncdot.maps.arcgis.com/apps/webappviewer/index.html?id=5f6fe58c1d90482ab9107ccc03026280>
- Quattlebaum, J. B., Harries, K. A., & Petrou, M. F. (2005). Comparison of Three Flexural Retrofit Systems under Monotonic and Fatigue Loads. *Journal of Bridge Engineering*, 10(6), 731–740. [https://doi.org/10.1061/\(asce\)1084-0702\(2005\)10:6\(731\)](https://doi.org/10.1061/(asce)1084-0702(2005)10:6(731))
- Oehlers, D. J. (2001). Development of design rules for retrofitting by adhesive bonding or bolting either FRP or steel plates to RC beams of slabs in bridges and buildings. *Composites Part A: Applied Science and Manufacturing*, 32, 1345-1355.
- Oehlers, D. J., and Bradford, M. A. (1995). *Composite steel and concrete structural members: Fundamental behavior*. 549. Kidlington, UK: Elsevier.
- Oehlers, D. J., and Seracino, R. (2004). *Design of FRP and Steel Plated RC Structures: Retrofitting Beams and Slabs for Strength, Stiffness, and Ductility*. Elsevier, Kidlington, U.K., 228.
- O'Neill, C. R., and French, C. E. (2012) Validation of Prestressed Concrete I Beams Deflection and Camber Estimates. *Research Report MN-RC-16.*, University of Minnesota.
- OSHA (Department of Labor Occupational Safety and Health Administration). 2018. "Construction industry regulations." Accessed September 12, 2018.
- Piatek, B., Siwowski, T., Michalowski, J., and Blazewicz, S. (2020). Flexural strengthening of RC beams with prestressed CFRP strips: Development of novel anchor and tensioning system. *J. Compos. Constr.* 24 (3):04020015.
- Precast Prestressed Concrete Institute. (2017). *PCI Design Handbook: Precast and Prestressed Concrete 8th Ed.* (8th ed.). Chicago, IL.
- Rahman, A. H., Kingsley, C., Richard, J., and Crimi, J. (1998). Experimental investigation of the mechanism of deterioration of FRP reinforcement for concrete. *Fiber Composites in Infrastructure, Proceedings of the Second International Conference on Fibre Composites in Infrastructure*, ICC-98, Tucson, AZ, Vol. 2, 501-511.
- Ramberg, W., and W. R. Osgood. (1943). Vol. 902 of *Description of stress-strain curve by three parameters: NACA technical notes*. Washington, DC: National Advisory Committee for Aeronautics.

- Realfonzo, R., Martinelli, E., Napoli, A., and Nunziata, B. (2013). Experimental investigation of the mechanical connection between FRP laminates and concrete. *Composites Part B: Engineering*, 45(1), 341-355.
- Rosenboom, O., and Rizkalla, S. H. (2008). *Experimental study of intermediate crack debonding in fiber-reinforced polymer strengthened beams*. 41–50. Farmington Hills, MI: American Concrete Institute.
- Sena-Cruz, J. M., Barrow, J. A. O., Coelho, M. R. F., and Silva, L. F. F. T. (2012). Efficiency of different techniques in flexural strengthening of RC beams under monotonic and fatigue loading. *Construction and Building Materials*, 29, 175-182.
- Stöcklin, I., and Meier, U. (2003). Strengthening of concrete structures with prestressed and gradually anchored CFRP strips. *Proc. of the 6th Int. Symp. Fiber Reinforced Polymer Reinforcement for Concrete Structures (FRPRCS-6)*, World Scientific, Singapore, 1321–1330
- Strongwell. (2016). “SAFSTRIP® Fiber Reinforced Strengthening Strip.” Online at www.strongwell.com [accessed 11/13/2017].
- Triantafillou, T. C., and Deskovic, N. (1991). Innovative Prestressing with FRP Sheets: Mechanics of Short-Term Behavior. *Journal of Engineering Mechanics*, 117(7), 1652-1672.
- Tan, K. H., and Ng, C. K. (1997). Effects of deviators and tendon configuration on behavior of externally prestressed beams. *ACI Struct. J.*, 94(1), 13–22.
- Tan, K. H., and Saha, M. K. (2007). *Mechanically Fastened FRP-Strengthened RC Beam under Cyclic Loading* (pp. 368–369). Fibre-Reinforced Polymer Reinforcement for Concrete Structures: Proceedings of the 8th International Symposium on Fibre-Reinforced Polymer Reinforcement for Concrete Structures, Patras, Greece, July 16- 18, 2007.
- Tan, K. H., and Tjandra, R. A. (2007). Strengthening of RC continuous beams by external prestressing. *J. Struct. Eng.* 133 (2): 195-204.
- Wight, J. K., and MacGregor, J. G. (2016). *Reinforced concrete: Mechanics and design*, Pearson, N.J.
- Xie, H., and Kang, Y. (2015). Digital image correlation technique. *Opt. Lasers Eng.* 65 (2): 1–2.
- Yang, D. S., Park, S.K., and Neale, K. W. (2009). Flexural behavior of reinforced concrete beams strengthened with prestressed carbon composites. *Compos. Struct.* 88 (4): 497–508.

APPENDICES

Appendix A: Detailed Installation Procedure of the MF-FRP Repair System

Appendix A presents the detailed installation procedure of the MF-FRP repair system for a DOT maintenance crew. The content is an updated version of Appendix C and D from McCoy (2019). This Appendix also includes the required materials, recommended tools, and general suggestions when considering the MF-FRP system as a retrofit application. Table A.1 presents the materials needed for *a single MF-FRP repair system*. The maximum MF-FRP repair systems that can be installed on either a C-channel beam (one on each stem) or cored slab (one under each core) is two.

All hardware is readily available from multiple commercial service. The 22-bolt pattern is designed based on the FRP plate manufactured by Strongwell. Therefore, the FRP plate has to be purchased directly from this manufacturer. The turnbuckle system is the element used to prestress the repair system. It is readily available; however, the turnbuckle needs to have a right- and left-hand thread at either end of the turnbuckle body to ensure only one end moves during the prestressing process. Figures A.1 and A.2 show the MF-FRP repair system applied on a C-channel beam and a cored slab, respectively. Figures A.3 to A.14 show the design drawing details and welding plan of the steel elements of the MF-FRP repair system. It is worth mentioning that the tapping thread direction for the turnbuckle couplers (refer to Figures A.6(a) and A.8(b)) have to be consistent with the thread direction of the turnbuckle rods.

Table A.1: Required material for a single C-channel beam stem repair.

Item	Quantity	Note
½ in.-13 Bolts (1.5" Long) (Grade A325 Steel)	44	Bolts (Mechanically Fastened FRP Plate to FRP Connector Plate)
½ -13 in. Nuts (Steel – Grade 8)	44	
½ in. Flat Washers	88	
Alloy steel shoulder bolts: 1.5 in. shoulder diameter (1-1/8 in. threaded shank)	2	Alloy Steel Shoulder Bolts (Anchor Plate to FRP Connector to provide pinned connections) (Black-Oxide coated steel bolts and nuts)
1-1/8 in.-7 Nuts (Grade 8)	2	
1-1/8 in. Flat Washer	2	
¾ in.-10 Bolts (7" Long) (Grade A325 Steel)	12	Anchor Bolts (FRP System to Concrete Section)
¾ -10 in. Nuts (Black-Oxide Steel – Grade 8)	12	
¾ in. Flat Washers	12	
0.812 in. Wedge Washers	12	
Hex bar ($W_d = 2$ in.)	8 in. x 2	Turnbuckle System to FRP Connector Plate and Turnbuckle Plate (One right-hand thread, and one left-hand thread)
Fixed Anchor Plates	2	Steel Elements (Grade 50 Steel)
FRP Connector – Dead-end	1	
FRP Connector – Live-end	1	
Turnbuckle Pates	1	Prestressing System (Available from Cleveland City Forge, or other manufacturer with similar product)
Turnbuckle Sets (body with thread rod) (TB27 - TBKL ASSY. 1-1/8 x 12 with 13" - All thread stubs, RH/LH C1030/35)	1	
FRP Plate	Length varies depending on location of anchor plates on beam	Composite Material (From Strongwell)

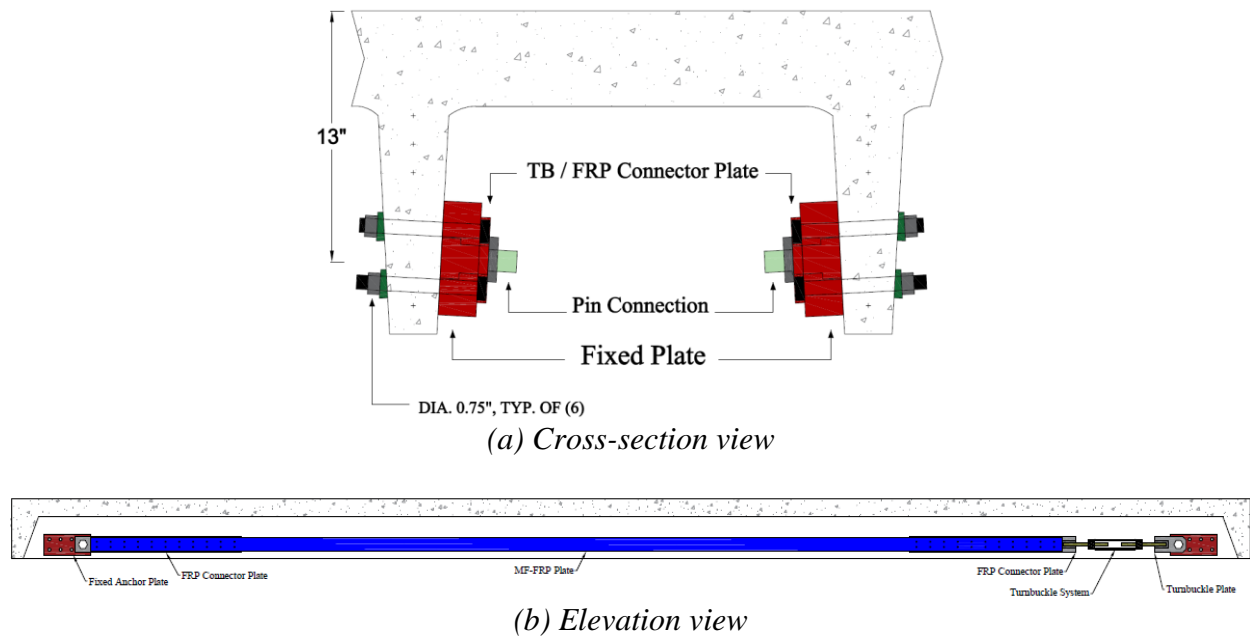


Figure A.1: MF-FRP repair system installed on typical C-channel beam.

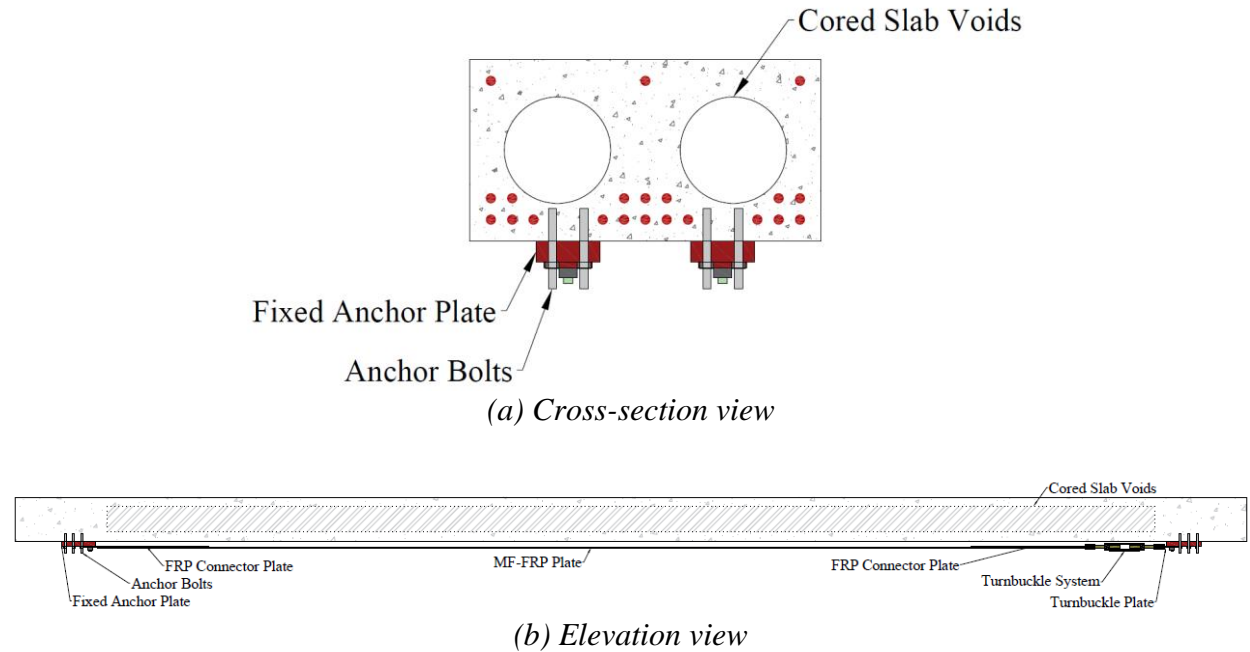


Figure A.2: MF-FRP repair system on typical cored slab.

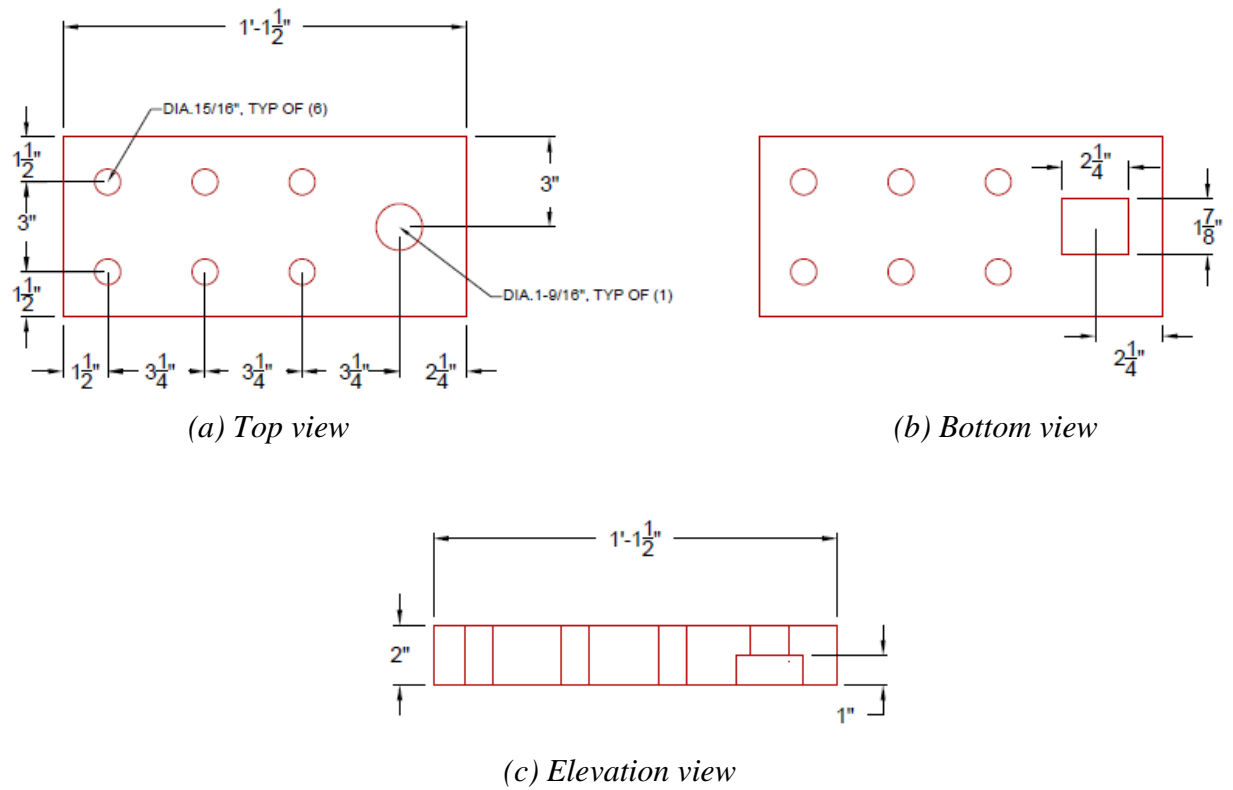


Figure A.3: Fixed anchor plate design detail.

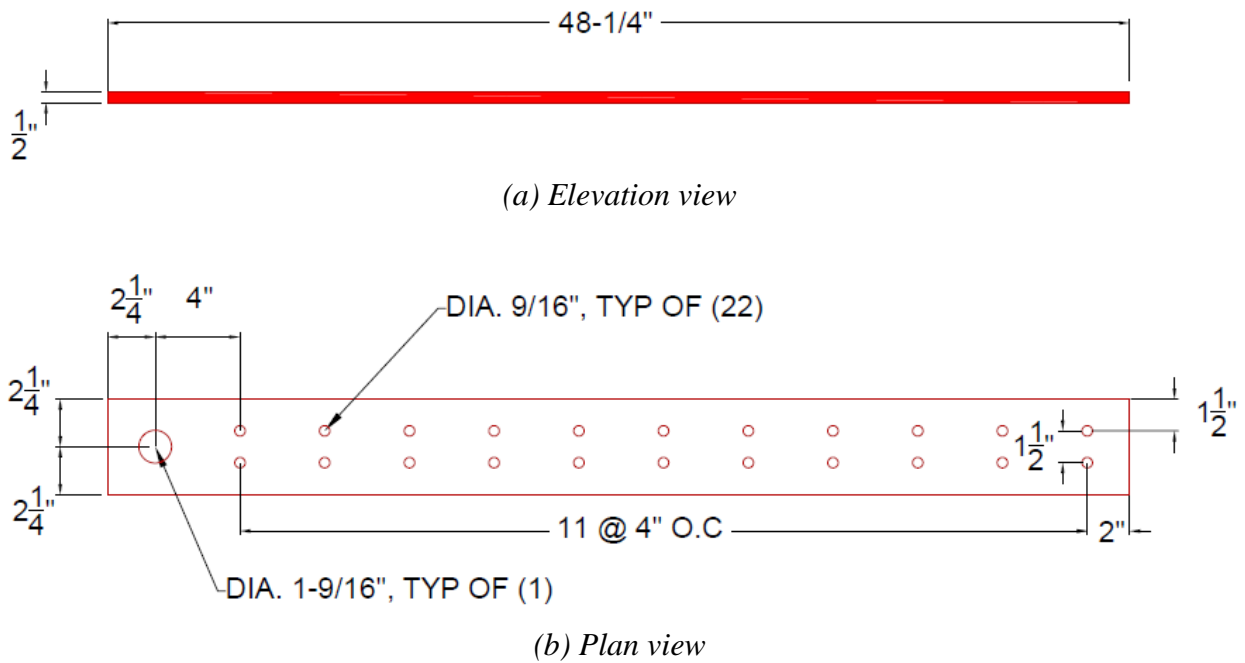
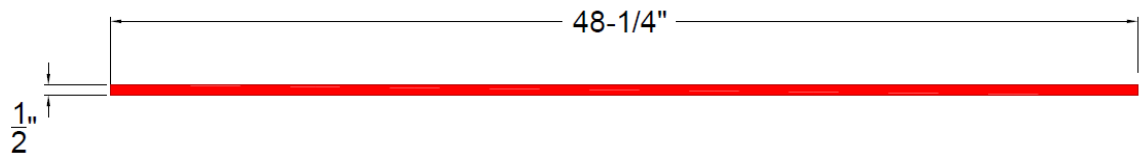
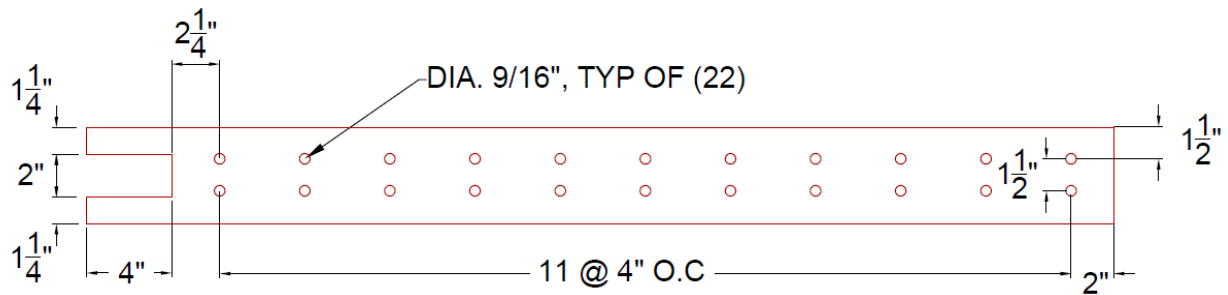


Figure A.4: FRP connector plate 1 design detail.

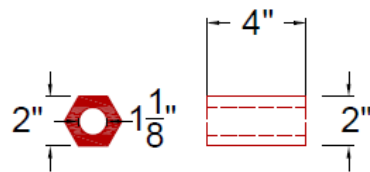


(a) Elevation view

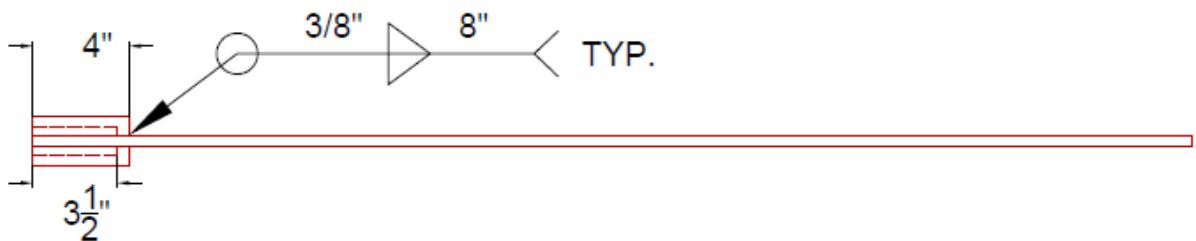


(b) Plan view

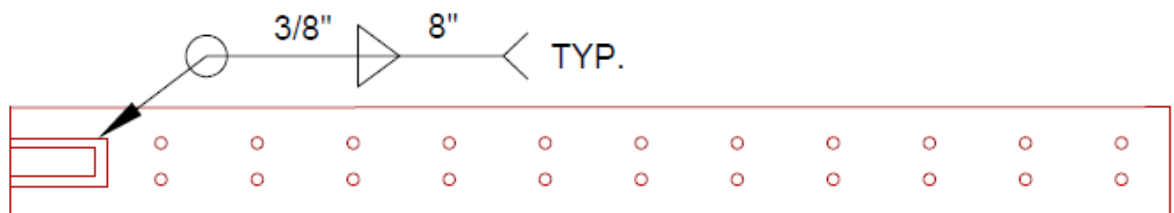
Figure A.5: FRP connector plate 2 design detail.



(a) Turnbuckle coupler



(b) Elevation view



(c) Plan view

Figure A.6: FRP connector plate 2 – weld detail.

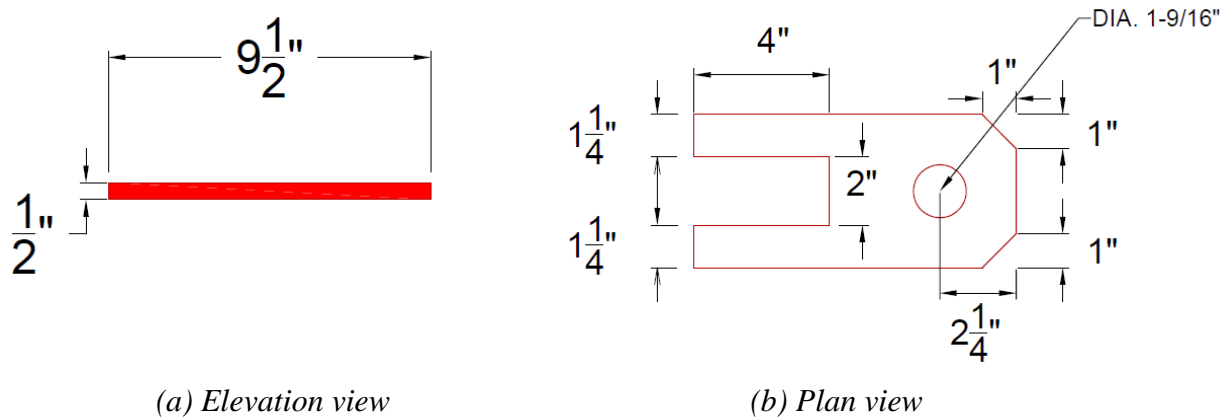
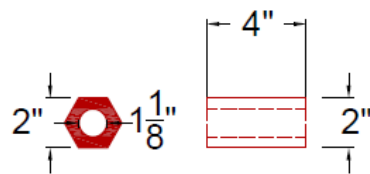


Figure A.7: Turnbuckle plate design detail.



(a) Turnbuckle coupler

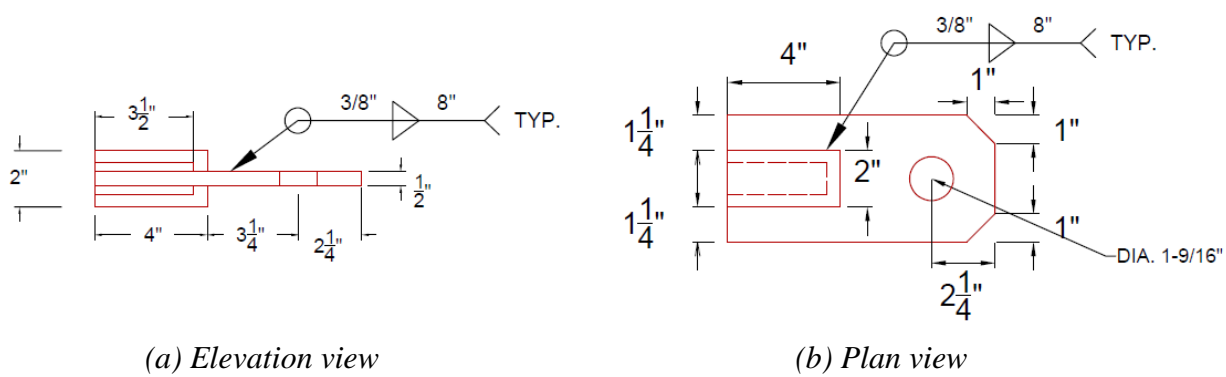


Figure A.8: Turnbuckle plate - weld detail.

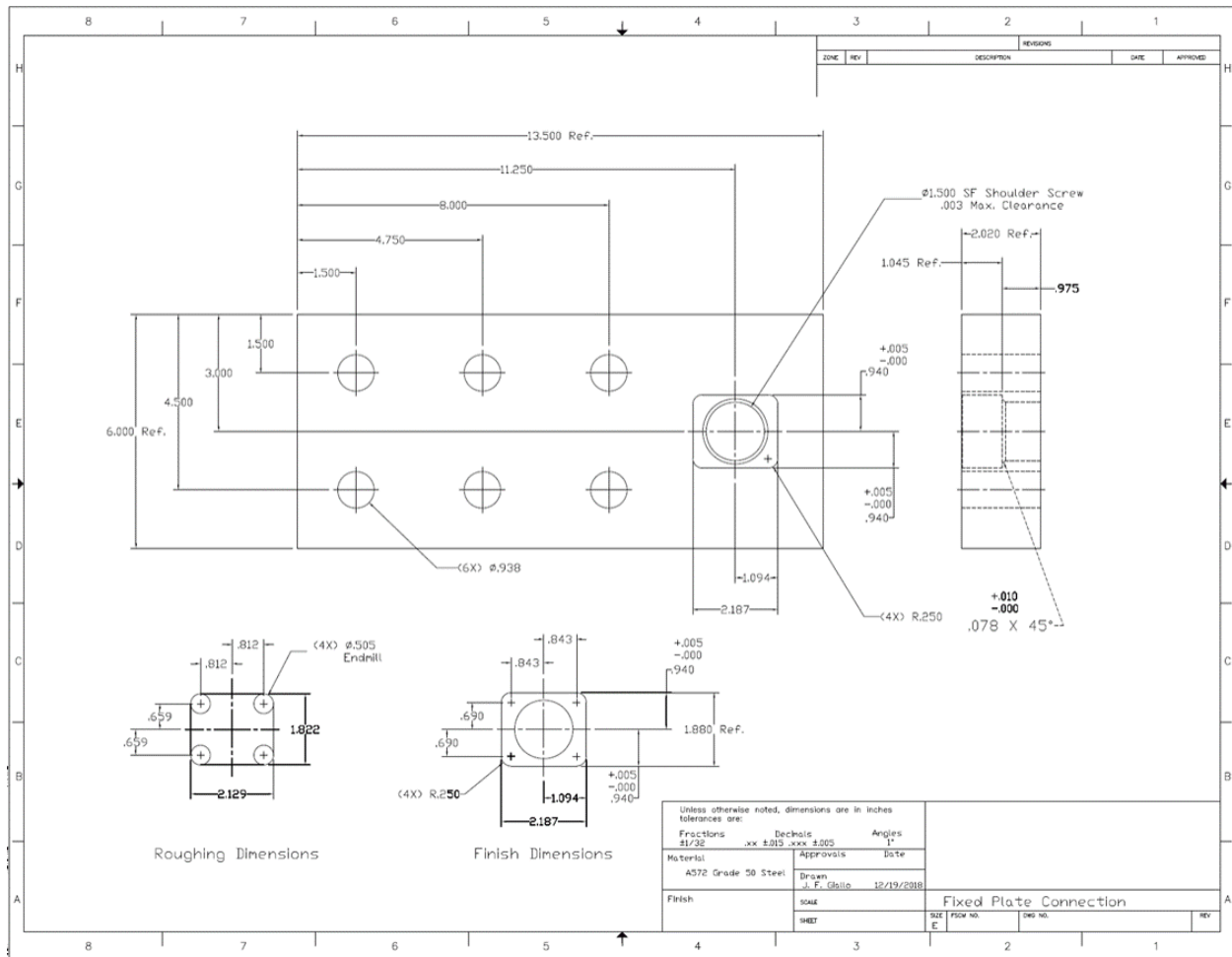


Figure A.9: Fixed anchor plate machinist as-built drawing.

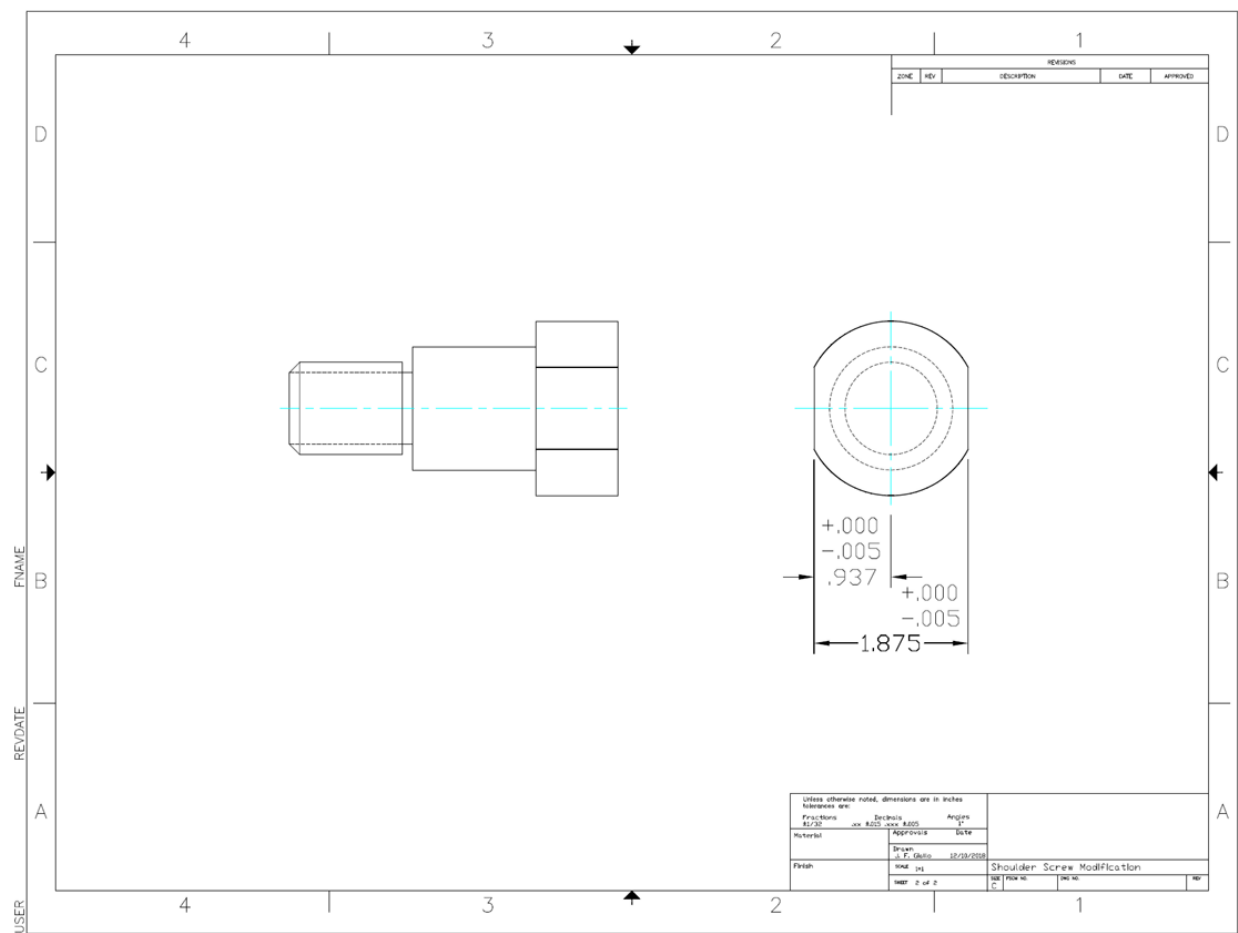


Figure A.10: Shoulder bolt (pin) machinist as-built detail.

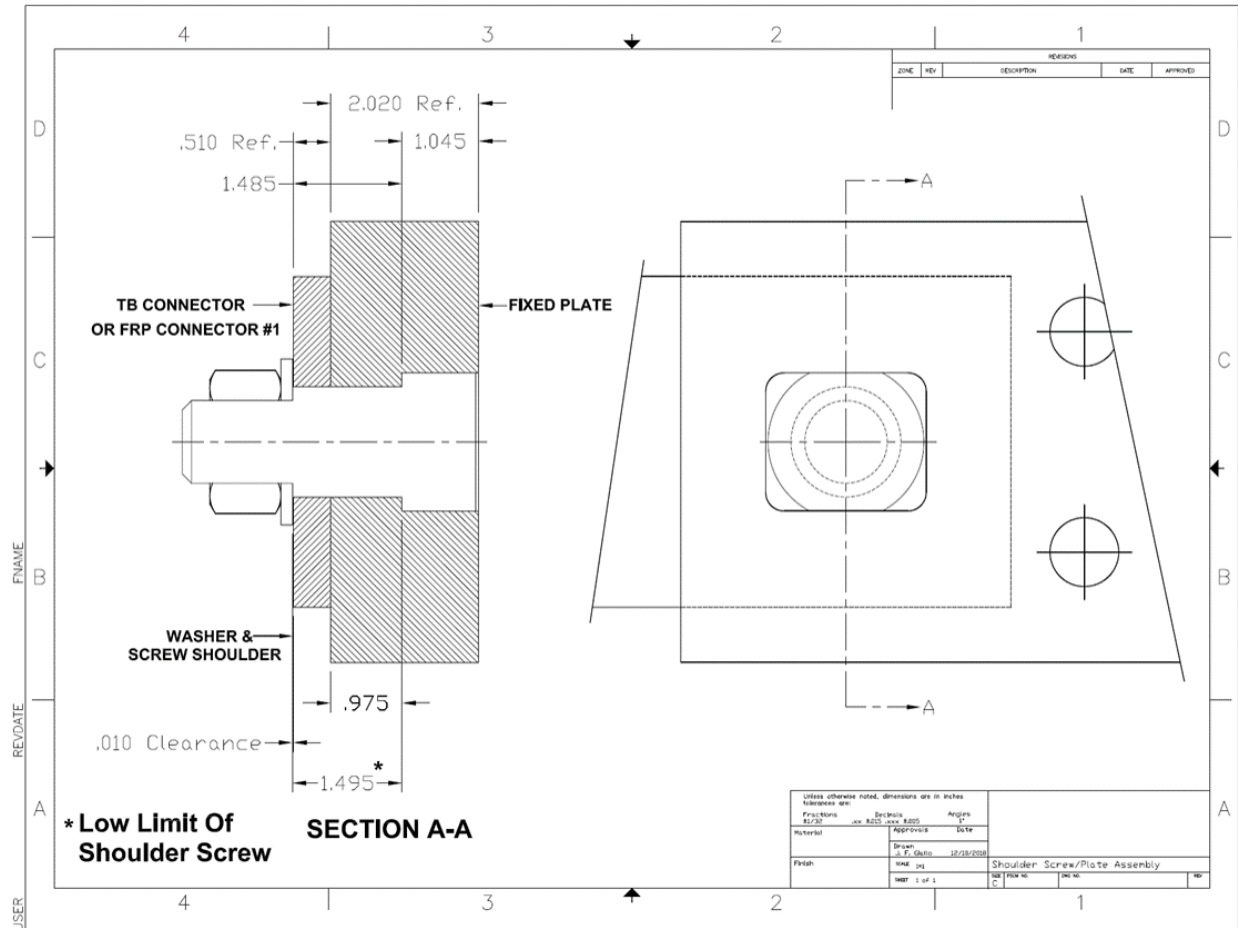


Figure A.11: Fixed anchor plate-pin as-built assembly detail.

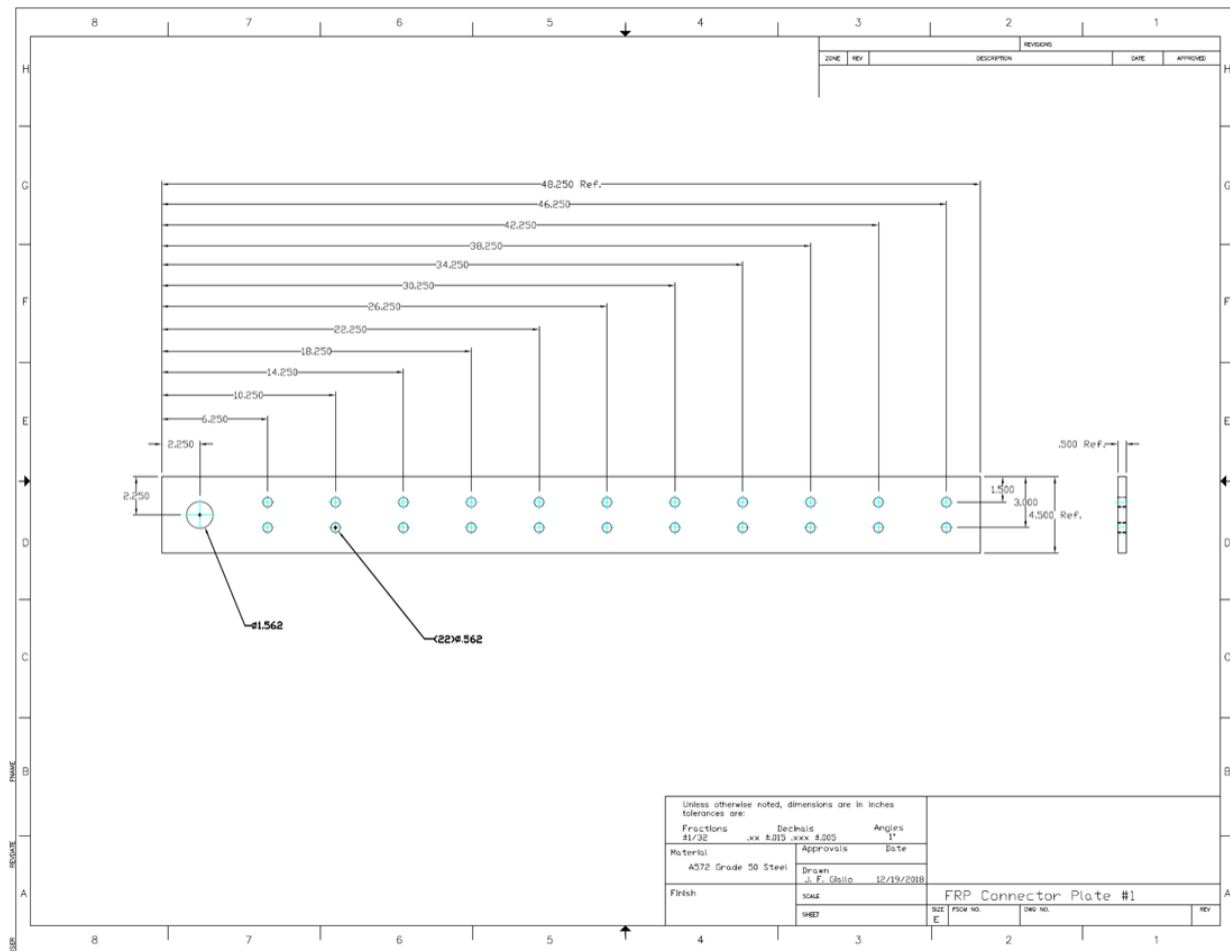


Figure A.12: FRP connector plate 1 machinist as-built drawing.

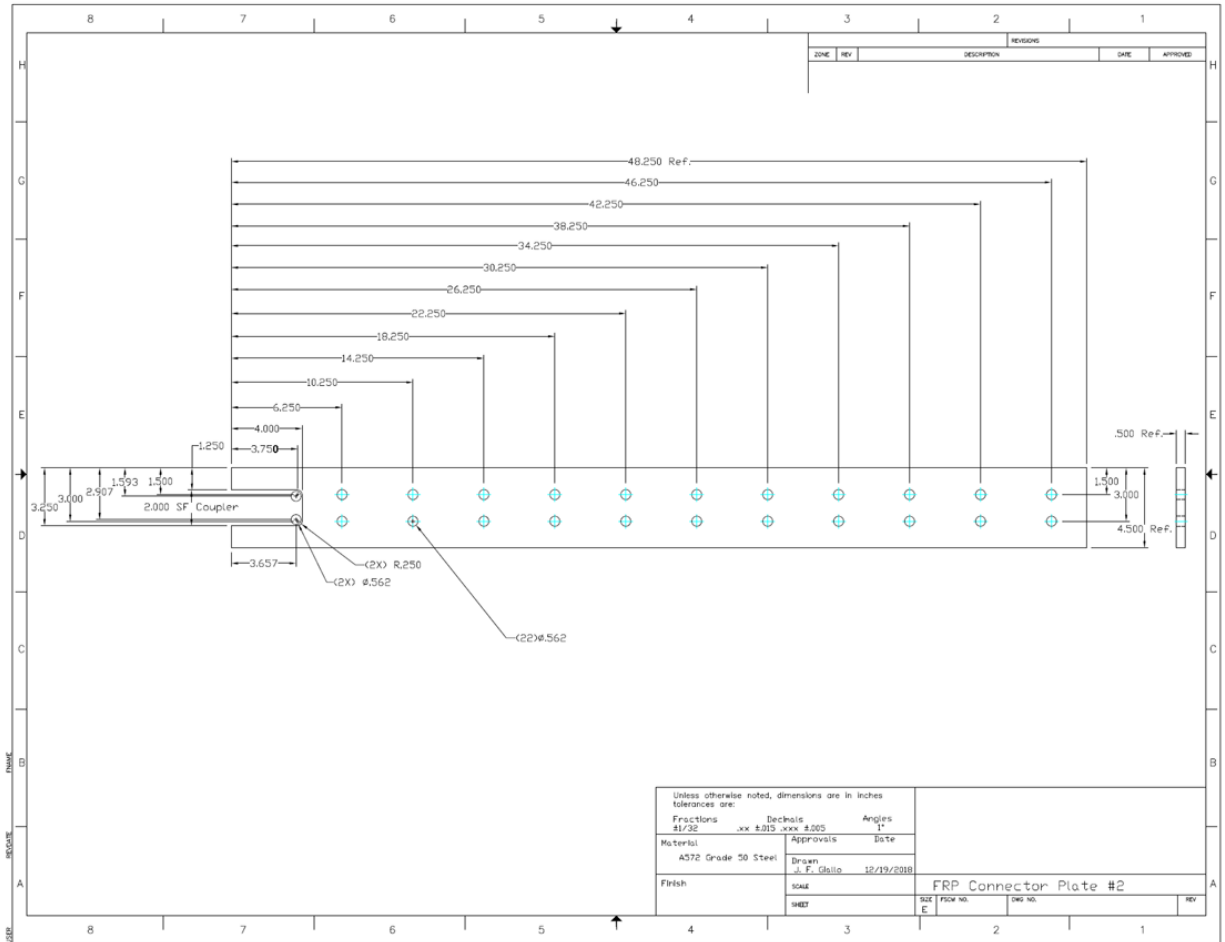


Figure A.13: FRP connector plate 2 machinist as-built drawing.

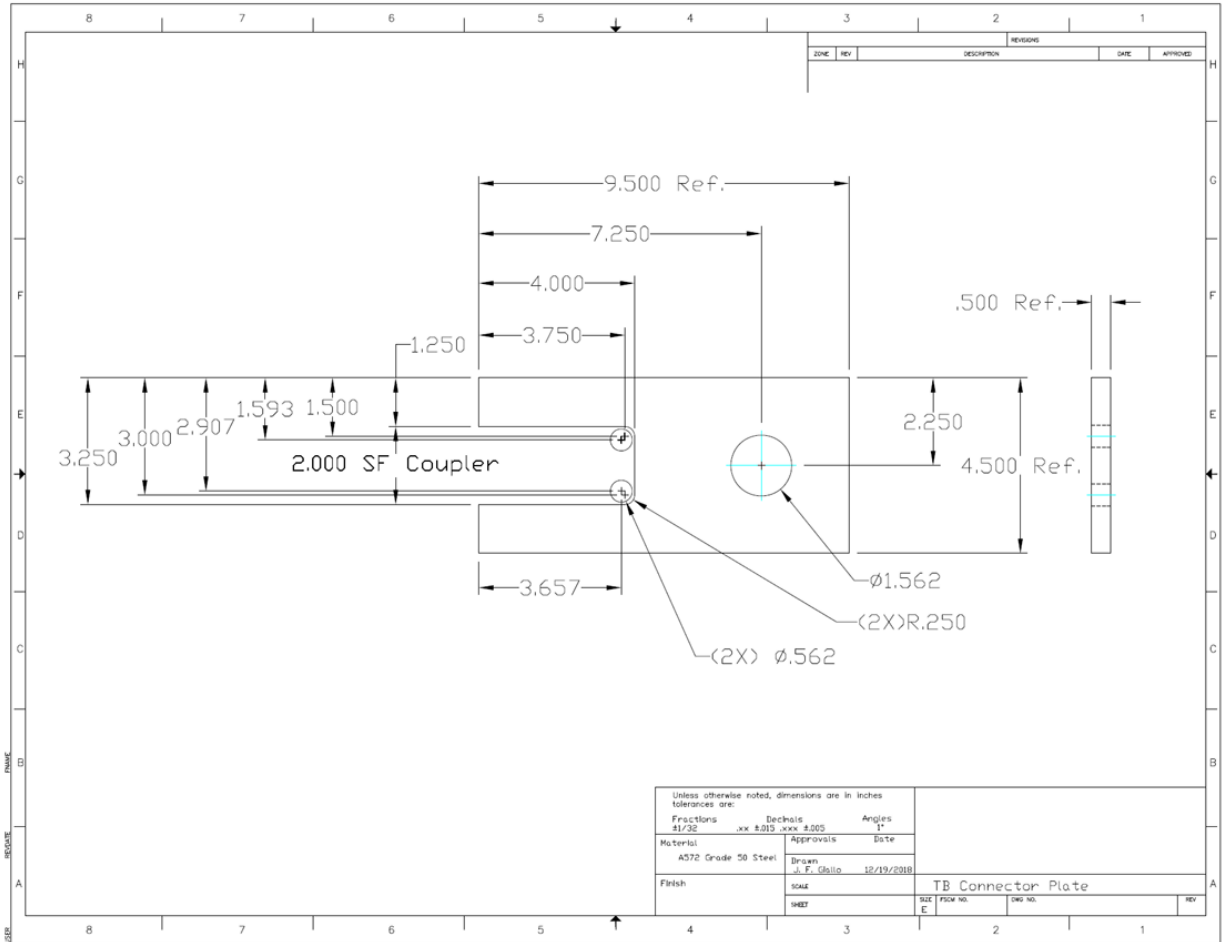


Figure A.14: Turnbuckle (TB) plate machinist as-built drawing.

Table A.2 presents the tools required for the installation. Table A.3 gives a detailed installation procedure of the MF-FRP repair system, to provide DOT maintenance crews a useful reference.

Table A.2: Required tools for the installation.

Item	Note
Hammer Drill	To drill concrete holes for the fixed anchor bolts.
7/8" Drill Bit	To create holes with 1/8" diameter larger for the 3/4" anchor bolts.
9/16" Drill Bit	To drill additional holes on the FRP plates if needed.
Hand-cutting Wheel	To shorten the FRP plates if needed.
Drill Bit to cut steel	To cut through the stirrups or prestressing strands if they are hit during drilling anchor holes.
Wrenches	Use for tightening the nuts on each bolt with different diameters and for prestressing the MF-FRP repair system.
C-clamps	To hold the wooden template of the fixed anchor plate and shear strengthening plate while drilling.
Torque Wrench	To provide the 60 ft.-lbs. on the FRP bolts.

Witness marks can be used to provide an easy way to apply the prestress force at the time of installation, as well as to inspect the level of prestress while in-service through the relative displacement between the MF-FRP and the concrete (that is, the FRP elongation). The maximum recommended prestress force on each MF-FRP plate for a C-channel beam and cored slab installation is 18.5 kips and 21.7 kips, respectively.

The following describes the procedure to calculate the required FRP elongation during the initial prestressing operation:

1. Determine the length of each FRP plate.
 - 1.1. Determine the location of the fixed anchor plates at both ends of the concrete member.
 - 1.2. At each end, measure the distance from the beam end to the edge of the fixed anchor plate.

1.3. The required FRP length is obtained by subtracting the distances measured in Step 1.2 and 68 in. (length of steel elements and turnbuckle system). The turnbuckle system should be set to 25 in. initially to leave some flexibility for the system.

2. The required FRP elongation (ΔL_{TOT}) is calculated according to the following:

$$\Delta L_g = \frac{P_{FRP} L_g}{A_{FRP} E_{FRP}}$$

$$\Delta L_{TOT} = \Delta L_g + \Delta L_{slip}$$

where, ΔL_g is the elastic elongation of the FRP plate due to the prestressing force,

L_g is the gauge length over which ΔL_g is measured, and is equal to the required FRP length minus 65 in.,

P_{FRP} is the applied prestressing force (typically 18.5 kips or 21.7 kips for C-channel beams or cored slabs, respectively),

A_{FRP} is the FRP cross-sectional area, equal to 0.5 in² for the FRP plate used,

E_{FRP} is the FRP elastic modulus, equal to 9020 ksi for the FRP plate used, and

ΔL_{slip} is the axial displacement of the FRP considering bolt slip in all of the connections, which is taken as 0.4375 in.

Design recommendations and inspection criteria are presented in the following:

1. *Design and Installation Recommendations*

- 1.1. The flexural MF-FRP repair system is recommended only for C-channel beams with the equivalent of up to one lost prestressing strand per stem. For cored slabs, the repair system can be used when up to the equivalent of four prestressing strands are lost.
- 1.2. The shear strengthening plate is only designed for C-channel beams with deteriorated end-regions, including spalled concrete and with exposed stirrups or prestressing strands. All loose concrete must be removed and patched with a suitable material to enable the drilling of the anchor bolt holes and the transfer of forces from the bolts to the concrete section without failure of the patch. The shear strengthening plate is not needed if the end region of stems have solid and solid concrete.
- 1.3. There are no restrictions on the use of the prestressed MF-FRP retrofit system for typical cross-sectional geometry, material properties, span length, and steel prestressing strand layout of C-channel beams and cored slab prestressed concrete bridge superstructures
- 1.4. All steel elements are required to be Grade 50 steel, and should be coated to prevent, or delay, corrosion. Alternatively, stainless steel equivalents may be used.
- 1.5. The fixed anchor plate should be located as close as practically possible to the end of the beam, typically around 12-20 in.
- 1.6. The location of prestressing strands and stirrups at the end-regions should be identified to locate the anchor plate such internal steel is avoided when drilling the anchor bolt holes.
- 1.7. To make the drilling process more efficient in C-channel beam applications, the need for an angular chuck should be avoided, if possible.

2. Field Inspection Criteria

2.1. The current level of prestress force in the MF-FRP plates can be determined by measuring the distance between the witness marks identified at the time of installation to apply the initial prestress force.

2.1.1. Before prestressing, but after tensioning to remove the slack out of the system, create a witness mark by placing a mark (point A) on the concrete stem and a mark (point B) on the FRP plate, 1 ft. from the edge of the FRP connector plate (refer to Figure 4.30A.15). The witness mark (point A) can also serve the dual role of monitoring the level of prestress force in the MF-FRP during the prestressing operation

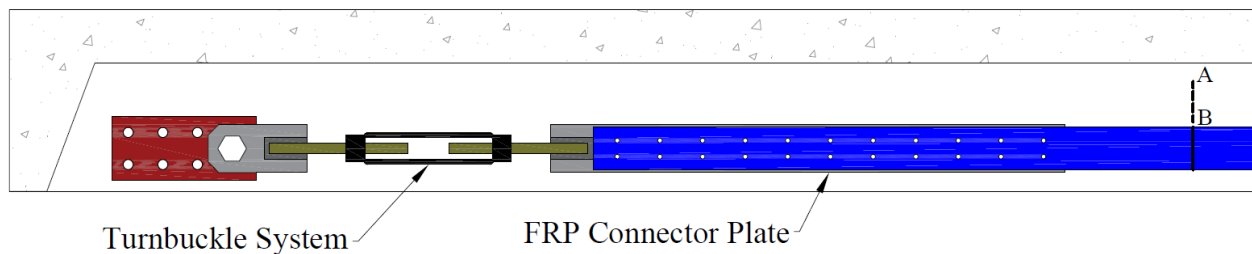


Figure A.15: Witness mark before prestressing the MF-FRP system.

2.1.2. During prestressing of the repair system, the distance between points A and B is the total axial displacement to achieve the desired prestressing force level (ΔL_{TOT}). Upon achieving the desired prestress force level, place a mark (point C) on the MF-FRP aligned with the edge of the FRP connector plate for the creep effect measurement. Figure 4.31A.16 shows the MF-FRP repair system labeling after prestressing

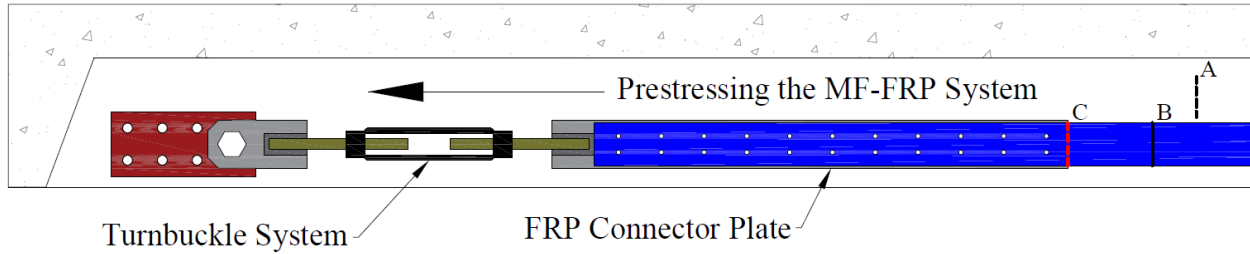


Figure A.16: MF-FRP repair system labeling after prestressing.

2.1.3. Approximately two weeks after the initial prestressing operation, the distance between point C and the edge of the FRP connector plate corresponds to the creep displacement, ΔL_{creep} . If the measured displacement at this point in time (ΔL_{creep}) exceeds 0.15 in. for 0.5 in. bolts (or 0.375 in. for 0.375 in. bolts), then the FRP plate has experienced an excessive amount of bearing creep deformation and should be replaced. If ΔL_{creep} is within allowable limits, then place a mark (point F) on the MF-FRP plate aligned with the edge of the FRP connector plate as the reference mark for the fatigue effect measurement. Figure 4.32 shows the MF-FRP repair system labeling at this time.

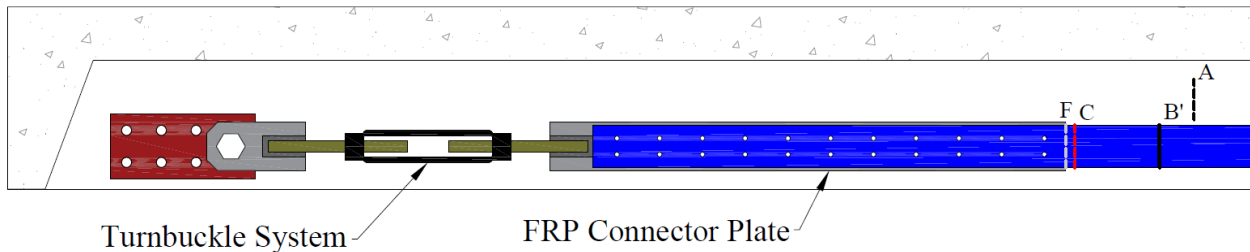


Figure A.17: MF-FRP repair system labeling 14 days after prestressing.

2.1.4. At least as part of the bi-annual bridge inspection, measure the distance between point F and the edge of the FRP connector plate. This measurement corresponds to the fatigue displacement, $\Delta L_{fatigue}$. Figure 4.33A.18 shows the MF-FRP repair system labeling condition during the bi-annual bridge inspection. IF $\Delta L_{fatigue}$

exceeds 0.25 in. (for either bolt size), then the FRP plate is approaching the end of its fatigue life and should be replaced.

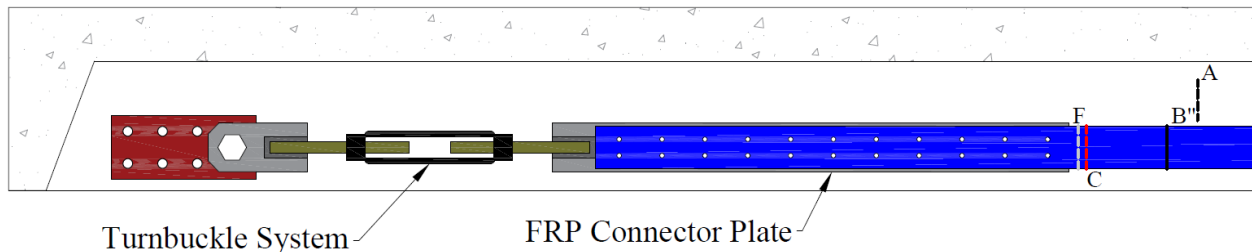


Figure A.18: MF-FRP repair system labeling condition during the bi-annual bridge inspection.

Measured displacements can be equated to prestress losses in the MF-FRP plates using the measured distance between points A and B" (see Figure A.18), following the procedure using Hooke's Law as described in Section 4.1.7.1. These losses can be predicted at the design stage, and can be restored by twisting the turnbuckle to stretch the MF-FRP plates to compensate for the lost elongation observed.

- 2.2. Inspect the concrete condition at the fixed anchor plates. Remove the repair system if concrete splitting has initiated and propagated along a line of bolt holes.
- 2.3. Inspect the surface condition of the MF-FRP plates for damage. Longitudinal shear cracks along the first 2 rows of bolts are typical and expected. However, if the longitudinal shear cracks have propagated beyond the first 4 rows of bolts, the MF-FRP system should be replaced.
- 2.4. All bolts should be checked to confirm their tightness. The tightness of the FRP bolts to 60 ft.-lbs. torque should be confirmed.
- 2.5. If too much prestress force in the MF-FRP plates has been lost, and the retrofit system is otherwise in good condition, the MF-FRP plates may be re-tensioned using the turnbuckle system.

Table A.3: Detailed installation procedure.

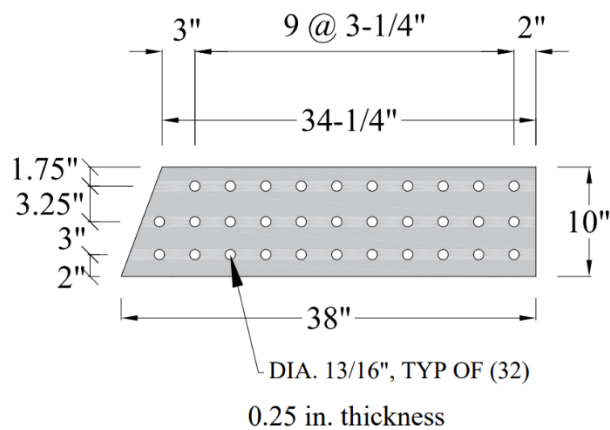
Steps	Detailed Activity
1.	Determine the extent of damage, including near the end-region anchor zone
1.1	Assess the condition in the anchor plate region and determine whether a shear strengthening plate is needed.
2.	Evaluate concrete quality
2.1	Estimate concrete strength using a Schmidt-Hammer.
2.1.1	If NDT (e.g., impact echo or shear wave tomography) is used, measure C_p before cutting core.
2.1.2	For C-channel beams, take at least one core in the stem, if possible.
3.	Prepare the MF-FRP repair system elements – Flexural/shear MF-FRP repair system (refer to Figure A.19).
4.	Prepare FRP for installation
4.1	Identify position of the MF-FRP anchor plate by locating stirrups and prestressing strands using a pachometer (rebar detector) to avoid hitting them (refer to Figure A.20).
	Cut FRP to appropriate length and numbers for the target beam.
4.2	<ul style="list-style-type: none"> Use a wet tile saw (best choice) or regular concrete saw with water sprayed to control crystalline SiO_2 and dust (refer to Figure A.21).
	Drill holes in the FRP plate.
4.3	<ul style="list-style-type: none"> Use a good quality 9/16" diameter drill bit for 1/2" diameter bolts. Take care to ensure the alignment of each row of bolts holes to avoid uneven bearing of the bolts (refer to Figure A.22)
5.	Installation Activities
5.1	Clamp a wooden template of the anchor plate to provide a reference for drilling (refer to Figure A.23).
5.2	Drill holes for the dead-end and live-end anchor plate (refer to Figure A.24).
5.3	Install dead-end and live-end fixed anchor plates using wrenches to fasten the anchor bolts (refer to Figure A.25).
5.3.1	Repeat Steps 5.1 to 5.3 for shear strengthening plate, if needed. Note that the shear strengthening plate is to be located behind the fixed anchor plates, adjacent to the concrete substrate.
	Attach FRP to the FRP connector plates.
5.4	<ul style="list-style-type: none"> Apply 60 ft.-lbs. torque on each FRP bolt using a torque wrench to prevent premature fatigue failure (refer to Figure A.26).
5.5	Attach FRP connector plate to the turnbuckle and turnbuckle plates.
5.6	Attach the FRP connector plate and turnbuckle plate to the dead-end and live-end anchor plates, respectively.
5.7	Remove FRP slack using wrenches to turn the turnbuckle until the FRP plate becomes straight with minor tension force.
5.8	Mark elongation witness marks for the desired prestress level on the concrete substrate and FRP plate (refer to Figure A.27) with the elongation witness marks before and after prestressing the MF-FRP repair system.
	Prestress MF-FRP plate to the designed prestress force.
5.9	<ul style="list-style-type: none"> A second wrench will be required to brace the FRP at the FRP connector plate to prevent the system from rotating while turning the turnbuckle during prestressing (refer to Figure A.28).
5.10	Demobilization



(a) FRP connector plates (Live-end) and turnbuckle plates



(b) FRP connector plates (Dead-end) and shear strengthening plates



(c) Detail of shear strengthening plate (Grade 50)



(d) Turnbuckle and hardware



(e) Fixed anchor plates



(f) MF-FRP plate

Figure A.19: Repair elements.



Figure A.20: Locating steel using a pachometer.



Figure A.21: Precutting FRP plates with a wet tile saw.



Figure A.22: Drilling holes in the FRP plates.



Figure A.23: Wooden template on stem.



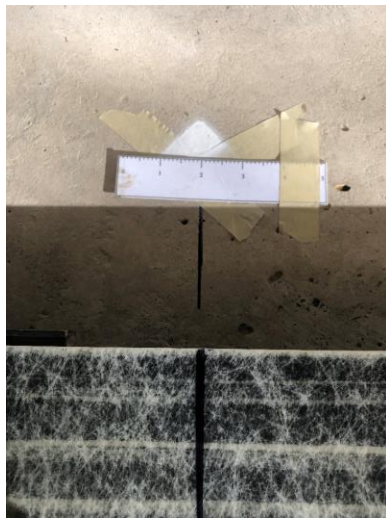
Figure A.24: Drilling anchor plate holes.



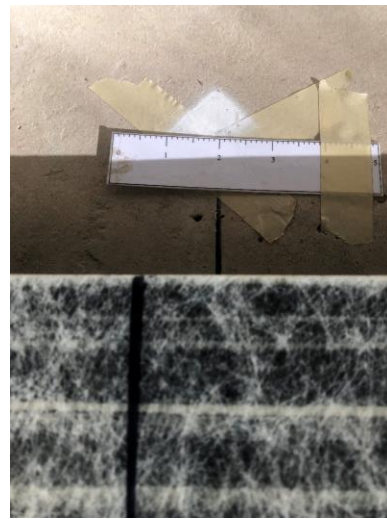
Figure A.25: Installing bolts of the fixed anchor plate (similar for shear strengthening plate).



Figure A.26: Tightening of FRP bolts to 60 ft.-lbs. torque.



(a) Before prestressing



(b) After prestressing

Figure A.27: Elongation witness mark.



Figure A.28: Prestressing the MF-FRP plates.